UNIVERSITÀ DEGLI STUDI DI FIRENZE

Dipartimento di Biologia Vegetale

Scuola di Dottorato "Ubaldo Montelatici"
Dottorato di ricerca in Biosistematica ed Ecologia Vegetale
XXI ciclo

SSD BIO07
anno 2008

Tesi di dottorato

Pigment variability and photosynthetic parameters of natural and cultured Raphidophyceans

Fabiola Fani

Prof. Paolo Grossoni
Coordinatore

Dott. Caterina Nuccio
Tutore

Prof. Luigi Lazzara
Cotutore

1. Introduction

1.1 Photoacclimation in phytoplankton

Phytoplankton distribution in the sea is strongly coupled with light and nutrients availability, which are the main factors limiting photosynthesis. Light and nutrients vary in time and space, both on a short- and/or a long-scale. In particular, light availability depends mostly on depth, in fact it is progressively absorbed and scattered by seawater, phytoplankton, tripton and yellow substance, as a consequence both light intensity and quality lower with depth. Moreover, water mass hydrodynamics can largely contribute to light-field variation, changing the microalgal position along the water column. Finally, light is subjected to natural daily and seasonal variations, which determine photoperiod length depending on solar elevation, and to more chaotic changes at the water-air interface as well, due to wind mixing, which modifies the subsurface focusing by wave, or to clouds cover (Kirk 1994).

Phytoplanktonic algae developed a great pigment variability and plastic photosystems, for taking advantage of light availability, though the different scales of its variations. The term 'photoacclimation' indicates a generally reversible adjustment in the components of the photosynthetic apparatus in response to environmental light-variations. It's worth noting that photoacclimation re-organization can determine changes both in pigment content and in the components of the electron-transfer chain, and in the Calvin cycle enzymes as well (for example RUBISCO, Falkowski and Raven 1997).

The type of acclimation mechanisms depends on the scale of the perturbation. Generally, on a short-time scale (microscale: from seconds to hours), photoacclimation is realized by regulation of pigments and enzymes activity and efficiencies (named the "dynamic" acclimation, Claustre *et al.* 1994), which are not dependent on their turnover, but on coupling mechanisms and activation states (MacIntyre *et al.* 2000). In particular, in *Cyanophyta* and *Chlorophyta* subjected to very fast light changes (for example, in samples from estuarine waters, Schubert *et al.* 1995), the relative energy distribution between the two photosystems PSII and PSI can be adjusted by state transitions. This mechanism assures a balanced energy distribution between the photosystems, especially at low light, due to phicobilins (in *Cyanophyta*) and chlorophyll-*b* (in *Chorophyta*) almost-exclusive energy transfer to PSII (Krause e Weis 1991). On a similar time-scale,

the RUBISCO activity can change according to activation/deactivation transition states (MacIntyre and Geider 1996), though detecting these mechanisms is not easy in very rapid mixing conditions, due to the different states trigging time.

On a longer-time scale (meso- and macroscale: from hours to days), pigments and enzymes concentrations vary, in particular, in photo-limiting conditions both chlorophyll-*a* and accessory pigments content increase, so as to increase the probability of photons capture, while on the contrary, in high-light conditions, pigments concentrations lower. Thus, on a longer time scale both the size and the number of photosystems can vary, through mechanisms of neo-synthesis and turnover (named the "static" acclimation, Claustre *et al.* 1994), resulting in variation of light-harvesting and, finally, in the efficiency of utilization of energy for photosynthesis (Falkowski, 1997).

However, independently from the scale of variations, photoacclimation can thus affect both light harvesting efficiency and photosynthetic capacity. The link between pigments and carbon fixation likely lay in regulatory mechanisms involving the redox state of the plastoquinone pool, which would determine a transcriptional control on mDNAs coding for pigments and proteins (Kana *et al.* 1997).

1.2 Photoprotective and photoinhibiting mechanisms

Changes in the photosynthetic apparatus composition are also involved in non-photochemical dissipation of energy when phytoplankton is subjected to high light, thus allowing photoprotection and photoinibition. These mechanisms are quite common in surface assemblages at midday, moreover they may be induced by a fast shift to higher irradiance, thus they depend on the rate of vertical mixing in the water mass, finally they can be triggered in microalgae when reaching the sub-surface in a mixed upper layer. Excessive energy absorption can be dangerous to the photosynthetic apparatus, because it may determine reactive oxygen species (ROS) formation, resulting in photodamage to photosystems, in particular to PSII (Falkowski 1997).

Photoprotective mechanisms can (i) decrease the fraction of incident light which is actually absorbed, through a reduction in energy transfer to the reaction centers by lowering the absorption and/or effective quantum cross-section, or (ii) provide alternative energy sinks, which deviate electrons from the Calvin cycle, using them in different pathways.

The intersystem-crossing from singlet of the chlorophyll-a excited molecule (^{1}chl a*) to its corresponding triplet state (^{3}chl a*) allow excessive energy dissipation when light has already been absorbed. This process is mediated by carotenoids, which dissipate

energy as heat in their triplet state, thus avoiding ^{1}chl a* reaction with oxygen (and ROS formation, Niyogi 2000). A very powerful tool in energy dissipation is the xanthophylls cycle: xanthophylls capture photons, avoiding potentially photodamaging excitation of chlorophyll-*a* in the reaction centers. Photons are used in reversible reactions of de-epoxidation of violaxanthin to antheraxanthin and then to zeaxanthin in *Chlorophyta,* and *Raphidophyceae*, of diadinoxanthin to diatoxanthin in *Bacillariophyceae* and other flagellates (Evens *et al.* 2001, Lavaud *et al.* 2002), and of lutein (Niyogi *et al.* 1997).

The *Cyanophyta* lack of the xanthophylls cycle, but in high light conditions the Mehler's reaction (also named water-water cycle or pseudo-cyclic electron transport) dissipate excessive electrons and reductants produced by the electron transport chain for oxygen re-reduction to water at the PSI, trough the superoxide-dismutase and ascorbate-peroxidase enzymes activity (Asada 1999).

Moreover, the different balance between oxygen evolution at the PSII and rate of plastochinone pool turnover can determine de-coupling of photosystems, i.e. the cyclic transports at both PSII (Prasil *et al.* 1996).

Nitrate reduction reactions can constitute an important electron sink as well, especially in diatoms (Lomas and Gilbert 1999), while in Cyanophyta chlororespiration or enhanced post-illumination respiration can dissipate excessive reductants, due to competition between photosynthesis and respiration for the plastochinone. In fact, these two pathways can be close in the same membrane, thus sharing the same electron carriers, due to the absence of real organelles in this taxon (Schmetterer 1994).

Finally, photorespiration allow ATP and reductants dissipation in high light conditions, through the RUBISCO oxygenase-activity. However, it is widely admitted that photorespiration cannot largely contribute to photoprotection in microalgae, because both *Cyanophyta* and many eukaryotic algae (*Chlorophytae*, diatoms and dinoflagellates) have developed CO_2-concentration mechanisms (Badger and Price 1992).

1.3 How to measure photoacclimation: photosynthesis-irradiance (PE) curves

One of the main widely used tool for assessing photoacclimation is measuring of a photosynthesis-irradiance (PE) curve (Henley, 1993), i.e. measuring the variation of the photosynthetic rates P with changing irradiance E (fig.i.1). Generally, the photosynthetic rates are measured by gas exchange, thus P is the rate of net evolved oxygen or of net fixed carbon (as moles of gas with time). Sperimentally, a microalgal

sample is acclimated to a series of irradiances and mean photosynthetic rates of gas exchange are measured at each E value during the acclimation time lag. In the dark (i.e. E=0), generally P<0, due to oxygen consumption or to carbon dioxide evolution by respiration. Then, P increases with increasing E, due to further photosynthetic oxygen evolution (or carbon dioxide fixation), as far as P=0, i.e. E=Ec, the compensation irradiance. Finally, for higher E values, P>0 and keeps on increasing with E, until reaching a constant and maximum photosynthetic carte value, Pmax.

A typical PE curve is thus characterized by a photo-limiting phase, i.e. the first phase of linear variation of P with E, and by a photo-saturating phase, i.e. P is constant at its maximum (Pmax) and independent from E.

Finally, for increasing E values, P can lower, due to photoinhibiting processes in progress (photo-inhibiting phase): this latter phase is quite common in aquatic autotrophs.

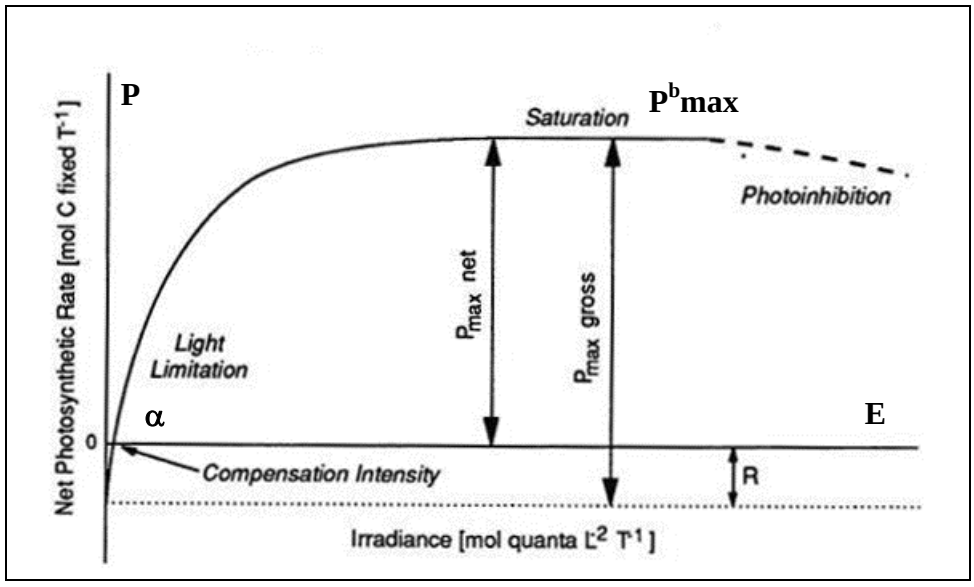

Fig.i.1: example of a photosynthesis-irradiance (PE) curve: on the x-axis, irradiance (E), on the y-axis the net photosynthetic rate (P) (adapted from Kirk 1994).

Any PE curve is associated to its corresponding photosynthetic parameters α, Pmax, Ek and β: α is the light-limited slope, Pmax is the light-saturated rate, β is the light-inhibiting slope. Ek is the light-saturation index and Ek=Pmax/α (Kirk, 1994). Generally α, Pmax and β are normalized by a biomass index (for example, chlorophyll-*a* concentration), so as to calculate the corresponding parameters α^b, P^bmax, and β^b.

Since Steeman Nielsen and Jørgensen (1968), the light-limited slope α^b has been considered traditionally linked to the light-harvesting mechanisms and to the photosynthetic energy conversion efficiency, and it is relatively constant when assuming that chlorophyll-*a* is the main light-harvesting pigment and that the ratio

between the photosystems PSII and PSI is constant. In fact, small variations in α^b are mainly due to specific absorption cross-section coefficient a*676 variations, induced by differences in pigments content and packaging (see for a review, MacIntyre *et al*. 2002). α^b is not constant when (1) chlorophyll-*a* is not the main light-harvesting pigment, (2) the ratio between the photosystems PSII and PSI vary, (3) non-photochemical quenching and/or (4) photoinibition processes are in progress ("upstream" of PSII processes, according to Behrenfeld *et al*. 2004).

On the contrary, P^bmax has been traditionally considered linked to the photosynthetic electron transport components, and/or to the Calvin cycle components, i.e. carbon content (MacIntyre *et al*. 2002), and concentration and/or activity of the enzyme RUBISCO (the so-called "downstream" of PSII processes, according to Behrenfeld *et al*. 2004). Only in very high-light conditions, P^bmax can be closely linked to PSII, in particular to f_{PSII}, the fraction of photochemically active PSII (Behrenfeld *et al*. 1998).

Thus, the possibility to parameterize light-limited and light-saturated photosynthesis, through the calculation of α and Pmax, respectively, determines PE curves key role in describing photoacclimation, which is the result of regulatory mechanisms that, independently from the time-scales of variations, determine changes in both light-limited and light-saturated photosynthetic rates. Under continuous light, the same species generally shows different PE curves, i.e. different α^b and P^bmax values, as a result of photoacclimation to the growth irradiance. As a consequence, it's generally possible to distinguish between a typical low-light acclimated curve, which has a high value of α but reaches a lower Pmax, and a high-light acclimated response, when the species reaches a much higher Pmax, though a lower α. These two long-time scale responses may be found, for example, in a shade-acclimated deep sample or, on the contrary, in a sub-surface light-acclimated assemblage (Kirk, 1994). However, the most important application of PE curve measurements is the interpretation of the physiological adjustment through the photosynthetic parameters variations, thus allowing the analysis of short-term scale responses (from minutes to hours, MacIntyre *et al.* 2002).

1.4 Photosynthetic parameters covariation

Both in field PE curves measurements and in particular during laboratory experiments on diel rhythms, a covariation between α^b and P^bmax is largely documented when the sampling frequency is high ($\leq$ 2 hours), and it is apparently unexplained when considering, as traditionally is, α^b and P^bmax as depending on different phases of the

photosynthetic process. Thus, the PE parameters variability is generally referred to as 'Ek-independent', because when α^b and P^bmax covary, Ek is constant. On the contrary, if α^b is constant, P^bmax is the only variable determining Ek, thus the parameters show an 'Ek-dependent variability'.

Behrenfeld *et al*. (2004) suggested that α^b and P^bmax are indeed linked through reductants (ferredoxin + NADH + NADPH), which are, together with ATP, the main product of light-harvesting and electron transport chain. When metabolism ask for ATP in the light, reductants can be used not only for carbon fixation through the Calvin cycle, but also in many other pathways, like nitrogen reduction, photorespiration, chlororespiration, mitochondrial respiration and in the Mehler's reaction, finally in very rapid back-reactions which involve an electron transport back to the photosystems, resulting in additional ATP generation. The cellular metabolic flux would be directed by the ATP/reductants balance variations depending on the different cell cycle phases ("time-regulated diversion of reductants", Behrenfeld *et al*. 2004): in particular, on a diel time scale, ATP demand is high during the light period, when cells are actively growing, i.e. photosynthetically active, fixing carbon and stocking organic compounds through an intensive nutrients uptake. On the contrary, reductants demand is high during the night, when cell division takes place, nutrient uptake rates are low and no new biomass is built up, i.e. when a nocturnal maintenance metabolism is in progress. That would determine a strong link between α^b and P^bmax, thus causing their covariation.

1.5 Aim of the research

The aim of this research was the study and measurement of both short- and long-term scale photoacclimation in natural phytoplankton. For this purpose, we took part to the oceanographic cruise MEDGOOS13 (in collaboration with CNR – ISMAR, CNR – IAMC, and Università della Tuscia), which took place in the Western Mediterranean Sea, in autumn 2006. The Western Mediterranean Sea, and in particular its western area, the Alboran Sea, resulted an interesting case to study microalgal photoacclimation: this part of the basin is in fact characterized by a strong hydrodynamism, determining a high degree of variability both in light and nutrients availability, both in time and space scales of their variation.

The hydrodynamism of the basin is due to the entering of the Atlantic water in correspondence of the Gibraltar Strait. The Atlantic water mass proceeds its circulation into the basin as a surface layer, which is progressively modified by both air-sea

interaction and mixing with the other water masses (Send *et al.* 1999). Once entered at Gibraltar, generally the jet of Atlantic water proceeds along the Spanish coasts following an anticyclonic circulation and gradually mixing with the resident Mediterranean water, giving origin to coastal upwellings (Morán and Estrada 2001) and a semi-permanent anticyclonic gyre (the Western Anticyclonic Gyre, WAG, Tintoré *et al.* 1991, Rodriguez *et al.* 1998). Moreover, mesoscale cyclonic eddies associated with the edges of the WAG have been reported as well (Minas *et al.* 1991, Tintoré *et al.* 1991, Prieur and Sournia 1994, Rodriguez *et al.* 1998). Then the jet turns southward in a geostrophic frontal-structure, the Almeria-Oran jet, generally associated westward with a second more-dynamic anticyclonic gyre (the Eastern Anticyclonic Gyre, EAG, Minas *et al.* 1991) and with small cyclonic eddies as well (Davies *et al.* 1993). Finally it continues eastward along the Algerian coasts as 'the Algerian Current', that is an unstable current which may give origin to mesoscale structures, i.e. filaments, meanders, eddies, both cyclonic and/or anticyclonic, coastal and open-sea mesoscale structures different in diameter and stability (Millot 1999, Send *et al.* 1999).

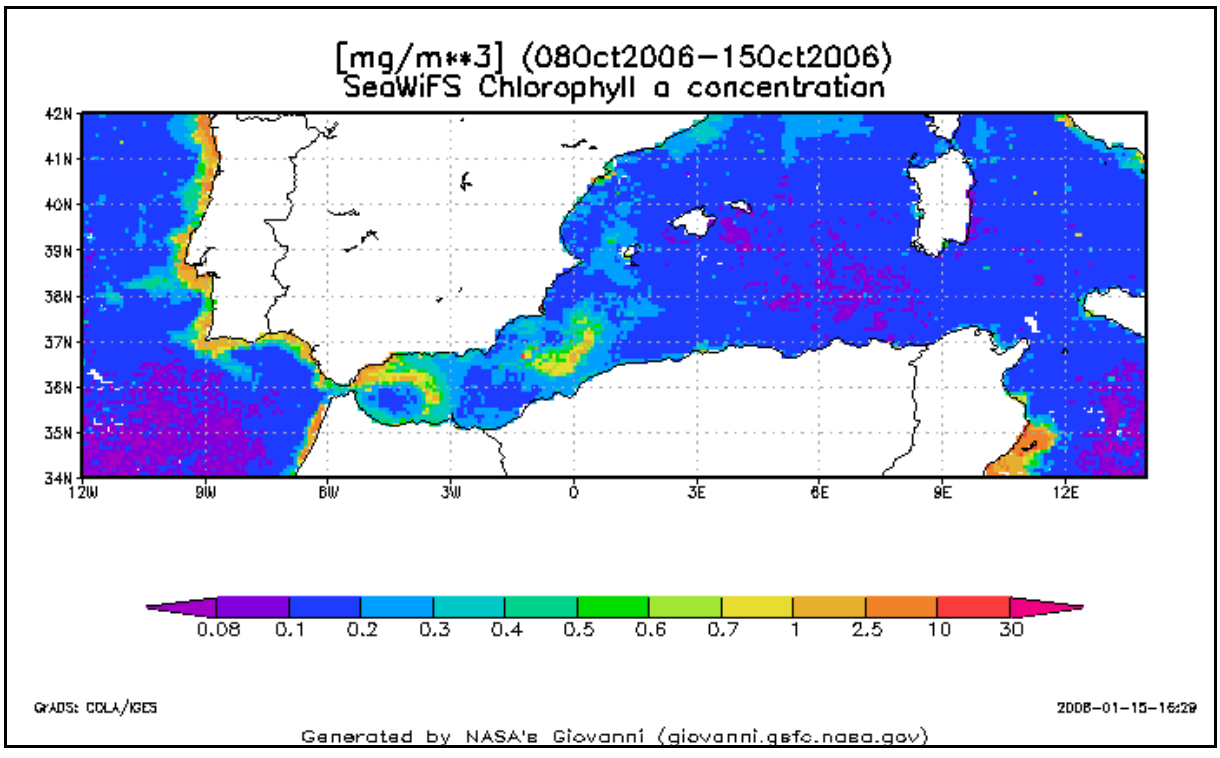

Fig. i.2: SeaWiFS map of surface chlorophyll-*a* distribution in the Western Mediterranean Sea at the time of sampling. Data are integrated on 8 days (8^{th}-15^{th} October 2006). Web source: http://reason.gsfc.nasa.gov/Giovanni.

The consequence of these fertilization events is thus an enhanced productivity (fig.i.2), which is typically detected at upwelling (Gomez *et al.* 2000, Moran *et al.*

2001, Arin *et al.* 2002) and frontal zones (Fiala *et al.* 2004, Videau *et al*. 1994, Rodriguez *et al.* 1998, Leblanc *et al*. 2004). So, the Western Mediterranean Sea represented an interesting area to assess photoacclimation through the pigment and taxonomic characterization of the field assemblages. For these purpose, the collection of samples was based on CTD and *in vivo* fluorescence vertical profiles, and the following interpretation of the analysis on phytoplankton composition, by microscopic countings and by pigment HPLC analysis, resulted strongly coupled with the highly-variable light and nutrients availability.

Nevertheless, to assess short-time scale variability, laboratory experiments under controlled environmental conditions, simulating natural changes in resources, may constitute a more proper instrument for a more detailed analysis.

For this purpose, we took part to three series of experiments, aimed to study photoacclimation and photoprotection under controlled conditions. All the experiments were conducted on a potentially toxic alga, *Heterosigma akashiwo* (*Raphidophyceae*), at the "Laboratoire d'Oceanographie" (Observatoire Oceanologique, Villefranche-sur-mer, Université Pierre et Marie Curie, CNRS, France).

Since the main objective was the analysis of PE parameters variation with varying light and nutrients availability, in particular α^b and P^bmax covariation, *H.akashiwo* was thus grown under sinusoidal light, so as to simulate the light variation a surface alga can experience in nature, or the day cycle which, summed to the vertical mixing, is experienced in the upper mixed layer (experiments 1 and 4). A high-frequency sampling was adopted to assess the presence of diel periodicity, both in PE parameters and in pigment content, organic and inorganic compounds and optical properties, to establish the reason of the possible covariation between α^b and P^bmax.

Moreover, a second series of experiments was made to analyse the effects on photosynthetic performances of a shift in light, from sinusoidal to continuous (experiments 2 and 5). Both the few sinusoidal hours before the shift and the hours following it were high-frequency sampled. The aim of these experiments was assessing whether a diel periodicity was still present and analysing the effects with time of a continuous light availability, likely simulating a surface light-field which can be experience in a costal stratified water column. This resulted of particular interest due to common coastal Raphidophyceans (and toxic algae) blooms.

On the contrary, in experiment 6 the light cycle was switched back to sinusoidal and the sampling allowed us to determine the possible recovery back to a cyclic light utilization.

Finally, with experiment 3 we managed to determine whether nitrogen-limitation first, and nitrogen-starvation then, had effects on photosynthesis, in particular on PE parameters. Thus we simulated, under constant light, a condition of strong nutrient stress, which can be experienced in an oligotrophic sea like the Mediterranean Sea. Then, re-supplying nitrogen, we assessed if a complete recovery was possible and its time-scales after the re-supply.

The choice of an harmful alga was thus determined by the interest in whether such competitive organisms would be a good photosynthetic performer under light and nutrient stress conditions.

2. Materials and Methods

2.a Field measurements

2.a.1 Sampling strategy and measurements

Samples were collected during the leg II of the MEDBIO06-MEDGOOS13 oceanographic cruise, which took place in the western Mediterranean Sea, between longitude -7° and 11° long. E and 39° and 44° lat. N, on board of the NO Urania (CNR) in autumn 2006 (October 7^{th}-28^{th}). In particular, data presented here were collected along the Algerian Basin, the Alboran Sea and the Strait of Gibraltar, between -7° and 1° long. E and 34° and 37° lat. N (October 13^{th}-18^{th}). Tab.1 shows the stations examined: sampling took place along three transects: a long NE-SW transect (the M-transect) and 2 short NW-SE transects (the A-transect, and the G-transect between Almeria and Oran). The sampling locations are shown in fig.m.1.

station	Lat (N)	Long (E)	Date (UTC)
M15	37° 05.39'	0° 53.19'	13/10/2006
A1	36° 34.37''	0° 23.43’	13/10/2006
A2	36° 40.18'	0° 13.12'	14/10/2006
M16	36° 47.36'	0° 00.23’	14/10/2006
A4	37° 01.93'	- 0° 15.44'	14/10/2006
A5B	37° 13.53'	- 0° 29.30'	14/10/2006
A6	37° 23.46'	- 0° 42.61'	14/10/2006
M17	36° 37.95'	- 1° 00.58'	15/10/2006
J8	35° 54.55'	- 1° 10.69'	15/10/2006
G4	36° 04.64'	- 1° 23.67'	15/10/2006
G3	36° 15.02'	- 1° 36.40'	15/10/2006
M18	36° 28.54'	- 1° 29.47'	16/10/2006
G2	36° 28.08'	- 1° 52.93'	16/10/2006
G1	36° 36.01'	- 2° 06.04'	16/10/2006
M19	36° 11.30'	- 2° 05.51'	16/10/2006
M20	36° 06.71'	- 2° 39.44'	16/10/2006
M21	36° 01.98'	- 3° 23.43'	16/10/2006
M22	35°57.96'	- 4° 03.22'	17/10/2006
M23	35° 56.01'	- 4° 43.32’	17/10/2006
M24	35° 57.85'	- 5° 10.10'	17/10/2006
M25	35°57.20'	- 6° 22.14'	18/10/2006

Tab. 1: list of the sampling stations analyzed here, with coordinates and dates of sampling. MEDBIO06-MEDGOOS13 oceanographic cruise, leg II.

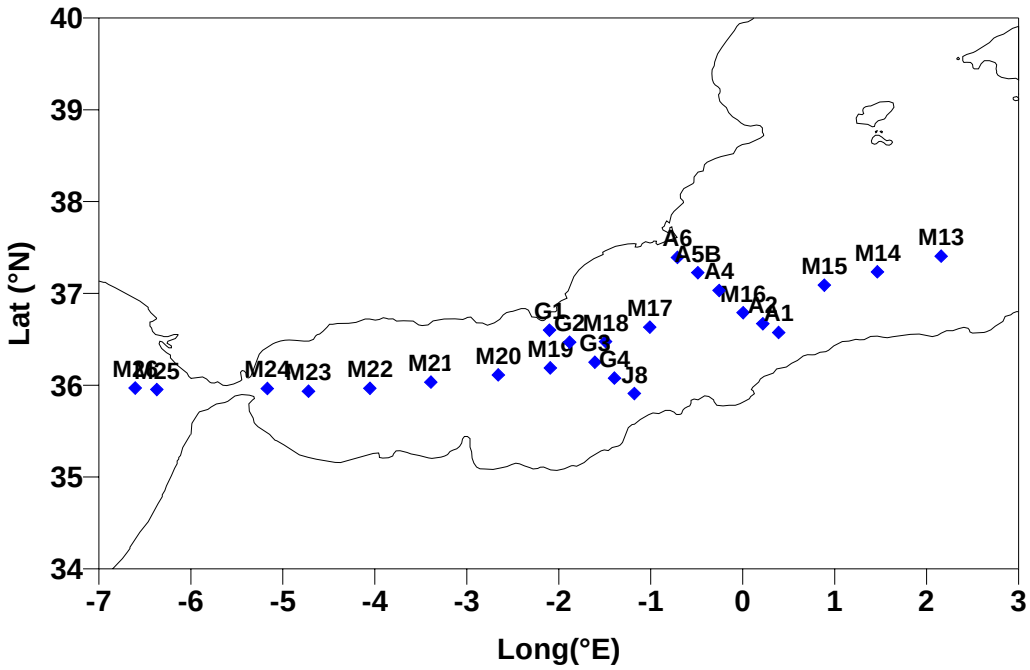

Fig. m.2: map showing the analysed sampling locations, along the 3 transects: (a) M-transect NE-SW, stM13-M26, (b) G-transect N-S, and (c) A-transect N-S. MEDBIO06-MEDGOOS13 oceanographic cruise, leg II.

In each station, vertical profiles of temperature, salinity, density and fluorescence emission were measured by a SBE-911 plus CTD system (Seabird) equipped with a fluorometer (SeaTech). Water samples for nutrient and biological analysis were collected with 12-l Niskin bottles mounted on a rosette sampler (General Oceanic, 24x) attached to the CTD.

The upper mixed layer depth (Z_{uml}, in m) was determined considering both a density difference from the surface of 0.05 (according to Lévy *et al.* 1998), and the depth where the change in density is ≥ 0.05 kg m^{-3} (according to Mitchell and Holm-Hansen 1991).

Water samples were collected at discrete depths (generally 0m, 25-35m, 40-65m, 75m, 100-150m, 200m, 400-500m) after examining the fluorometric profile.

2.a.2 Pigments analysis

4-l samples of marine water from surface to 100-150 m were filtered onto GF/F filters (47 mm, Whatman), subsequently stored at -20°C, until high performance chromatography (HPLC) analysis. HPLC was performed by a Class VP HPLC system (Shimadzu), according to Vidussi *et al.* (1996) and Barlow *et al.* (1997) after modifications of elution times (tab.2) (for more details, see tab.3 and Pierattini 2005).

minutes	% eluent A	% eluent B
0	75	25
1	50	50
17.50	20	80
21.50	20	80
24.50	0	100
29.90	75	25
30	75	25

Tab. 2: eluents A and B addiction during the 30 minutes-long run. Eluent A is 70% methanol, 30% (w/v) 1 M ammonium acetate and BHT (Carlo Erba), eluent B is 100% methanol.

PIGMENTS	Retention time
Chlorophyll c_3	3.150
Chlorophyll c_2	3.992
Peridinin	4.758
19'-Butanoyloxyfucoxanthin	5.683
Fucoxanthin	6.050
19'-Hesanoyloxyfucoxanthin	6.792
Prasinoxanthin	6.983
Violaxanthin	7.208
Diadinoxanthin	8.358
Alloxanthin	9.742
Diatoxanthin	10.233
Zeaxanthin	11.417
Lutein	11.625
APO (internal standard)	13.592
Chlorophyll *b*	18.358
Divinil chlorophyll *a*	22.325
Chlorophyll *a*	22.817
β-ε carotene	27.775
β-β carotene	27.775

Tab. 3: pigments and their retention times (in minutes).

2.a.3 Nutrients analysis

50-100 ml of samples were collected in polyethylene flasks and immediately fixed with mercury chloride (final concentration in the sample: 20 μg ml^{-1} $HgCl_2$, Kirkwood 1992). Nutrient (NO_2, NO_3, PO_4, Si) concentrations were determined by the AutoAnalyzer3 (Bran-Luebbe) equipped with the AACE software (AutoAnalyzer Control and Evolution), according to the standard methodologies (Catalano *et al.* 1990; Ribera d'Alcalà *et al.* 1990a, 1990b; Saggiomo *et al.* 1990).

2.a.4 Microscopic analysis

250-500 ml of samples from surface to 100-150 m were collected in dark polyethylene flasks and immediately fixed with neutralized formalin to the final concentration of 1%.

50-100 ml of samples were analysed in the Laboratory of Ecology of the University of Florence within a few months from sampling, after sedimentation with a Utermöhl's chamber, and cells were observed and counted on an inverted optical microscope (objective 40 x, ZEISS IM, Zingone *et al.* 1990). We chose a random cells counting strategy and at least 700 optical fields (corresponding to ¼ of the sedimented volume) were observed. Taxa indicated as 'sp. cf.' were not identified at the species level, but the species name following 'cf.' has been adopted as a useful morphological reference. The taxa examined fall in the following main group: *Bacillariophyceae*, *Dinophyceae*, *Raphidophyceae*, *Prymnesiophyceae* and other plankton (including *Cryptophyceae*, *Chrysophyceae*, *Prymnesiophyceae Prymnesiales*, *Prasinophyceae*, unidentified < 10-μm flagellates and *incertae sedis*).

The following sources were used for the taxonomic identification (for a list of the identified taxa see appendix 1):

- Bérard-Therriault *et al.* 1999;
- Hasle and Syversten 1997;
- Heimdal 1997;
- Horner 2002;
- Peragallo and Peragallo 1965 ;
- Rampi and Bernhard 1980;
- Rampi and Bernhard 1981;
- Schiller 1933-1937;
- Sournia 1986;
- Steidinger and Tangen 1997;
- Throndsen 1983.

2.a.5 Statistical analysis

Temperature, salinity, density, fluorescence, nutrients, pigments and cell countings data were mapped using the Surfer 7.0 software, by Kriging geostatistical gridding method (Journel and Huijbregts 1978). Griddings were made on the three transects separately: temperature, salinity, density and fluorescence data were gridded from surface to 500 m, nutrients from surface to 200 m, pigments from 0 to 100-150 m, while only the 3 superficial samples (from 0 to 40-65 m) were used for cell countings gridding.

Similarity of natural populations from cell counting data of selected samples (A-transect, G-transect and stM15-M16-M17-M18 and M19) was quantified using the non-parametric Kendall's coefficient of rank correlation τ (Kendall 1948). This test determines the direction of 140 taxa, which were selected between the 240 total taxa, because present in at least 5 samples, and ranks were associated to each taxon in each sample according to the product between presence (number of samples) and abundance (number of cells in 1-l sample). Then τ-index was calculated using the Statistica 6.0 software (StatSoft) for couples of adjacent samples: between adjacent depths of the same station and between the same depths of adjacent stations (Venrick 1992).

Finally, temperature, salinity, density, nutrients, chlorophyll-*a* and total cells concentration data were submitted to the Principal Component Analysis (PCA, Hotelling 1933): this kind of analysis allows the detection of the principal components which produce data variance, then the description of samples distribution according to them, finally a quantification of relationships between hydrological and biological data variance. Data were standardized in cases both (1) by log-transformation (named stand1), and (2) by the ratio between each data subtracted by its mean and its standard deviation (named stand2), and (3) by the ratio between each data and the square root of the sum of squares (named stand3). The PCA was carried out by the Statistica 6.0 software (StatSoft).

2.a.6 Genomic DNA extraction and PCR amplification

DNA extraction and PCR amplification of *Raphidophyceae*-specific nuclear internal transcriber spacer (ITS) region were performed on a few natural samples. 40-100 ml of 1% neutralized formalin fixed samples were centrifuged (3000 rpm for 5 min), then the supernatants were removed. Each pellet was resuspended in 10 ml of 0.2 μm-filtered sea water, then centrifuged again (3000 rpm for 5 min), finally the supernatant was removed. Each pellet was added with 750 μl DNA-extraction buffer 2xCTAB (2% (w/v) CTAB, 1.4 M NaCl, 20 mM EDTA pH=8.0, 100 mM TRIS-HCl, 0.2% (w/v) PVP, 0.01% (w/v) SDS, 0.2% (w/v) β-mercaptoethanol), then incubated at 65°C for 10 min. DNA was extracted with the PCI method (Sambrock *et al.* 1989). Since DNA was not visible, we added 30 μl 3 M NaCl, incubated at -80°C for 30 min, then centrifuged at 13000 rpm for 6 min, finally the supernatant was removed, DNA pellets washed in 500 μl 70% ethanol and centrifuged 6 min (13000 rpm). Finally ethanol was removed, pellets dried at 60°C for 10 min and then added with 150 μl DNAse, RNAse Free

Distilled water (GIBCO, Invitrogen). DNA samples were stored at -20°C until PCR reactions. Primers oBTG 005B (5'CTG GGG AAG GAT CAT TAC C-3') and oBTG 006B (5'-TCG CTG CGT TCT TCA TCG T-3', MWG, M-Medical) were chosen according to Connell 2002. PCR amplifications were carried out by a GeneAmp PCR system 2720 thermocycler (Applied Biosystems), in (a) 20-µl volume with 1U (=0.2 µl) or 1.5U(=0.3 µl) XtraTAQ (GeneSpin), 1x buffer, 0.2 mM dNTPs (Invitrogen), 2.5 µM primers, or (b) 10-µl volume with Hot Start Taq, 1x MasterMultiplexMix, 0.5x Q-solution (Qiagen), and 0.2 µM primers. The PCR cycles were: (a) an initial step at 95°C (15'), then 94°C (30"), 57°C (1'30") and 72°C (1'30") for 45 cycles, with a final extension at 72°C (10'), and (b) an initial 5' step at 95°C, then 95°C (1'), 55°C (1') and 72°C (1') for 35 cycles, with a final extension at 72°C for 7'. (a) 10 or (b) 20 µl, respectively, of PCR-generated product were resolved on a 1.5% agarose (Invitrogen), 0.5x TBE buffer (45 mM Tris Base, Fluka, 44 mM boric acid, J. T. Baker, 0.05 M EDTA pH=8., Sigma) gel with ethidium bromide / UV visualization.

The same extraction and amplification methods were applied on a 10-ml 1% neutralized formalin fixed sample of an *Heterosigma akashiwo* culture, which was provided by the Provasoli-Guillard National Centre for Culture of Marine Phytoplankton and was cultivated in the growth chamber of the Laboratory of Genetics of the University of Florence. The culture was cultivated in f/2 medium (Guillard and Ryther 1962) at 25°C under a 16L:8D light cycle at 75 µE m^{-2} s^{-1}. Negative control samples were prepared and amplified in the same way using 1% neutralized formalin 0.2-µm filtered seawater.

These analysis were performed in the Laboratory of Molecular Ecology, at the University of Florence.

2.b Laboratory experiments

All measurements were made by an international equipe of researchers at the "Laboratoire d'Oceanographie", Observatoire Oceanologique, Université Pierre et Marie Curie, CNRS - Villefranche sur mer, France.

2.b.1 Experimental design and sampling strategy

Laboratory experiments were conducted on the Raphidophycean *Heterosigma akashiwo*, which was provided by the Provasoli-Guillard National Centre for Culture of Marine Phytoplankton.

2 monospecific chemostat cultures (named C1 and C2) of the same strain were grown under the same nutrient, temperature, light and pH conditions until they had reached the same steady state. The culture vessels consisted of 2 water-jacked cylinders: 10 l for experiments 1, 2 and 3 (culture volumes = 9.5 l) and 6 l for experiments 4, 5 and 6 (culture volumes = 5.5l), so as to be large enough to minimize perturbation caused by intensive sampling. The vessels were connected to a circulating water bath at the constant temperature of 25°C ± 0.5°C. Cells were growth in f/2 medium (Guillard and Ryther 1962), prepared using 0.22 μm Millipore-filtered and autoclaved (105°C for 30 minutes) natural seawater and nutrient enrichments according to the f/2 formulation. The medium was prepared in batches of 100 l (5 Nalgene tanks of 20 l connected together). After cooling and sterile addition of nutrients, the medium was transferred to the culture vessels through a 0.22 μm sterile filter (SpiralCap, Gelman and MediaKap-5, Microgon). The chemostat cultures were subjected to continuous gentle stirring and bubbling with sterile-filtered air. pH was measured by an electrode pH-meter after collection of a sample (pH-Mètre 744, Metrohm) or by immersion of the pH-meter (Fisher) in the chemostat.

Light was provided by an array of six dimmable U-shaped fluorescent tubes (OSRAM, DULUX®L, 2G11, 55W/12-950, LUMILUX DE LUXE, daylight) on each side of the 2 culture vessels, providing a smooth light-dark circadian cycle. The vessels were covered with blue filters (Lee) to grow the culture in spectral conditions as much similar as possible to the light sources spectra used for photosynthesis-irradiance curves measurements (fig.m.2) and to simulate light condition which are common in the natural environment. Photosynthetically available radiation was measured with a quantum scalar irradiance meter (QSL-100, Biospherical Instruments) by immersing the spherical collector in the centre of the culture vessel.

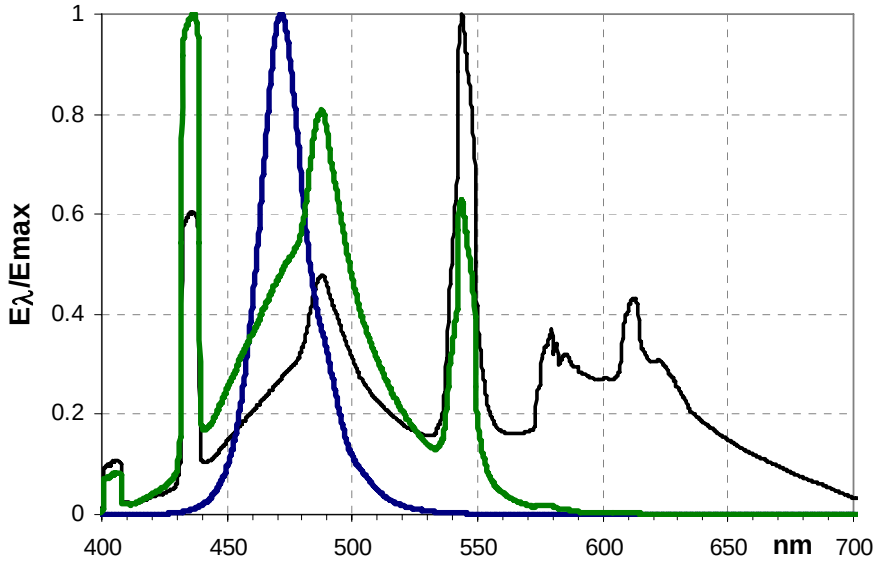

Fig. m.2: comparison between emission spectra normalized with their maximums between 400 and 700 nm (Eλ/Emax) of different light sources used during the experiments: in blue, the HPL-C LED diode used for oxygen evolved measurements; in black, the fluorescent tubes used as growth light for the chemostats; in green, the same fluorescent tubes with the blue filters on.

During experiments 1 and 4, the cultures were grown under sinusoidal light, with a photoperiod 12L:12D:

1) experiment 1: the light period started at 8.00h (dawn) and ended at 20.00h (sunset), the maximum of irradiance being 220 µE m^{-2} s^{-1} at 14.00h (midday). We sampled for 26 hours every two hours on both chemostats (from 7.30h on day 1 to 9.30h on day 2);

2) experiment 4: the light period started at 10.00h (dawn) and ended at 22.00h (sunset), the maximum of irradiance being 300 µE m^{-2} s^{-1} at 16.00h (midday). We sampled for 3 days at 0.00, 4.00, 8.00, 10.00, 12.00, 14.00, 16.00, 18.00 and 21.00h, on both chemostats: from 8.00h on day 1 (11^{th} of July) to 21.00h on day 3 (13^{th} of July).

During experiment 2, light was shifted from sinusoidal to continuous at the constant value of 110 µE m^{-2} s^{-1} (half the maximum), at 11.00h. We sampled for 26 hours every two hours on both chemostats (from 7.30h on day 1 to 9.30h on day 2).

During experiment 5, at about 13.00h light was shifted from sinusoidal to continuous at the constant value of 150 µE m^{-2} s^{-1} (half the maximum). We sampled for 2 days at 0.00, 4.00, 8.00, 10.00, 12.00, 14.00, 16.00, 18.00 and 21.00h, on both chemostats: from 0.00h on day 1 (14^{th} of July) to 11.00h on day 2 (15^{th} of July).

During experiment 6, light went back to its sinusoidal regime at 7.30h, the maximum of irradiance being 150 µE m^{-2} s^{-1} at 16.00h (midday). We sampled for 2 days at 8.00,

10.00, 12.00, 14.00, 16.00, 18.00, 21.00 and 0.00h, on both chemostats: from 8.00h on day 1 (20^{th} of July) to 11.00h on day 2 (21^{st} of July).

Due to technical problems with the oxymeter, a second experiment 1 was conducted. Only oxygen PE-curves and HPLC measurements were repeated, sampling every hour on each chemostat alternatively (from 8.30h on day 1 to 10.30h on day 2). All the other measurements were made a few times during that day too: since they show that the cultures were in the same conditions of experiment 1, we are going to consider these repeated oxygen and HPLC data as experiment 1 and relate them to all the other measurements.

During experiment 3, chemostat cultures were grown at constant light (100-120 $\mu E\ m^{-2}\ s^{-1}$). We sampled for 8 days every day once a day at the same time (9:30h). N-starvation was induced by addiction of N-free f/2 medium to the culture vessels, starting at 13.00h on the 1^{st} day of measurements (the 8^{th} of December), and it was interrupted (N-resupply) at 16.30h on the 4^{th} day of measurements (11^{th} of December), by addiction to the culture vessels of f/2 medium with nitrate (NO_3^-) concentration 100 μM (i.e. the same concentration which was measured in the culture medium before the beginning of N-starvation).

2.b.2 Nutrient measurements and particle counting and sizing

Cell concentration and cell size distribution and concentration of nitrate and nitrite of both chemostat cultures were routinely high-frequency monitored (at least every 2-3 hours). The concentrations of nitrate and nitrite were measured with a Technicon Auto-analyzer and an automated data-acquisition system (Malara and Sciandra 1991), while cell concentration and size distribution were measured with an optical particle counter using the principle of light blockage (Hiac/Royco, Pacific Scientific Instruments). Data by the particle counter were smoothed using the constrained cubic spline Savitzky-Golay (1964) estimation, using the Table Curve 2D software.

2.b.3 Particulate organic and inorganic carbon and nitrogen (POC, PON and DIC)

To determine the concentrations of particulate organic carbon (POC) and particulate organic nitrogen (PON), triplicate samples of 50 ml were filtered onto precombusted glass-fiber filters (Whatman GF/F); these were dried at 60°C and analyzed with a LECO

900 CHN analyzer. Dissolved inorganic carbon (DIC) was measured on 15-ml duplicate samples by a TOC-V CPH analyzer (Shimadzu).

2.b.4 Pigments analysis

Triplicate samples of 20 ml were filtered onto GF/F filters, which were subsequently stored in liquid nitrogen until high performance chromatography (HPLC) analysis according to Vidussi *et al.* (1996).

2.b.5 Light absorption coefficients a(λ)

The spectral absorption coefficient $a(\lambda)$ was measured on cell suspensions in 1-cm quartz cuvette with a dual beam spectrophotometer equipped with an integrating sphere (Perkin-Elmer Lambda 19). Measurements were made between λ = 300 nm and λ =800 nm at 1-nm intervals. 0.2 μm-filtered medium from the cultures was used as the reference. The spectra were smoothed using a moving average.

2.b.6 Photosynthesis-irradiance (PE) curves by oxygen measurements

Net oxygen evolution was measured by a liquid-phase Clark-type electrode oxymeter (Oxygen Electrode Disc, equipped with a DW2/2 Oxygen Electrode Chamber, Hansatech**).** A new calibration of the electrode (with MilliQ water and sodium dithionite, according to the instrument manual, System Manual, Hansatech, 2000) was made every day of sampling, before the beginning of the measurements and every 24-hours (at around 20.30h) during experiments 4+5+6. Measurements were made on 1-ml sample magnetically stirred (60 r/min) and kept at the constant temperature of 25°C by a circulating water bath. If necessary, each sample was first degassed with N_2 to low the oxygen concentration in the reaction chamber up to an oxygen value of ~ 80% the O_2-saturation value in marine water (150-200 nmol/ml, according to Green and Carritt 1967), then the reaction chamber was air-tightened by the plunger and the sample kept for 10 minutes in the dark. Finally, the sample was acclimated for 5 minutes at each PAR of a series: a series of 9 PAR in experiments 1 and 2 (28, 57, 86, 147, 277, 393, 499, 776 and 1130 μE m^{-2} s^{-1}); a series of 10 PAR in experiment 3 (0, 15, 32, 46, 63, 156, 235, 293, 414 and 525 μE m^{-2} s^{-1}); and a series of 10 PAR (12, 28, 57, 85, 116, 147, 278, 501, 770 and 1091 μE m^{-2} s^{-1}) in experiments 4, 5 and 6. The light was driven to the sample by inserting the fiber ending through the cuvette optical port. A blue light

LED was used as actinic light source (High Power LED-LAMP, HPL-C, Walz) and PAR was measured before the beginning of the measurements in the chamber filled with 0.22-μm filtered sea water, using the spherical quantum sensor US-SQS/LI connected with the light meter LI-250 (LI-COR).

Mean net oxygen evolution rates during the 5 min interval at each PAR (the last 5 of 10 min in the dark) were automatically calculated by the oxymeter software (Oxygraph OXYG32 software, Hansatech) and data were interpolated according to Platt *et al*. (1980)'s equation: $P = Ps\ [1–\exp(-aE)]\ \exp(-bE)$, using the Table Curve 2D software. So we obtained the fitted PE curves, the parameters α, β, Pmax and Ek and calculated the corresponding α^b, β^b and P^bmax, by normalization with chlorophyll-*a* concentration.

Due to each PE measurements duration (almost 1 hour), we didn't sample every 2 hours on both chemostats, but every hour on alternate chemostats.

During experiment 3, oxygen concentration lowered, so measurements were made on gravity-concentrated samples (5-μm polycarbonate filters, SMWP 04700, Millipore) and duplicate 1-4 ml of concentrated samples were filtered for biomass estimation (by HPLC analysis).

2.b.7 Photosynthesis-irradiance (PE) curves by variable fluorescence

During experiment 3, photosynthetic rates were measured also by variable fluorescence, using the fluorometer PAM 100 (pulse amplitude modulation, Walz), equipped with the PAM-101 unit, the ED-101 detector with 2 short-pass RG9 filters (Schott), the L450 diode as measuring light source and the HPL-C blue lamp (Walz) as actinic and saturating light source (saturation pulse: length 0.8 s, intensity 1200 μE m^{-2} s^{-1}). Samples were stirred (1.5 r/s) from above the cuvette during the measurements. Each sample was dark acclimated for 15 minutes, then acclimated for 5 minutes at each PAR of a series of 10 (15, 28, 42, 70, 108, 157, 214, 287, 364, 466 and 565 μE m^{-2} s^{-1}). PAR was measured in the chamber filled with 0.22-μm filtered sea water before the beginning of the measurements, using the spherical quantum sensor US-SQS/LI connected with the light meter LI-250 (LI-COR). The light was driven to the sample by inserting the fiber endings through the cuvette optical ports: the sat-pulse source was perpendicular to the ED detector and head-on the measuring light. The WINC-192 software (Walz) measured the Fo and Fm values in the dark and Ft and Fm' values at each PAR after the sat-pulses, finally it calculated the corresponding maximum quantum yield of PSII Fv/Fm (= (Fm-Fo)/Fm, Krause and Weis 1991), the effective

quantum yield Y (= (Fm'-Ft)/Fm', Genty *et al*. 1989) and the electron transport rate ETR(=Y*PAR, Falkowski 1997) values. Data were interpolated according to Platt *et al*. (1980)'s equation using the Table Curve 2D software, so as to obtain the fitted PE curves and the parameters α, β, ETRmax and Ek.

Due to each PE measurements duration (almost 1 hour), we didn't sample every 2 hours on both chemostats, but every hour on alternate chemostats.

Other measurements were made (Xenon-PAM PE-curves and ^{14}C PE-curves; σ_{PSII} and n_{PSII} by FRRF measurements; brevitoxin, Rubisco-activase and other individual proteins analysis; antibodies for Rubisco; spectrofluorimetric and part of the spectrophotometric measurements), but they will not be discussed here since they were not yet available at the time of writing.

3. Results

3.a Field measurements

3.a.1 Hydrology

The 38.3 isoline of salinity (s) indicates that the dense Mediterranean water (DMW) reaches low depths in correspondence of stations M16-M17-M18 (at depths of 90, 110 and 125 m, respectively) and stM21 (at 100 m, as shown in fig.f.1a). The same isoline is at least 150-m deep along the G-transect (fig.f.1b), while only 120 and 80 m deep in stA4 and A2 (fig.f.1c), respectively. On the contrary, the light modified Atlantic water (MAW) lays on the surface (s=36.5-36.9) and reaches the depth of 130 m in stM13 and M19, and 110 m in stM22, while the Atlantic seawater (MAW) is the only component of water in the Atlantic and Gibraltar stations (M25-M26). This indicates the presence of two main mesoscale structures, in correspondence of stM16-A2-M17 and stM21, with a sub-surface mixing interface between the Atlantic and the Mediterranean water: the 37.5-isoline is 26, 25 and 31 m deep, and 34 m deep, respectively. The presence of mesoscale water mass movements means upwelling of dense cold deep water (stM16-M17-A2 and stM21) which mixes with warmer downwelling water (stM15-M19 and stM20-22). The G-transect shows a large picnocline (the DMW-MAW interface, i.e. the AMI, Atlantic Mediteranean Interface, according to Lacombe and Richez, 1982, reaches the depth of 66 m only in the northern coastal station G1, fig.f.1b), while in stA6 it's only 17 m deep, likely due to the presence of cold north-east Mediterranean water (fig.f.1c).

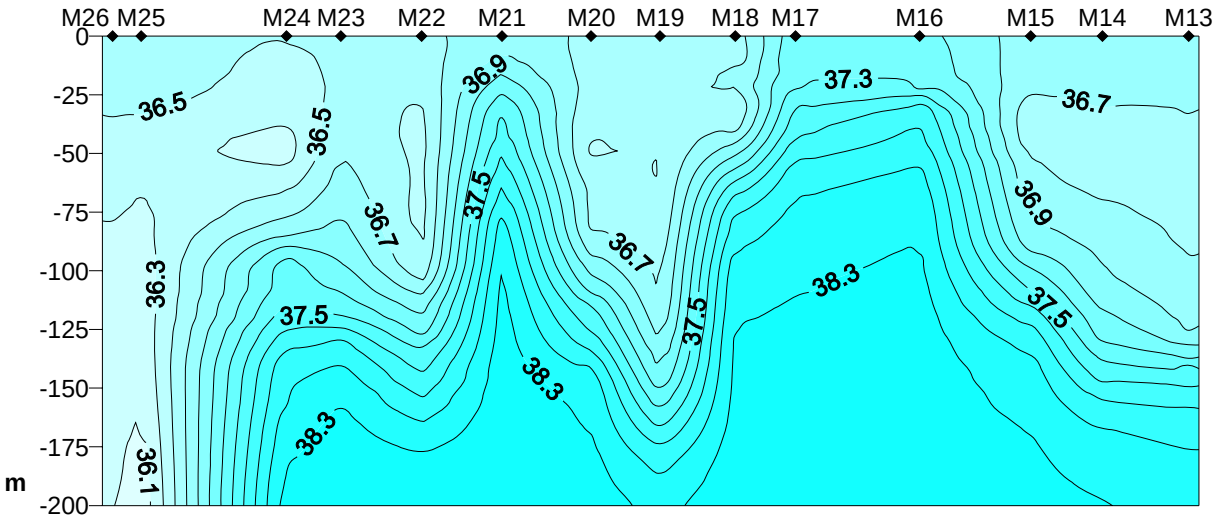

(*a)*

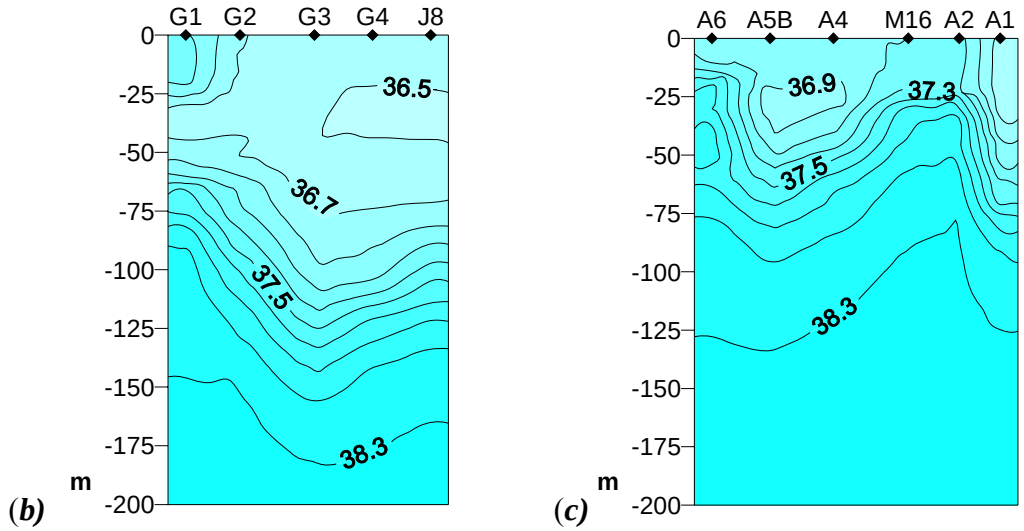

Fig.f.1: seawater salinity from surface to 200 m deep, along the 3 transects: (a) M-transect NE-SW, stM13-M26 (b) G-transect N-S, and (c) A-transect N-S. Distances between stations in miles. Data gridded with Surfer 7.0.

This is confirmed by the upper mixed layer depths (Z_{uml}, in m): Z_{uml} is maximum for stM19 (40 m), which is located between the 2 mesoscale structures, while it's minimum for stM21 (13 m), where deep mediterranean water reaches almost the surface (fig.f.2). Moreover, Z_{uml} is the same for the 3 mesoscale stations M16-M17-A2 (23 m), while it's stable along the G-transect.

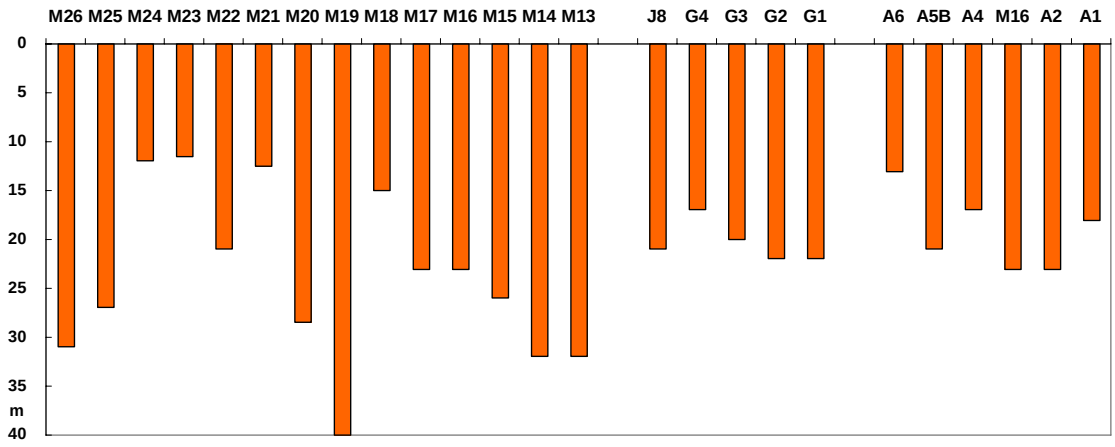

Fig.f.2: the Upper Mixed Layer depth (UML, in m) along the 3 transects.

The density σ_τ (kg/m^3, fig.f.3) and temperature T (°C, fig.f.4) profiles confirm the vertical structure of the transects: the DMW is salty (σ_τ>27.7 kg/m^3) and cold (T<15°C), while the surface MAW has salinity values σ_τ<27 kg/m^3 and temperature >20°C, finally the mixed interface (AMI) has σ_τ =27-27.5 kg/m^3 and T=15-20°C. Both profiles show a net separation between Atlantic water and AMI in correspondence of the eastern mesoscale structure (stM16-M17-A2) and strong halocline and thermocline on the Spanish side of A-transect.

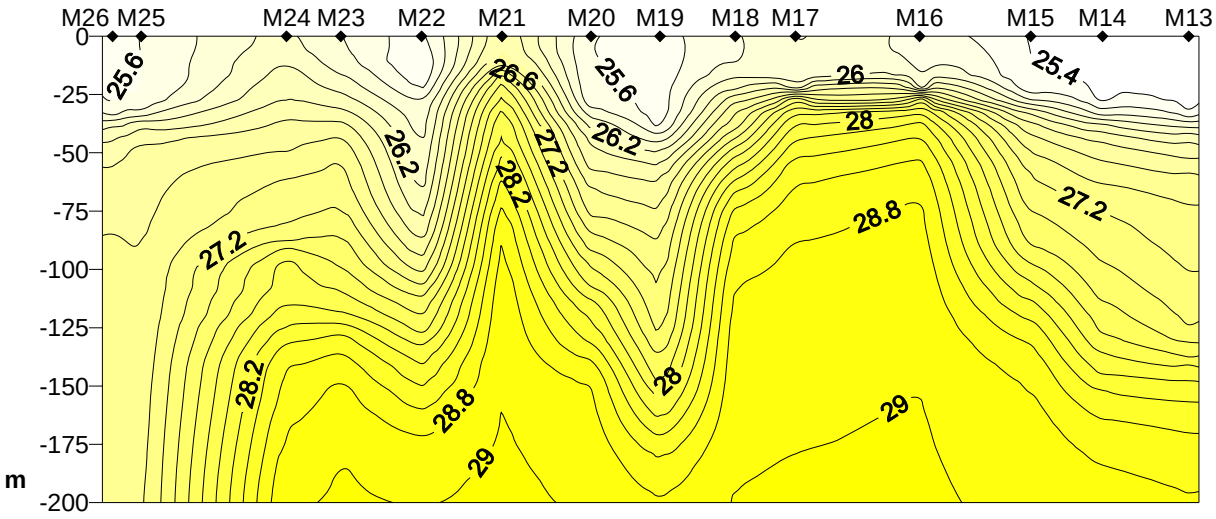

(a)

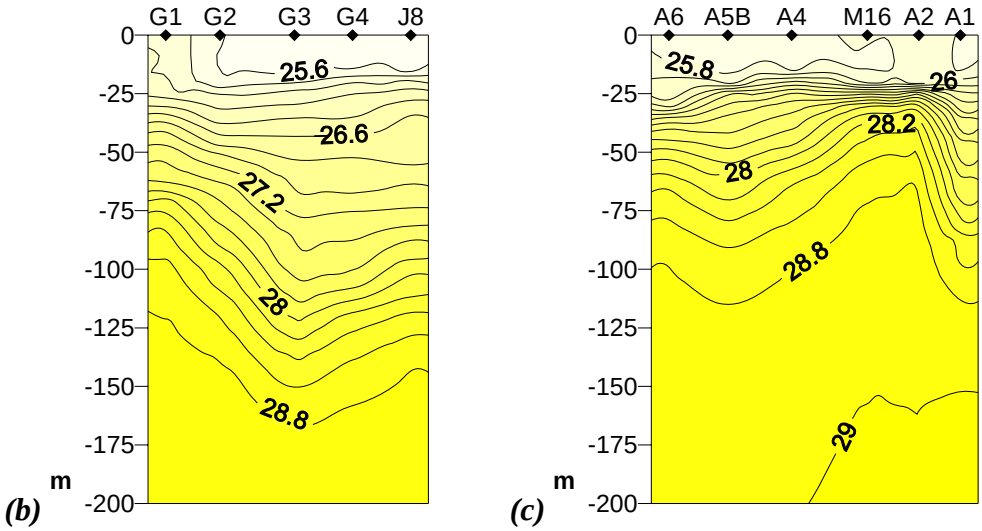

(b) *(c)*

Fig.f.3: seawater density σ_τ (kg/m^3) from surface to 200 m deep, along the 3 transects: (a) M-transect NE-SW, stM13-M26, (b) G-transect N-S, and (c) A-transect N-S. Distances between stations in miles. Data gridded with Surfer 7.0.

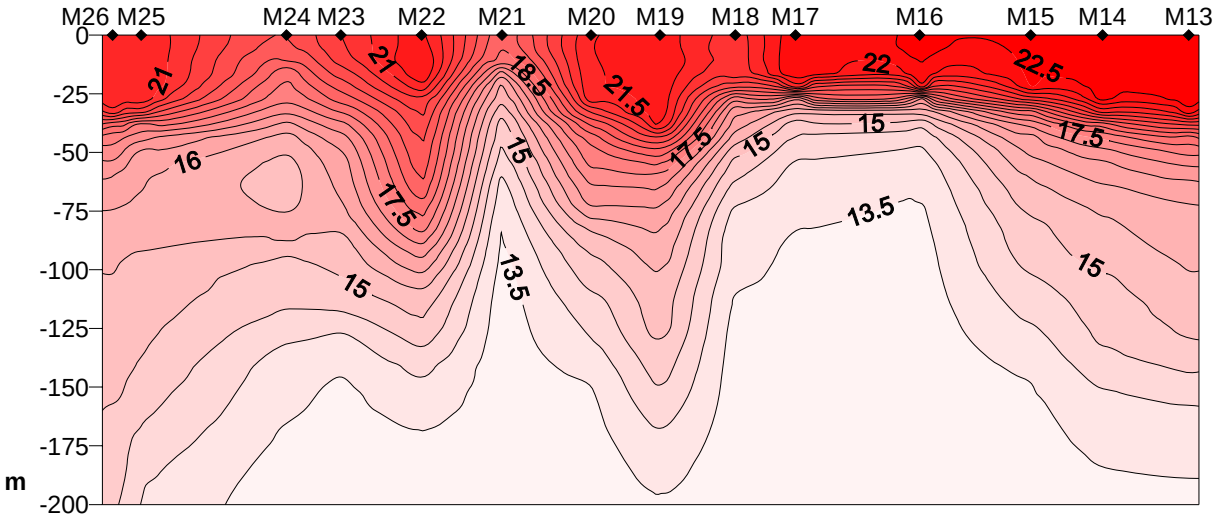

(a)

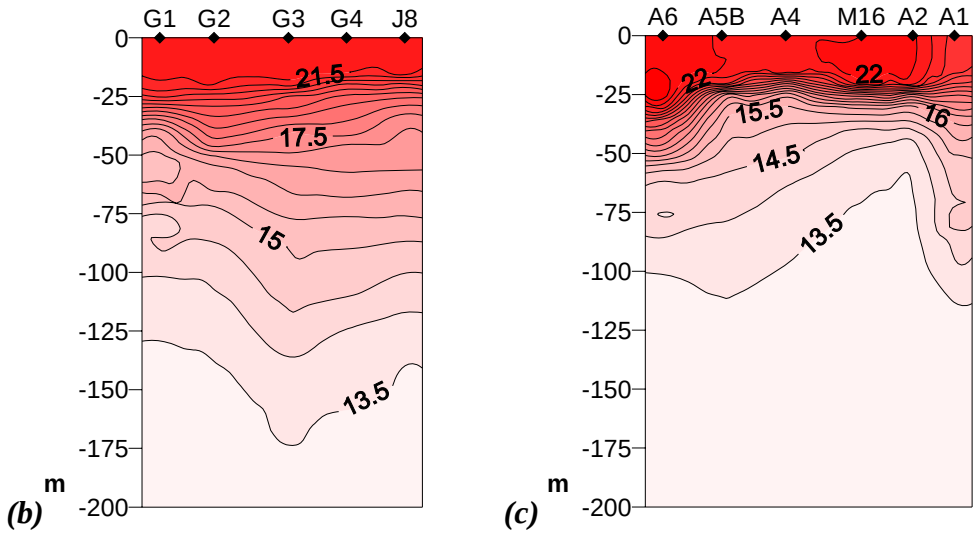

Fig.f.4: seawater temperature T (°C) from surface to 200 m deep, along the 3 transects: (a) M-transect NE-SW, stM13-M26, (b) G-transect N-S, and (c) A-transect N-S. Distances between stations in miles. Data gridded with Surfer 7.0.

Nutrient concentrations are generally high in the deep Mediterranean waters, with values as high as 9 µmol/l for nitrogen, 0.3 µmol/l for phosphate and 6 µmol/l for silicate around 200 m deep, while Atlantic surface waters are generally depleted in all nutrients. The upwelling of deep water determines high nitrogen concentrations just beneath the picnocline in correspondence of stM16-M17-A2 and from surface to 25m in stM21 (figs.f.5a and c), while Atlantic waters show very low nitrogen values along the 3 transects (<0.85 µmol/l, figs.f.5a, b and c).

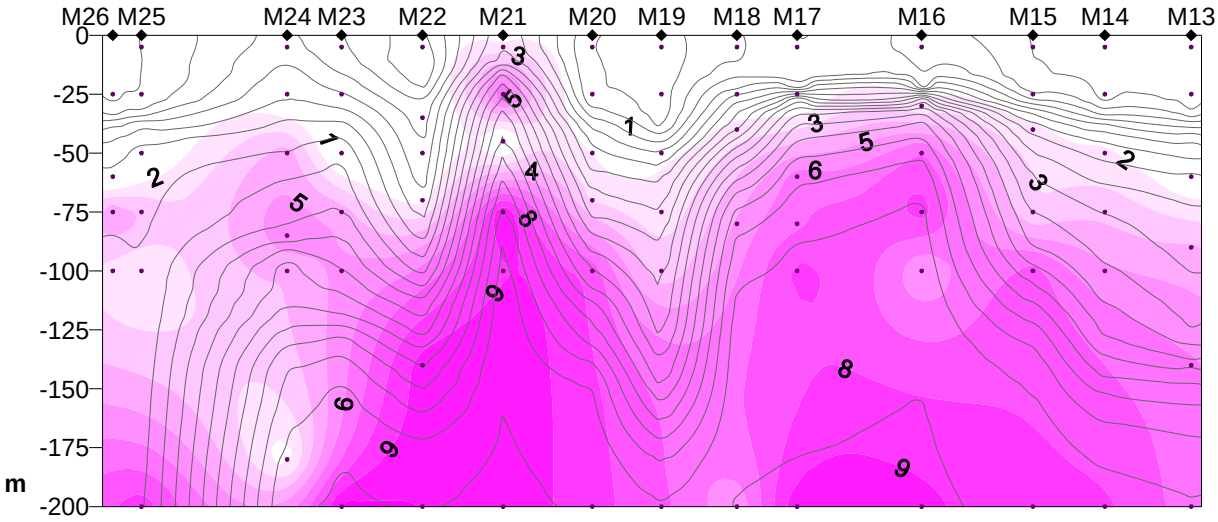

(a)

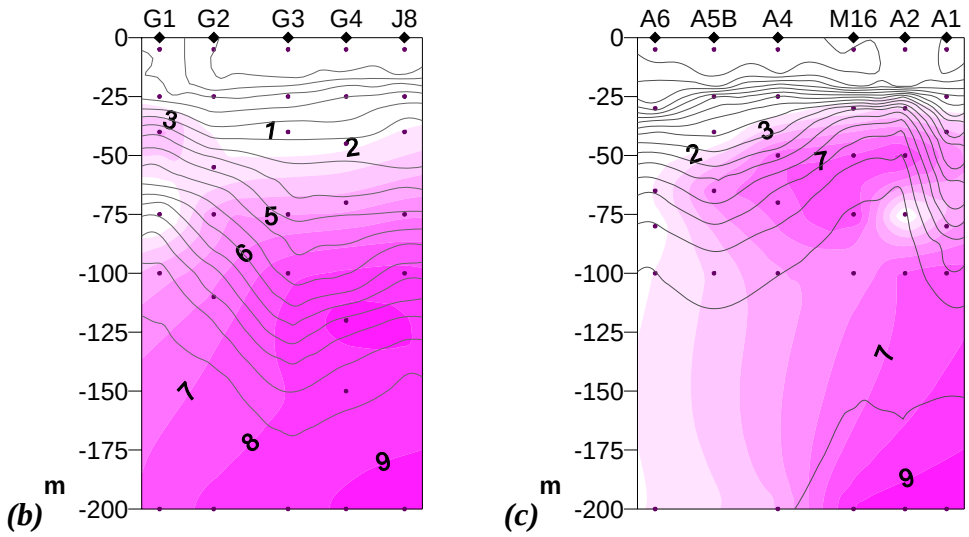

Fig.f.5: inorganic nitrogen (nitrate + nitrite, NO_3^-+NO_2^-) concentration map (µmol/l, in purple) overlapped to density isolines (σ_τ, kg/m^3, in grey), from surface to 200 m deep, along the 3 transects: (a) M-transect NE-SW, stM13-M26, (b) G-transect N-S, and (c) A-transect N-S. Distances between stations in miles, spots indicate the depths of sampling. Data gridded with Surfer 7.0.

Like nitrogen concentration, phosphate is higher at the mixing interface between Mediterranean and Atlantic modified waters, but also over the picnocline of stM16-M17-A2 (stA2 0m: 0.042 µmol/l, stM16 0m: 0.058 µmol/l, figs.f.6a and c). Moreover, phosphate concentration pattern is patchy, with large areas of depletion, both in deep water, deeply along the edges of the 2 mesoscale structures and in correspondence of the Spanish coastal stations stG1 and A6 (figs.f. 6a, b and c).

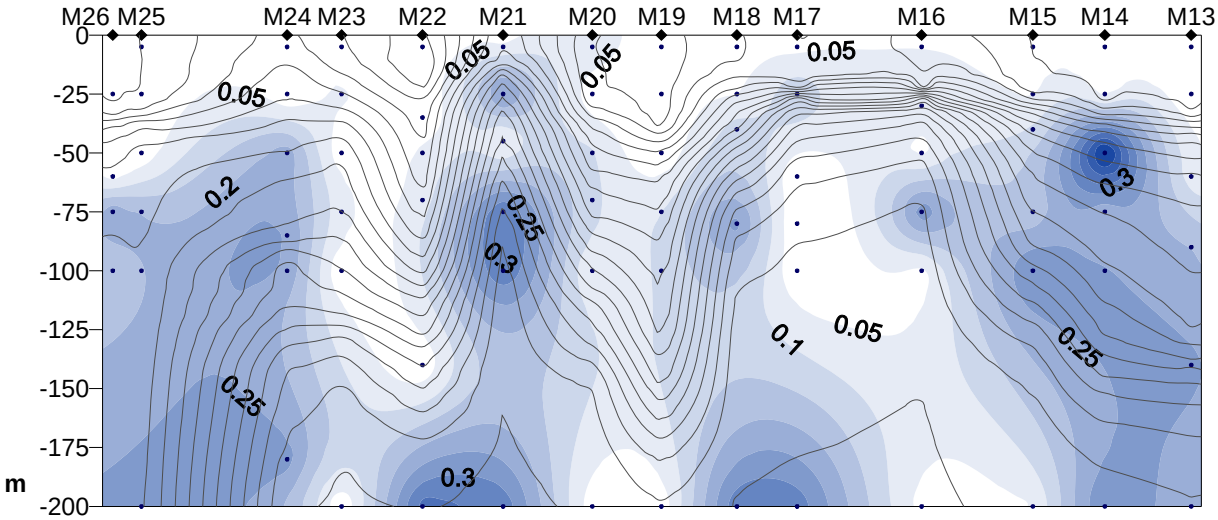

(a)

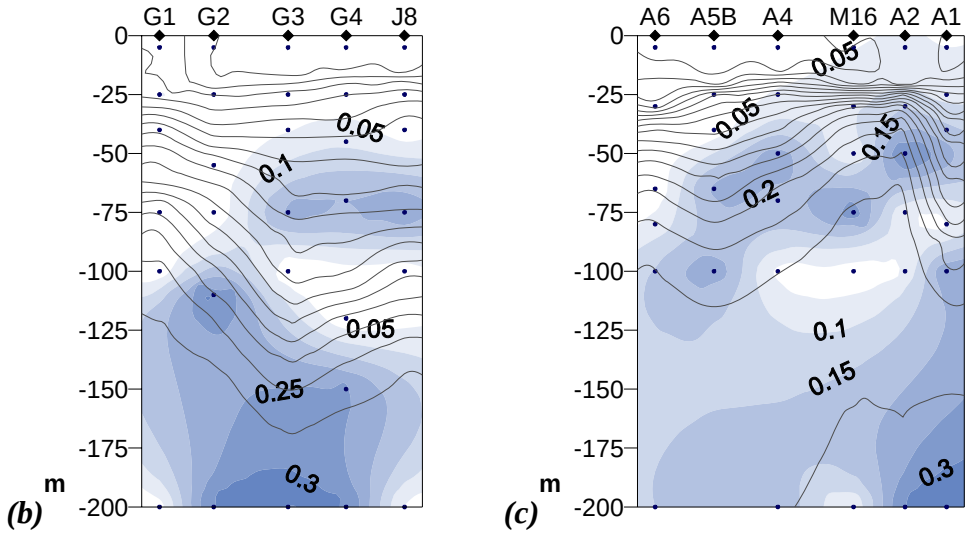

Fig.f.6: phosphate concentration map (PO_4^-, µmol/l, in blue) overlapped to density isolines (σ_τ, kg/m^3, in grey), from surface to 200 m deep, along the 3 transects: (a) M-transect NE-SW, stM13-M26, (b) G-transect N-S, and (c) A-transect N-S. Distances between stations in miles, spots indicate the depths of sampling. Data gridded with Surfer 7.0.

Along the M-transect, silicate distribution follows phosphate trend, with deep high values right beneath the mesoscale picnocline (ranging from 6 µmol/l around 200 m to 4 µmol/l), but also over it, in correspondence of stM16-M17-A2 (0m: stM16 0.62 µmol/l, stM17 0.59 µmol/l, stA2 0.62 µmol/l, figs.f.7a and c). Moreover, silicate concentration is generally high and homogeneously distributed in the deep Mediterranean and at the interface water (>1 µmol/l), while Atlantic surface waters are generally poor in silicate (<1 µmol/l, figs.f.7a, b and c).

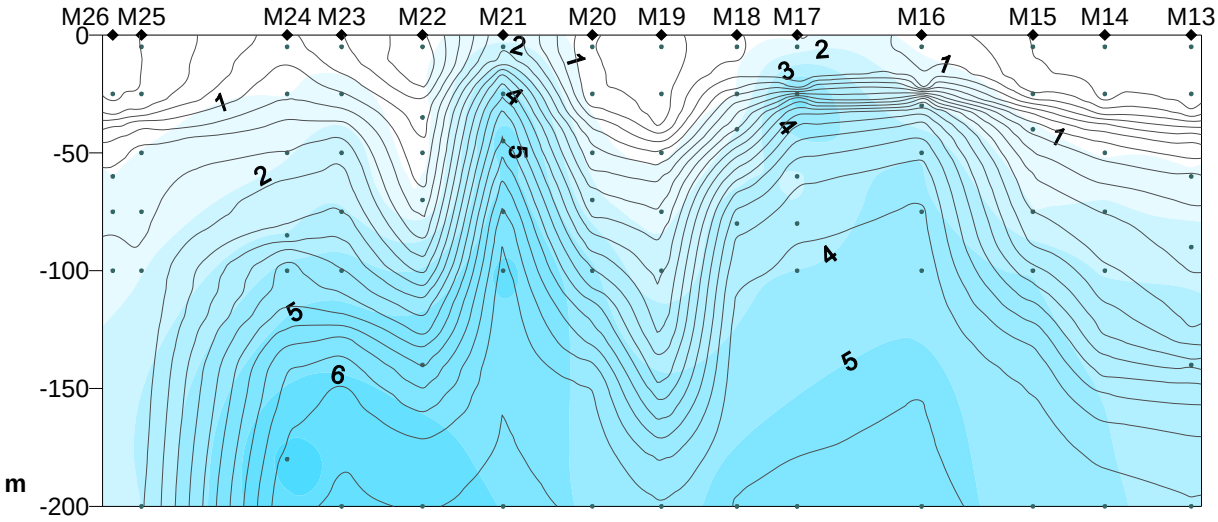

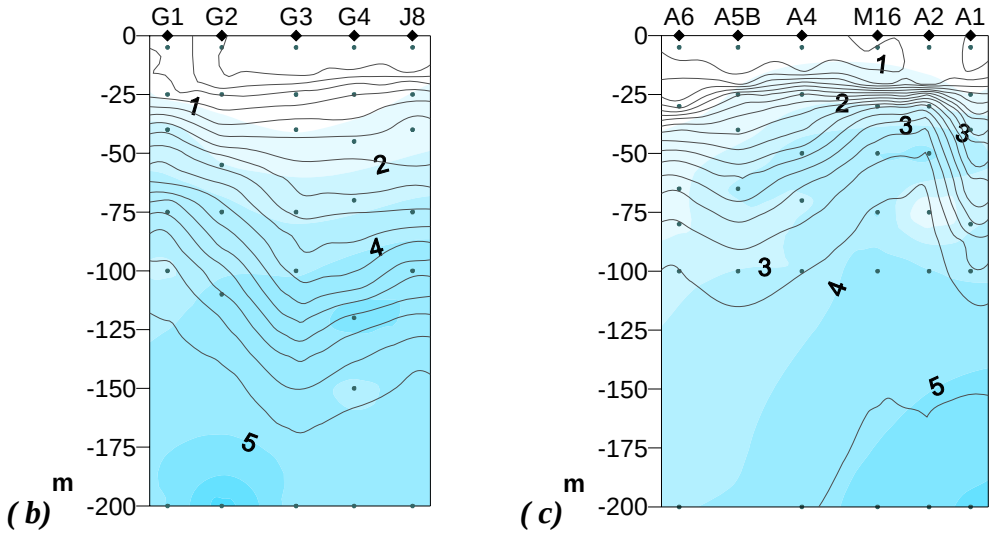

Fig.f.7: silicate concentration map (µmol/l, in light blue) overlapped to density isolines (σ_τ, kg/m^3, in grey), from surface to 200 m deep, along the 3 transects: (a) M-transect NE-SW, stM13-M26, (b) G-transect N-S, and (c) A-transect N-S. Distances between stations in miles, spots indicate the depths of sampling. Data gridded with Surfer 7.0.

3.a.2 *In vivo* fluorescence

Chlorophyll-*a* fluorescence profiles (u.r.) indicate that autotrophic biomass is mainly located from surface to 75 m and that its distribution follows the lowest density isolines (fig.f.8). Along the M-transect, the highest fluorescence values can be found just beneath the strong thermo-halocline in stations stM16 (0.82 u.r., 26 m) and stM17 (0.88 u.r., 27 m), deeper along the edges of the eastern mesoscale structure (stM15 0.43 u.r. at 43 m, and stM18 0.74 u.r. at 40 m, fig.f.8a). High values can be found also in correspondence of the upwelling of stM21 (0.99 u.r. at 33 m) and deeper on its eastern edge at stM20 (0.72 u.r. at 50 m). At Gibraltar, biomass is located between surface and 25 m in stM24, and deeper (25-50 m) in stM25-M26, according to the modified Atlantic water MAW isolines. Along the G-transect, fluorescence values are very low in the surface water, while they increase with depth in the coastal stations: 1.7 in stG1 at 42 m, and 1.1 and 0.94 u.r. in stG4-44 m and stJ8-50 m (fig.f.8b). StA1 shows the highest value of fluorescence, 2.56 u.r. at 47m, and the whole A-transect has higher values beneath the thermo-halocline, decreasing from around 25 to 50 m, moving in direction S-N (stA2-M16-A4 to A6, fig.f.8c).

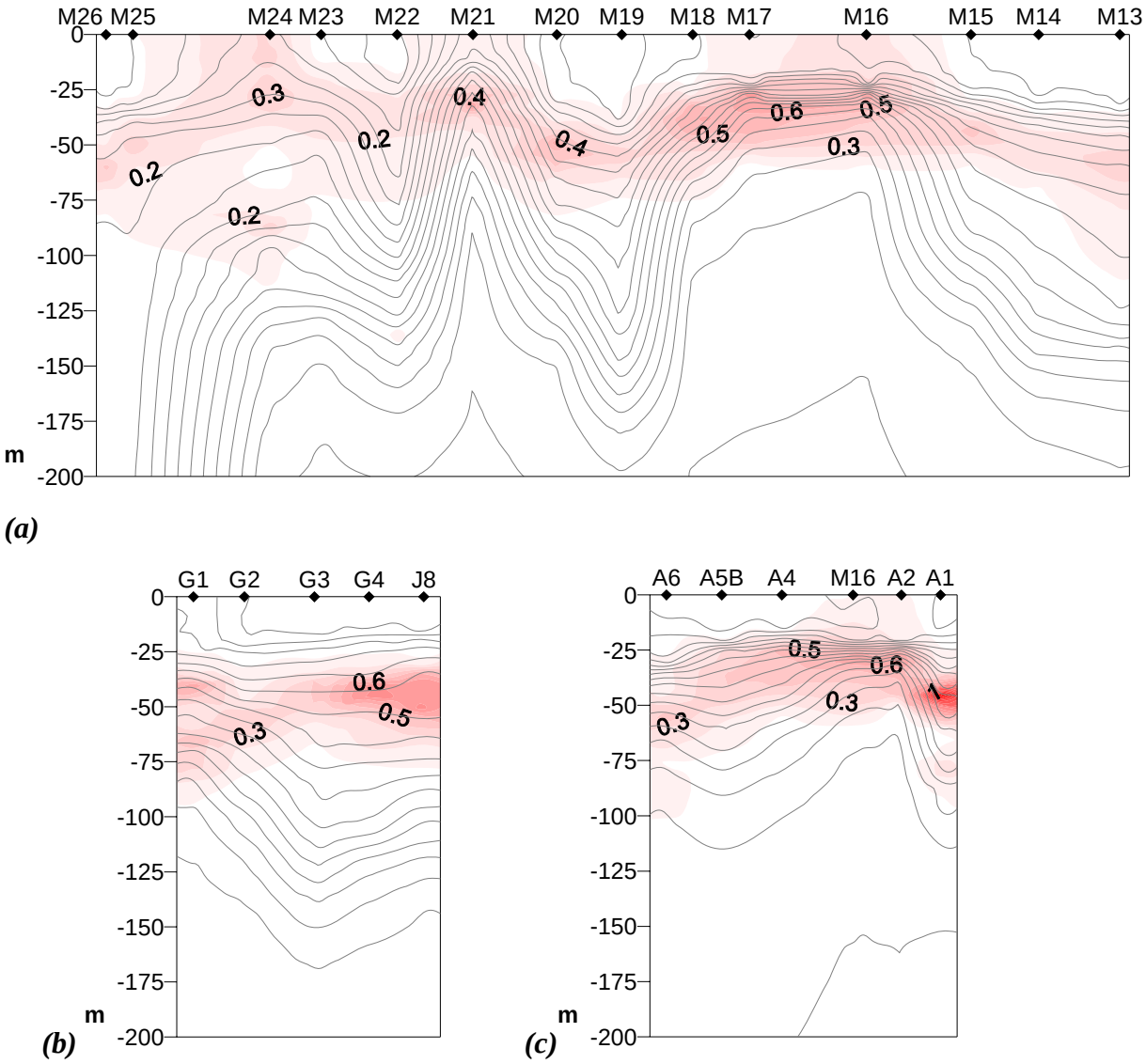

Fig.f.8: chlorophyll-*a* fluorescence map (u.r., in red) from surface to 200 m deep, along the 3 transects, overlapped to density isolines (σ_τ, kg/m^3, in grey): (a) M-transect NE-SW, stM13-M26, (b) G-transect N-S, and (c) A-transect N-S. Distances between stations in miles. Data gridded with Surfer 7.0.

3.a.3 Phytoplankton biomass density and composition

Microscopic countings (as total cell number from surface to a maximum depth 65 m, cell/l) indicate that phytoplanktonic cells are localized mainly in correspondence of the 2 mesoscale structures along the M and A-transects (figs.f.9a and c). High cell abundances can be found in the surface and picnocline waters of stM16-M17-A2 and stM21 (0-30 m, with 200000 cell/l at stM17, 25 m), or in the picnocline and beneath it in the stations at their sides: 25-40 m in stM15-M18 and stA1-A4-A5B, respectively (figs.f.9a and c). Cell number is high also beneath the picnocline along the G-transect in the coastal stations (40-45 m deep), both northern (stG1, fig.f.9b) and southern (stJ8-

A1, figs.f.9b and c), with the maximum number of cells, between the 63 analysed samples, of 393000 cell/l in stA1, 25 m deep.

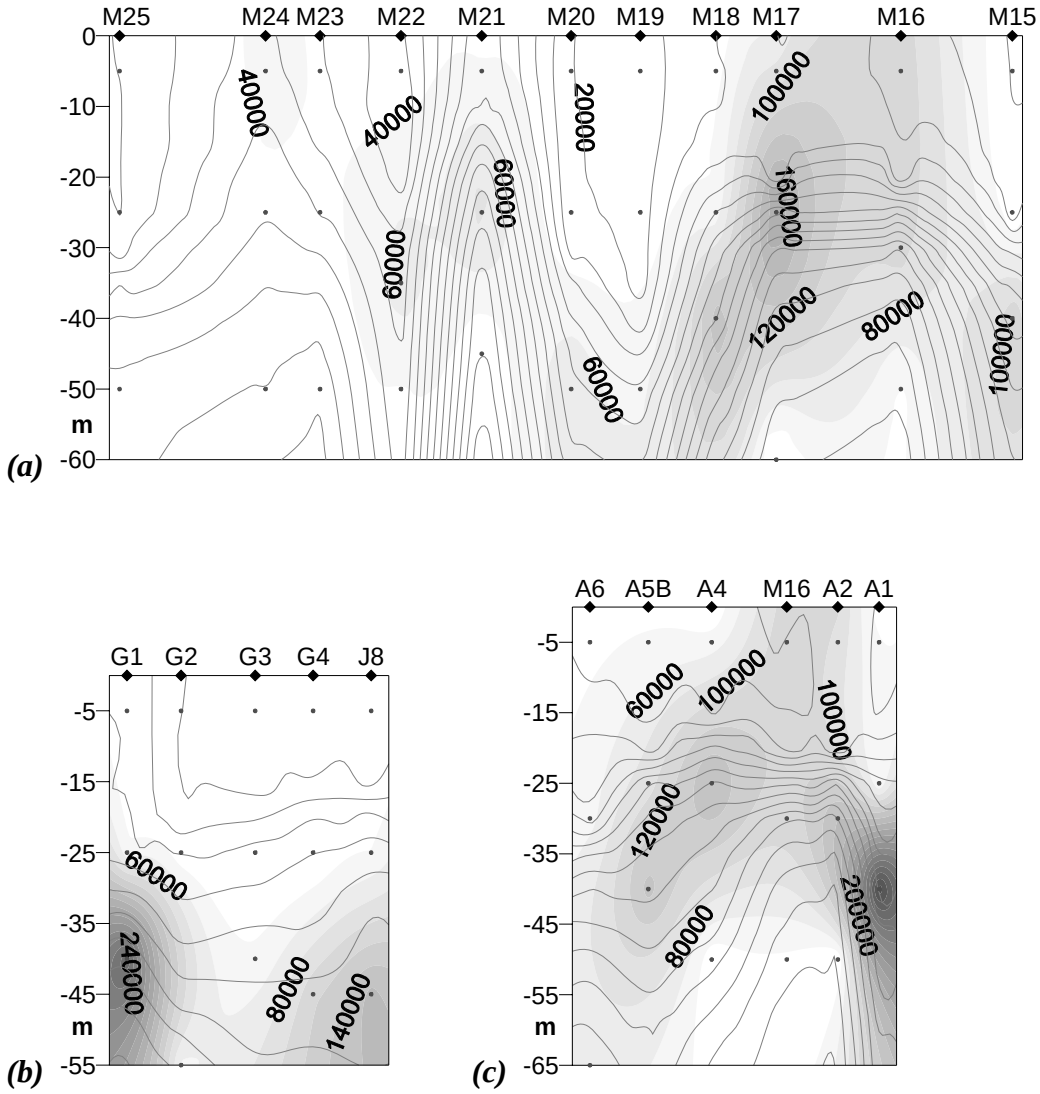

Fig.f.9: cell number map (cell/l) from microscopic countings, overlapped to density isolines (σ_τ, kg/m^3), from surface to 65 m deep, along the 3 transects: (a) M-transect NE-SW, stM13-M26, (b) G-transect N-S, and (c) A-transect N-S. Distances between stations in miles, spots indicate the depths of sampling. Data gridded with Surfer 7.0.

Bacillariophyceae have a patchy distribution: they show very low concentrations along the 3 transects, except for a station of the edge of the eastern mesoscale upwelling structure (stM18 at 40 m), where they represent the 55% of the phytoplankton (88000 cell/l, fig.f.10a), and for the coastal stations stG1 270000 and J8 45% 72000 along the G-transect, and stA1 72% 282000 (the highest abundance) for the A-transect (fig.f.10b and c). In particular, diatoms contribute to the 82% (270000 cell/l) and 72% (282000) of the phytoplankton in stG1 and stA1, respectively. The samples were dominated by a single species, a small centric diatom (diameter: 3-12 μm), likely *Thalassiosira partheneia* Schrader. At the microscope, cells were frequently aggregated in colonies

and interconnected by dark threads. This species is known to bloom in the Alboran sea and it has been observed forming gelatinous colonies (Gould and Wiesenburg 1990, Fiala *et al.* 1994).

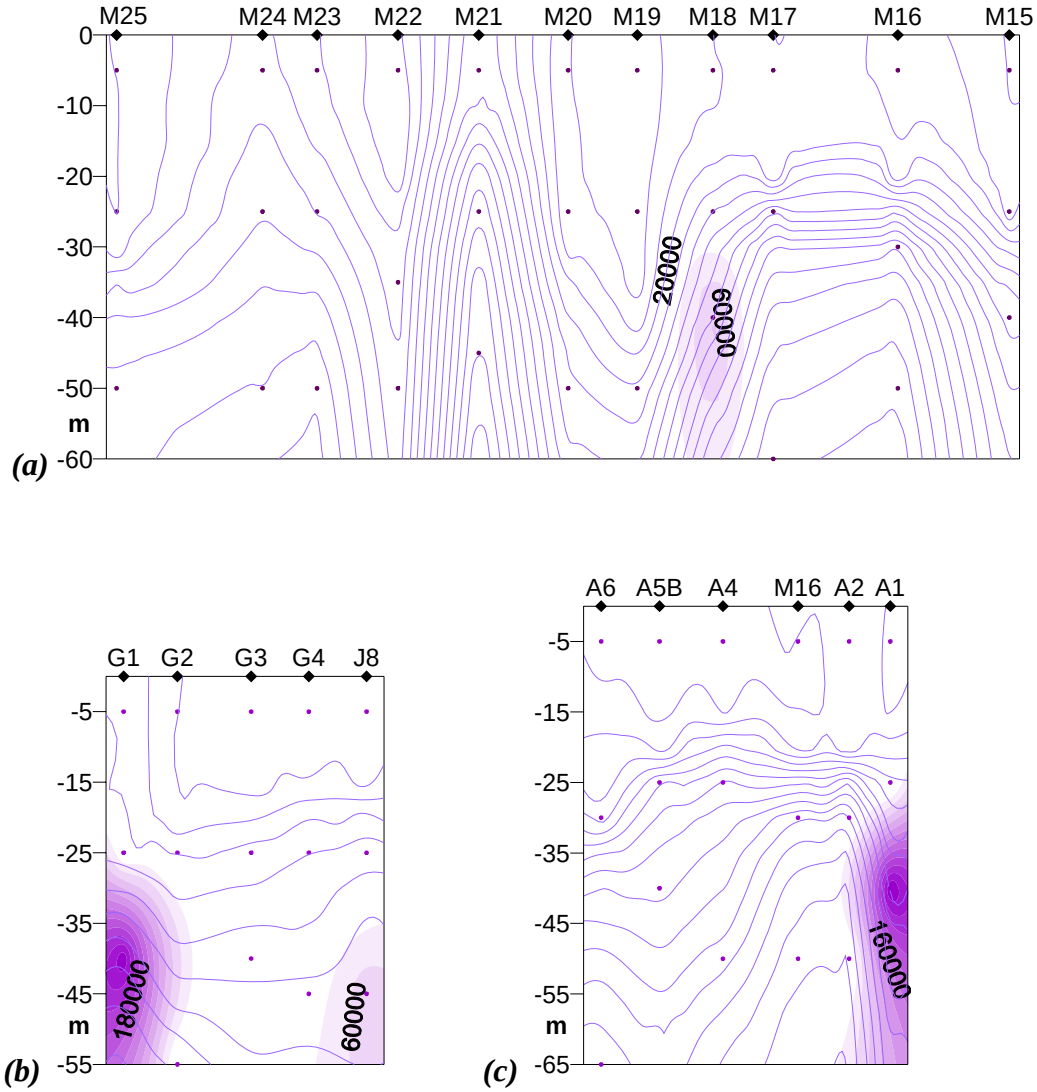

Fig.f.10: *Bacillariophyceae* cell number map (cell/l) from microscopic countings, overlapped to density isolines (σ_τ, kg/m^3), from surface to 65 m deep, along the 3 transects: (a) M-transect NE-SW, stM13-M26, (b) G-transect N-S, and (c) A-transect N-S. Distances between stations in miles, spots indicate the depths of sampling. Data gridded with Surfer 7.0.

Samples from stations stM16-M17 and from the A-transect are characterized by the presence of the Raphidophycean *Fibrocapsa japonica* Toriumi & Takano, a potentially harmful alga, which co-dominates the population together with Dinophyceans (see below). *F. japonica* contributes to 36% (40000 cell/l) of the assemblage in the surface sample of stM16, but it's generally abundant beneath the picnocline, in particular at 25 m in stM17 (29%, 59500 cell/l, the highest abundance, fig.f.11a) and at 30 m in stA2

(33%, 53000 cell/l, fig.f.11c). On the contrary, it's absent both western to stM18 and along the G-transect (fig.f.11b). Hence, *F. japonica* distribution is a very localized one.

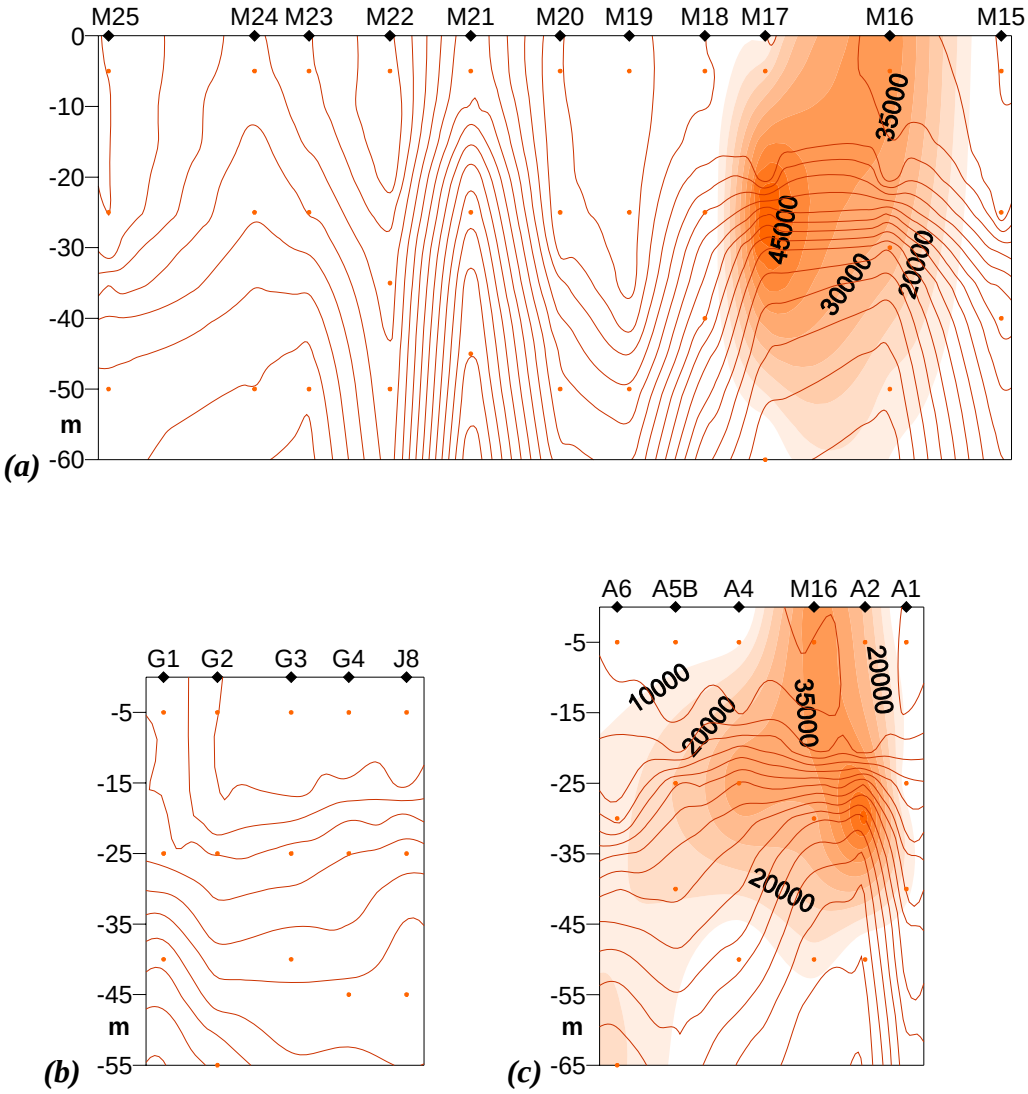

Fig.f.11: *Fibrocapsa japonica (Raphidophyceae)* cell number map (cell/l) from microscopic countings, overlapped to density isolines (σ_τ, kg/m^3), from surface to 65 m deep, along the 3 transects: (a) M-transect NE-SW, stM13-M26, (b) G-transect N-S, and (c) A-transect N-S. Distances between stations in miles, spots indicate the depths of sampling. Data gridded with Surfer 7.0.

Raphidophyceae are fragile naked flagellates which are usually lysed by common fixatives, like formalin. As a consequence, it can be difficult to recognize them after fixation. Indeed, at the microscope *F. japonica* cells appeared mainly broken ("raspberry" shaped, fig.f.12a), with trichocysts and ejectosomes discharged (figs.f.12a, b and c), but they still showed the typical rod-shaped posterior mucocysts (indicated by the arrow in figs.f.12b and c), which made the identification easier. They were often aggregated in a mucous net, which entrapped also other cells (fig.f.12d).

F. japonica microscopic identification was confirmed by a preliminary investigation by PCR amplification of nuclear internal transcriber spacer regions. The amplification has been conducted on a few field samples, which resulted both free from *F. japonica* and containing it by microscopic observation. The amplification produced fragments of suitable sequence sizes: fragments were around 350 bp long for samples stM17 25 m, stM16 30m, stA2 0m, stA1 40m, around 260 bp for *Heterosigma akashiwo* cultured sample, while they didn't work for samples stM19 25m and stG2 0m.

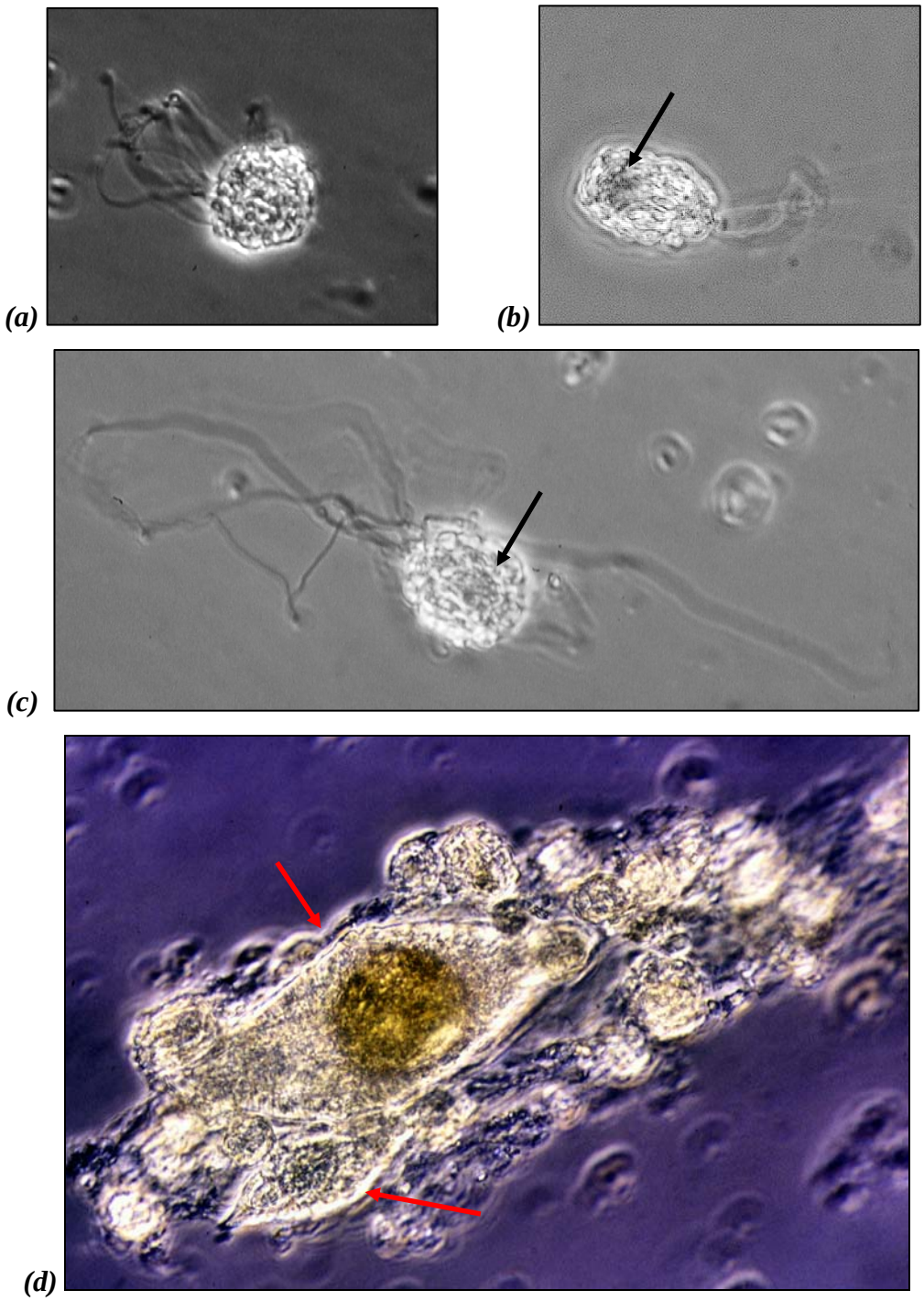

Fig.f.12: pictures of *Fibrocapsa japonica (Raphidophyceae)* from microscopic observations: cell diameter is generally 15-30 μm: in (a) a raspberry-like cell, in (b) and (c) are clearly visible discharged trichocysts and ejectosomes and the rod-shaped posterior mucocysts (indicated by the black arrows), in (d) a mucous net, containing F. japonica cells as well as two dinoflagellates (indicated by the red arrows).

Dinophyceae co-dominate together with *Fibrocapsa japonica* in samples from stations stM16-M17 and from the A-transect, for example they contribute to 46% of the population in stM17 (94000 cell/l, 30 m), while stA4, 25 m, has the highest abundance (96000 cell/l, 59% of the population) and its surface sample consist for 73% of *Dinophyceae* (figs.f.13a and c). Hence in correspondence of the eastern mesoscale upwelling, dinoflagellates are generally distributed along the whole water column (between 0 and 50 m deep), but they are generally abundant right beneath the picnocline. However, a large contribute of dinoflagellates to the cell densities can be detected along the whole A-transect, from 39% to 56% in the Atlantic waters of stA5B and A6 (fig.f.13c). Lower concentrations can be found also westerly, in the modified Atlantic waters of stM21-M24 (maximum 16000 cell/l, fig.f.13a) and along the G-transect (maximum 29000 cell/l, stG4, 45 m, fig.f.13b).

Between athecates, the most common species observed along the A-transect and in stM16-M17 were *Gyrodinium* sp. cf. *fusiforme* Kofoid et Swezy, with mean values of 2000 cell/l) and small *Gymnodinium* spp., with sizes ranging from 9 to 30 μm. Between thecates, *Heterocapsa* spp. (*H.* cf. *minima* Pomroy, *H.* cf. *niei* (Loeblich) Morrill & Loeblich III, and *H.* cf. *rotundata* (Lohmann) G. Hansen) were the most abundant species, reaching values as high as 64500 cell/l in stM17 25 m and 54000 cell/l in stA4 25 m). An other abundant species observed is *Scrippsiella trochoidea* (Stein) Loeblich III, reaching 7800 cell/l in stA4 25 m, while small techates with size ranging from 9 to 30 μm were detected in all the analysed samples.

It's worth noting the presence of chain of the toxic *Gymnodinium catenatum* Graham in correspondence of stM21-M22-M23 and along the G-transect, with a maximum value of 3800 cell/l in stG4, 45 m. In general, a few harmful species of dinoflagellates were detected: *Karenia* sp., *Lingulodinium polyedricum* (Stein) Dodge, *Prorocentrum* spp., *Gonyaulax hyalina* Ostenfeld and Schmidt, and *Gonyaulax polygramma* Stein.

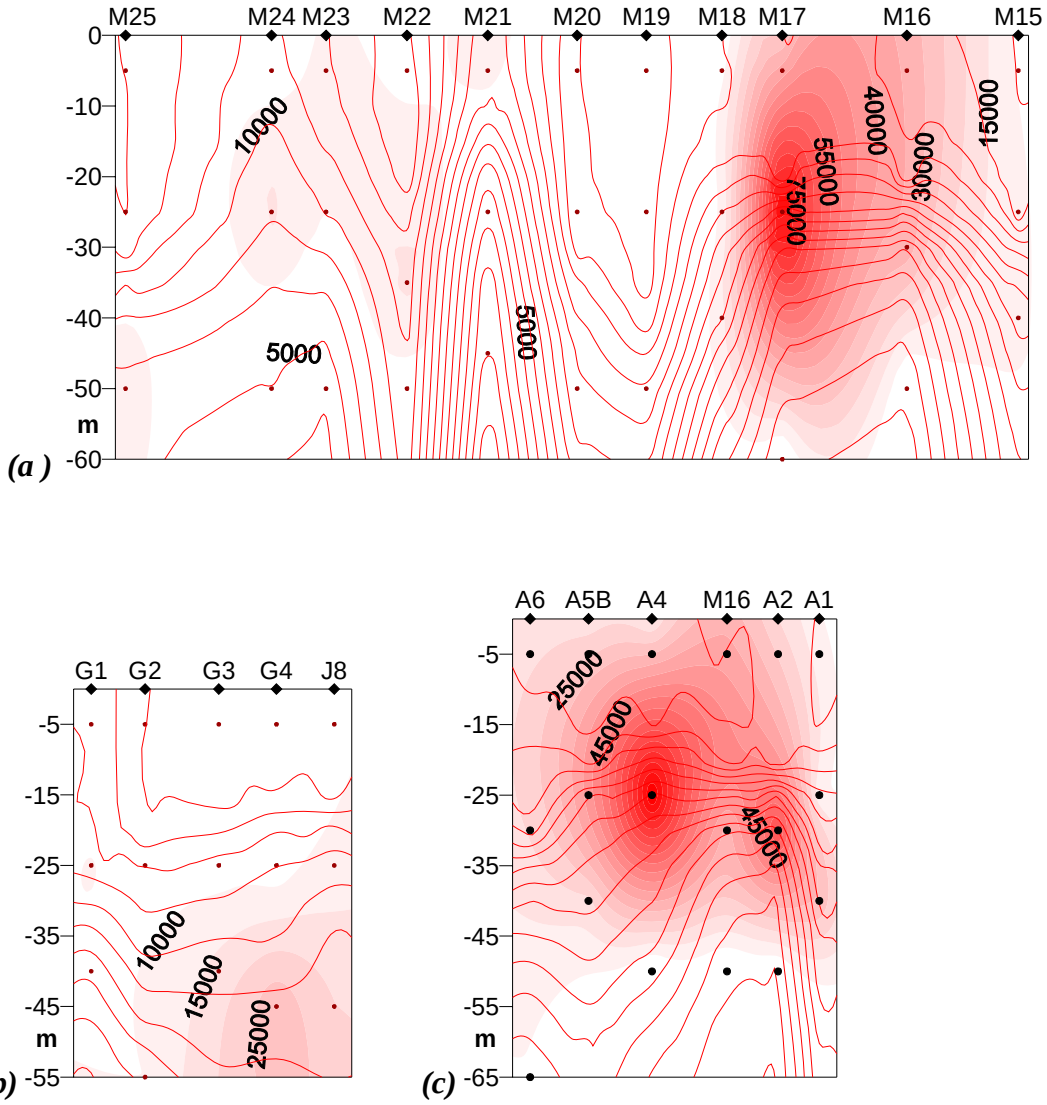

Fig.f.13: *Dinohyceae* cell number map (cell/l) from microscopic countings, overlapped to density isolines (σ_τ, kg/m^3), from surface to 65 m deep, along the 3 transects: (a) M-transect NE-SW, stM13-M26, (b) G-transect N-S, and (c) A-transect N-S. Distances between stations in miles, spots indicate the depths of sampling. Data gridded with Surfer 7.0.

Prymnesiophyceae were ubiquitous in the samples analysed, except for surface samples. In particular, high concentrations can be found in correspondence of the edges of the upwelling mesoscale structures, where deep Mediterranean and modified Atlantic waters mix, and at the coastal stations, in any case at a depth around 40-60 m (fig.f.14). The highest value were found in the 40 m samples in stM15 (92700 cell/l, 79% of the assemblege), stA5B (79500 cell/l, 54%) and stA1 (62500 cell/l, only 19% due to the massive presence of diatoms).

The most abundant species were *Emiliania huxleyi* (Lohmann) Hay et Mohler, and *Gephyrocapsa oceanica* Kamptner, generally co-present but in a largely variable

relative ratio. Other frequent species were *Calciosolenia murrayi* Gran, mainly along the A-transect and in the eastern stations of the M-transect, and *Algirosphaera robusta* (Lohmann) Norris, which is uniformly present along the 3 transects and abundant in the western M-stations.

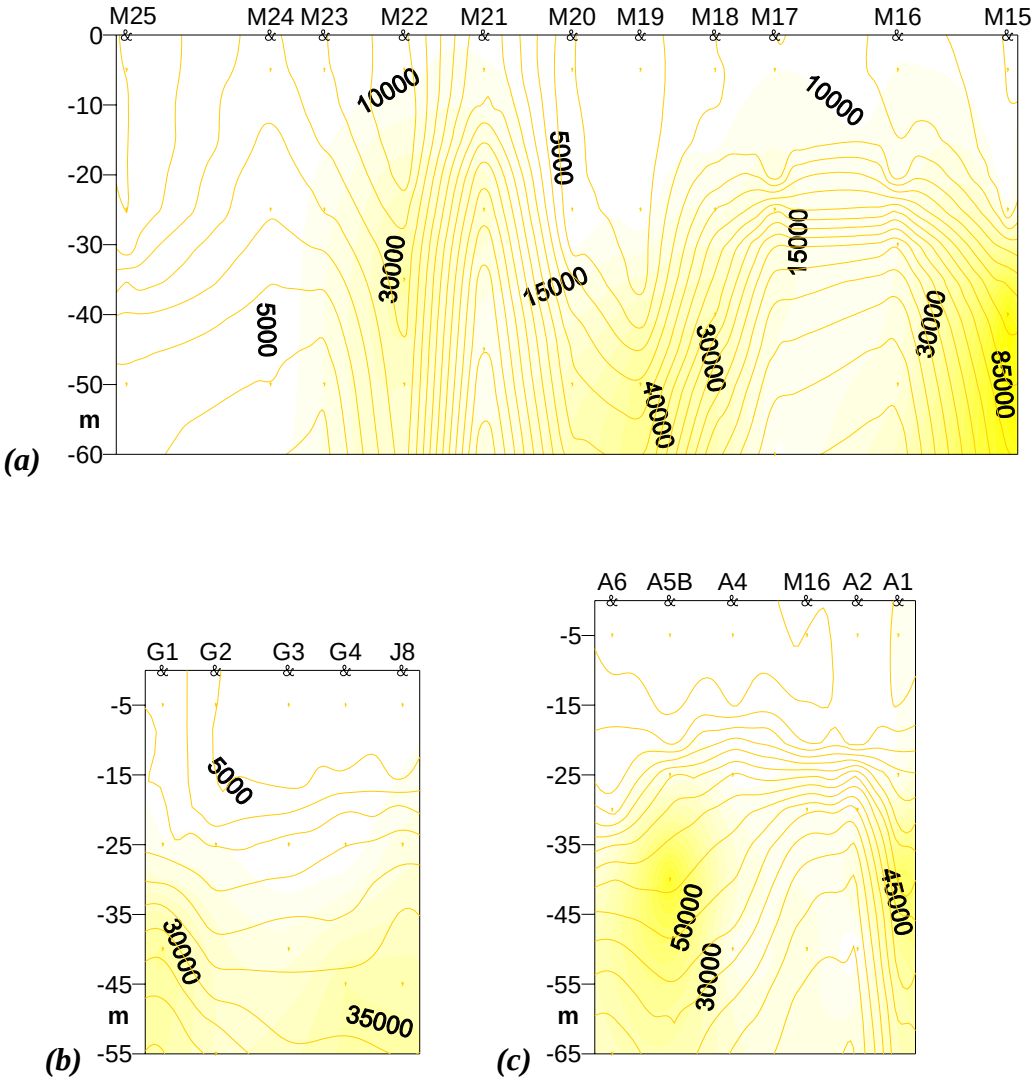

Fig.f.14: *Prymnesiophyceae* cell number map (cell/l) from microscopic countings, overlapped to density isolines (σ_τ, kg/m^3), from surface to 65 m deep, along the 3 transects: (a) M-transect NE-SW, stM13-M26, (b) G-transect N-S, and (c) A-transect N-S. Distances between stations in miles, spots indicate the depths of sampling. Data gridded with Surfer 7.0.

Finally, in both the 2 main upwelling structures and their edges we detected high abundances of the so-named "other plancton", an heterogeneous group of generally nanoplanktonic flagellates, including *Cryptophyceae*, *Chrysophyceae*, *Prymnesiophyceae Prymnesiales*, *Prasinophyceae*, other unidentified < 10-µm flagellates and *incertae sedis* (fig.f.15). The most ubiquitous and abundant species is the so-named flagellate sp.e, a 3-6 µm in diameter biflagellate, it is possible that it belongs

to the *Phaeocystis* genus (*Haptophyta 4s*): this species reaches values as high as 46000 cell/l in stA2 0 m (45% of the sample population, fig.f.15c) and stM21 25 m (42%, fig.f.15a). On the contrary, both surface Atlantic waters (western stations M, fig.f.15b) and stJ8-G4 (fig.f.15b) are characterized by the co-presence of *Cryptomonadaceae* (*Cryptomonas* spp., cf. *Teleaulax acuta* (Butcher) Hill, which represents the 16% and 31% of the cell densities in stM23 and M24, 0 m, respectively) and *Prasinophyceae* (3-6 µm in diameter, *Tetraselmis* spp. and *Pyramimonas* spp., 43% of sample stM24 0 m, fig.f.15a).

Also heterotrophic cells can contribute to the composition of the samples, in particular *Leucocryptos marina* (Braarud) Butcher, which reaches the 21% of the sample in stM22 0 m (fig.f.15a) and other small flagellates.

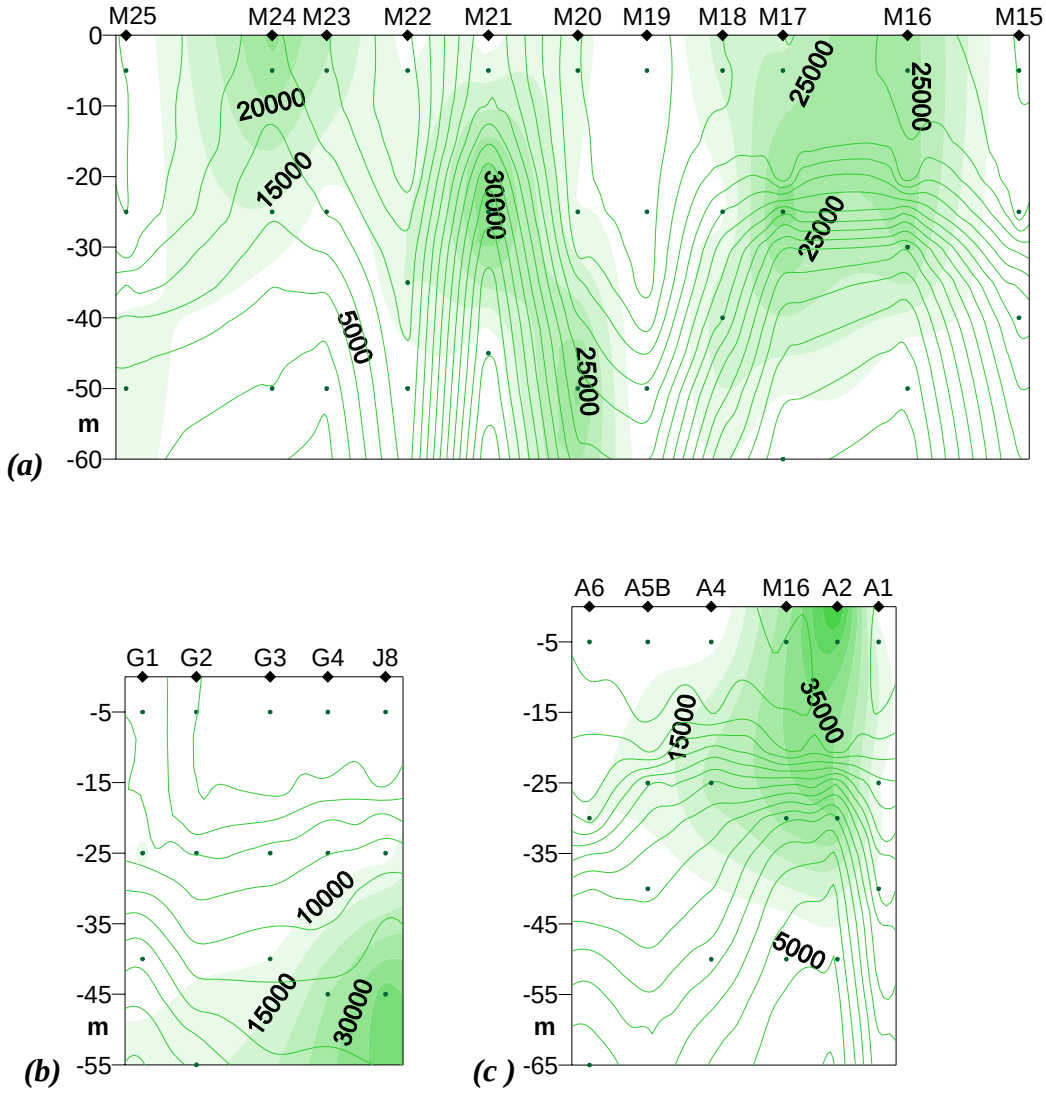

Fig.f.15: map of the so-named "other plancton" (*Cryptophyceae*, *Chrysophyceae, Prymensiophyceae Prymnesiales, Prasinophyceae*, unidentified < 10-µm flagellates and *incertae sedis*, in cell/l) cells number, from microscopic countings, overlapped to density isolines (σ_τ, kg/m^3), from surface to 65 m deep, along the 3 transects: (a) M-transect NE-SW, stM13-M26, (b) G-transect N-S, and (c) A-transect N-

S. Distances between stations in miles, spots indicate the depths of sampling. Data gridded with Surfer 7.0.

3.a.4 Pigment composition

Biomass distribution both as fluorescence emission (fig.f.5) and as cells number (fig.f.9) is confirmed by total chlorophyll-*a* (chlorophyll-*a* + divinil chlorophyll-*a*) concentration map (fig.f.16): chlorophyll-a (chla) value is high in correspondence of the eastern mesoscale structure, where it reaches its maximum of 4.7 mg/m^3 (stM17, 25 m, fig.f.16a). The A-transect shows chla concentration > 1 mg/m^3 in surface samples from the upwelling (stM16 0 m and 30 m, 1.1 and 1.0 mg/m^3) and from below the picnocline (stA1-40 m 1.8, stA2-30 m 1.3, stA4-25m 1.8, and stA5B-25 m 1.3 mg/m^3, respectively), while the western M-stations and the G-transect have generally low values (< 0.6 mg/m3), except for the coastal stations at the depth of 40-45 m: stG1 and J8 (0.9 mg/m^3), and stG4 (1.2 mg/m^3).

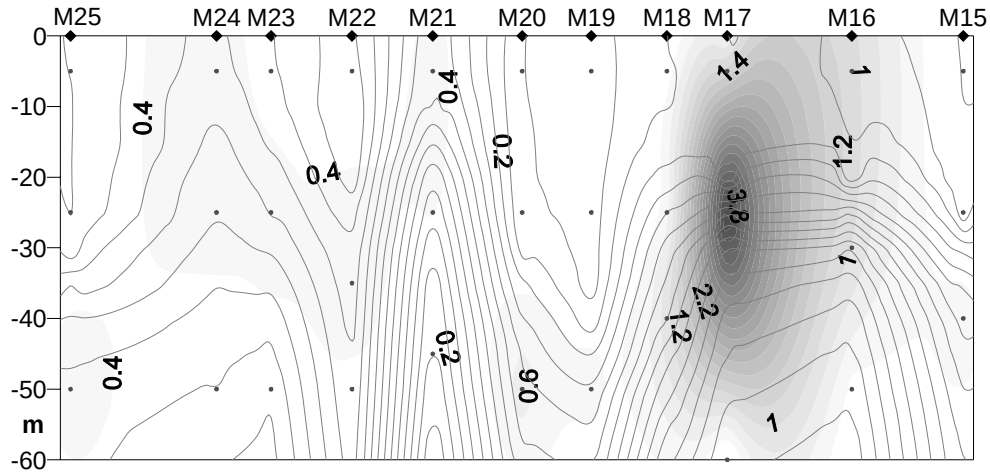

(a)

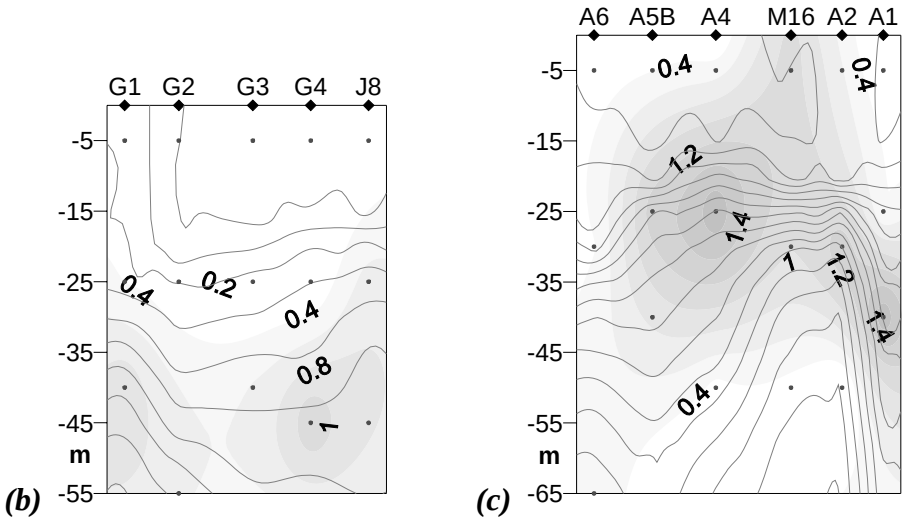

Fig.f.16: total chlorophyll-*a* concentration (chlorophyll-*a* + divinil-chlorophyll-*a*, mg/m^3) from HPLC analysis, overlapped to density isolines (σ_τ, kg/m^3), from surface to 65 m deep, along the 3 transects: (a) M-transect NE-SW, stM13-M26, (b) G-transect N-S, and (c) A-transect N-S. Distances between stations in miles, spots indicate the depths of sampling. Data gridded with Surfer 7.0.

Fig.f.17 shows the linear correlation (R^2=0.447, n=112, fig.f.17a) between total chlorophyll-*a* (in mg/m^3) and fluorescence (u.r.) for all the sampled depths, from stM13 to stM25 + the A- and G-transect stations: selecting the surface samples from depths z < z_{uml} improves the linear correlation (R^2=0.78) and increases the fluorescence / chlorophyll-*a* ratio (from 0.33 to 0.54, fig.f.17b).

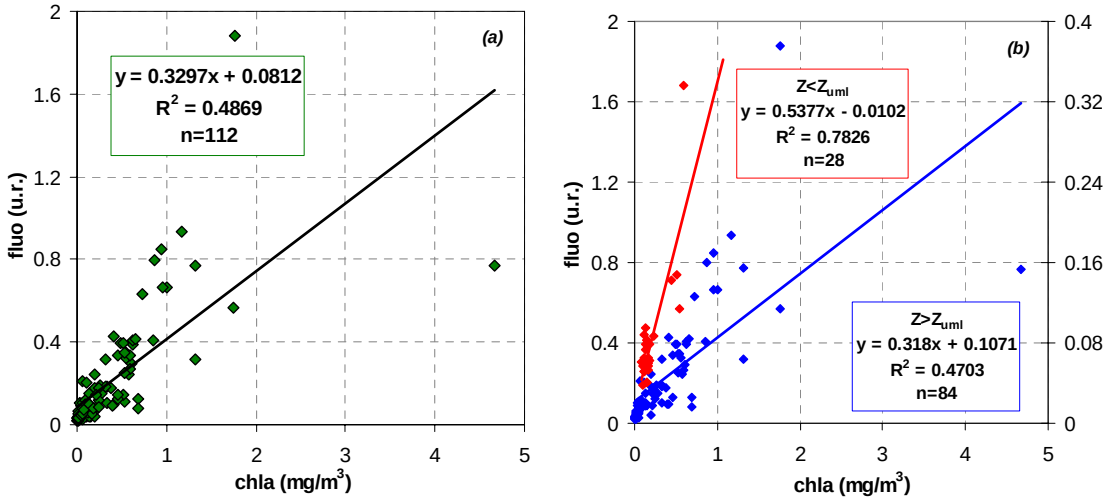

Fig.f.17: linear correlation between total chlorophyll-a (mg/m^3) from HPLC analysis and fluorescence emission (u.r., by SeaTech fluorometer), (a) for all the samples (in green), along the 3 transects: M-transect NE-SW, stM13-M25, G-transect N-S, and A-transect N-S, and (b) after the separation between samples from z<z_{uml} (in red, right y-axis,) and z>z_{uml} (in blue, left y-axis,).

Moreover, the distribution of the different taxa along the three transects by cell countings is supported by diagnostic pigments maps. Fucoxanthin concentration map

confirms *Bacillariophyceae* and *Raphidophyceae* maps of distribution (fig.f.18), with the highest value (1.2 mg/m^3) at stM17 25 m, the richest sample in *F. japonica* cells. Except for stM16, which has fucoxantin values of 0.3 mg/m^3, again due to the presence of *F. japonica*, the M-transect shows low fucoxanthin concentrations (<0.2 mg/m^3, fig.f.18a). Along the G-transect, fucoxanthin has the highest values in correspondence of the coastal *Thalassiosira sp.* contributes (stG1 40 m: 0.25 mg/m^3, and stJ8 40 m: 0.13 mg/m^3, fig.f.17b), while along the A-transect values > 0.3 mg/m^3 are due to the presence of *F. japonica*, except for stA1, which is the richest in diatoms (fig.f.18c).

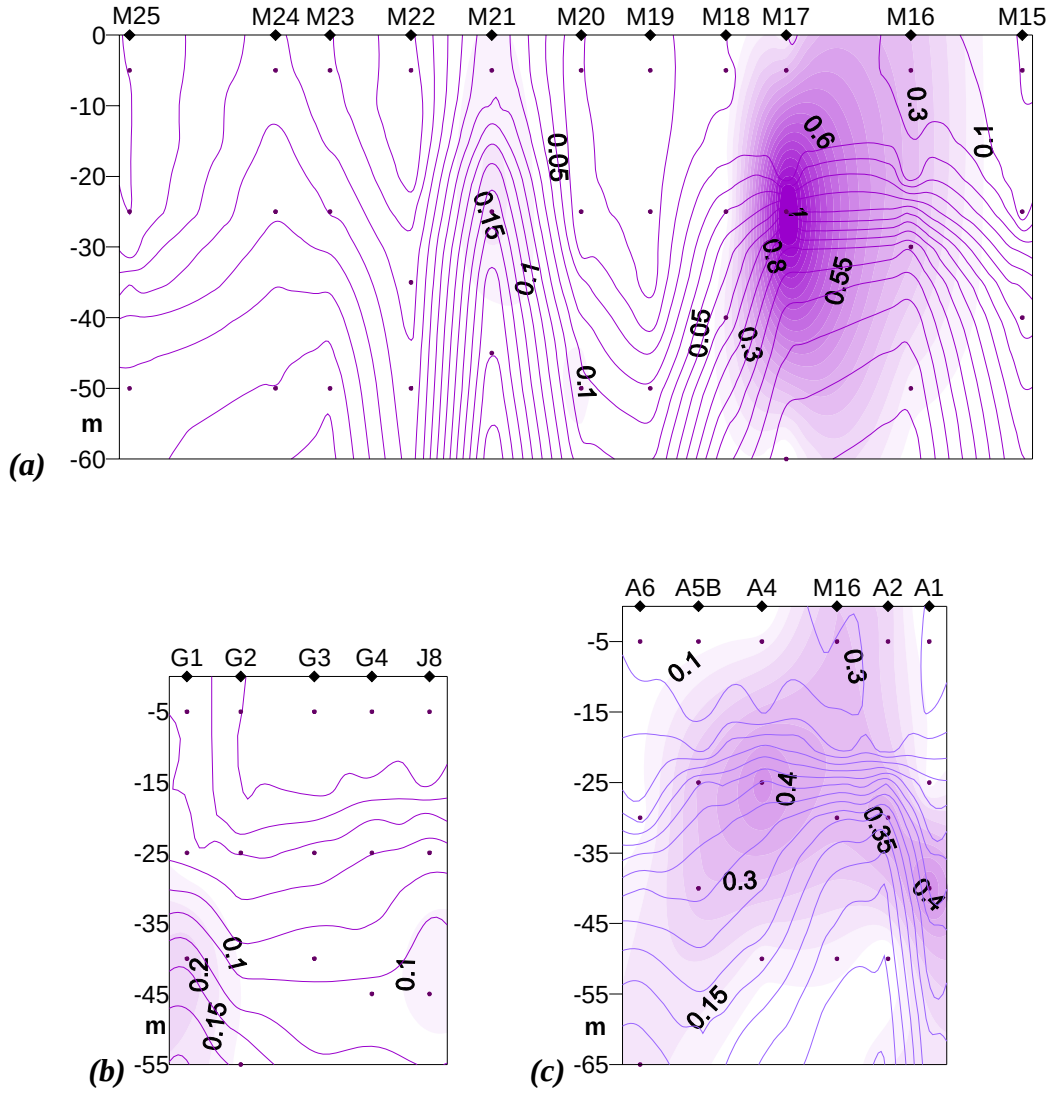

Fig.f.18: fucoxanthin concentration (mg/m^3) from HPLC analysis, overlapped to density isolines (σ_τ, kg/m^3), from surface to 65 m deep, along the 3 transects: (a) M-transect NE-SW, stM13-M26, (b) G-transect N-S, and (c) A-transect N-S. Distances between stations in miles, spots indicate the depths of sampling. Data gridded with Surfer 7.0.

Peridinin reflects *Dinophyceae* distribution: it has low values along the G-transect (<0.04 mg/m^3, except for stG4 45 m, fig.f.19b) and the western M-transect (<0.06 mg/m^3, fig.f.19a), while the stations of the mesoscale upwelling show the highest values of 0.25 mg/m^3 in stM17 25 m and 0.22 mg/m^3 in stA4 25 m, which are rich in *Heterocapsa* spp. (figs.f.19a and c).

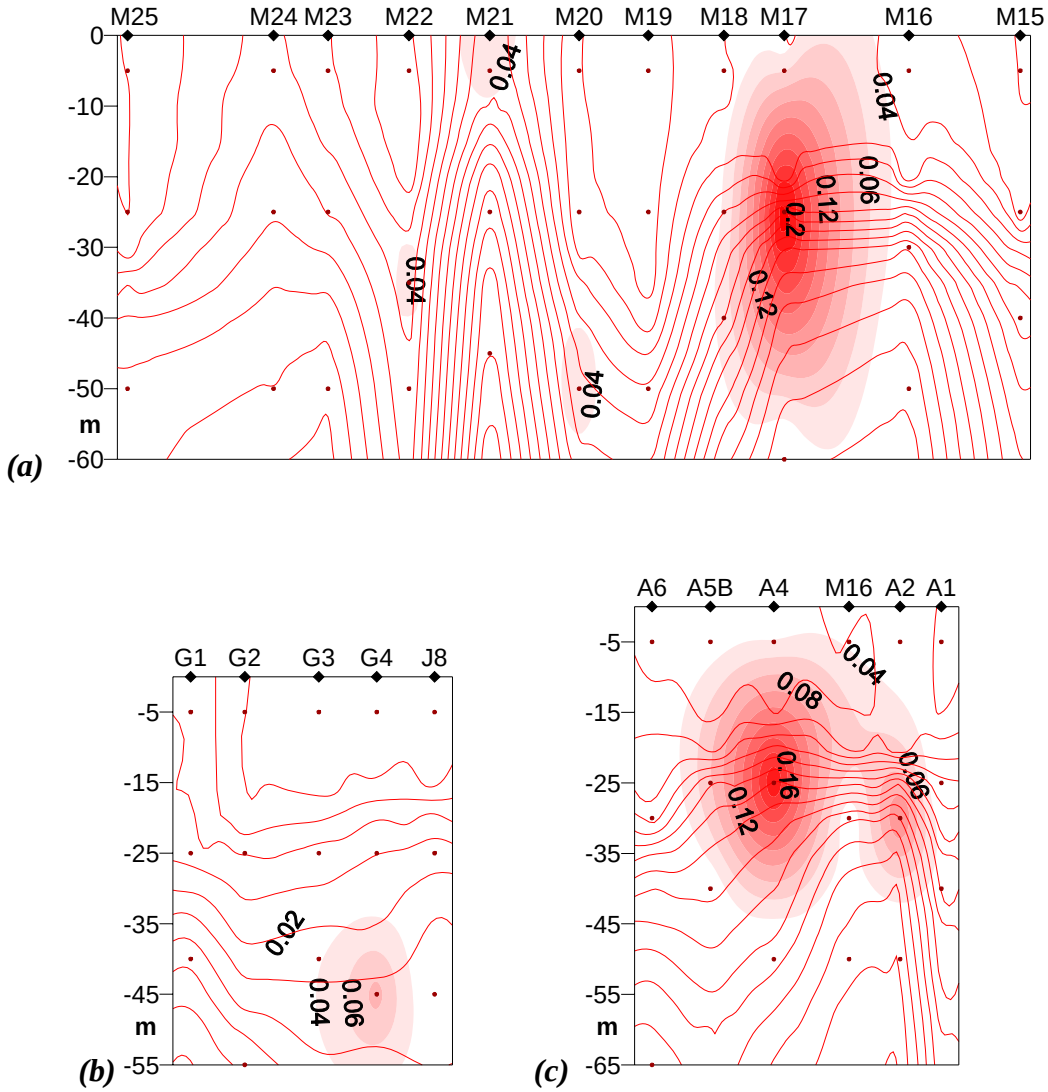

Fig.f.19: peridinin concentration (mg/m^3) from HPLC analysis, overlapped to density isolines (σ_τ, kg/m^3), from surface to 65 m deep, along the 3 transects: (a) M-transect NE-SW, stM13-M26, (b) G-transect N-S, and (c) A-transect N-S. Distances between stations in miles, spots indicate the depths of sampling. Data gridded with Surfer 7.0.

19'-Hesanoyloxyfucoxanthin confirms the diffuse presence of *Prymnesiophyceae not Coccolithophorales* in the deeper waters, especially at the picnocline between deep Mediterranean and modified Atlantic waters (stM17 and stA4 25 m, 0.20 and 0.23 mg/m^3, respectively, figs.f.20a and c), in correspondence of the edges of the upwelling mesoscale structures (stM20 50 m 0.14 mg/m^3, stM22 35 m 0.17 mg/m^3, fig.f.20a), and

at the coastal stations (stJ8 40 m 0.24 mg/m^3, stG4 45 m 0.20 mg/m^3, fig.f.20b). 19'-Hesanoyloxyfucoxanthin map indicates also high concentrations at the Atlantic stations: stM24 25 m 0.20 mg/m^3, and stM25 50 m 0.19 mg/m^3 (fig.f. 20a), presumably due to a higher abundance of rare species, like *Discosphaera tubifer* (Murray & Blackman) Ostenfeld, and *Helicosphaera carteri* (Wallich) Kamptner.

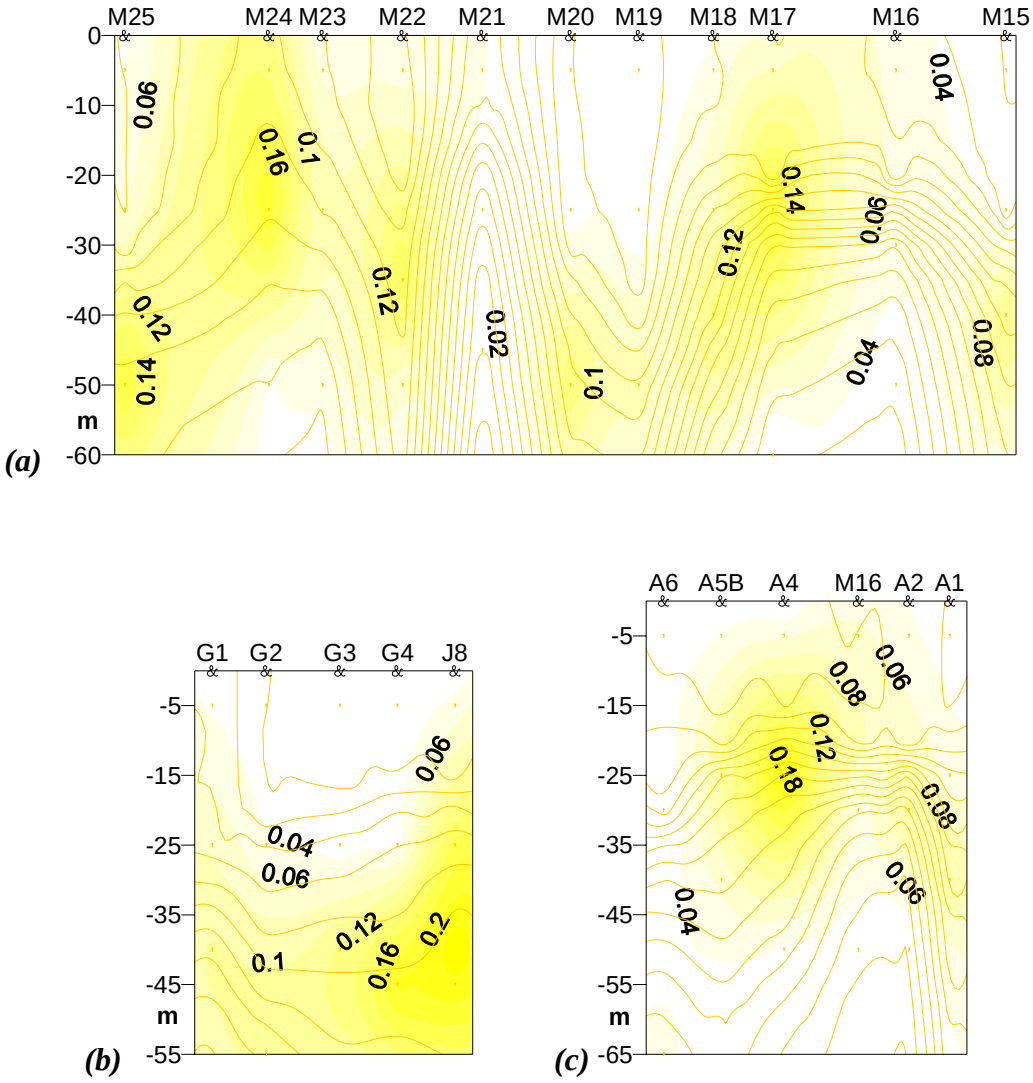

Fig.f.20: 19'-Hesanoyloxyfucoxanthin concentration (mg/m^3) from HPLC analysis, overlapped to density isolines (σ_τ, kg/m^3), from surface to 65 m deep, along the 3 transects: (a) M-transect NE-SW, stM13-M26, (b) G-transect N-S, and (c) A-transect N-S. Distances between stations in miles, spots indicate the depths of sampling. Data gridded with Surfer 7.0.

Finally, *Cryptophyceae, Prymensiophyceae Prymnesiales* and *Prasinophyceae* maps are validated by the corresponding diagnostic pigments: alloxanthin, 19'-Butanoyloxyfucoxanthin and prasinoxanthin (figs.21, 22 and 23). Alloxanthin has high values both in MAW waters (western stations M: stM23 25 m 0.012 mg/m^3, fig.f.21a) and below the picnocline along the G-transect (maximum value at stG4 45m, 0.021

mg/m^3, and stJ8 40 m, 0.014 mg/m^3, fig.f.21b) and along the edges of the upwellings in the A-transect (stA5B and stA1 40 m, 0.010 and 0.013 mg/m^3, respectively, fig.f.21c).

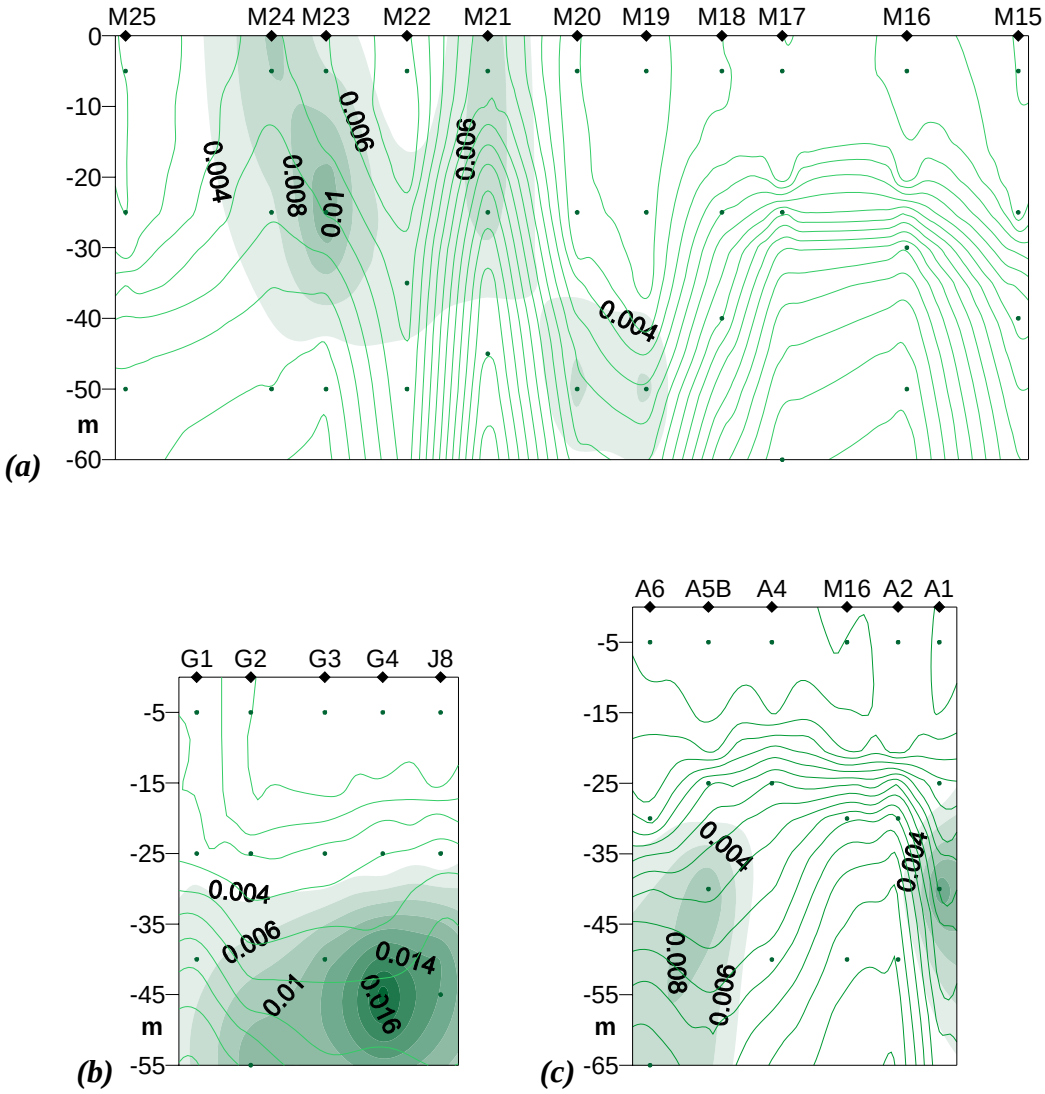

Fig.f.21: Alloxanthin concentration (mg/m^3) from HPLC analysis, overlapped to density isolines (σ_τ, kg/m^3), from surface to 65 m deep, along the 3 transects: (a) M-transect NE-SW, stM13-M26, (b) G-transect N-S, and (c) A-transect N-S. Distances between stations in miles, spots indicate the depths of sampling. Data gridded with Surfer 7.0.

19'-Butanoyloxyfucoxanthin map proves the widespread distribution of *Prymnesiophyceae Prymnesiales* and *Chrysophyceae*, except for the surface Atlantic waters, for the mesoscale upwelling of stM21 and for the coastal stations of transect A (concentrations > 0.05 mg/m^3, fig.f.221). In particular, the maximum values can be found in stJ8 (45 m, 0.13 mg/m^3) and stG4 (40 m, 0.12 mg/m^3, fig.f.22a).

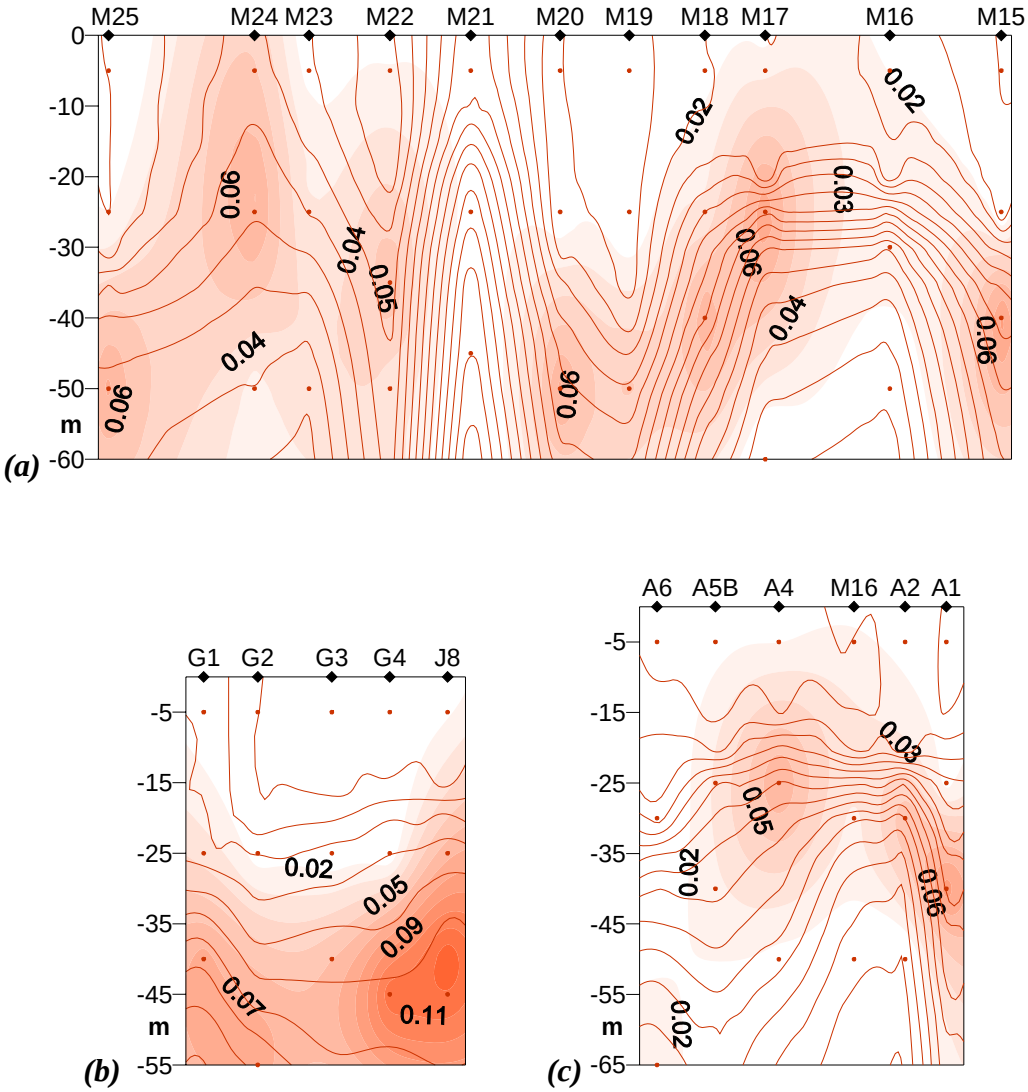

Fig.f.22: 19'-Butanoyloxyfucoxanthin concentration (mg/m^3) from HPLC analysis, overlapped to density isolines (σ_τ, kg/m^3), from surface to 65 m deep, along the 3 transects: (a) M-transect NE-SW, stM13-M26, (b) G-transect N-S, and (c) A-transect N-S. Distances between stations in miles, spots indicate the depths of sampling. Data gridded with Surfer 7.0.

Moreover, prasinoxanthin map confirms the high abundances of *Prasinophyceae* in correspondence of both the surface Atlantic waters (stM24 0 m: 0.022 mg/m^3, fig.f.23a) and along the upwelling edges (stM18 40 m: 0.033 mg/m^3, stM15 40 m: 0.024 mg/m^3, stA1 40 m: 0.042 mg/m^3, figs.f.23a and c) of transect M, and below the picnocline in the G-transect, with values ranging from 0.037 to 0.056 mg/m^3 around 40-55 m of depth in stJ8-G2 (fig.f.23b).

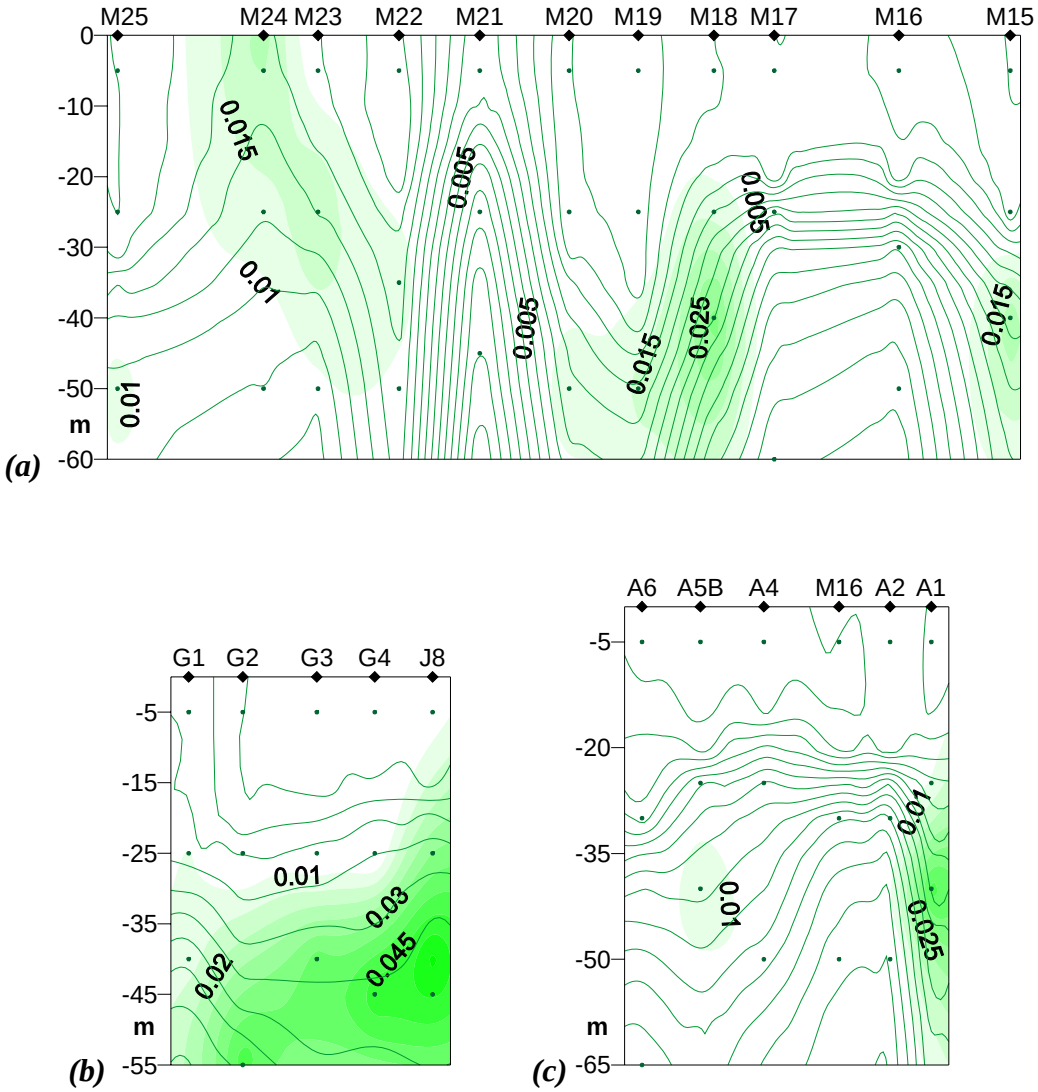

Fig.f.23: Prasinoxanthin concentration (mg/m^3) from HPLC analysis, overlapped to density isolines (σ_τ, kg/m^3), from surface to 65 m deep, along the 3 transects: (a) M-transect NE-SW, stM13-M26, (b) G-transect N-S, and (c) A-transect N-S. Distances between stations in miles, spots indicate the depths of sampling. Data gridded with Surfer 7.0.

Finally, figs.f24 and 25 show the pattern of distribution of *Cyanophyta* and *Prochlorophyta*. Maps show data by HPLC analysis of the corresponding diagnostic pigments alone (zeaxanthin and divinil chlorophyll-*a*, respectively), due to the small sizes of these cells, which prevent from countings by optical microscope.

Zeaxanthin map suggests that *Cyanophyta* are distributed mainly in the surface Atlantic waters, along all the three transects (fig.f.24). The mean surface concentration values are generally > 0.04 mg/m^3, except for the northern side of the A-transect, which reaches values as high as 0.22 mg/m^3 in correspondence of the picnocline (stA 25 m, fig.f.24c).

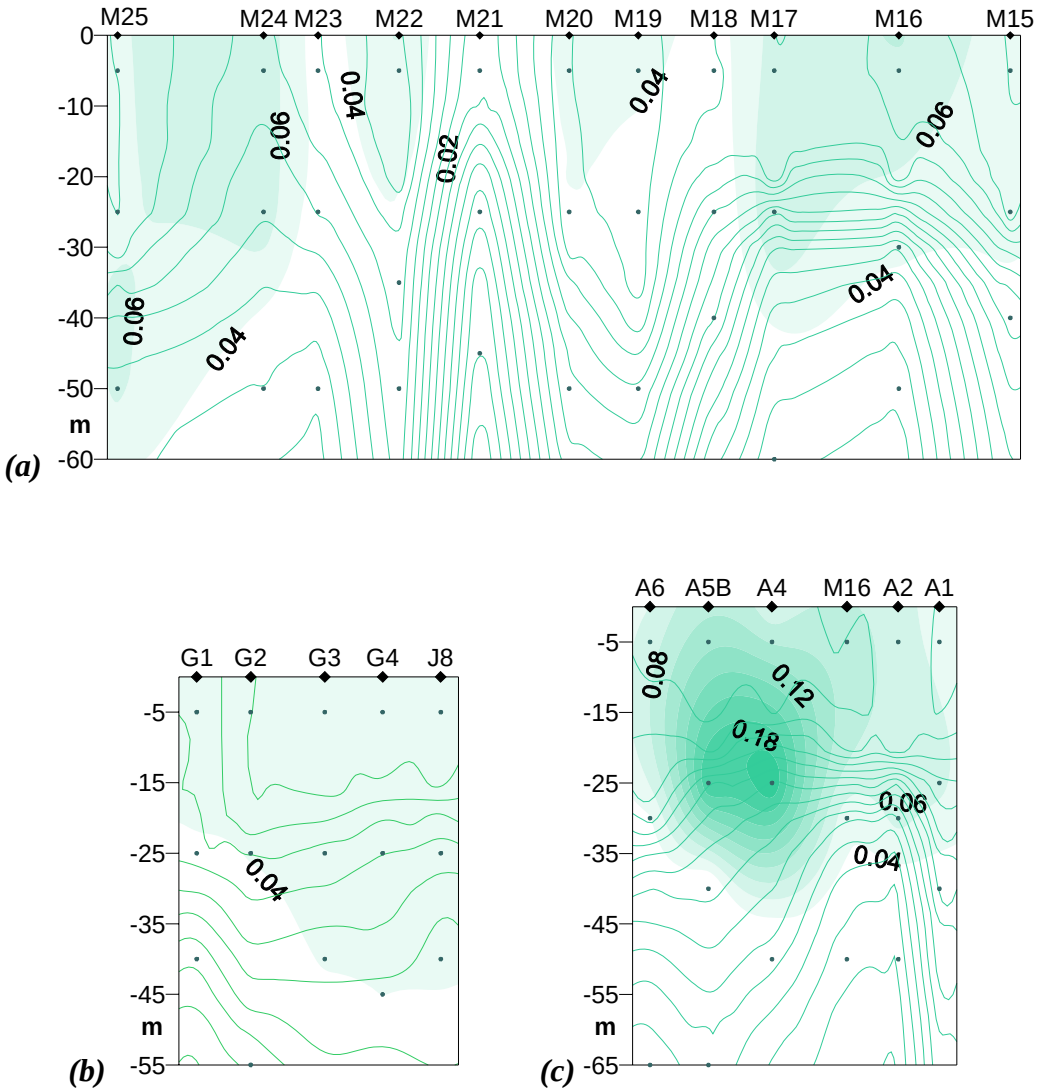

Fig.f.24: Zeaxanthin concentration (mg/m^3) from HPLC analysis, overlapped to density isolines (σ_τ, kg/m^3), from surface to 65 m deep, along the 3 transects: (a) M-transect NE-SW, stM13-M26, (b) G-transect N-S, and (c) A-transect N-S. Distances between stations in miles, spots indicate the depths of sampling. Data gridded with Surfer 7.0.

Likewise, divinil chlorophyll-*a* shows high values in correspondence of surface and picnocline waters of transect A (maximum value: 0.21 mg/m^3 at stA4 25 m, fig.f.25c). Nevertheless, its concentration is very low in surface waters along the G- and M-transects (figs.f.25a and b), while it increases with depth in the Atlantic stations, reaching the value of 0.15 mg/m^3 at stM25 50 m (fig.f.25a).

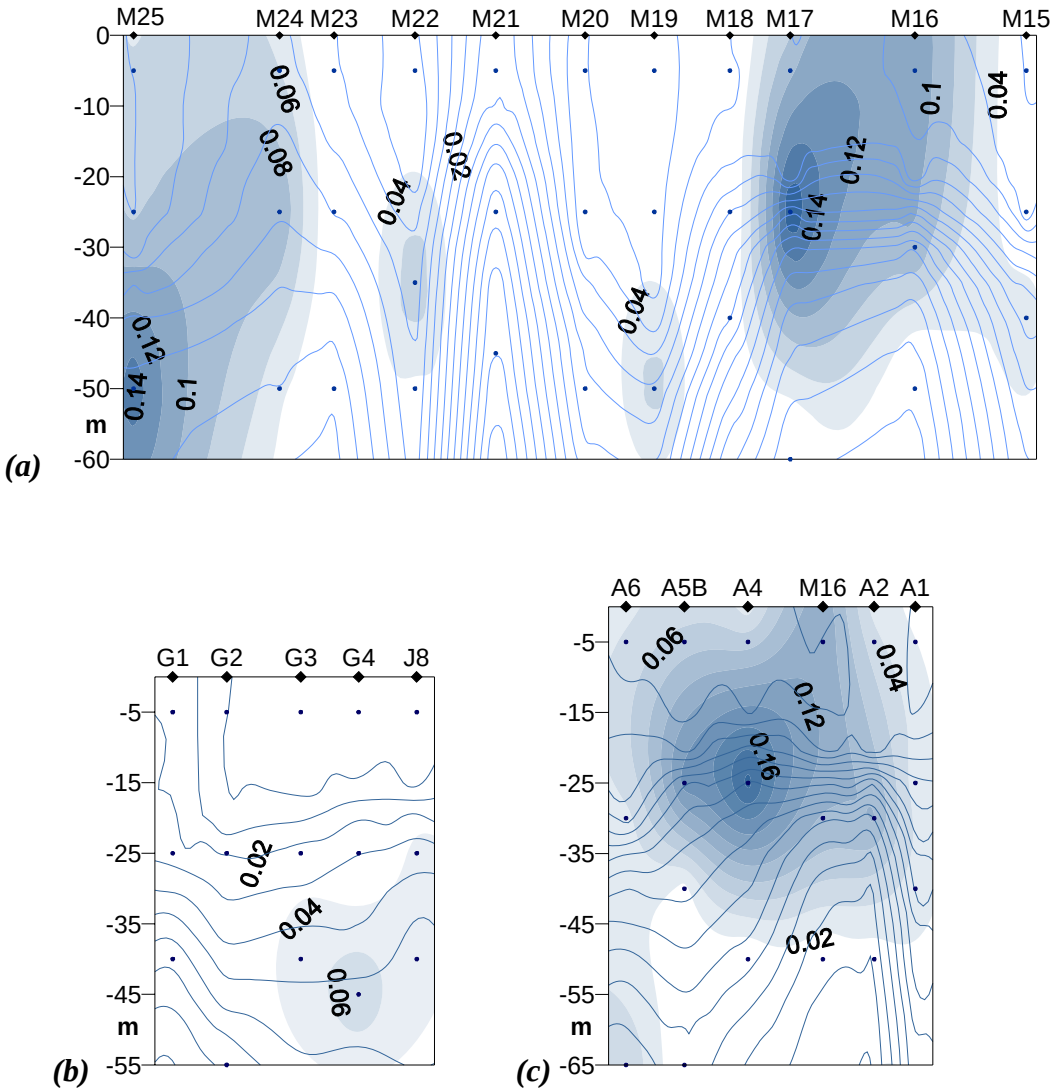

Fig.f.25: Divinil chlorophyll-a concentration (mg/m^3) from HPLC analysis, overlapped to density isolines (σ_τ, kg/m^3), from surface to 65 m deep, along the 3 transects: (a) M-transect NE-SW, stM13-M26, (b) G-transect N-S, and (c) A-transect N-S. Distances between stations in miles, spots indicate the depths of sampling. Data gridded with Surfer 7.0.

3.a.5 Photoprotective carotenoids

The map of the ratios between photoprotective carotenoids (zeaxanthin + violaxanthin + diatoxanthin + diadinoxanthin + lutein + alloxanthin) and total chlorophyll-*a* (PPC/Tchla, according to Barlow *et al.* 2007, fig.f.26) indicates higher values in the MAW along all the transects, reaching the maximum value of 0.67 in stG4 0 m (fig.f.26b). Moreover, the ratios decrease progressively with depth along the water column, indicating reduced photoprotection mechanisms at the picnocline and in the deep Mediterranean waters. On the contrary, surface samples from the mesoscale upwellings, both of stM16-M17 and of stM21, show minimum ratios (0.12 in stM16,

0.16 in stM16, and 0.10 in stM21, 0 m fig.f.26a), that means very low photoprotection even in higher irradiance conditions.

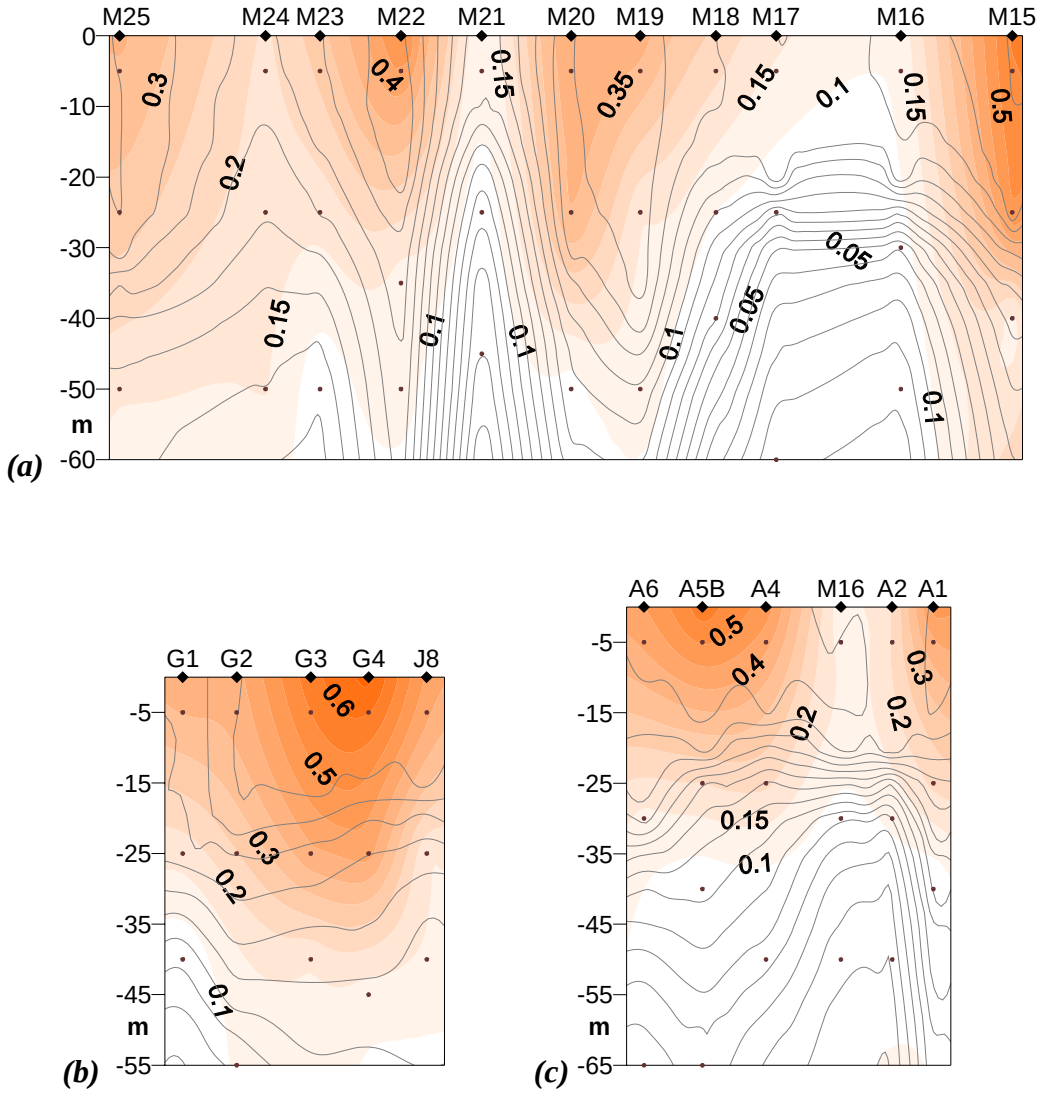

Fig.f.26: The ratio between photoprotective carotenoids (zeaxanthin + violaxanthin + diatoxanthin + diadinoxanthin + lutein + alloxanthin) and chlorophyll-*a* (PPC/chla) from HPLC analysis, overlapped to density isolines (σ_τ, kg/m^3), from surface to 65 m deep, along the 3 transects: (a) M-transect NE-SW, stM13-M26, (b) G-transect N-S, and (c) A-transect N-S. Distances between stations in miles, spots indicate the depths of sampling. Data gridded with Surfer 7.0.

PPC values is determined by the sum of the different photoprotective carotenoids, which can be not exclusive of a taxon: for example, zeaxanthin is both a diagnostic (for *Cyanophyta*) and a photoprotective (in *Raphidophyceae*) pigment. That means that high zeaxanthin concentrations may indicate abundant cianobacteria and/or many photoprotected (in our case) *F. japonica* as well. Moreover, fucoxanthin is a diagnostic pigment both for diatoms and for Raphidophyceans, though its concentrations on a chlorophyll-*a* basis is much higher in Raphidophyceans (Mostaert *et al.* 1998). Finally, the photoprotective xantophylls are diatoxanthin + diadinoxanthin in diatoms, while they are violaxanthin + antheraxanthin + zeaxanthin in *Raphidophyceae*. Since the most

abundant taxa were diatoms and *Raphidophyceans*, we attempted to characterize each sample with its corresponding values of the ratios zeaxanthin / fucoxanthin and violaxanthin / zeaxanthin. The aim of the correlation in fig.f.27 was to discriminate, between the samples dominated by these 2 taxa, the photoprotective / diagnostic contributes of the pigments. First of all, high values of the zea/fuco ratio (1 < zea/fuco < 10) indicate high contributes of cianobacteria to the total cells abundance (fig.f.27, in blue), that is the case of samples coming from surface Atlantic waters: all surface samples of the G-transect and 25-m deep samples from stG2-G3-G4, surface and subsurface samples of stations stM13-M14-M15-M19-M20, finally surface samples from stM18-M22-M23 and stA1-A4-A5B-A6.

On the contrary, high values of the ratio viola/zea (viola/zea > 0.45) indicate low percentage of photoprotected *F. japonica* and/or high contributes of diatoms to the assemblage (fig.f.27, in red). This is the case of samples coming from deep waters: generally beneath the depth of 40 m from the upwelling systems (stA5B 40 m, stM16 50 m, stM22 50 m, stA1 40 m, stM18 40 m, stA2 30 m, stM15 40 m, stG1 40 m), but also more surface samples containing deep-like water, like stM17 0 and 25 m and stM21 0 m.

Finally, the samples in-between, which show both zea/fuco < 1 and viola/zea < 0.45 (fig.f.27, in yellow), indicate more photoprotected *F. japonica* and/or a small contribute of diatoms to the cell abundances: this is the case of surface samples, like stM16 0 m, stA2 0m, stM17 0 m, and of 25/30-m deep samples from stations adiacent to the mesoscale structures: stM23-M18, stA1-A4-A5B-A6.

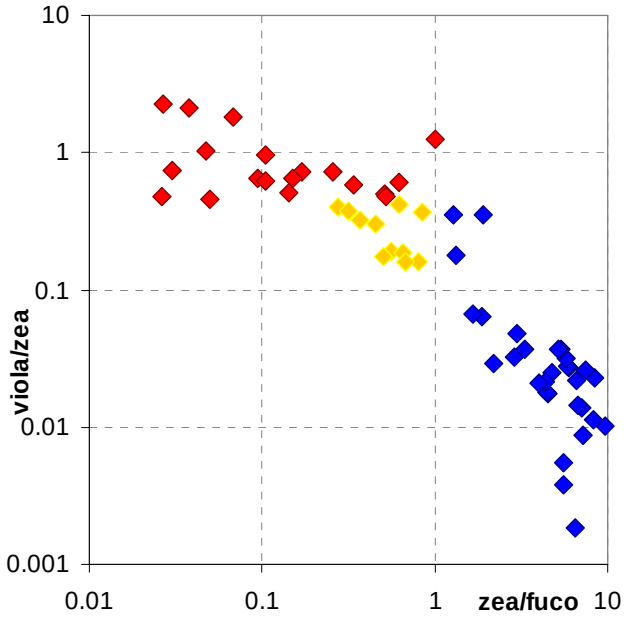

Fig.f.27: The ratio zeaxanthin/fucoxanthin (zea/fuco) *vs* the ratio violaxanthin/zeaxanthin (viola/zea) for all the samples between 0 and 65 m deep, along the 3 transects: the M-transect NE-SW (stM13-M26), the G-transect N-S, and the A-transect N-S. In blue, zea/fuco>1; in red, viola/zea>0.45; in yellow, zea/fuco<1 and viola/zea<0.45.

3.a.6 Statistical analysis

Fig.f.28 shows the τ coefficient calculated for couples of adjacent samples, i.e. belonging to adjacent depths in the same station. Along the M-transect, all the stations selected show higher values of τ when comparing samples which are both on the same side of the picnocline: both above or both beneath it. This is the case of the two deep samples (25 and 40 m) for stM18 (τ = 0.68), whose picnocline is 15-m deep (see fig.f.2), and of the surface and the 25/30-m deep samples (above or in correspondence of the picnocline) for all the other stations (fig.f.28a).

This is the same along the G-transect, where the 0 and 25-m deep population (above or right below the picnocline) are more similar than the deep one (40/55 m), except for the coastal station stJ8, whose 25-m sample is more similar to the 40-m deep than to the surface one (fig.f.28b).

Likewise, along the A-transect the coastal stations stA1 and stA6 have high τ values (0.60 and 0.63, respectively) above the picnocline (0-25 m and 0-30 m, fig.f.28c), while the index is low when comparing the 25/30-m samples with the deeper ones, indicating a smaller similarity between above and below the picnocline samples. Likely, in stA5B a high index between the 25-m deep and 40-m deep samples (0.62) indicates a higher similarity between the 2 samples beneath the picnocline than between the 0-m (above) and the 25-m (beneath) samples. The stA4 show very low τ values (<0.26) along the water column, indicating a high diversity between the assemblages 0-25 m and 25-40 m.

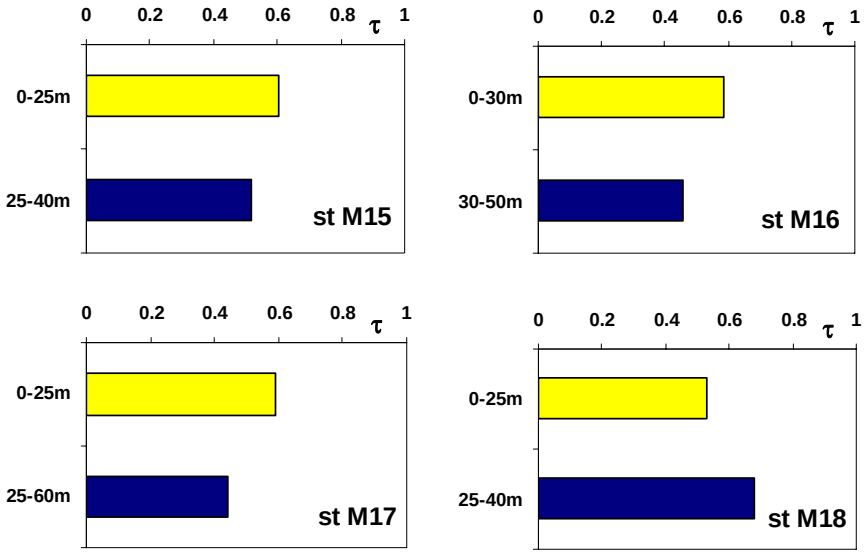

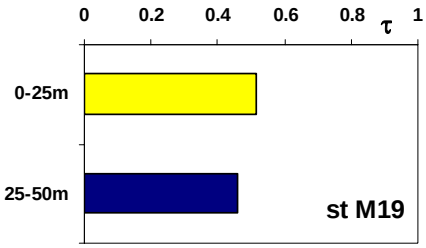
0
0.2
0.4
0.6
0.8
τ
1
0-25m
25-50m
st M19

(a)

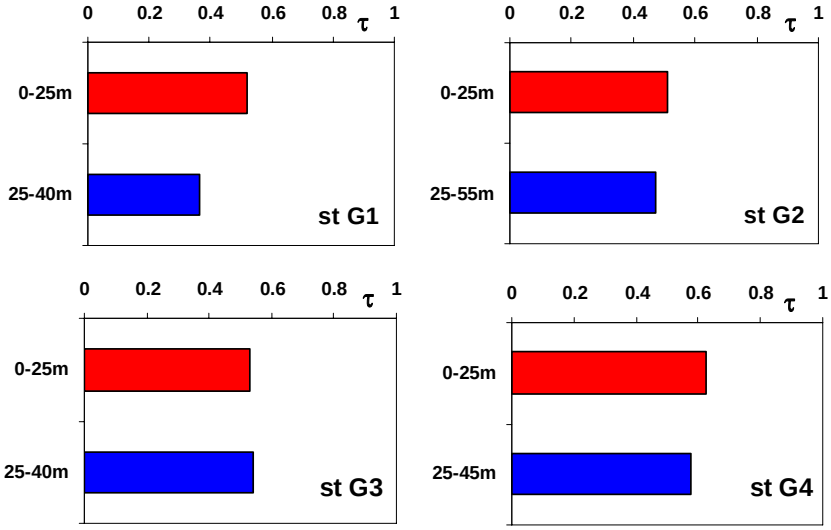
0-25m
25-40m
st G1
0-25m
25-55m
st G2
0-25m
25-40m
st G3
0-25m
25-45m
st G4

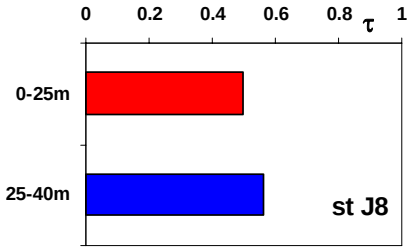
0-25m
25-40m
st J8

(b)

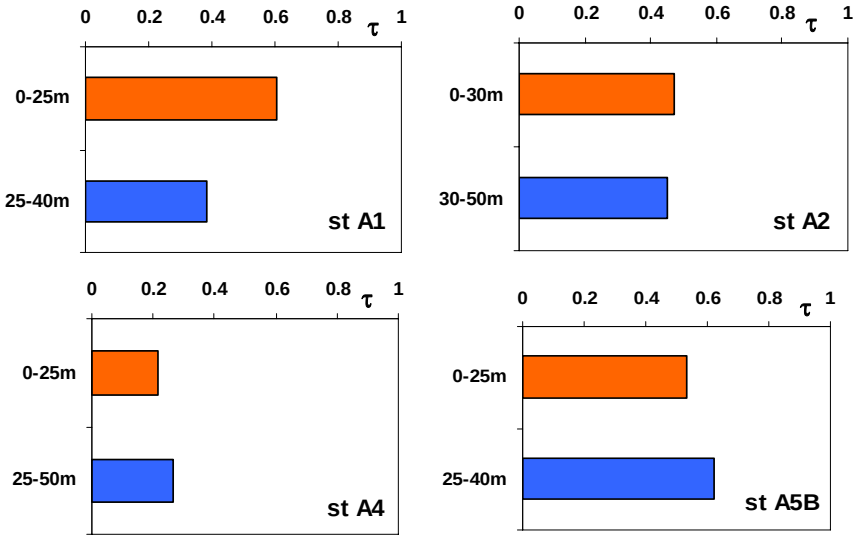
0-25m
25-40m
st A1
0-30m
30-50m
st A2
0-25m
25-50m
st A4
0-25m
25-40m
st A5B

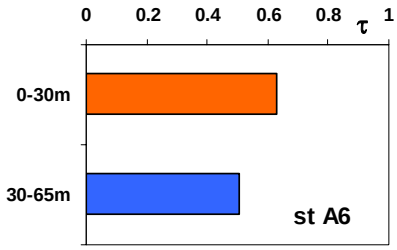

(c)

Fig.f.28: similarity of assemblages by the Kendall's coefficient of rank correlation τ, calculated for couples of adjacent samples, belonging to adjacent depths in the same station, on a selection of 140 taxa from cell counting data of selected samples: in (a) stM15-M16-M17-M18 and M19 from the M-transect, in (b) the G-transect, and in (c) the A-transect.

Moreover, fig.f.29 shows the τ coefficient calculated for couples of adjacent samples, belonging to the same depths of adjacent stations. The stations M selected show generally the lowest τ in correspondence of 25-30 m of depth and the highest when comparing adjacent deep samples, in particular the two stations belonging to the mesoscale upwelling stM16-M17 (τ = 0.54) and the station stM17 with the edge station stM18 (τ = 0.59, fig.f.29a).

Along the G-transect, higher τ values can be found when comparing adjacent surface samples, except for the stations stG1 and G2, where deep samples are more similar (τ = 0.48), and for stG4 and J8, which show τ = 0.53 at 25 m of depth (fig.f.29b).

Finally, along the A-transect τ is minimum when comparing the 25/30-m deep adjacent samples, that means comparing samples coming from right beneath the picnocline, except for stM16 and A2, whose τ = 0.50 is constant along the water column, indicating 3 similarly similar samples at the three depths (fig.f.29c).

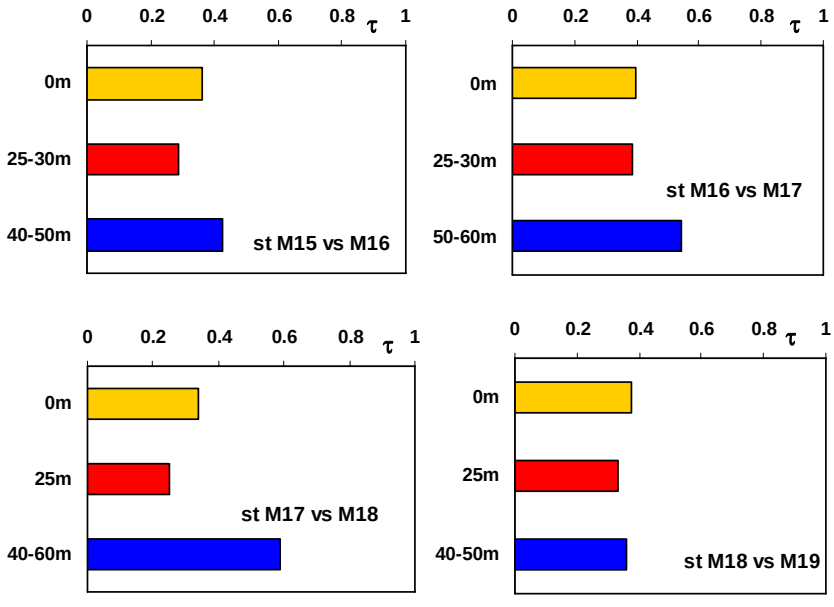

(a)

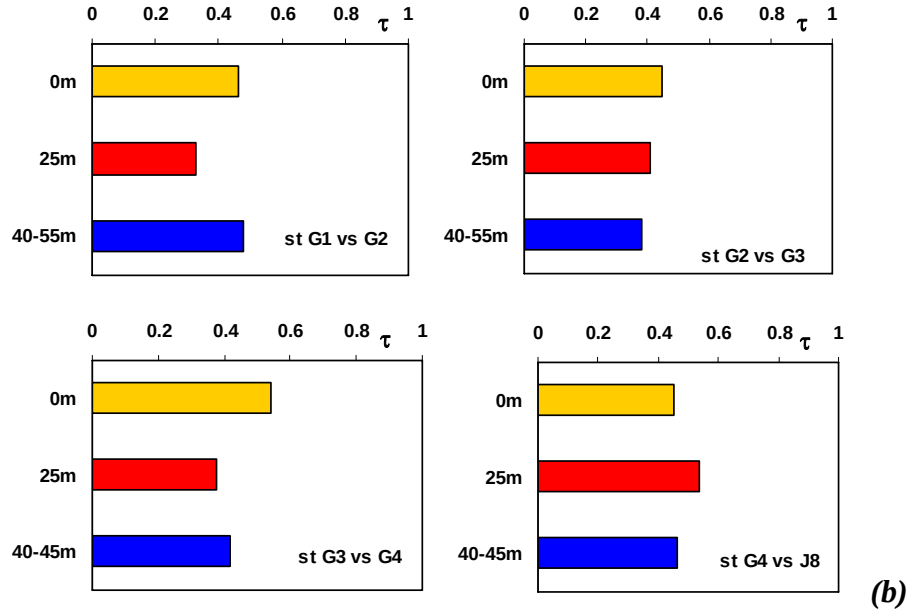

(b)

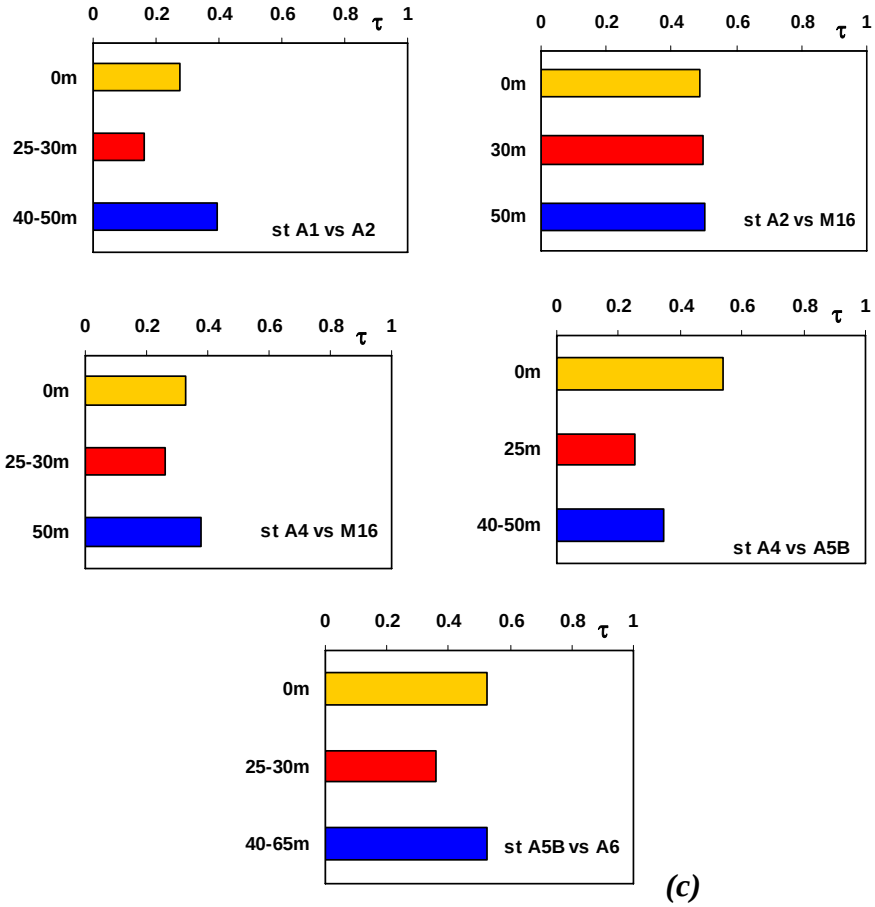

(c)

Fig.f.29: similarity of assemblages by the Kendall's coefficient of rank correlation τ, calculated for couples of adjacent samples, belonging to the same depths of adjacent stations, on a selection of 140 taxa from cell counting data of selected samples (A-transect, G-transect and stM15-M16-M17-M18 and M19 from the M-transect).

Finally, the Principal Component Analysis (PCA) was used to describe the total variability, i.e. the variance of both hydrological (temperature, salinity, density, nutrients) and biological factors (chlorophyll-*a* and total cells) data along the three transects. Results presented here were standardized by the stand3 standardization, but stand1 and stand2 standardizations gave similar results.

Tab.1 shows the linear correlation coefficients (r) between the 8 variables analyzed: temperature (T°C) has negative coefficients when correlated with any other variable, while density correlates well with salinity (r=0.648), nitrogen (NO_2+NO_3, r=0.733) and silicate (Si, r=0.809, tab.1). Moreover, nitrogen correlate well both with phosphate (PO_4, r=0.689) and silicate (r=0.654), and with density (r=0.733). Finally, cells number (cells/l) correlates well only with chlorophyll-*a* concentration (chla, r=0.682).

	T°C	salinity	density	NO_2+NO_3	PO_4	Si	chla	cells/l
T°C	1.000	-0.331	-0.933	-0.673	-0.433	-0.739	-0.312	-0.366
salinity	-0.331	1.000	0.648	0.501	0.266	0.561	0.148	0.067
density	-0.933	0.648	1.000	0.733	0.448	0.809	0.305	0.319
NO_2+NO_3	-0.673	0.501	0.733	1.000	0.689	0.654	0.033	0.235
PO_4	-0.433	0.266	0.448	0.689	1.000	0.554	0.201	0.195
Si	-0.739	0.561	0.809	0.654	0.554	1.000	0.453	0.322
chla	-0.312	0.148	0.305	0.033	0.201	0.453	1.000	0.682
cells/l	-0.366	0.067	0.319	0.235	0.195	0.322	0.682	1.000

Tab.1: linear correlation coefficients, calculated on the 8 variables examined: temperature (T°C), salinity, density, nutrients(nitrogen, NO_2+NO_3; phosphate, PO_4; silicate, Si), chlorophyll-*a* concentration (chla) and total cells number (cells/l), by the Statistica 6.0 software (StatSoft). The coefficients were calculated on data from samples from surface to 65 m deep, along the 3 transects: (a) M-transect NE-SW, stM13-M26, (b) G-transect N-S, and (c) A-transect N-S.

In tab.2 the eigenvalues of the correlation matrix are shown: the first principal component (PC1) has an eigenvalue = 4.35 and it's responsible of the 54.33% of total variance, while the second one (PC2) has an eigenvalue of 1.48 and it explains the 18.46% of total variance.

Value number	Eigenvalue	% Total variance	Cumulative eigenvalue	Cumulative %
1	4.346264	54.32829	4.346264	54.3283
2	1.476811	18.46014	5.823075	72.7884
3	0.820094	10.25117	6.643168	83.0396
4	0.632713	7.90891	7.275882	90.9485
5	0.430337	5.37921	7.706219	96.3277
6	0.176062	2.20077	7.882280	98.5285
7	0.117368	1.46710	7.999648	99.9956
8	0.000352	0.00440	8.000000	100.0000

Tab.2: Eigenvalues of the correlation matrix, the percentage of variance explained by each of the eigenvalues, the cumulative eigenvalues and the cumulative percentage, calculated on the 8 variables examined: by the Statistica 6.0 software (StatSoft). The eigenvalues were calculated on data from samples from surface to 65 m deep, along the 3 transects: (a) M-transect NE-SW, stM13-M26, (b) G-transect N-S, and (c) A-transect N-S.

The projection of the variables on the factor-plane indicates that temperature is positively correlated by PC1, while it is not linked to PC2. Likewise, silicate is negatively correlated with PC1, while it's completely independent from PC2. Nitrogen, phosphate, salinity and density are negatively correlated with PC1 too, but also slightly with PC2. On the contrary, chlorophyll-*a* and cells number correlate markedly positively with PC2 and are negatively correlated with PC1 (fig.f.31).

The PC1 is related to the hydrodynamics of the water column, in fact temperature varies inversely with nutrients and density/salinity along the water column.

The PC2 is related to phytoplanktonic biological activities, in particular to rapid nutrient (nitrogen and phosphate) assimilation by actively growing cells, in fact high concentration of chlorophyll-*a* (i.e. large numbers of cells) can cause a lowering of nutrients in surface waters, while deep, dense, salty and nutrient rich waters are poor in biomass.

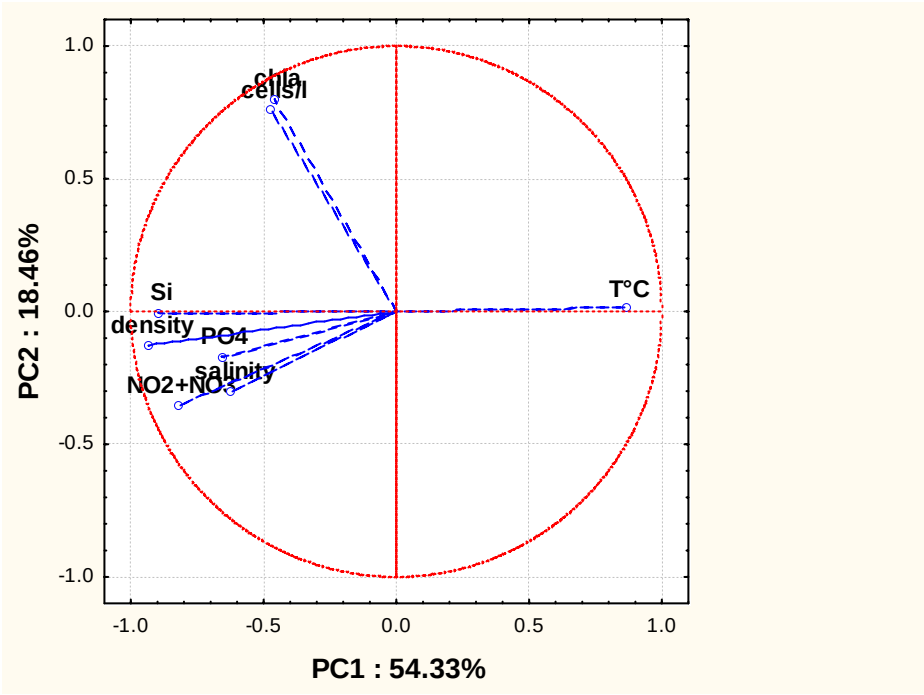

Fig.f.31: projection of the 8 variables on the factor plane, where the x-axis is PC1 and the y-axis is PC2, calculated by the Statistica 6.0 software (StatSoft).

This is confirmed also by the projection of the cases (=samples) on the factor-plane (fig.f.32): deep samples (45 to 60 m deep), which have low cells abundances, can be found on the left side of the x-axis (i.e. they are negatively correlated with both PC1 and PC2), while cells-rich samples are found upwards along the y-axis, with the richest (stM17-25m) on top. Along the x-axis, 0-m deep samples from the surface Atlantic waters are on the right side, while samples from the less stable part of the water column

(around the picnocline) are near the origin of the factor plane, finally samples from the DMW are on the left side of the x-axis (fig.f.32).

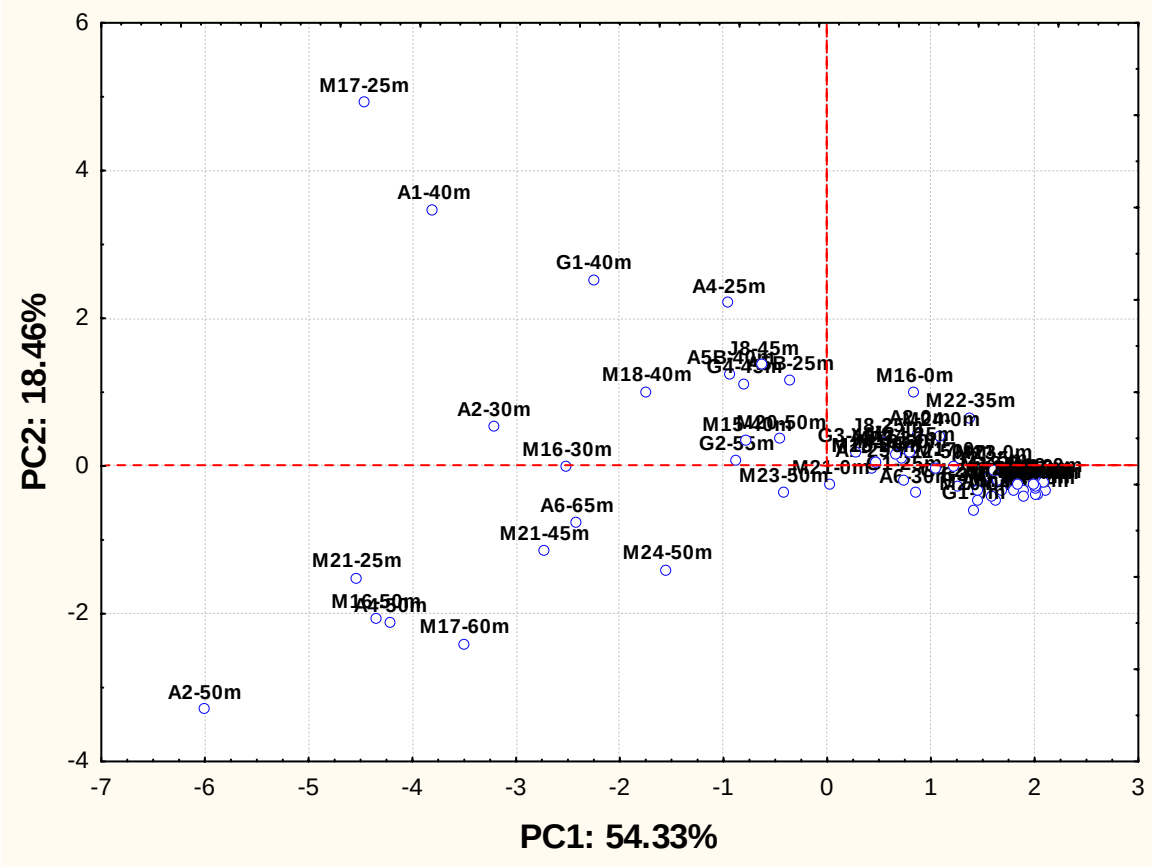

Fig.f.32: projection of the 63 cases on the factor plane, where the x-axis is PC1 and the y-axis is PC2, calculated by the Statistica 6.0 software (StatSoft).

PCA has been conducted also on a selected group of 24 samples which resulted rich in *F. japonica* (the A-transect + stM16-M17-M18), on the usual 8 hydrological (temperature, salinity, density, nutrients) and biological variables (chlorophyll-*a* and total cells) + *F. japonica* abundance (in cells/l). In tab. 3, the linear correlation coefficients between the 9 variables analyzed: again, temperature (T°C) has negative coefficients when correlated with any other variable, while density correlates well with salinity (r=0.676), nitrogen (NO_2+NO_3, r=0.614) and silicate (Si, r=0.524). Moreover, nitrogen correlate well both with phosphate (PO_4, r=0.663) and silicate (r=0.708), and with density (r=0.801). Finally, chlorophyll-*a* concentration (chla) correlates well with cells number (cells/l, r=0.684) and with *F. japonica* (r=0.765).

	T°C	salinity	density	NO_2+NO_3	PO_4	Si	chla	*F. japonica*	cells/l
T°C	1.000	-0.379	-0.938	-0.715	-0.395	-0.702	-0.177	-0.080	-0.224
salinity	-0.379	1.000	0.676	0.614	0.255	0.524	-0.022	0.249	-0.179
density	-0.938	0.676	1.000	0.801	0.412	0.754	0.128	0.152	0.109
NO_2+NO_3	-0.715	0.614	0.801	1.000	0.663	0.708	-0.163	-0.199	-0.053
PO_4	-0.395	0.255	0.412	0.663	1.000	0.470	-0.080	-0.107	0.099
Si	-0.702	0.524	0.754	0.708	0.470	1.000	0.524	0.285	0.272
chla	-0.177	-0.022	0.128	-0.163	-0.080	0.524	1.000	0.765	0.684
F. japonica	-0.080	0.249	0.152	-0.199	-0.107	0.285	0.765	1.000	0.500
cells/l	-0.224	-0.179	0.109	-0.053	0.099	0.272	0.684	0.500	1.000

Tab.3: linear correlation coefficients, calculated on the 9 variables examined: temperature (T°C), salinity, density, nutrients(nitrogen, NO_2+NO_3; phosphate, PO_4; silicate, Si), chlorophyll-*a* concentration (chla), total cells number and *F. japonica* abundance (cells/l), by the Statistica 6.0 software (StatSoft). The coefficients were calculated on data from samples from surface to 65 m deep, along the A-transect and the stations stM16-M17-M18.

Tab.4 shows the eigenvalues of the correlation matrix: the first principal component (PC1) has an eigenvalue = 4.16 and it's responsible of the 46.18% of total variance, while the second one (PC2) has an eigenvalue of 2.44 and it explains the 27.16% of total variance.

Value number	Eigenvalue	% Total variance	Cumulative eigenvalue	Cumulative %
1	4.156745	46.18606	4.156745	46.1861
2	2.444927	27.16585	6.601672	73.3519
3	1.005382	11.17091	7.607054	84.5228
4	0.656699	7.29666	8.263753	91.8195
5	0.386683	4.29648	8.650436	96.1160
6	0.264503	2.93892	8.914939	99.0549
7	0.073697	0.81886	8.988636	99.8737
8	0.011296	0.12551	8.999932	99.9992
9	0.000068	0.00075	9.000000	100.0000

Tab.4: Eigenvalues of the correlation matrix, the percentage of variance explained by each of the eigenvalues, the cumulative eigenvalues and the cumulative percentage, calculated on the 9 variables examined: temperature (T°C), salinity, density, nutrients(nitrogen, NO_2+NO_3; phosphate, PO_4; silicate, Si), chlorophyll-*a* concentration (chla), total cells number and *F. japonica* abundance (cells/l), by the Statistica 6.0 software (StatSoft). The eigenvalues were calculated on data from samples from surface to 65 m deep, along the A-transect and the stations stM16-M17-M18.

The projection of the variables on the factor-plane (fig.f.33) indicates again that temperature is positively correlated by PC1, while it is not linked to PC2. Silicate is markedly negatively correlated with PC1, while it's slightly negatively correlated with PC2. Nitrogen, phosphate, salinity and density are negatively correlated with PC1 as well, but also positively with PC2. On the contrary, chlorophyll-*a* and cells number negatively correlate with both PC1 and PC2.

Once more, the PC1 is related to the hydrodynamics of the water column, in fact temperature varies inversely with nutrients and density/salinity along the water column.

The PC2 is related to biological activities, in particular to nitrogen and phosphate release likely by slowly growing cells recycling metabolism and/or by bacterial re-mineralization following a bloom, in fact high concentration of chlorophyll-*a* (i.e. high abundances of cells, in particular *F. japonica* cells) are found in nutrient-depleted surface water, while deep dense salty waters are rich in nutrients and poor in cells.

As previously noticed, *F. japonica* cells appeared often aggregated in mucous nets: mucous production is often related to stress conditions (Decho 1990, de Boer *et al.* 2005), for example to N-limitation (see also our laboratory results section). Moreover though *F. japonica* was the dominant species in the selected samples, we did not count cell abundances as high as those of a typical bloom event (maximum $6x10^4$ cell/l against bloom values as high as 10^7 cell/l, Liu *et al.* 2008), so we can assume that the assemblages were in a post-bloom phase.

It's worthy of notice that, on the contrary, silicate concentration is negatively related to the PC2, in fact surface waters are not Si-depleted and *F. japonica* likely doesn't assimilate it.

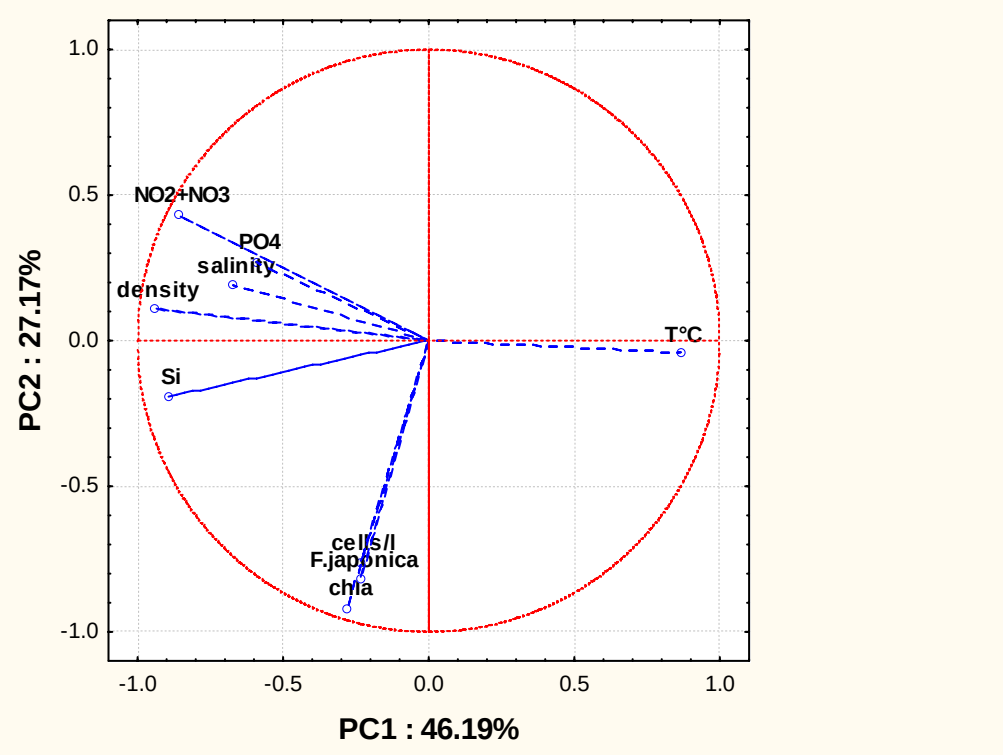

Fig.f.33: projection of the 9 variables on the factor plane, where the x-axis is PC1 and the y-axis is PC2, calculated by the Statistica 6.0 software (StatSoft).

This is confirmed by the projection of the cases on the factor-plane (fig.f.34): low-cells abundances samples, from deep waters (45-60 m), can be found now on top of the

y-axis (i.e. they are negatively correlated with PC1 and positively with PC2), while cells-rich samples are found downwards along the y-axis, with the richest (stM17-25m) on the bottom. Along the x-axis, samples from the surface Atlantic waters are on the right side, while samples from the picnocline (25-30 m) are near the origin of the factor plane, finally on the left side of the x-axis samples from the DMW.

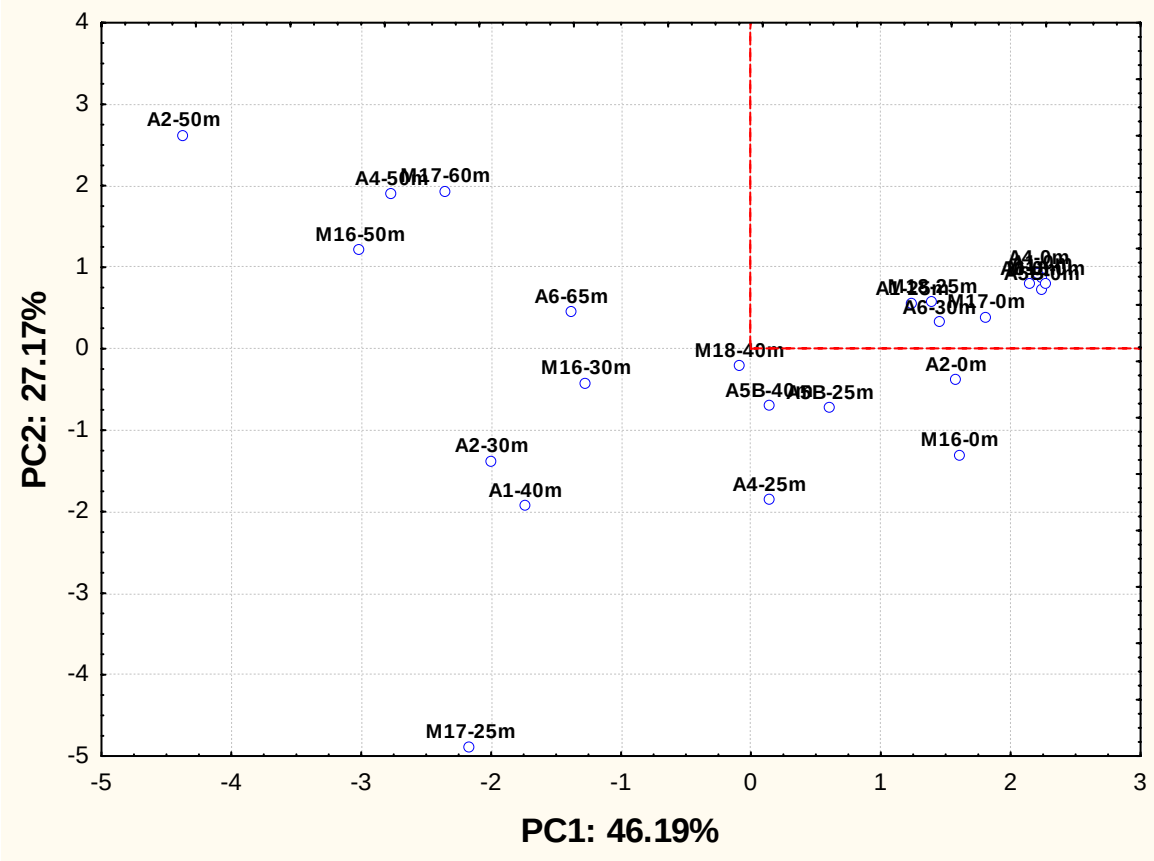

Fig.f.34: projection of the 24 cases on the factor plane, where the x-axis is PC1 and the y-axis is PC2, calculated by the Statistica 6.0 software (StatSoft).

3.b Laboratory experiment

3.b.1 Experiment 1: sinusoidal light (26-hours measurements)

Photosynthetic parameters by oxygen measurements: both α^b and P^bmax show diel variations. α^b has its maximum after dawn and its minimum before midnight (3-fold lower): it varies slightly from 10.30h to 14.30h (from after-dawn to midday), it lowers from 15.30h to 0.30h, then it increases during the night until after-dawn, from 1.30h to 9.30h (fig.L.1.1a). P^bmax decreases markedly from 10.30h as far as its minimum before sunset (4- fold lower), then it increases, first slowly (until 23.30h) then sharply back to its maximum after dawn (8.30-9.30h, fig.L.1.1b).

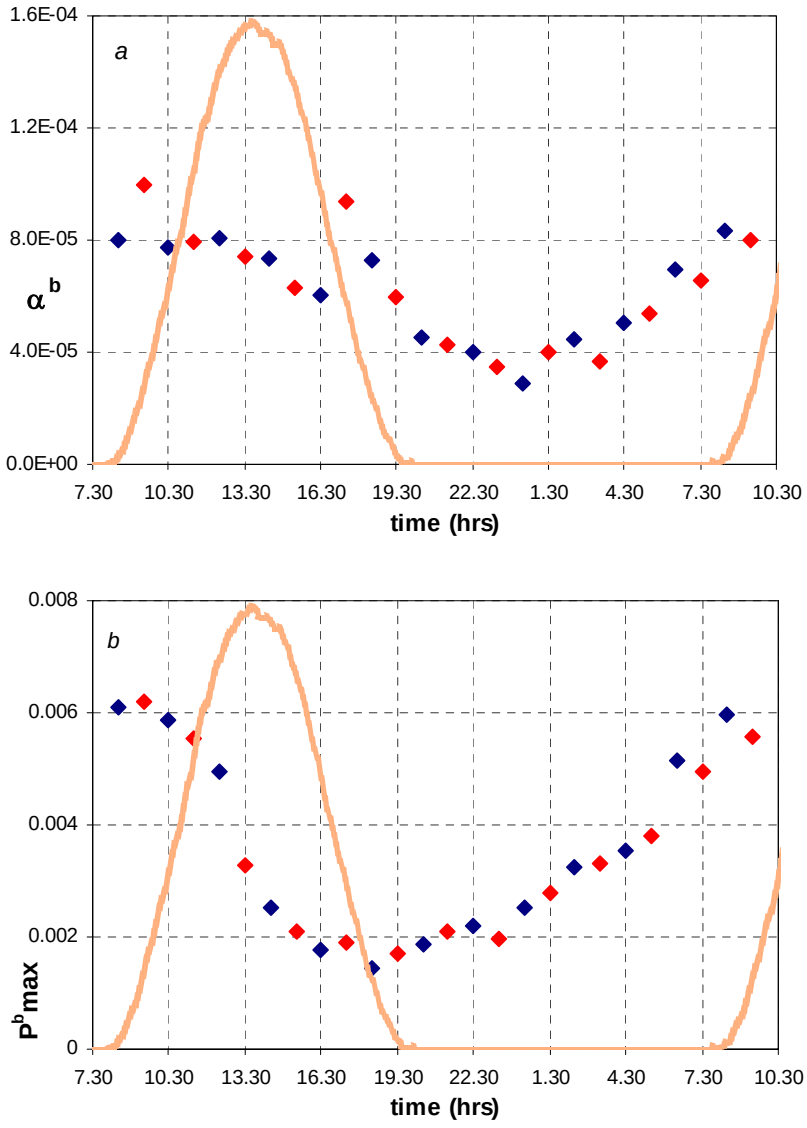

Fig.L.1.1: (a) the light-limited slope α normalized by chlorophyll-*a* (α^b, µmol O_2 (ml min)$^{-1}$ (µmol quanta m^{-2} s^{-1} µg chla l^{-1}) $^{-1}$, and (b) the light-saturated rates of photosynthesis normalized by chlorophyll-*a* (P^bmax, µmolO_2 µg chla^{-1} s^{-1}), by net oxygen evolved measurements, in chemostats C1 (red) and C2 (blue), with time, in sinusoidal light (orange, from 0 to 220 µE m^{-2} s^{-1}).

Fig.L.1.2 compares α^b and $P^b max$ variations: they strictly covary from 0.30h to 9.30h (R^2=0.94, n=12, fig.L.1.3a). The two parameters do not covary during the light period: around midday (10.30h-16.30h) $P^b max$ decreases while α^b shows only slight oscillations (fig.L.1.3b), so Ek is decreasing (fig.L.1.3d). From before-sunset to the first half of the dark period (17.30h-23.30h) $P^b max$ remains stable while α^b varies (fig.L.1.3c), so Ek is increasing (fig.L.1.3d). So the PE parameters show a 3-phases pattern of variability: one phase of Ek-independence during the night until after-dawn (Ek constant, fig.L.1.3d), followed by two phases of Ek-dependence (meaning photoacclimation).

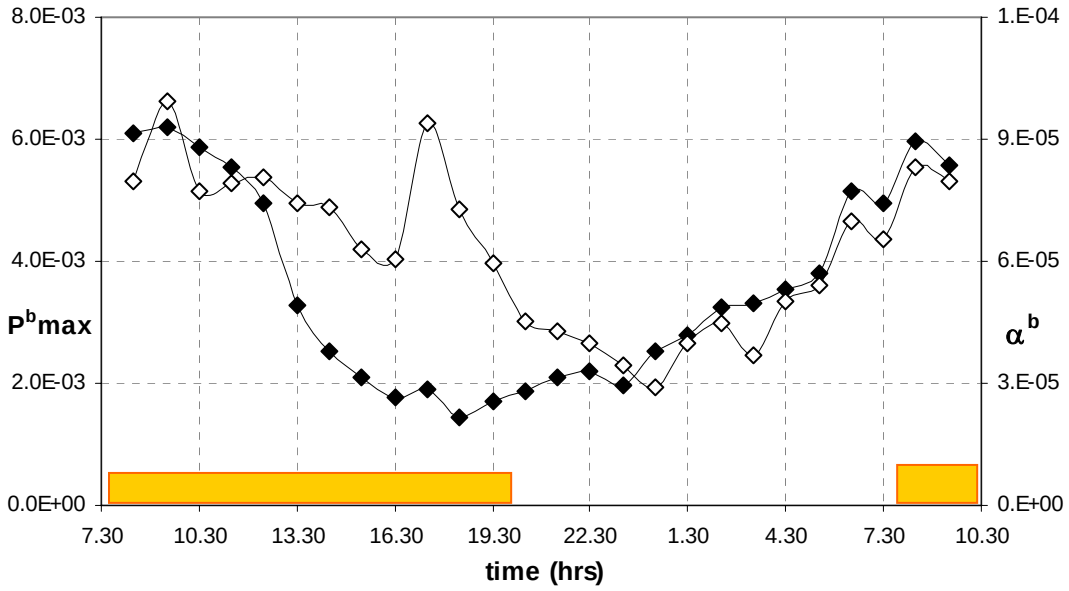

Fig.L.1.2: comparison of α^b (empty symbols, in µmol O_2 (ml min)$^{-1}$ (µmol quanta m^{-2} s^{-1} µg chla l^{-1}) $^{-1}$) and $P^b max$ (closed symbols, in µmolO_2 µg chla^{-1} s^{-1}) variations in both chemostats, with time, during the 26-hours measurements in sinusoidal light. The yellow bars indicate the light periods.

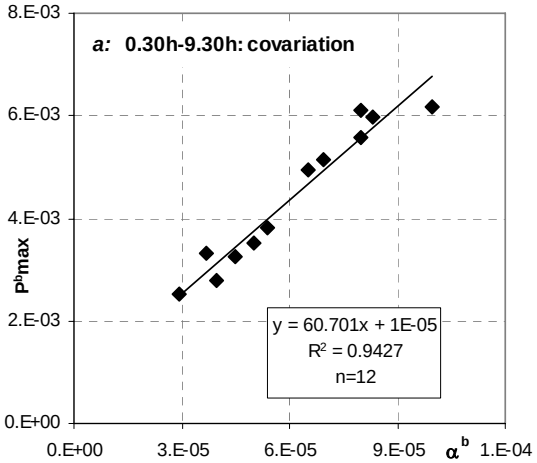

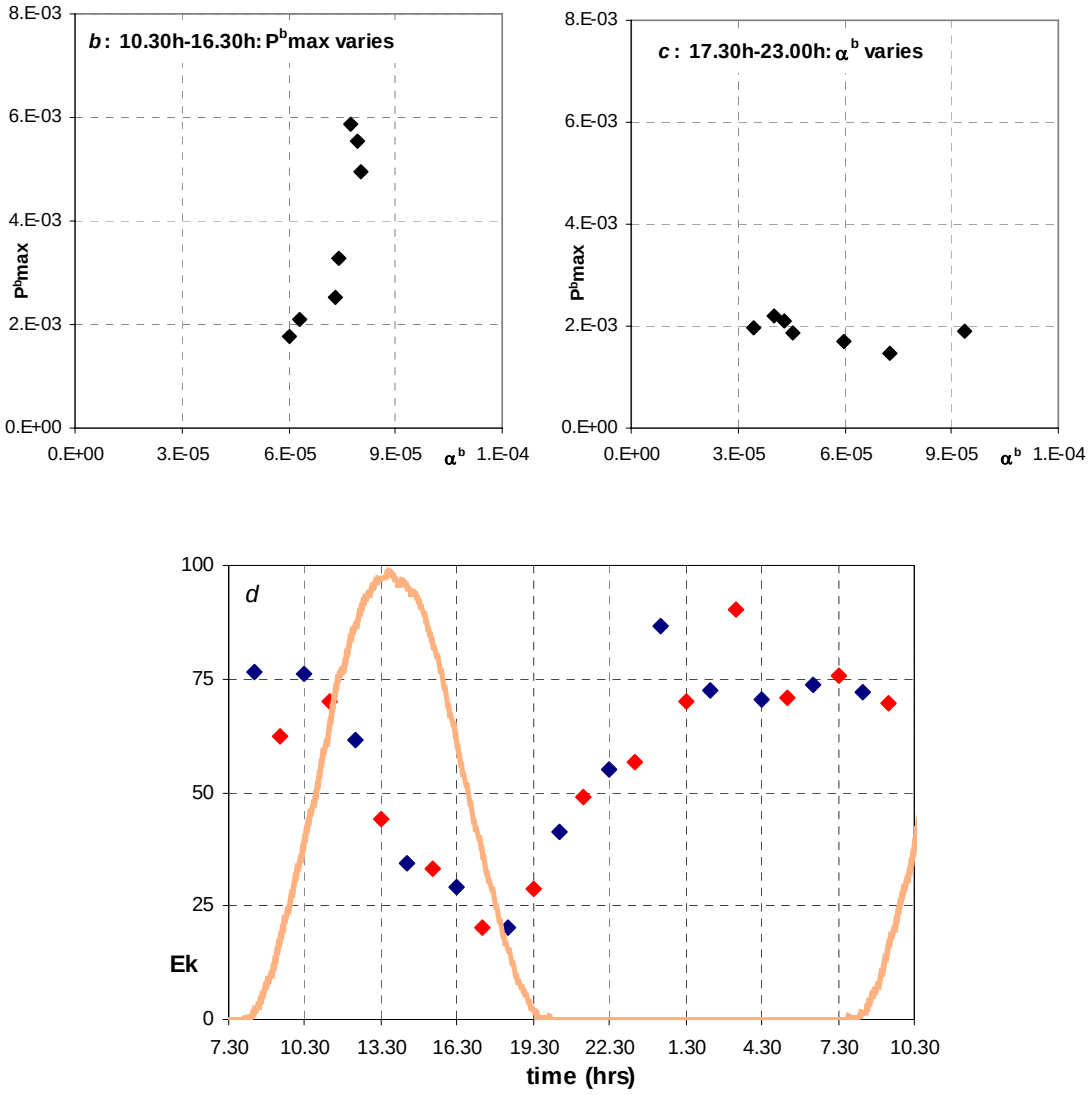

Fig.L.1.3: three-phases variation of α^b and P^bmax in both chemostats during 26-hours measurements in sinusoidal light: (a) covariation from 0.30h to 9.30h, (b) around midday (10.30h-16.30h) P^bmax varies more than α^b, (c) from 17.30h to 23.30h α^b varies more than P^bmax; (d) the light-saturation index Ek=P^bmax/α^b (in µE $m^{-2}s^{-1}$), by net oxygen evolved measurements, in chemostats C1 (red) and C2 (blue), with time, in sinusoidal light (orange, from 0 to 220 µE m^{-2} s^{-1}).

β^b shows diel changes too (fig.L.1.4a): β^b varies following P^bmax pattern (fig.L.1.4b), with a maximum around dawn, a decrease as far as midday, followed by small oscillations until 5.30h. Fig.L.1.4c shows the positive correlation (R^2=0.73, n=26) between P^bmax and β^b, that means higher photosynthetic rates with higher photoinibition after dawn.

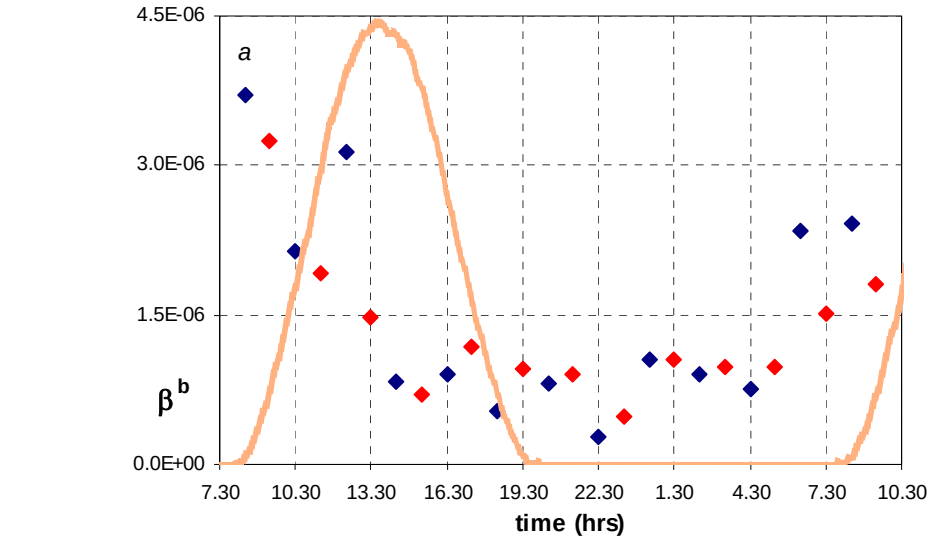

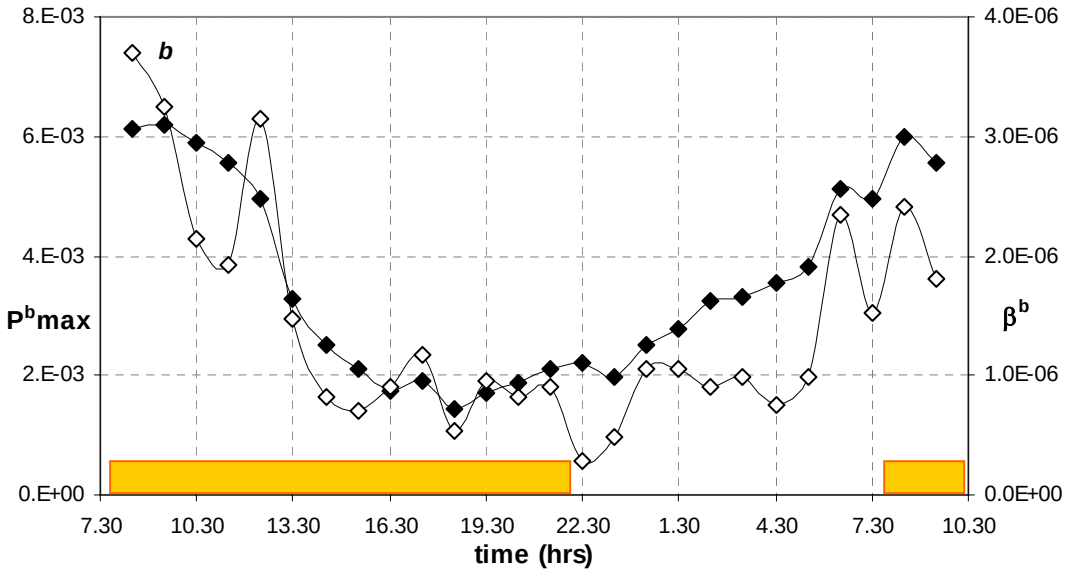

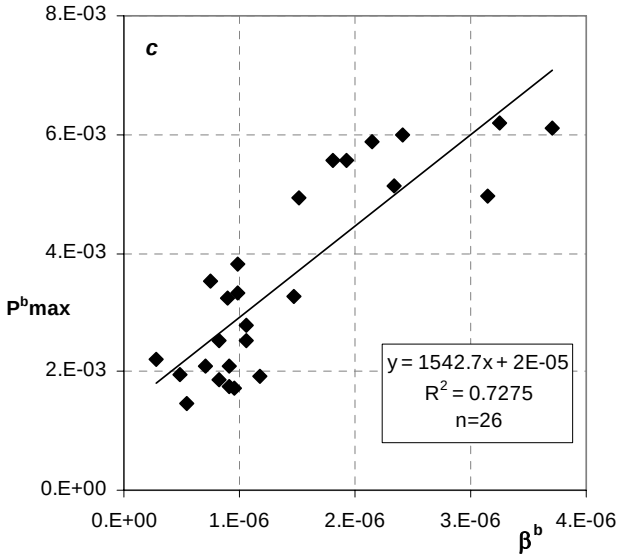

Fig.L.1.4: (a) the photo-inhibited slope β normalized by chlorophyll-*a* (β^b, µmol O_2 (ml min)$^{-1}$ (µmol quanta m^{-2} s^{-1} µg chla l^{-1}) $^{-1}$), by net oxygen evolved measurements, in chemostats C1 (red) and C2 (blue), with time, in sinusoidal light (orange, from 0 to 220 µE m^{-2} s^{-1}), (b) comparison of β^b (open symbols, in m^2 µg chla^{-1}) and P^bmax (closed symbols, in µmolO_2 µg chla^{-1} s^{-1}) variations in both chemostats, with time during 26-hours measurements in sinusoidal light, and (c) covariation between P^bmax and β^b in both chemostats in sinusoidal light. The yellow bars indicate the light periods.

Cell cycle: the number of cells is maximum at mid-morning (11.00-11.30h) and decreases during the day as far as the midnight minimum (1.5-fold lower, fig.L.1.5a). Cell volume is minimum at 9.00h, while it's maximum before sunset (1.5-fold higher, 17.30-18.00h, fig.L.1.5b). That means that all cell divisions are completed at dawn, while cells grow during the day and are ready to divide again at sunset. Moreover, around midnight (from 21.00h to 3.00h) cell volume is almost constant and the pattern of cells number shows a slighter slope (figs.L.1.5a and b).

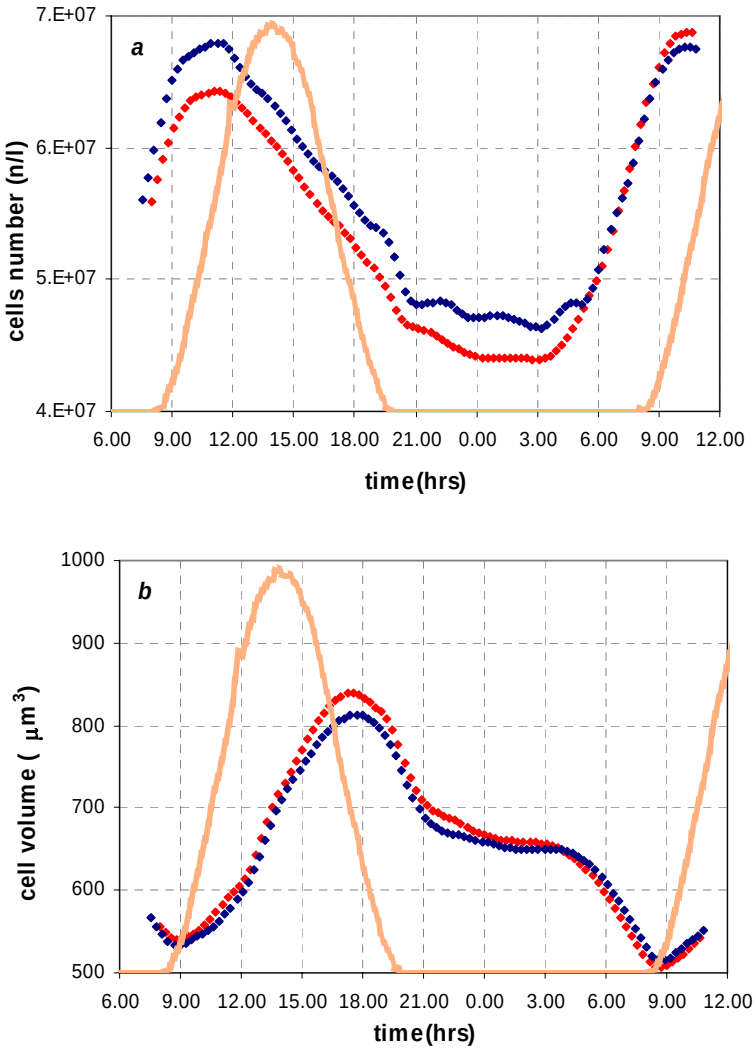

Fig.L.1.5: (a) cell number (n/l) and (b) cell volume (μm^3), in chemostats C1 (red) and C2 (blue), with time, in sinusoidal light (orange, from 0 to 220 $\mu E\ m^{-2}\ s^{-1}$).

Organic carbon and nitrogen: like cell size, also the ratio C/N has its minimum soon after dawn (9.30h, fig.L.1.6a) and it increases during the day to the sunset maximum (1.5-fold higher, 19.30h). C has its minimum at 9.30h too (fig.L.1.6b) and its maximum 2 hours earlier than C/N, after midday (1.2-fold higher, 17.30h), while N is minimum

from midnight to before-dawn (~2.00-7.00h) and has its maximum after midday (1.3-fold higher, 15.30h, fig.L.1.6c).

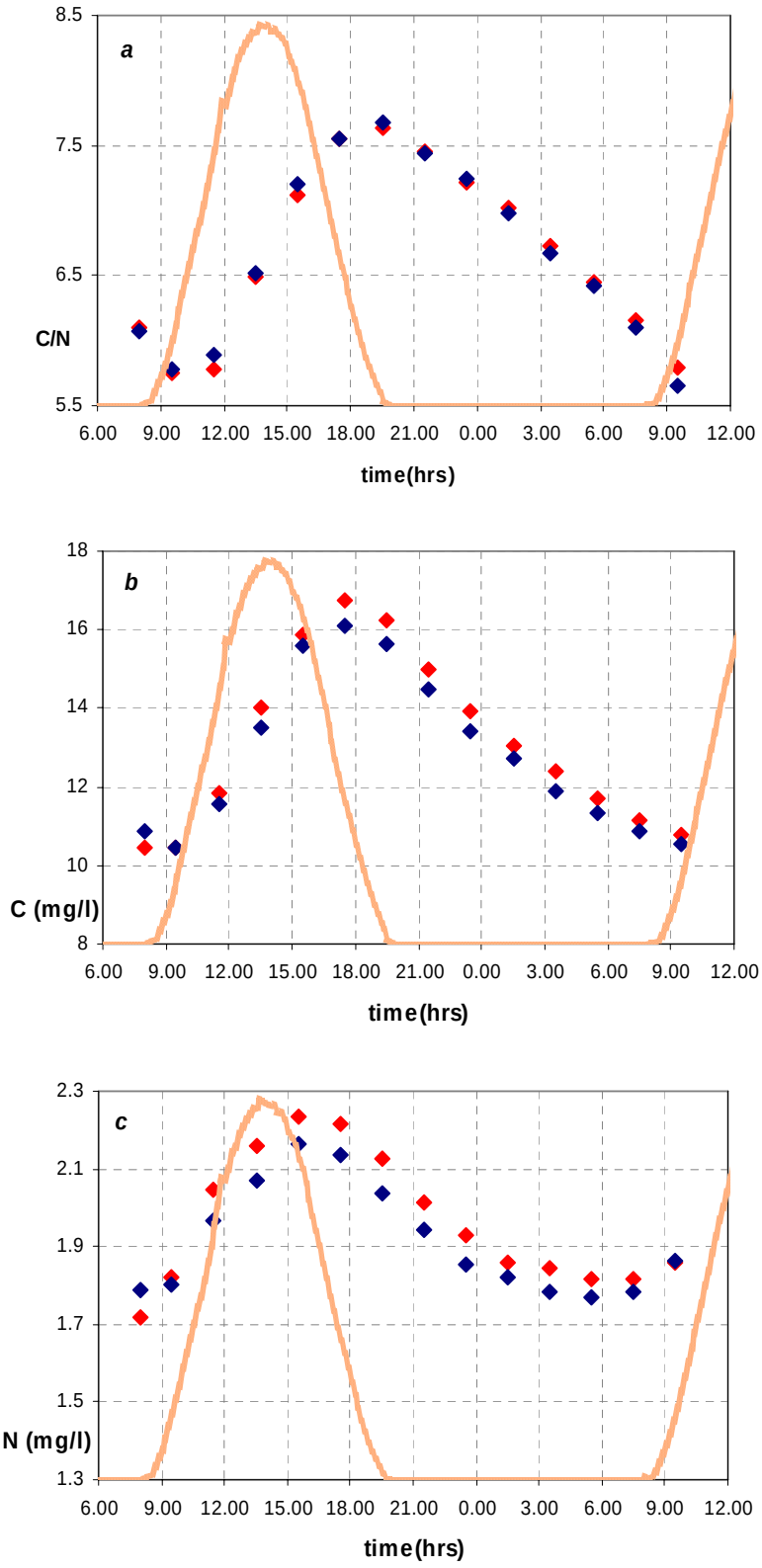

Fig.L.1.6: (a) C/N ratio, (b) C content (mg/l) and (c) N content (mg/l) in chemostats C1 (red) and C2 (blue), with time, in sinusoidal light (orange, from 0 to 220 µE m^{-2} s^{-1}).

Inorganic carbon and nitrogen: both inorganic carbon (DIC) and nitrogen (NO_2^-+NO_3^-) are maximum before dawn (7.30-8.00h) and minimum after midday (1.3 and 4-fold lower respectively, 15-15.30h), by photosynthetic assimilation, then they increase back during the dark period by C and N consumption (figs.L.1.7a and b).

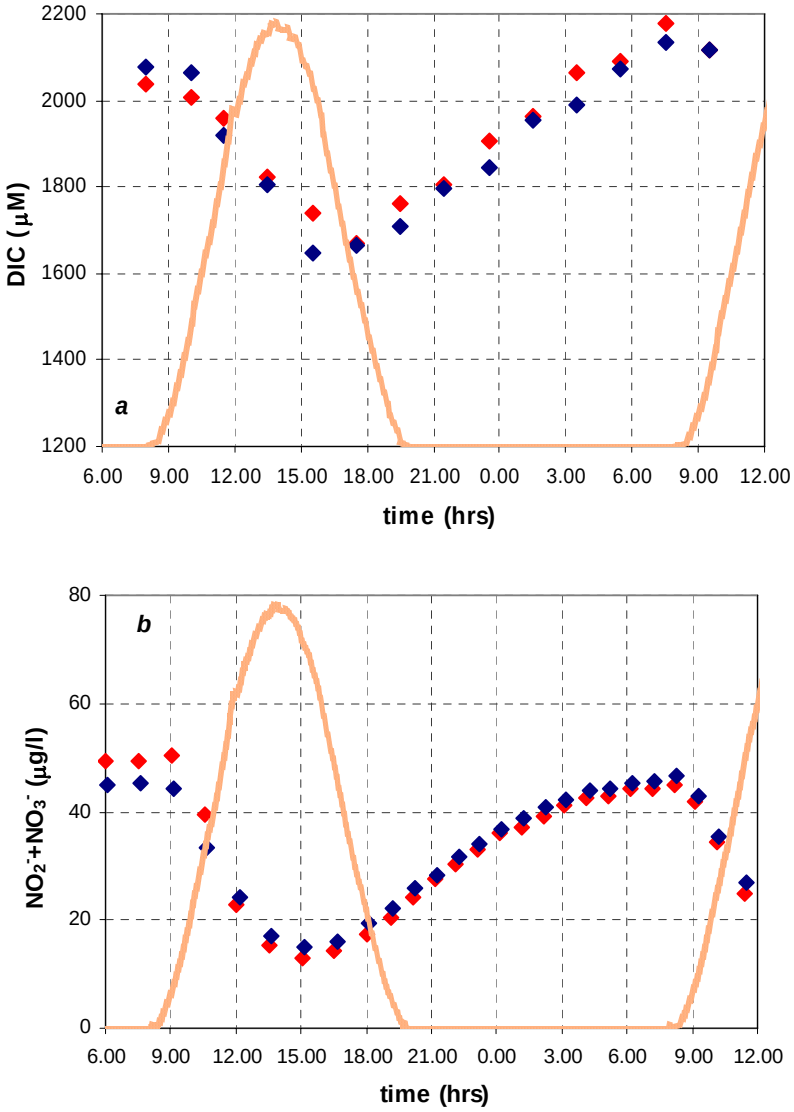

Fig.L.1.7: (a) Inorganic carbon (DIC, µM), and (b) nitrogen (NO_2^-+NO_3^-, mg/l), in chemostats C1 (red) and C2 (blue), with time, in sinusoidal light (orange, from 0 to 220 µE m^{-2} s^{-1}).

Pigments: chlorophyll-*a* (chla, fig.L.1.8a), chlorophyll-*c* (chlc(c1+c2), fig.L.1.8b) and fucoxanthin (fig.L.1.8c) vary from a minimum around dawn (8.30-9.30h) to a maximum before sunset (1.2-1.3-fold higher, 18.30-20.00h).

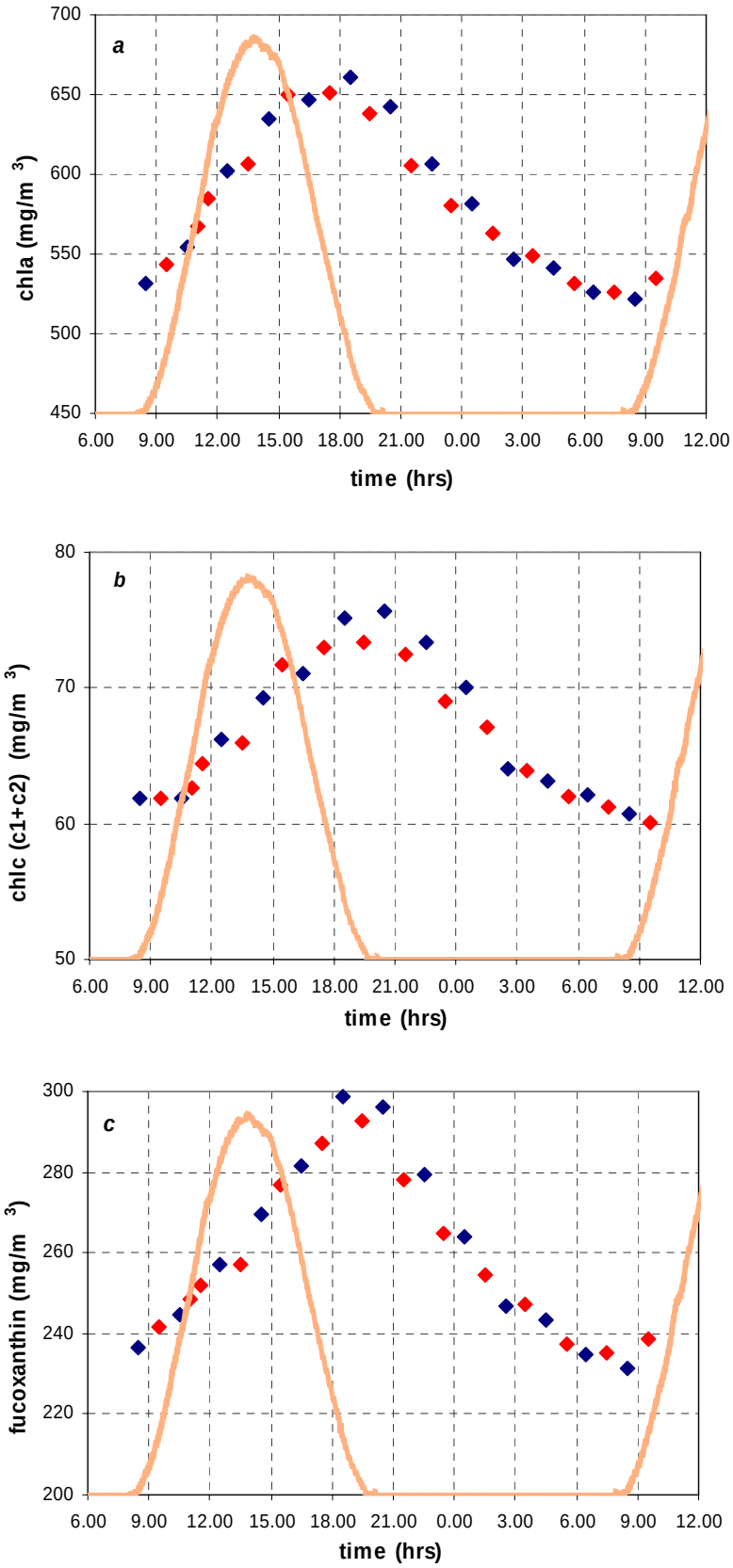

Fig.L.1.8: (a) Chlorophyll-*a* (chla, mg/m^3), (b) chlorophyll-*c1* + chlorophyll-*c2* (chlc(c1+c2), mg/m^3), and (c) fucoxanthin (mg/m^3) concentration, in chemostats C1 (red) and C2 (blue), with time, in sinusoidal light (orange, from 0 to 220 µE m^{-2} s^{-1}).

Both the ratios chlorophyll-c/chla (chlc/chla, fig.L.1.9a) and fucoxanthin/chla (fuco/chla, fig.L.1.9b) have a minimum at midday (13.30h), while chlc/chla has its

maximum 2 hours later (1.1-fold higher, 23.30h) than fuco/chla (1.1-fold higher too, 21.30h). Moreover, both the two patterns are constant in the second half of the night, respectively from 3.30 to 8.30h and from 5.30h to 9.30h.

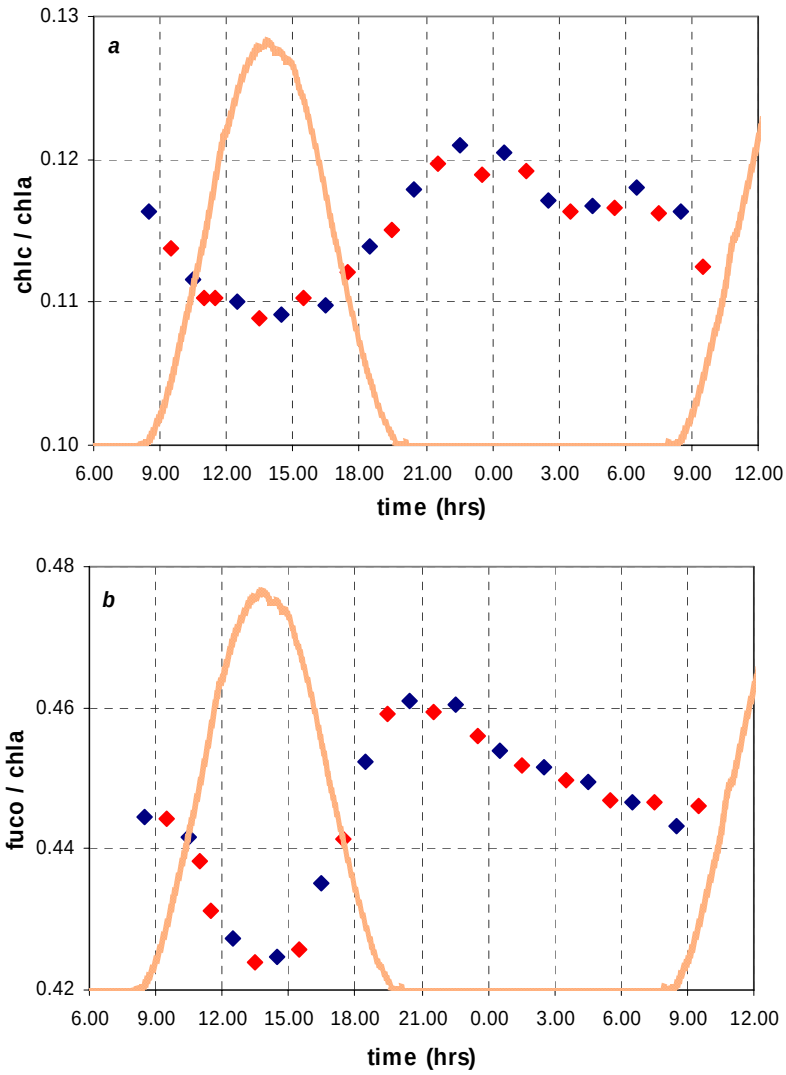

Fig.L.1.9: (a) The ratios chlorophyll-*c*/chlorophyll-*a* (chlc/chla), and (b) fucoxanthin/chlorophyll-*a* (fuco/chla), in chemostats C1 (red) and C2 (blue), with time, in sinusoidal light (orange, from 0 to 220 µE m^{-2} s^{-1}).

β-carotene has its maximum after midday (15.00h) and a minimum at midnight (1.3-fold lower, 3.00h, fig.L.1.10a). The ratio β-carotene/chla is maximum before midday (around 12.00h) and decreases as far as the after sunset minimum (1.1-fold lower, 21.00h, fig.L.1.10b).

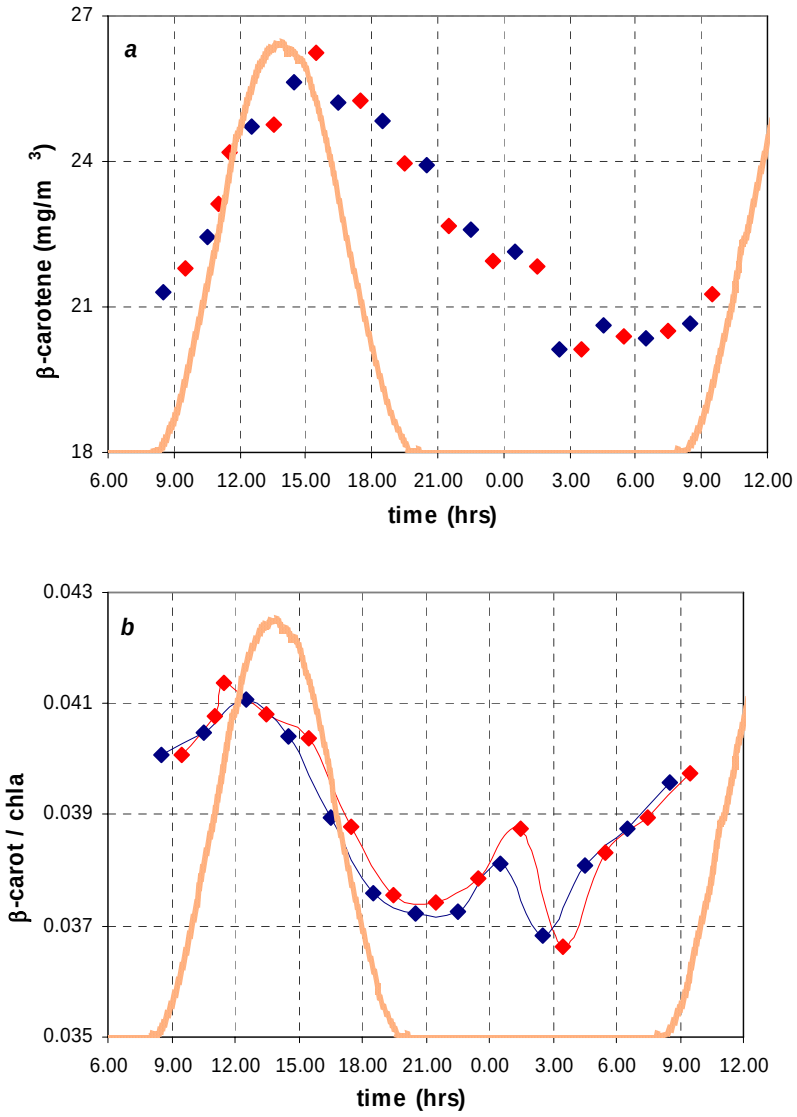

Fig.L.1.10: (a) β-carotene concentration (mg/m^3), and (b) the ratio β-carotene /chlorophyll-*a* (β-carot/chla), in chemostats C1 (red) and C2 (blue), with time, in sinusoidal light (orange, from 0 to 220 µE m^{-2} s^{-1}).

Violaxanthin concentration is the lowest after dawn (9.30h) and maximum at 16.00h, 2 hours after irradiance maximum (1.5-fold higher, fig.L.1.11a), then it decreases sharply as far as sunset, finally slowly during the night back to its minimum. Antheraxanthin and zeaxanthin follow a common pattern: maximum at midday (14.00h), then back to the minimum from sunset to mid-morning (10.1 and 7.8-fold lower respectively, 21.00-11.00h, fig.L.1.11b).

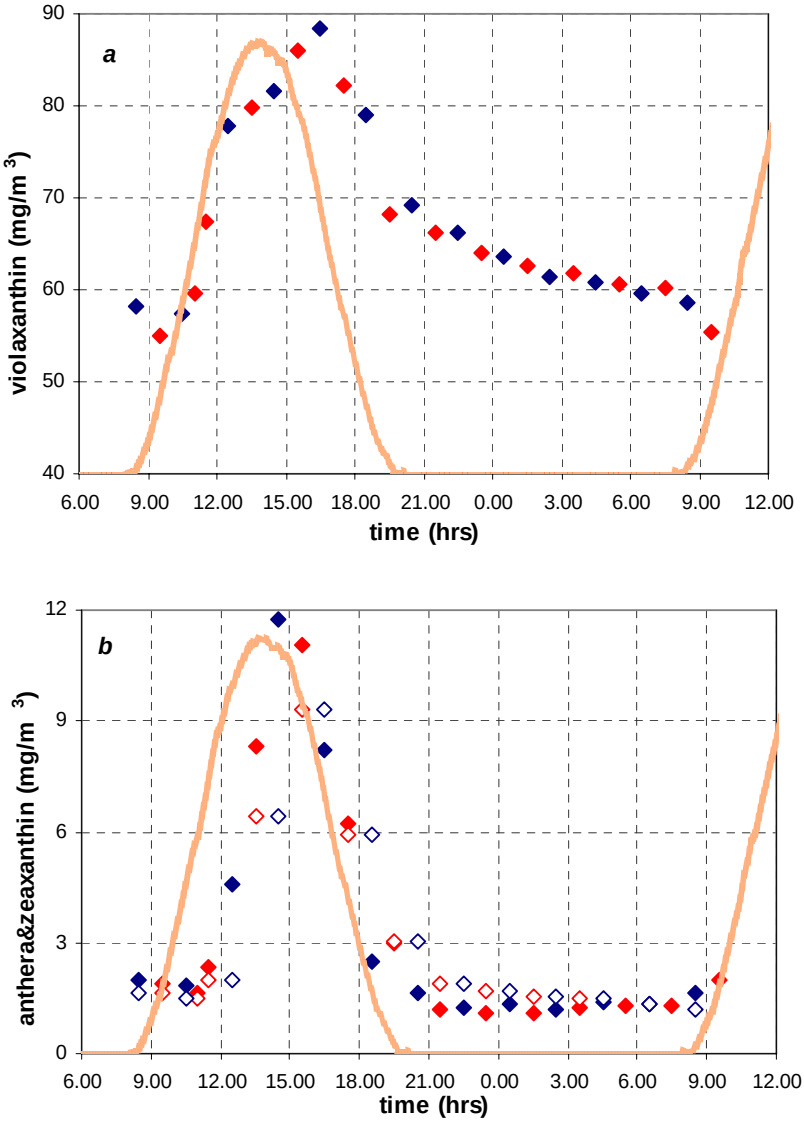

Fig.L.1.11: (a) Violaxanthin, and (b) antheraxanthin (closed symbols) & zeaxanthin (open symbols) concentrations (mg/m^3), in chemostats C1 (red) and C2 (blue), with time, in sinusoidal light (orange, from 0 to 220 µE m^{-2} s^{-1}).

The ratio violaxanthin/chla shares violaxanthin minimum soon after dawn (9.30h) and maximum after midday (around 16.00h), but it slowly increases from sunset during the night, then suddenly lowers to the morning minimum (1.3-fold lower, fig.L.1.12a). The ratios antheraxanthin/chla and zeaxanthin/chla follow the same pattern as antheraxanthin and zeaxanthin (the ratios between maximums and minimums being 8.9 and 6.4, respectively, fig.L.1.12b).

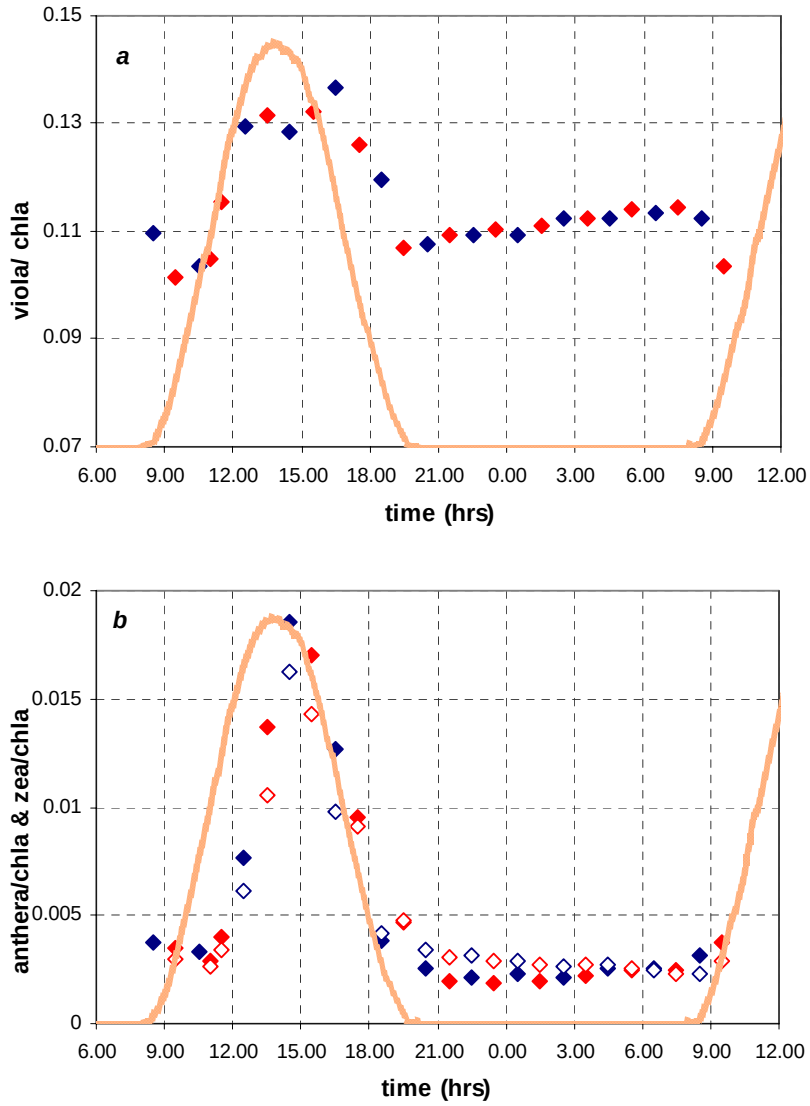

Fig.L.1.12: (a) The ratios violaxanthin/chlorophyll-*a* (viola/chla), and (b) antheraxanthin/chlorophyll-*a* (anthera/chla, closed symbols) & zeaxanthin/chlorophyll-*a* (zea/chla, open symbols), in chemostats C1 (red) and C2 (blue), with time, in sinusoidal light (orange, from 0 to 220 µE m^{-2} s^{-1}).

In vivo absorption: The optical absorption cross-section of cell suspension at 676 nm (a676, m^{-1}) decreases from the after-midday maximum (17.30h, fig.L.1.13a) to its after-midnight minimum (1.2-fold lower, 3.30h), then it increases first slowly as far as dawn, finally sharply back to the maximum.

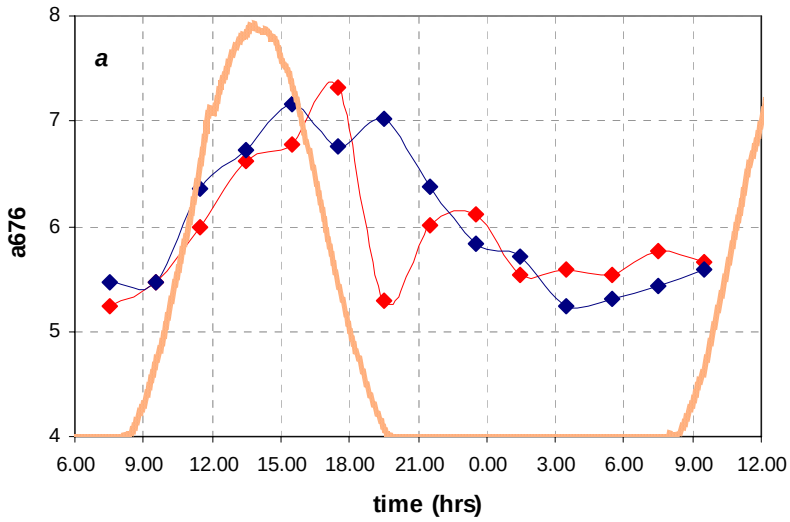

Fig.L.1.13a: The optical absorption cross-section at 676 nm (a676, m^{-1}), in chemostats C1 (red) and C2 (blue), with time, in sinusoidal light (orange, from 0 to 220 µE m^{-2} s^{-1}).

The specific absorption cross-section of cell suspension at 676 nm (a676 normalized by chlorophyll-*a* concentration, a*676, in m^2 mg^{-1}) is maximum around midday (15:30-17.30h, fig.L.1.13b) and decreases first sharply (as far as 21.30h), then slower until the minimum at 1.30h (1.2-fold lower).

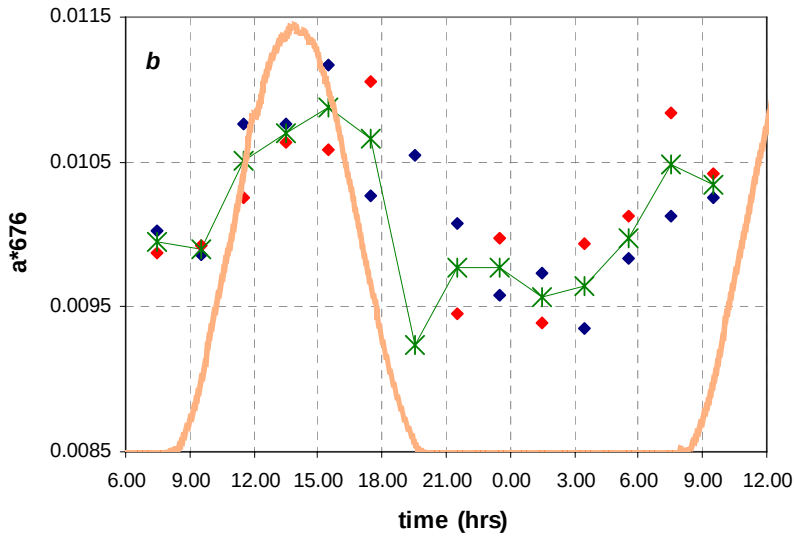

Fig.L.1.13b: The specific optical absorption cross-section at 676 nm (a*676=a676/chla, in m^2 mg^{-1}), in chemostats C1 (red) and C2 (blue), with time, in sinusoidal light (orange, from 0 to 220 µE m^{-2} s^{-1}). In green, the mean values between the 2 chemostats.

The blue/red ratio remains low and stable from before sunset (19.30h) to mid-morning (11.30h) then it increases to its maximum values around midday (13:30-17:30h, fig.L.1.13c).

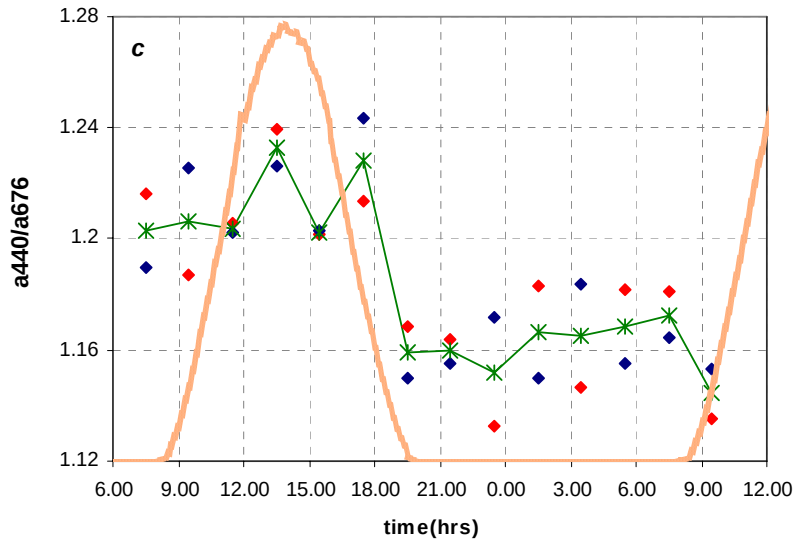

Fig.L.1.13c: The blue/red ratio (a440/a676), in chemostats C1 (red) and C2 (blue), with time, in sinusoidal light (orange, from 0 to 220 µE m^{-2} s^{-1}). In green, the mean values between the 2 chemostats.

The ratio C/chla has its minimum after dawn (9.30h) and reaches its maximum after midday, at 17.30h (1.3-fold higher, fig.L.1.14a). Moreover, like cell volume C/chla shows a slighter slope around midnight (0.00-3.00h).

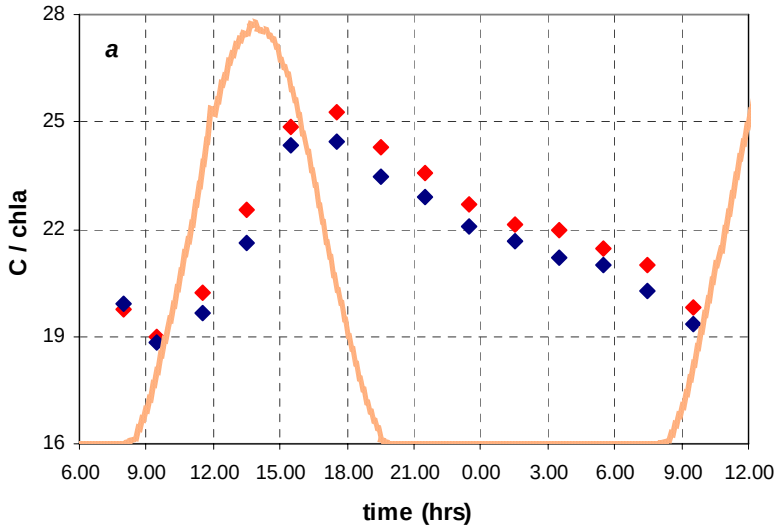

Fig.L.1.14a: The ratio C-content/chlorophyll-*a* (C/chla), in chemostats C1 (red) and C2 (blue), with time, in sinusoidal light (orange, from 0 to 220 µE m^{-2} s^{-1}).

Chlorophyll-*a* concentration per cell (chla/cell) follows C/N pattern, with a minimum after dawn (9.30h), then increasing as far as the first hours of the night (1.6-fold higher, 21.30h), finally decreasing sharply back to the morning minimum (fig.L.1.14b).

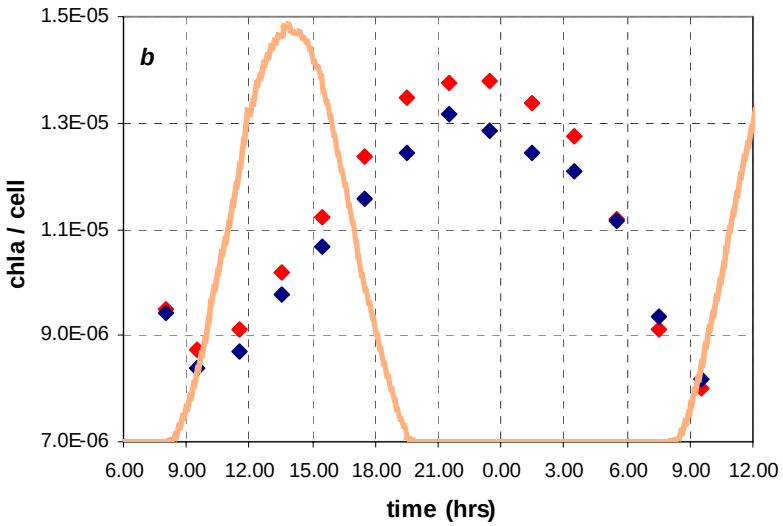

Fig.L.1.14b: The ratio chlorophyll-*a*/number of cells (chla/cell, µg $cell^{-1}$), in chemostats C1 (red) and C2 (blue), with time, in sinusoidal light (orange, from 0 to 220 µE m^{-2} s^{-1}).

Chlorophyll-*a* concentration per cell volume unit (chla/vol) has a 12 hours periodicity, with a higher maximum after dawn (9.30h) and a second lower one at 21:30h, and the lowest minimum at 17:30h and a second higher one at 5:30h (1.3-fold lower, fig.L.1.14c).

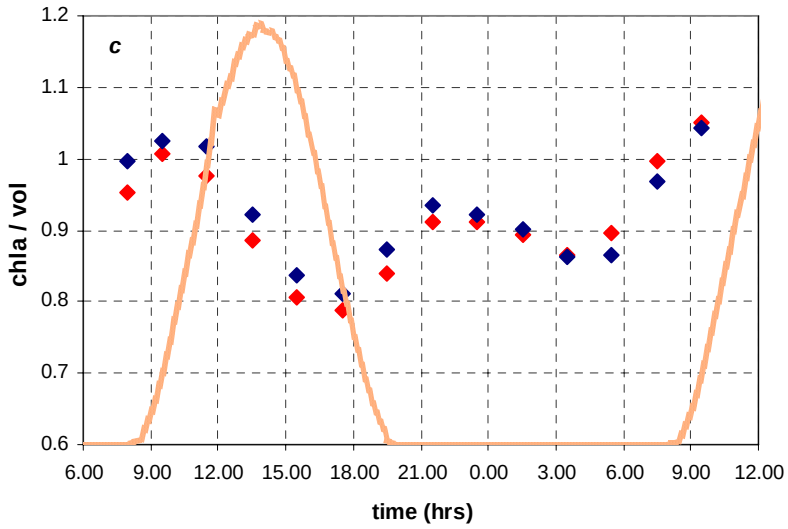

Fig.L.1.14c: The ratio chlorophyll-*a*/cell volume (chla/vol, µg l^{-1} $µm^{-3}$), in chemostats C1 (red) and C2 (blue), with time, in sinusoidal light (orange, from 0 to 220 µE m^{-2} s^{-1}).

3.b.2 Experiment 2: from sinusoidal to continuous light (26-hours measurements)

Photosynthetic parameters by oxygen measurements: shifting the light from sinusoidal to continuous, both α (and α^b) and Pmax (and P^bmax) loose their diel periodicity. α^b remains nearly constant from dawn to 20.30h, then it shows ample oscillations (fig.L.2.1a). P^bmax decreases from its maximum after dawn, first sharply, then slowly (fig.L.2.1b).

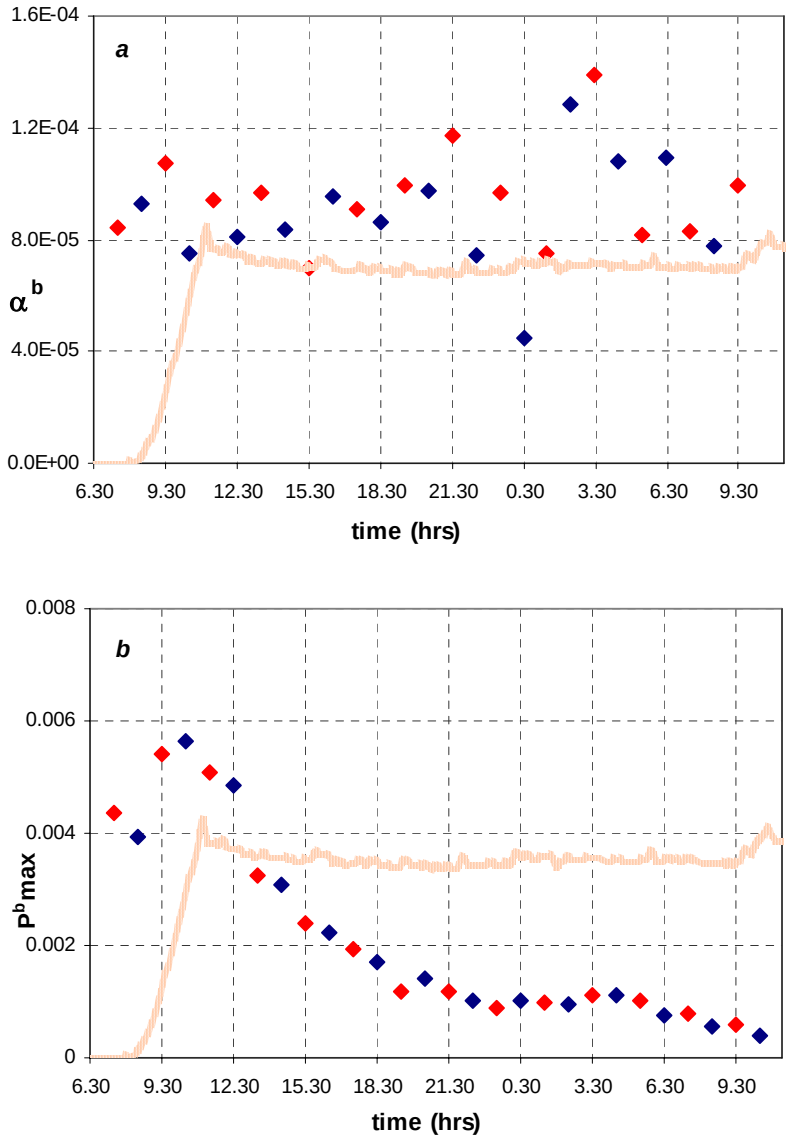

Fig.L.2.1: (a) the light-limited slope α normalized by chlorophyll-*a* (α^b, µmol O_2 (ml min)$^{-1}$ (µmol quanta m^{-2} s^{-1} µg chla l^{-1}) $^{-1}$), and (b) the light-saturated rates of photosynthesis normalized by chlorophyll-*a* (P^bmax, µmolO_2 µg chla^{-1} s^{-1}), by net oxygen evolved measurements, in chemostats C1 (red) and C2 (blue), shifting light from sinusoidal to continuous (orange, from 0 to 110 µE m^{-2} s^{-1}).

α^b and P^bmax do not covary anymore: they show an only 2-phases pattern variability: a first one from dawn to 20.30h, when P^bmax is much more variable than α^b (fig.L.2.2a), then a second one with α^b oscillation larger than P^bmax slow decrease (fig.L.2.2b). So

shifting light to continuous, PE parameters show only Ek-dependent variability, meaning photoacclimation in progress (fig.L.2.2c).

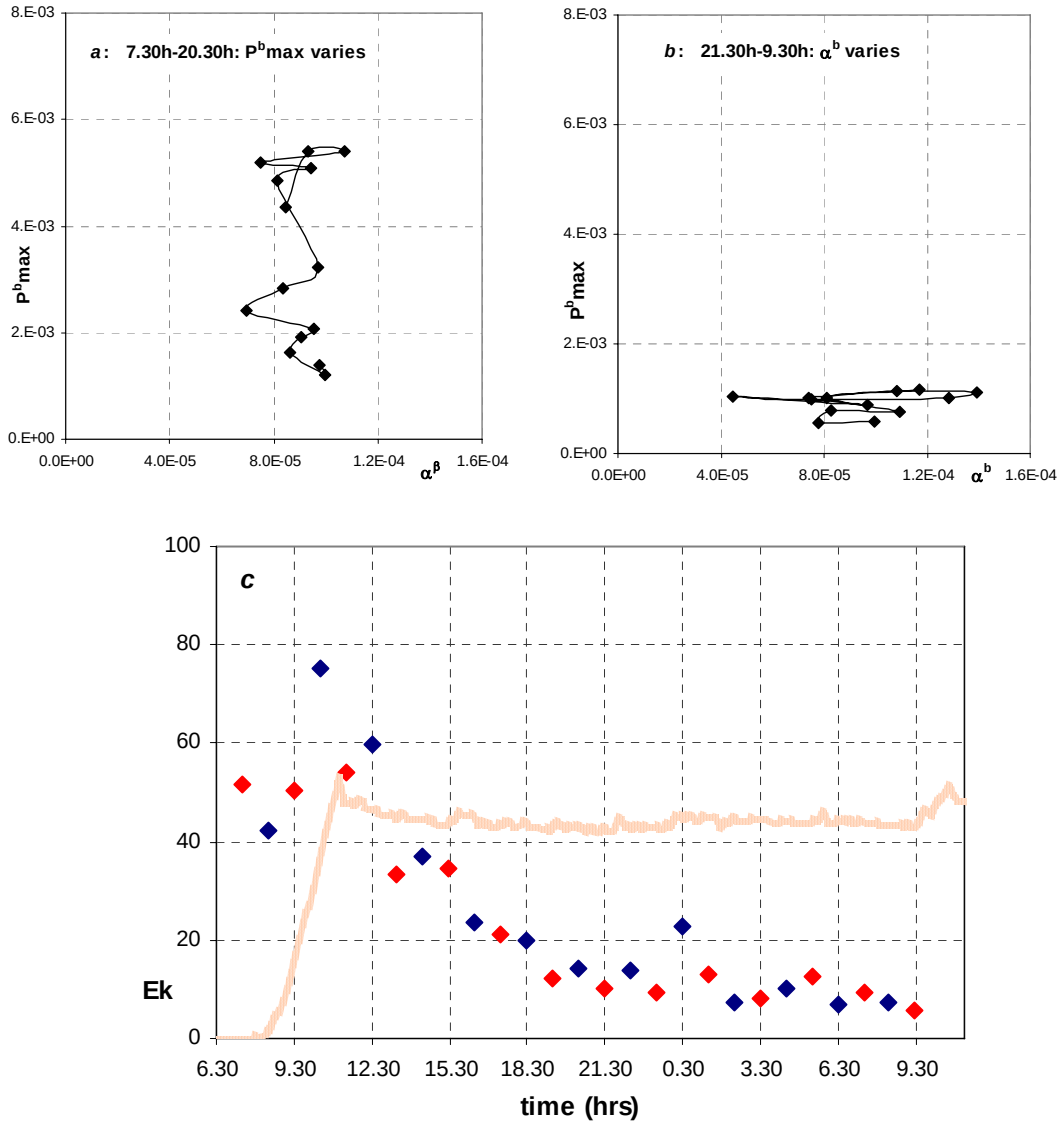

Fig.L.2.2: two-phases variation of α^b and P^bmax in both chemostats during 26-hours measurements shifting light from sinusoidal to continuous: (a) from 7.30h to 20.30h, P^bmax varies more than α^b, (b) from 21.30h to 9.30h α^b varies more than P^bmax, (c) the light-saturation index Ek (in µE $m^{-2}s^{-1}$), by net oxygen evolved measurements, in chemostats C1 (red) and C2 (blue), with time, shifting light from sinusoidal to continuous (orange, from 0 to 110 µE m^{-2} s^{-1}).

In continuous light β^b looses its diel periodicity too (fig.L.2.3a). However, β^b still varies following P^bmax pattern (fig.L.2.3b), with a maximum around dawn, then it decreases, first sharply, then slowly. Fig.L.2.3c shows the clear positive correlation (R^2=0.89, n=28) between P^bmax and β^b, that means lower photosynthetic rates with lower photoinibition.

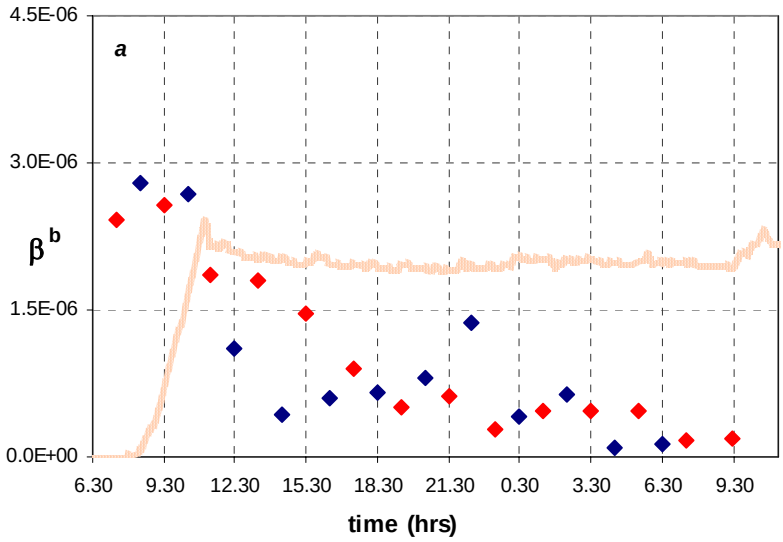

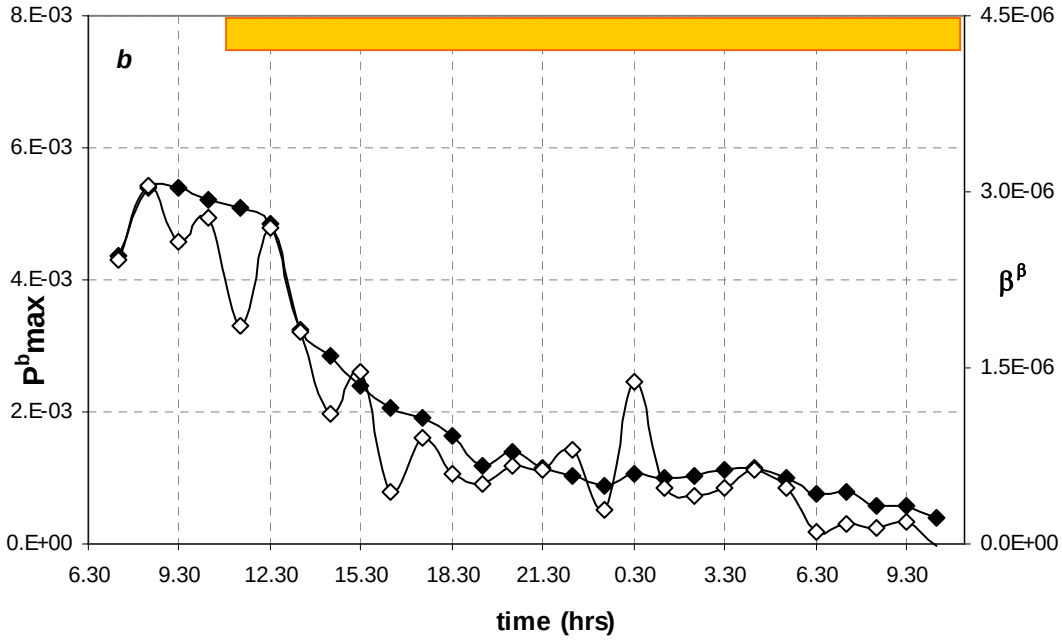

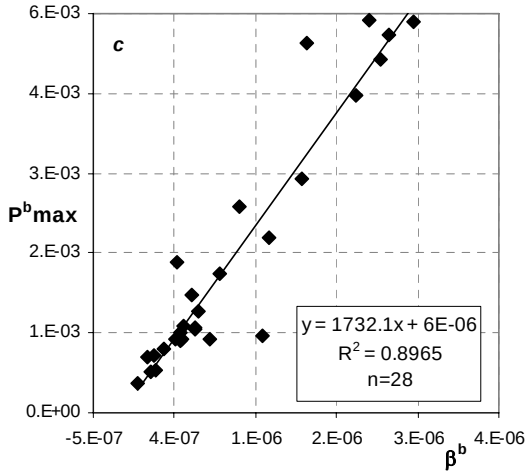

Fig.L.2.3: (a) the photo-inhibited slope β normalized by chlorophyll-*a* (β^b, µmol O_2 (ml min)$^{-1}$ (µmol quanta m^{-2} s^{-1} µg chla l^{-1}) $^{-1}$), by net oxygen evolved measurements, in chemostats C1 (red) and C2 (blue), with time, shifting light from sinusoidal to continuous (orange, from 0 to 110 µE m^{-2} s^{-1}), (b) comparison of β^b (open symbols, in m^2 µg chla^{-1}) and P^bmax (closed symbols, in µmolO_2 µg chla^{-1} s^{-1}) variations in both chemostats, with time during 26-hours measurements from sinusoidal to continuous light, and (c) covariation between P^bmax and β^b in both chemostats in continuous light. The yellow bar indicates the light period.

Cell cycle: the number of cells keeps on increasing as far as the sinusoidal midday, then it decreases and reaches a stable value at the sinusoidal midnight, which is lower than the sinusoidal minimum (fig.L.2.4a). Cell volume from its minimum at 9.00h increases linearly as far as 21.00h, then it remains constant for three hours, finally it increases again but slowly, as far as it reaches a stable value around 9.00h (fig.L.2.4b). That means that about 24 hours after the onset of continuous light, cells are constant in number and volume.

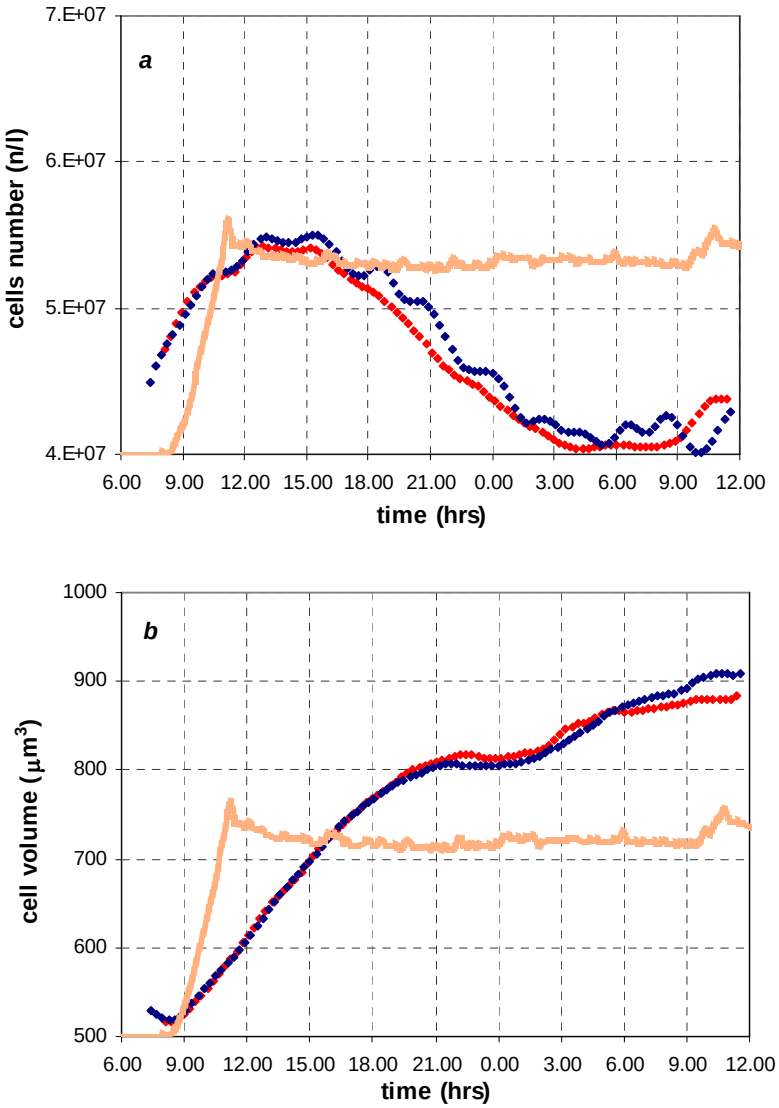

Fig.L.2.4: (a) cell number (n/l) and (b) cell volume (μm^3), in chemostats C1 (red) and C2 (blue), with time, shifting light from sinusoidal to continuous (orange, from 0 to 110 $\mu E\ m^{-2}\ s^{-1}$).

Organic carbon and nitrogen: the C/N ratio increases as far as 0.00h, then it decreases to a constant value 21 hours after the shift to continuous light (fig.L.2.5a). C-

concentration follows the same trend (fig.L.2.5b), while N-concentration increases for the first seven hours, then it's almost constant (fig.L.2.5c).

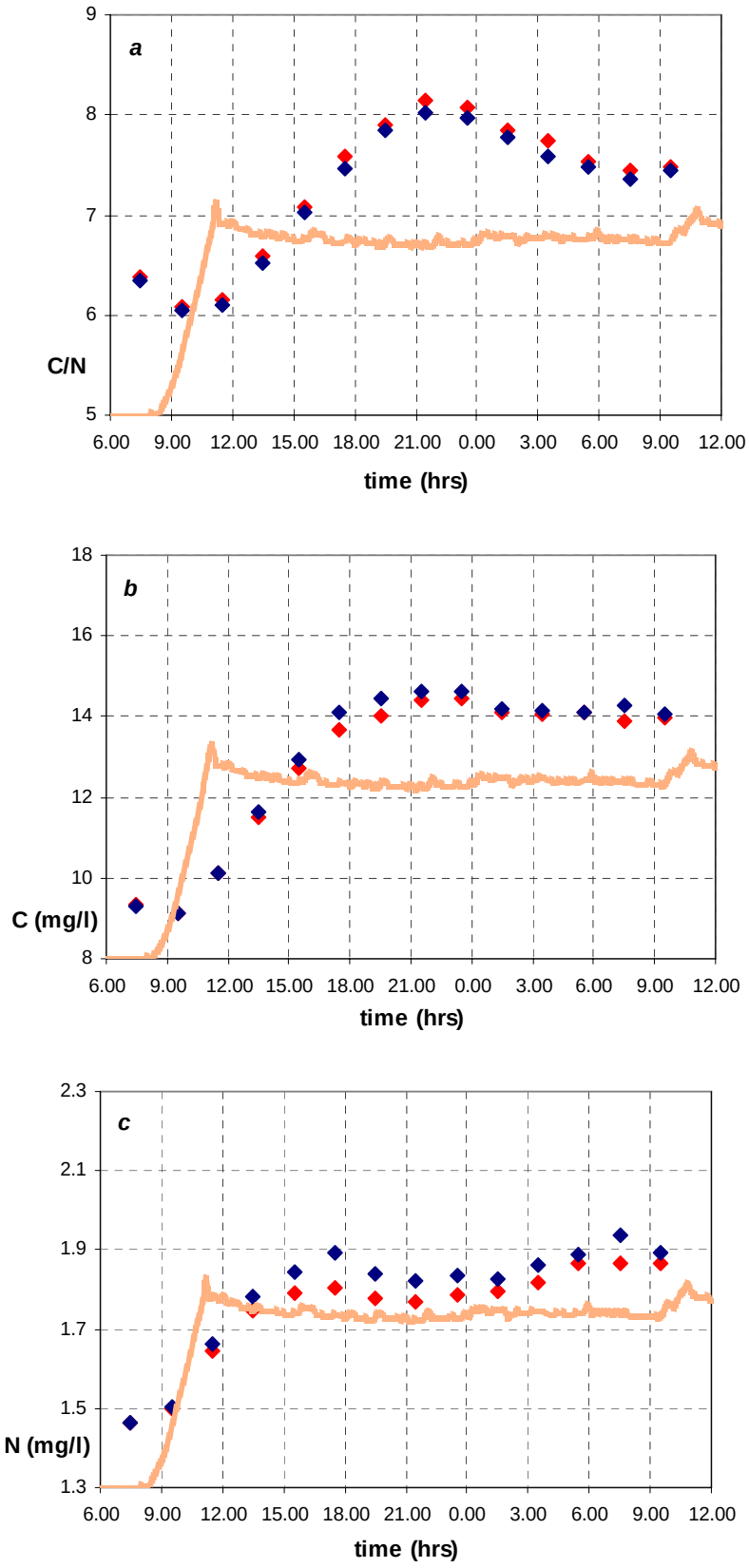

Fig.L.2.5: (a) C/N ratio, (b) C content (mg/l) and (c) N content (mg/l) in chemostats C1 (red) and C2 (blue), with time, shifting light from sinusoidal to continuous (orange, from 0 to 110 μE m^{-2} s^{-1}).

Inorganic carbon and nitrogen: from its maximum at dawn, DIC decreases as far as 18.00h, finally it becomes stable, that means constant rates of C-assimilation and fixation in continuous-light (fig.L.2.6a). Inorganic nitrogen concentration (NO_2^-+NO_3^-), which is three fold higher than in experiment 1, decreases to a minimum soon after the light shift (one hour and a half later), then slightly increases and remains almost constant for the following twelve hours, finally it lowers to the lowest value at 7.30h (fig.L.2.6b).

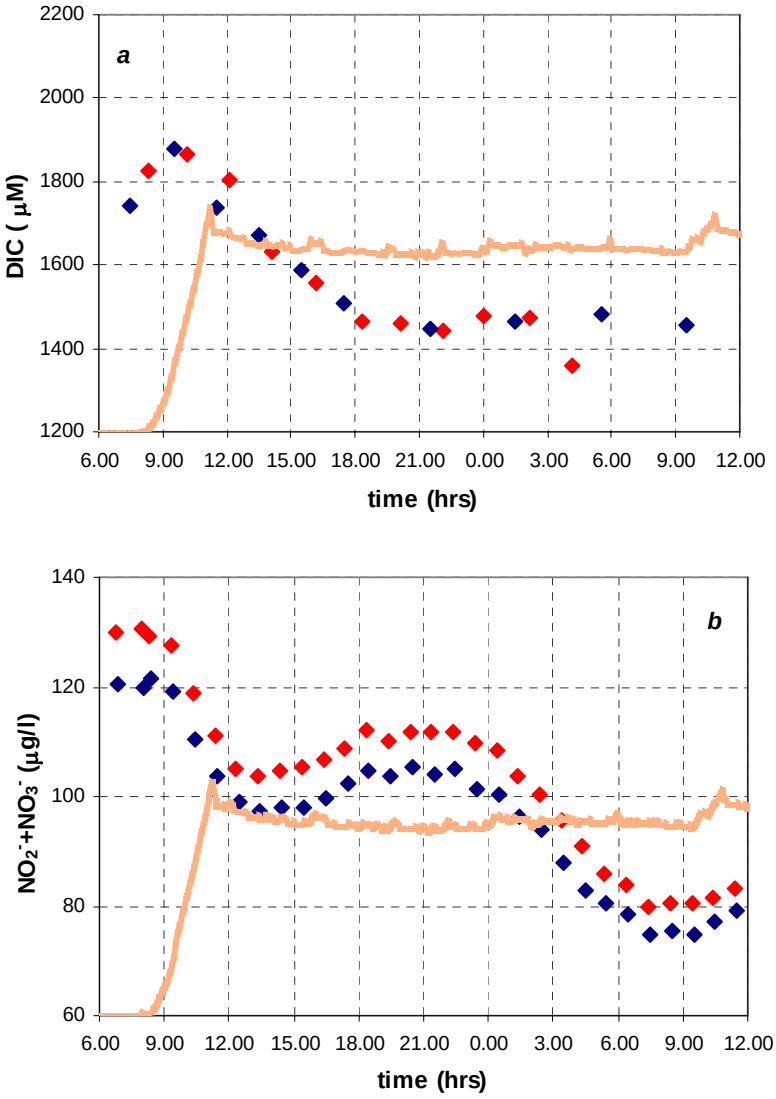

Fig.L.2.6: (a) Inorganic carbon (DIC, µM), and (b) nitrogen (NO_2^-+NO_3^-, mg/l), in chemostats C1 (red) and C2 (blue), with time, shifting light from sinusoidal to continuous (orange, from 0 to 110 µE m^{-2} s^{-1}).

Pigments: as in sinusoidal light, chlorophyll-*a* (fig.L.2.7a), chlorophyll-*c* (fig.L.2.7b) and fucoxanthin (fig.L.2.7c) concentrations increase from the dawn minimum to the after-sunset maximum, but the increase is higher than in sinusoidal light (1.2-fold larger) and it is followed by a decrease to a stable value, which is around the average value between continuous-light maximum and minimum.

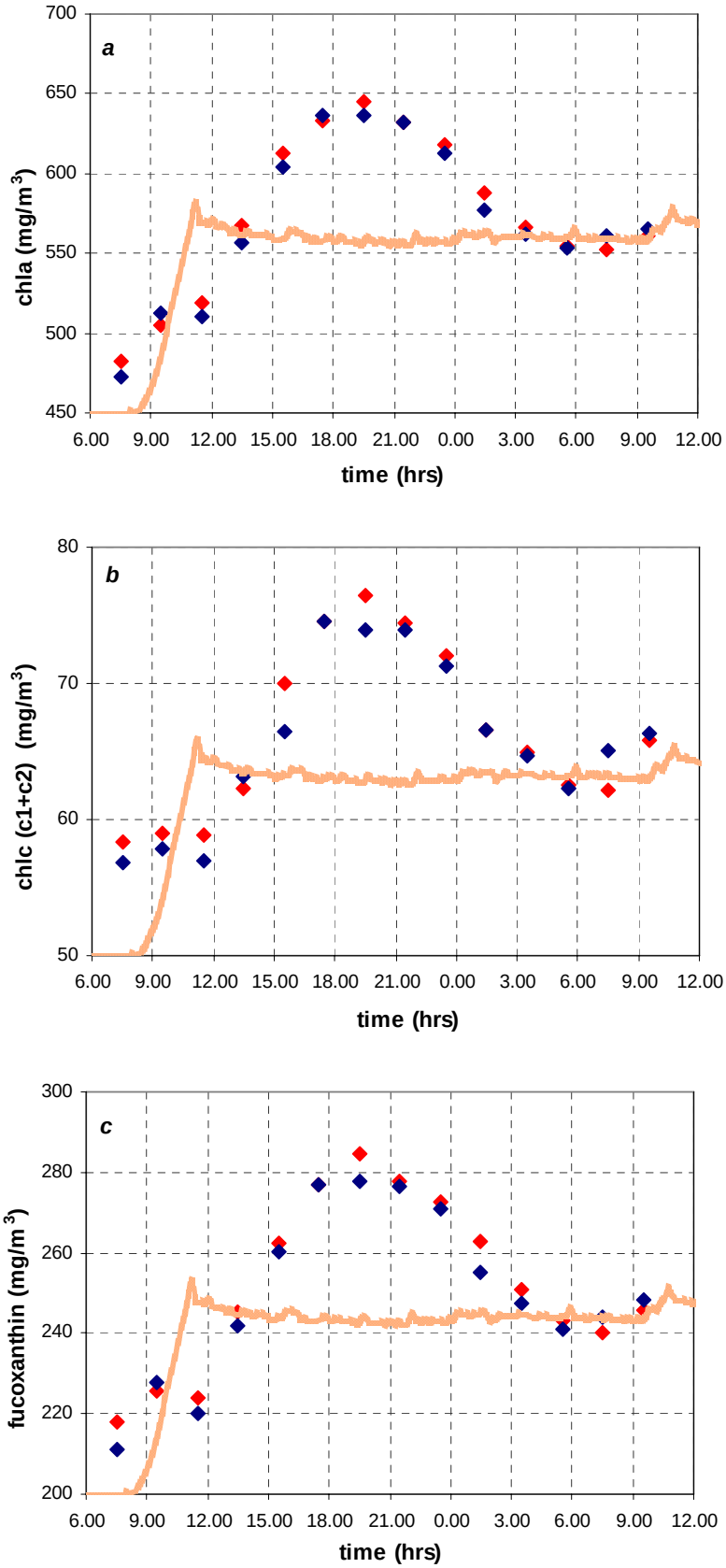

Fig.L.2.7: (a) Chlorophyll-*a* (chla, mg/m^3), (b) chlorophyll-*c1* + chlorophyll-*c2* (chlc(c1+c2), mg/m^3), and (c) fucoxanthin (mg/m^3) concentration, in chemostats C1 (red) and C2 (blue), with time, shifting light from sinusoidal to continuous (orange, from 0 to 110 µE m^{-2} s^{-1}).

Both the ratios chlorophyll-c/chla (fig.L.2.8a) and fucoxanthin/chla (fig.L.2.8b) keep their sinusoidal minimum at midday, then they reach their maximum two and four hours later than in sinusoidal light, respectively.

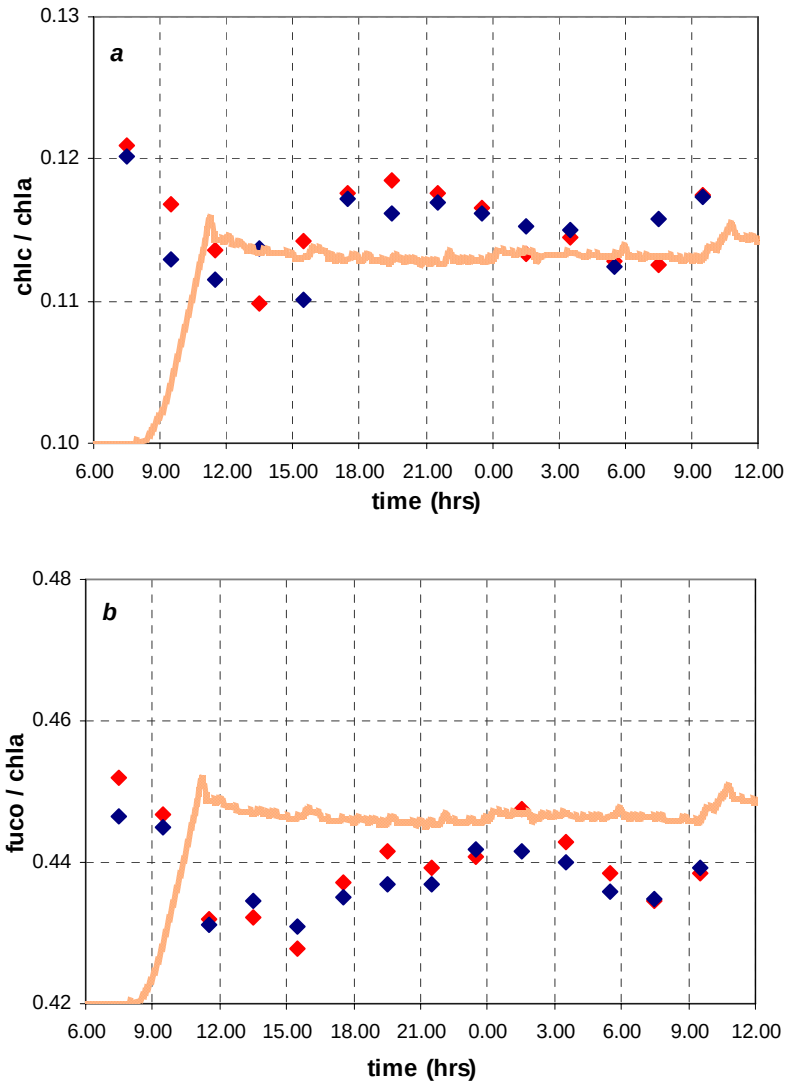

Fig.L.2.8: (a) The ratios chlorophyll-*c*/chlorophyll-*a* (chlc/chla), and (b) fucoxanthin/chlorophyll-*a* (fuco/chla), in chemostats C1 (red) and C2 (blue), with time, shifting light from sinusoidal to continuous (orange, from 0 to 110 μE m^{-2} s^{-1}).

When compared to sinusoidal light, β-carotene maximum has a three hours delay (fig.L.2.9a), so that it has the same pattern of all the other pigments, with a minimum 12 hours later, at the sinusoidal midnight. So β-carotene maintains a 24-hours periodicity but 4 hours later shifted. The ratio β-carotene/chla keeps its sinusoidal pattern (fig.L.2.9b).

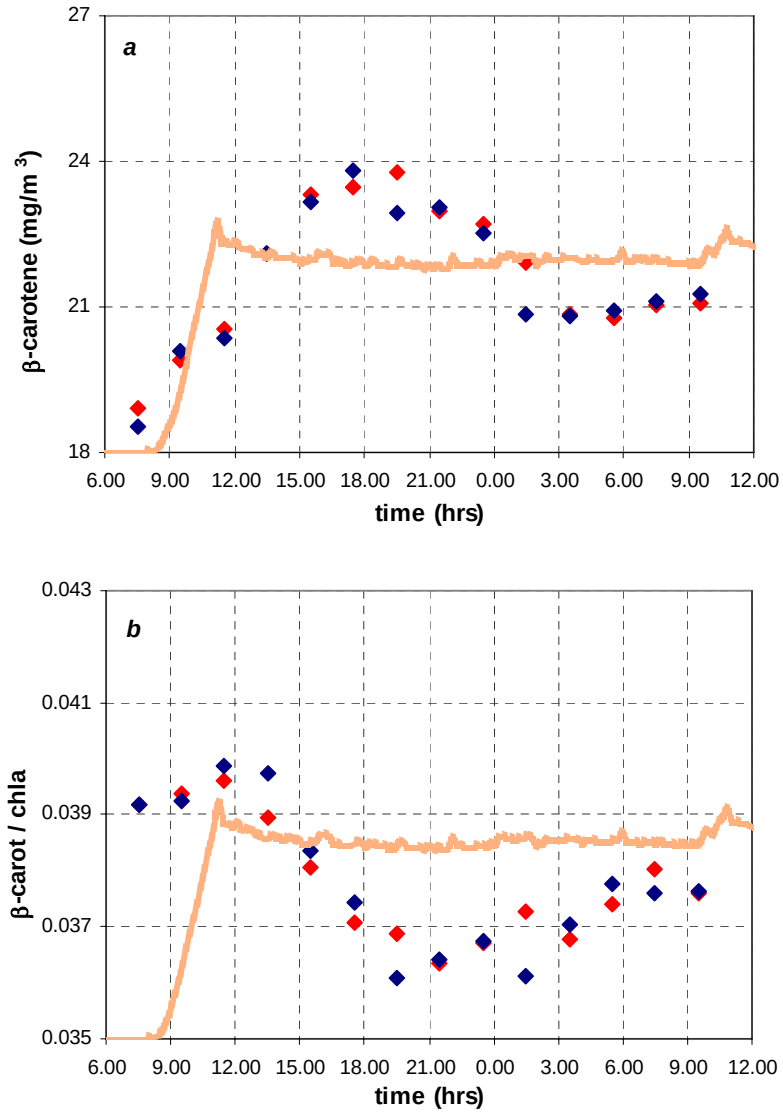

Fig.L.2.9: (a) β-carotene concentration (mg/m^3), and (b) the ratio β-carotene /chlorophyll-*a* (β-carot/chla), in chemostats C1 (red) and C2 (blue), with time, shifting light from sinusoidal to continuous (orange, from 0 to 110 μE m^{-2} s^{-1}).

Violaxanthin concentration peaks at 13.30h, then it lowers to 19.30h minimum (1.2-fold lower), finally it slowly linearly increases for the following twelve hours (fig.L.2.10a). Antheraxanthin and zeaxanthin reach their maximums at 17.30h (4.1-fold and 10-fold higher), then antheraxanthin remains stable, while zeaxanthin decreases as far as 23.30h and finally remains stable on that value.

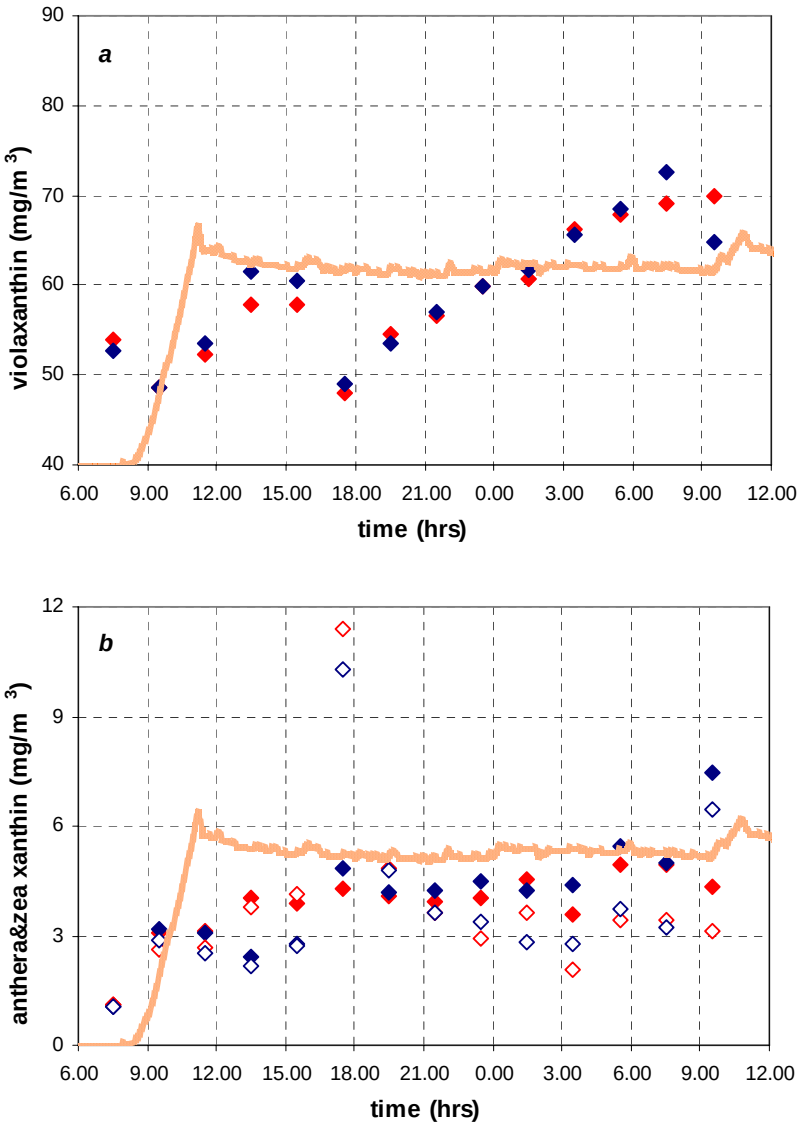

Fig.L.2.10: (a) Violaxanthin, and (b) antheraxanthin (closed symbols) & zeaxanthin (open symbols) concentrations (mg/m^3), in chemostats C1 (red) and C2 (blue), with time, shifting light from sinusoidal to continuous (orange, from 0 to 110 μE m^{-2} s^{-1}).

The ratios violaxanthin/chla (fig.L.2.11a), antheraxanthin/chla and zeaxanthin/chla (fig.L.2.11b) follow the patterns of their corresponding pigments., but they start decreasing at 12.00h.

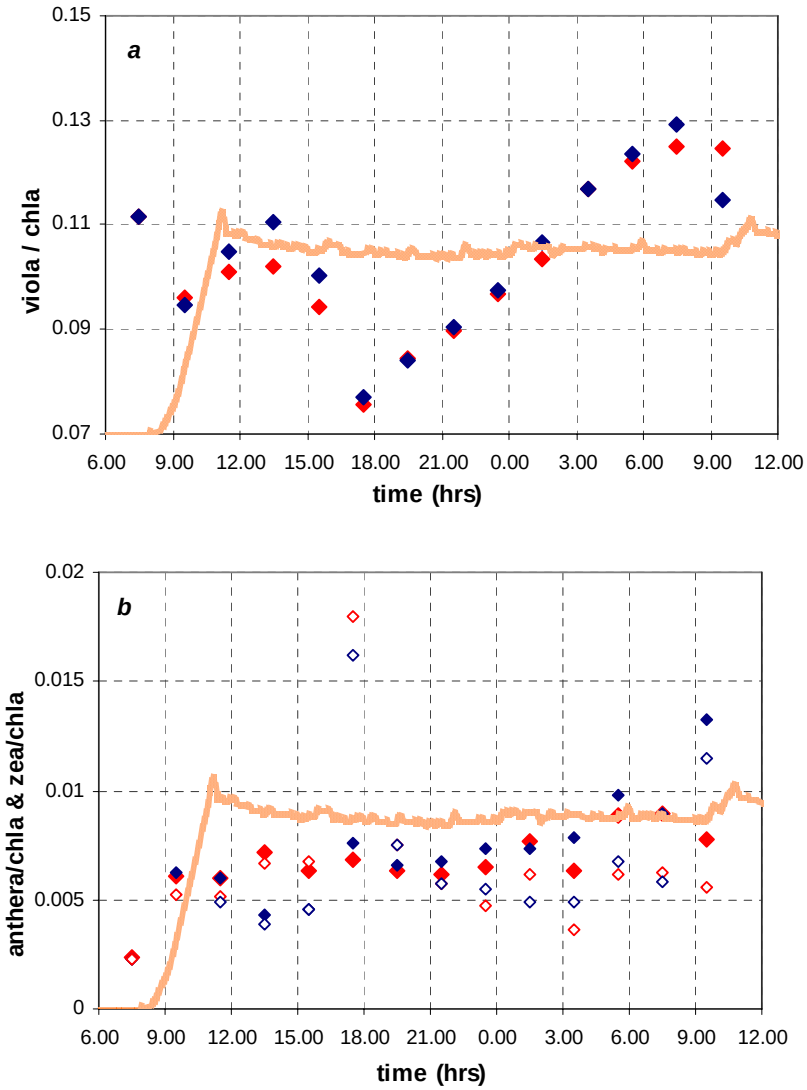

Fig.L.2.11: (a) The ratios violaxanthin/chlorophyll-*a* (viola/chla), and (b) antheraxanthin/chlorophyll-*a* (anthera/chla, closed symbols) & zeaxanthin/chlorophyll-*a* (zea/chla, open symbols), in chemostats C1 (red) and C2 (blue), with time, shifting light from sinusoidal to continuous (orange, from 0 to 110 µE m^{-2} s^{-1}).

In vivo absorption: The optical absorption cross-section of cell suspension at 676 nm (a676, m^{-1}) reaches its after-midday maximum (17.30h, fig.L. 2.12a), then remains stable.

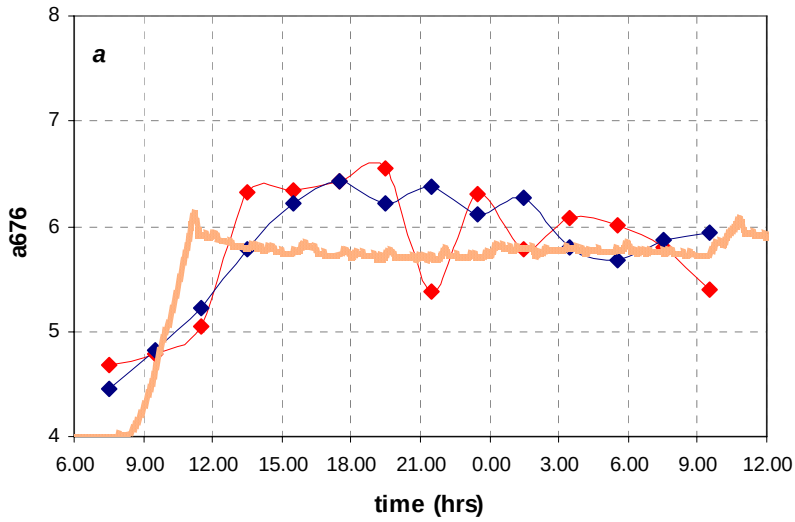

Fig.L.2.12a: The optical absorption cross-section at 676 nm (a676, m^{-1}), in chemostats C1 (red) and C2 (blue), with time, shifting light from sinusoidal to continuous (orange, from 0 to 110 µE m^{-2} s^{-1}).

The specific absorption cross-section of cell suspension at 676 nm (a676 normalized by chlorophyll-*a* concentration, a*676, in m^2 mg^{-1}) increases as far as 11.30h, then it lowers as far as 21.30h, finally it increases again to the mid-morning values (fig.L. 2.12b).

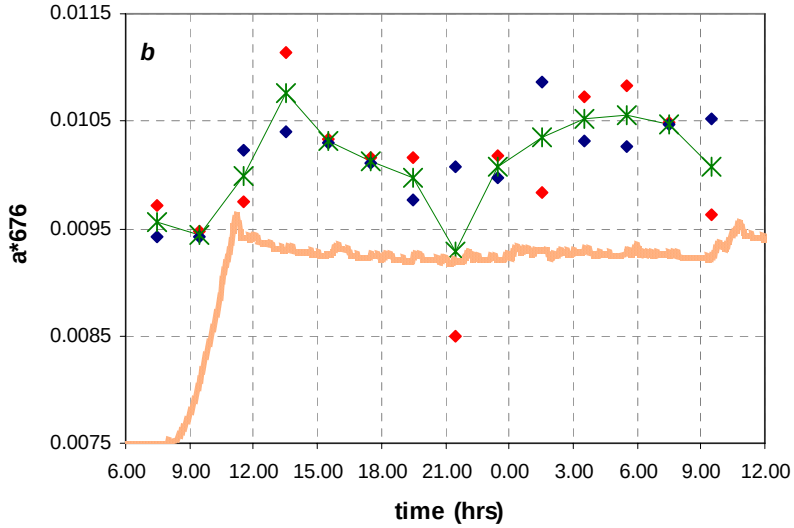

Fig.L.2.12b: The specific optical absorption cross-section at 676 nm (a*676=a676/chla, in m^2 mg^{-1}), in chemostats C1 (red) and C2 (blue), with time, shifting light from sinusoidal to continuous (orange, from 0 to 110 µE m^{-2} s^{-1}). In green, the mean values between the 2 chemostats.

Shifting light to continuous, the blue/red ratio lowers to nocturnal values for the first 9 hours following the shift, then it increases and remains to higher diurnal values (fig.L. 2.12c).

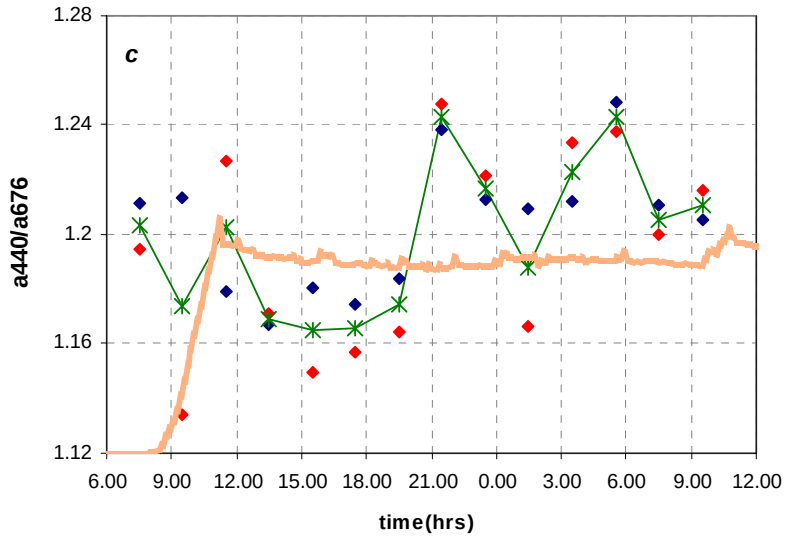

Fig.L.2.12c: The blue/red ratio (a440/a676), in chemostats C1 (red) and C2 (blue), with time, shifting light from sinusoidal to continuous (orange, from 0 to 110 µE m^{-2} s^{-1}). In green, the mean values between the 2 chemostats.

The ratio C/chla follows the same pattern as cell volume, with its minimum after dawn and its maximum at 6.00h (fig.L.2.13a).

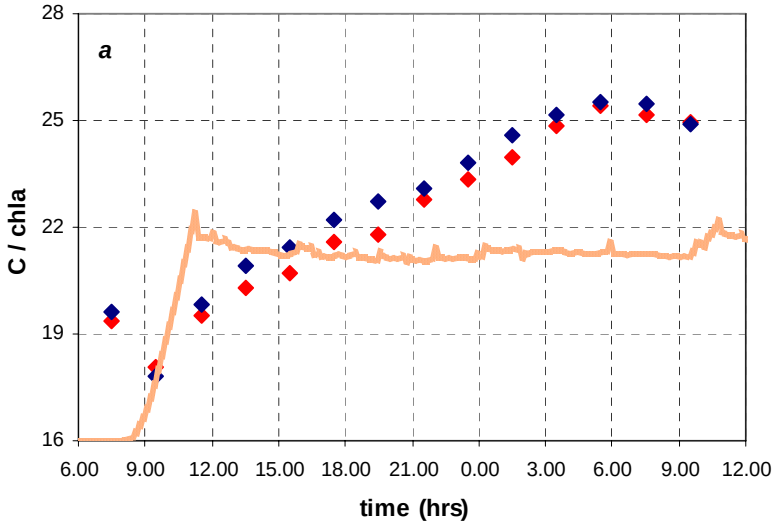

Fig.L.2.13a: The ratio C-content/chlorophyll-*a* (C/chla), in chemostats C1 (red) and C2 (blue), with time, shifting light from sinusoidal to continuous (orange, from 0 to 110 µE m^{-2} s^{-1}).

Chlorophyll-*a* concentration per cell (chla/cell, fig.L.2.13b) has a minimum at the moment of the light-shift, then it follows C-concentration pattern, increasing as far as 21.30h and finally remaining stable.

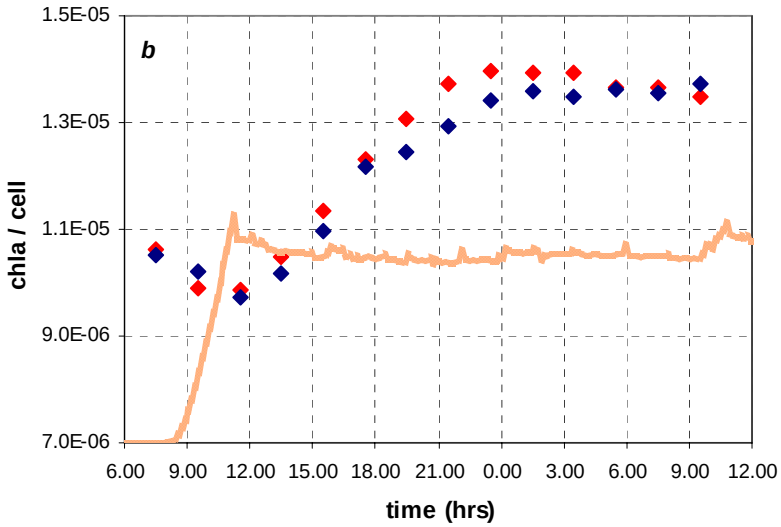

Fig.L.2.13b: The ratio chlorophyll-*a*/number of cells (chla/cell, µg cell^{-1}), in chemostats C1 (red) and C2 (blue), with time, shifting light from sinusoidal to continuous (orange, from 0 to 110 µE m^{-2} s^{-1}).

From its maximum after dawn, chlorophyll-*a* concentration per unit of cell volume (chla/vol, fig.L.2.13c) first lowers and remains stable from the moment of the light shift for 6 hours, then it decreases to a minimum at 6.00h.

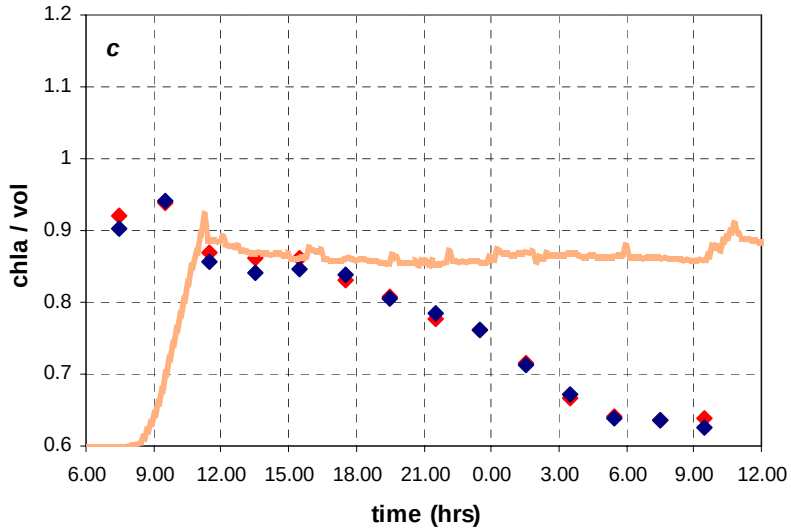

Fig.L. 2.13c: The ratio chlorophyll-*a*/cell volume (chla/vol, µg l^{-1} µm^{-3}), in chemostats C1 (red) and C2 (blue), with time, shifting light from sinusoidal to continuous (orange, from 0 to 110 µE m^{-2} s^{-1}).

3.b.3 Experiment 3: N-starvation in continuous light (8-days measurements)

Photosynthetic parameters by oxygen measurements: α^b lowers (C1) or remains stable (C2) in N-starvation, then recovers one day after N-resupply (fig.L.3.1a).

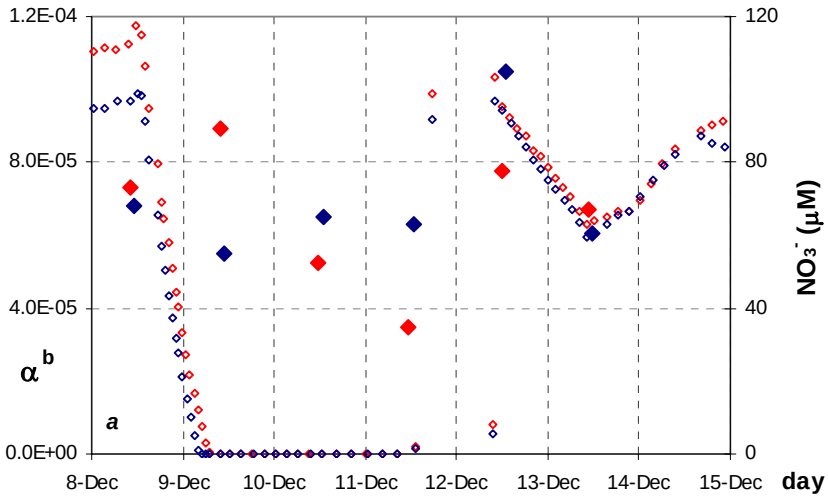

Fig.L.3.3: (a) the light-limited slope α normalized by chlorophyll-*a* (α^b, µmol O_2 (ml min)$^{-1}$ (µmol quanta m^{-2} s^{-1} µg chla l^{-1}) $^{-1}$) by net oxygen evolved measurements (closed symbols), and nitrate concentration (NO_3^-, µM, open symbols), with time, in chemostats C1 (red) and C2 (blue).

Both P^bmax (fig.L.3.1b) and β^b (fig.L.3.1c) decrease with N-starvation, then they recover quickly within one day from N-resupply, and keep on further increasing.

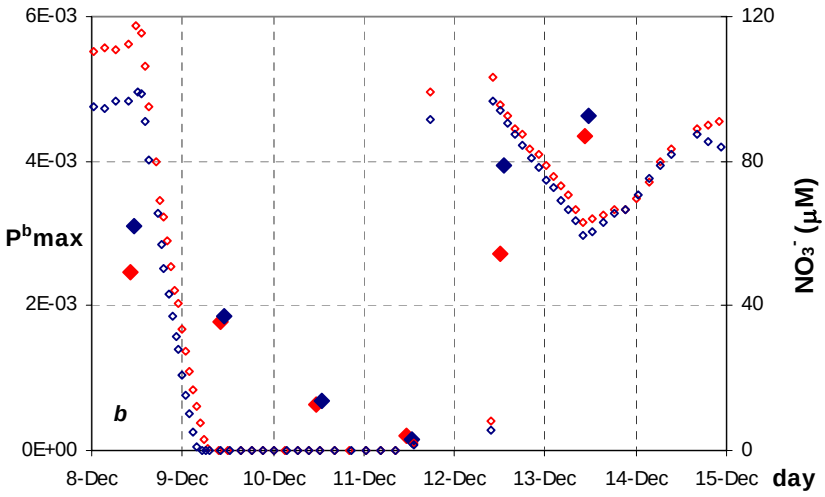

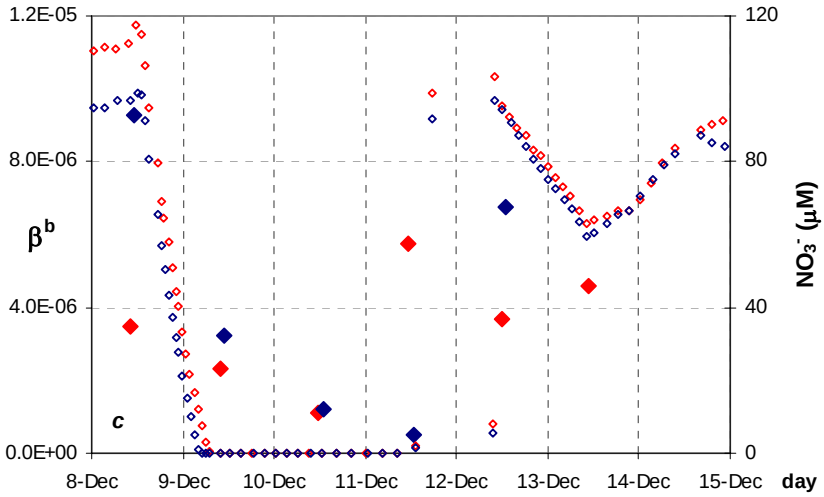

Fig.L.3.4: (b) the light-saturated rates of photosynthesis normalized by chlorophyll-*a* (P^bmax, µmolO_2 µg chla^{-1} s^{-1}), and (c) the photo-inhibited slope β normalized by chlorophyll-*a* (β^b, µmol O_2 (ml min)$^{-1}$ (µmol quanta m^{-2} s^{-1} µg chla l^{-1}) $^{-1}$), by net oxygen evolved measurements (closed symbols), and nitrate concentration (NO_3^-, µM, open symbols), with time, in chemostats C1 (red) and C2 (blue).

Photosynthetic parameters by variable fluorescence (PAM 100, Walz) measurements: the maximum quantum yield of PSII Fv/Fm decreases with N-starvation and recovers completely within two days from N-resupply (fig.L. 3.2a). α_f (the light-limited slope measured by fluorescence) decreases within one day from N-starvation, then it recovers within the following 24 hours (fig.L.3.2b). ETRmax remains stable during the first day of N-starvation, then it lowers (fig.L.3.2c). After N-resupply, both α_f and ETRmax recover to values higher then those of the beginning within two days from N-resupply. On the contrary, β_f increases within two days from N-starvation, then it lowers within two days from N-resupply (fig.L.3.2d).

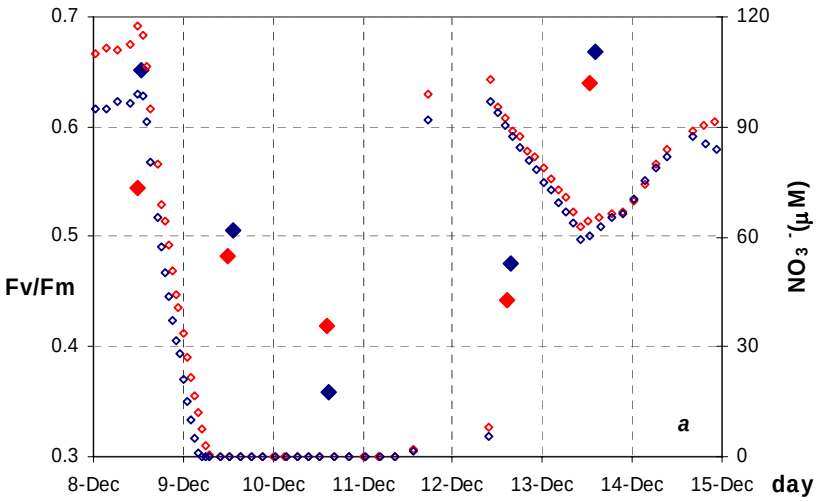

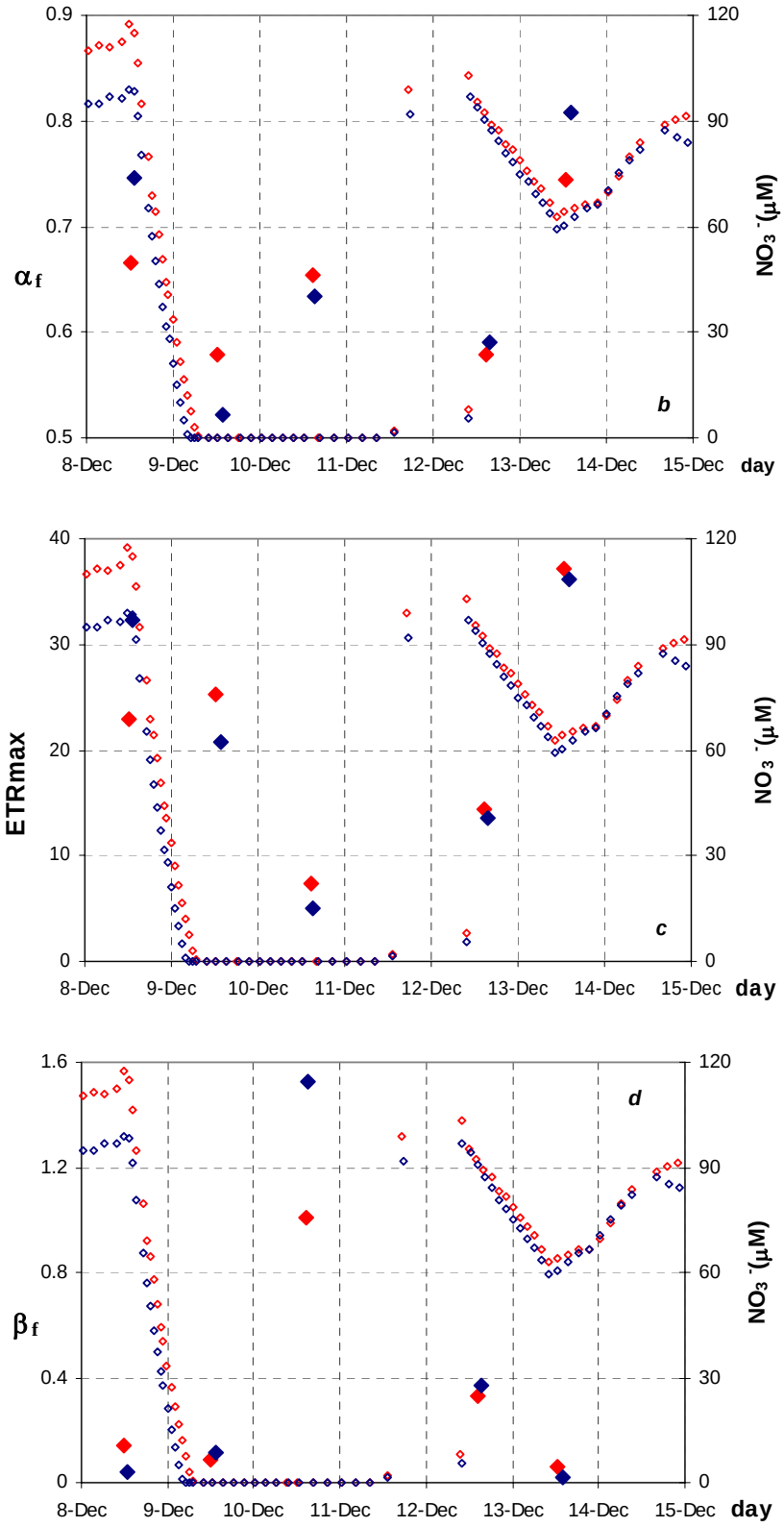

Fig.L.3.2: (a) the maximum quantum yield of PSII Fv/Fm (Fv/Fm = (Fm-Fo)/Fm, (b) the light-limited slope α_f (µmol e^- μE^{-1}), (c) the light-saturated rates of photosynthesis normalized by chlorophyll-*a* (ETRmax, µmol e^- m^{-2} s^{-1}), and (d) the photo-inhibited slope β_f (µmol e^- μE^{-1}), by variable fluorescence measurements (PAM-100, Walz, closed symbols), and nitrate concentration (NO_3^-, µM, open symbols), with time, in chemostats C1 (red) and C2 (blue).

<u>*Cell cycle:*</u> the number of cells decreases with N-starvation and it keeps on decreasing as far as 24 hours after N-supply (5.30h, 12th December), finally it increases back in

both the two chemostats to values which are higher than the starting (fig.L.3.3a). On the contrary, cell volume increases with N-starvation and decreases soon after N-resupply (4 hours later, fig.L.3.3b). So, cells are fewer but bigger when N-starved. Both cells number and size recover much quicker (= sharper slopes) than they decreased / increased.

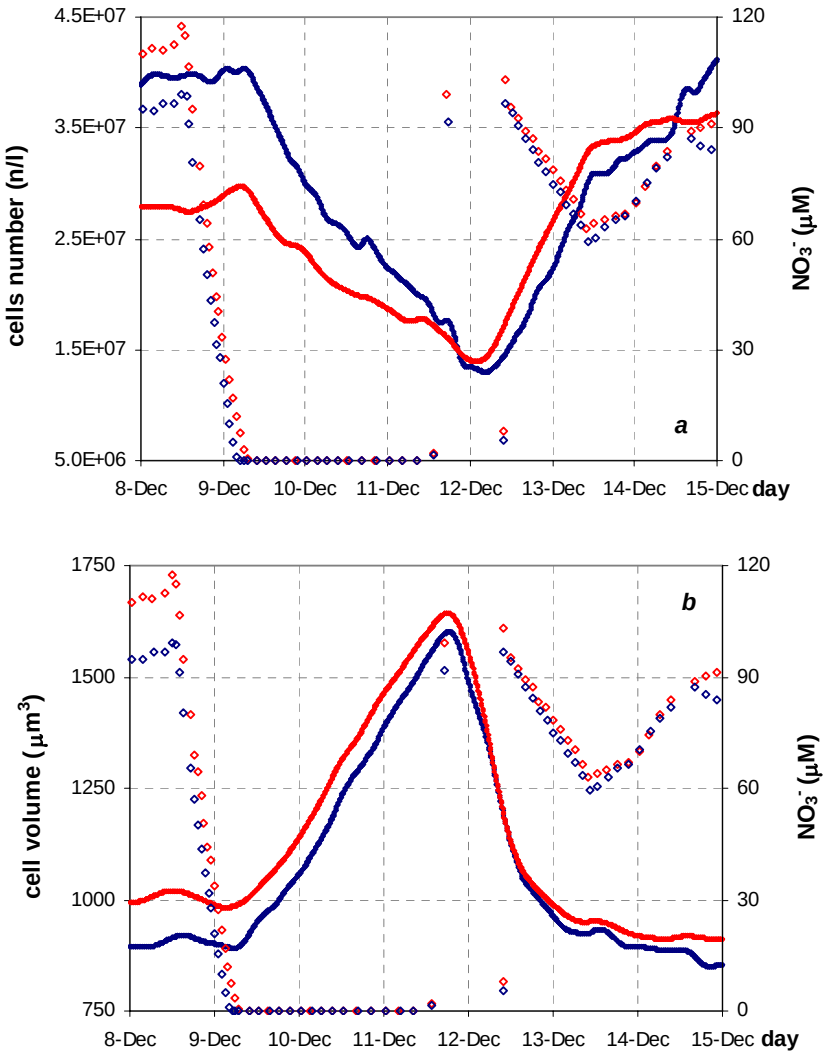

Fig.L.3.3: (a) cell number (n/l) and (b) cell volume (μm^3, closed symbols), and nitrate concentration (NO_3^-, µM, open symbols), with time, in chemostats C1 (red) and C2 (blue).

Organic carbon and nitrogen: the ratio C/N increases after N-starvation, because C content increases while N lowers (fig.L.3.4a). In both chemostats, C-content has not yet increased 21 hours after the beginning of N-starvation (10.00h, 9th December, fig.L.3.4b), then in C1 chemostat it recovers to this value < 1 day after N-resupply (10.00h, 12th December), while in C2 chemostat it recovers completely only on the last day of measurements. Cellular N-content decreases to the minimum value of 1 mg/l 24

hours after the beginning of the N-starvation, while both chemostats start recovering soon after the N-resupply (within the first day, fig.L.3.4c).

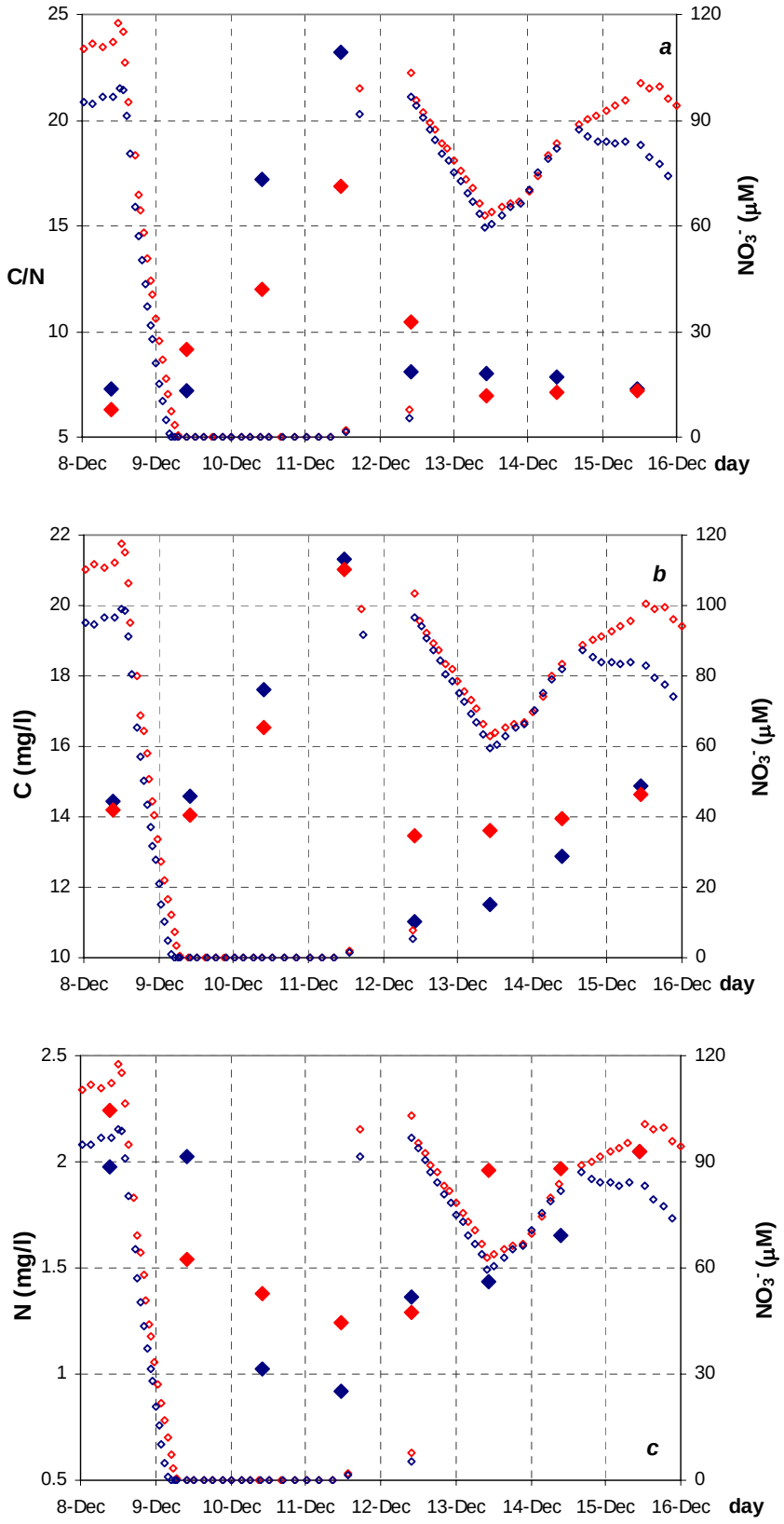

Fig.L.3.4: (a) C/N ratio, (b) C content (mg/l) and (c) N content (mg/l, closed symbols), and nitrate concentration (NO_3^-, µM, open symbols), with time, in chemostats C1 (red) and C2 (blue).

Inorganic carbon: DIC is constant for the first 48 hours after the N-starvation, then it increases to a 80% higher value on the day of N-supply (fig.L.3.5). Chemostat C1 recovers in three days, C2 in four.

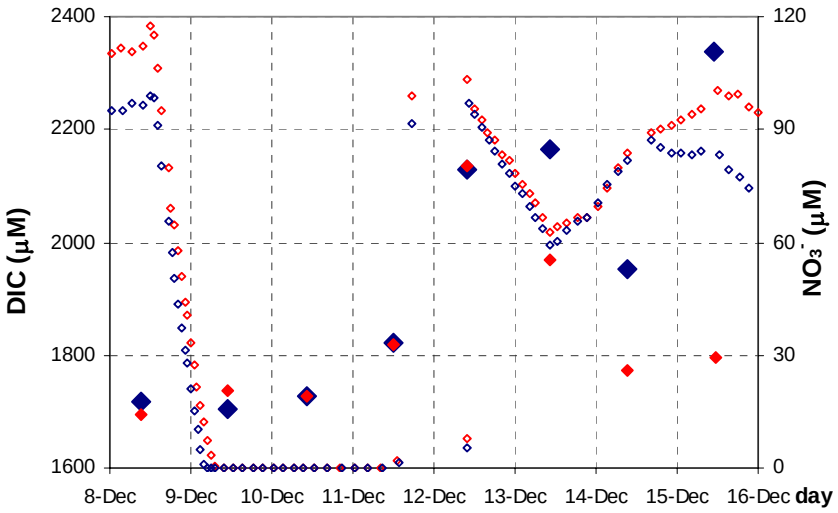

Fig.L. 3.5: Inorganic carbon (DIC, µM, closed symbols), and nitrate concentration (NO_3^-, µM, open symbols), with time, in chemostats C1 (red) and C2 (blue).

Pigments: N-starvation lowers chlorophyll-a (chla), chlorophyll-c, fucoxanthin, β-carotene and violaxanthin concentrations (figs.3.6a,b,c,d and e). They all decrease after the first day of N-starvation, then they all recover within the next day from N-supply.

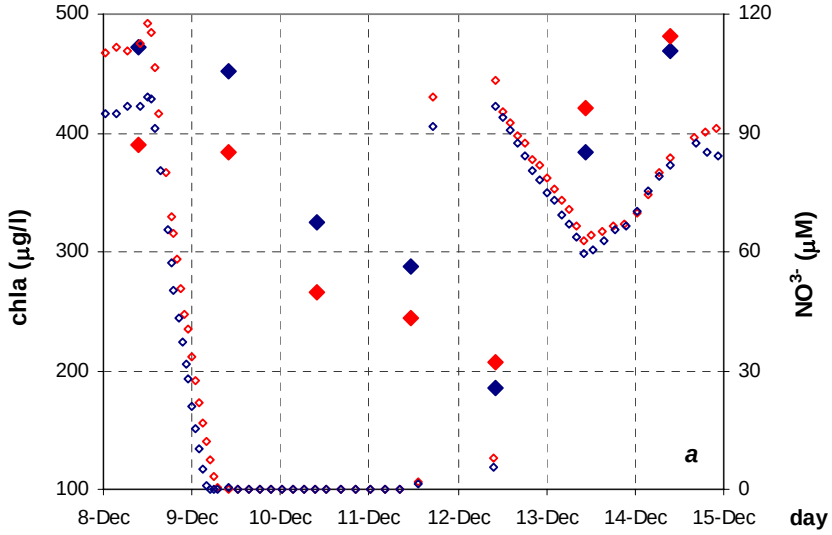

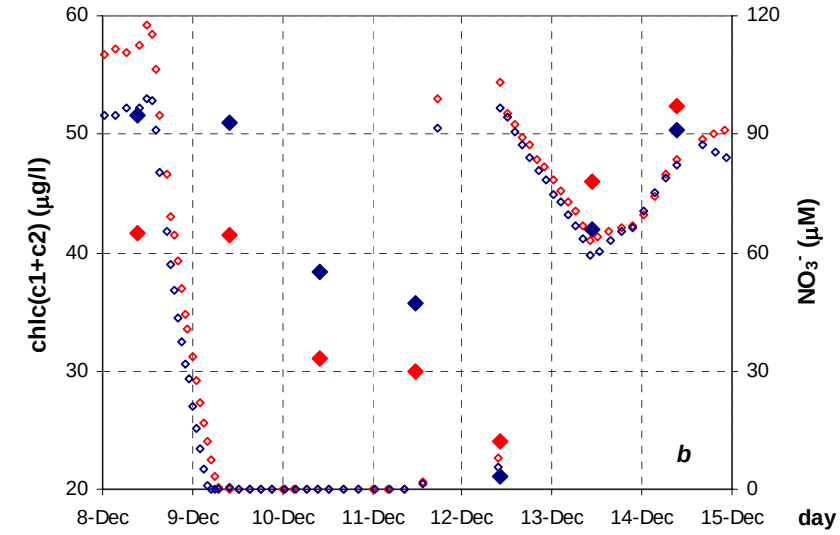
chlc(c1+c2) (µg/l)
60
50
40
30
20
120
90
60
30
0
NO3- (µM)
b
8-Dec
9-Dec
10-Dec
11-Dec
12-Dec
13-Dec
14-Dec
15-Dec
day

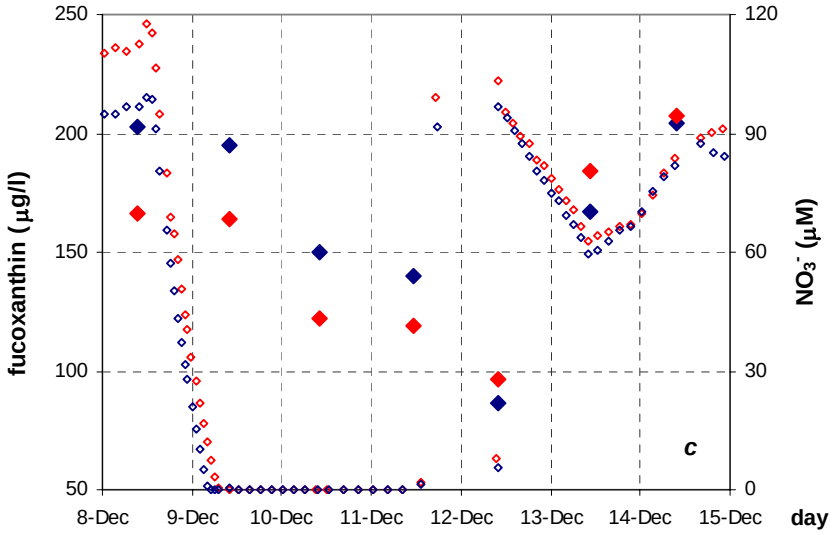
fucoxanthin (µg/l)
250
200
150
100
50
120
90
60
30
0
NO3- (µM)
c
8-Dec
9-Dec
10-Dec
11-Dec
12-Dec
13-Dec
14-Dec
15-Dec
day

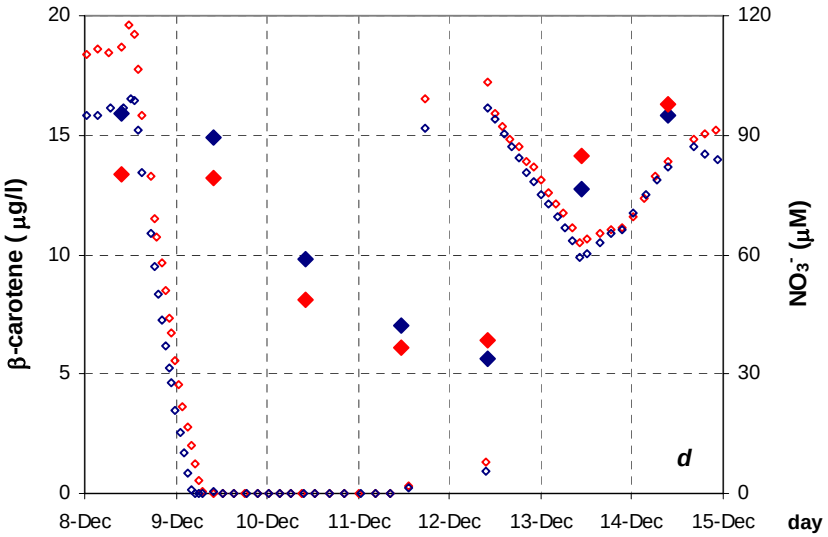
β-carotene (µg/l)
20
15
10
5
0
120
90
60
30
0
NO3- (µM)
d
8-Dec
9-Dec
10-Dec
11-Dec
12-Dec
13-Dec
14-Dec
15-Dec
day

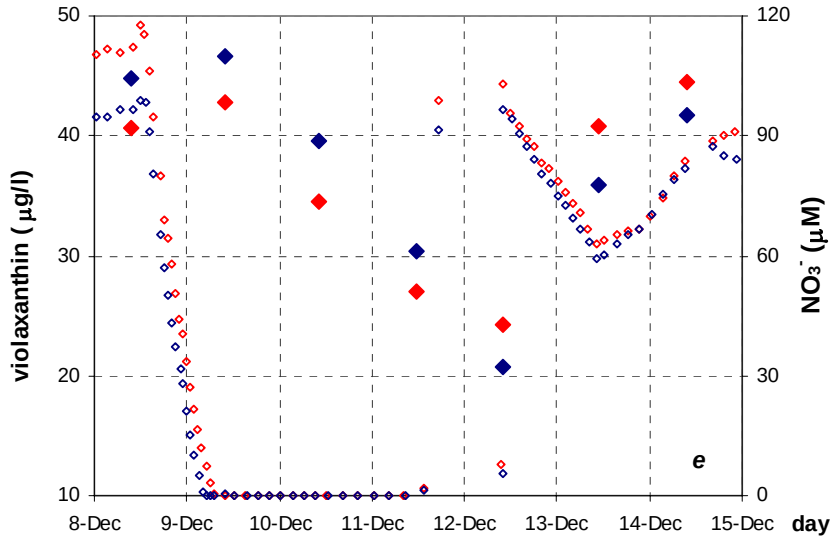

Fig.L.3.6: (a) Chlorophyll-*a* (chla), (b) chlorophyll-*c1* + chlorophyll-*c2* (chlc(c1+c2)), (c) fucoxanthin , (d) β-carotene, and (and) violaxanthin (µg/l, closed symbols), and nitrate concentration (NO_3^-, µM, open symbols), with time, in chemostats C1 (red) and C2 (blue).

N-starvation increases the ratios between chlorophyll-*c*, fucoxanthin and violaxanthin, and chlorophyll-*a* (figs.L.3.7a,b and d), in contrast the ratio β-carot/chla decreases (fig.L.3.7c).

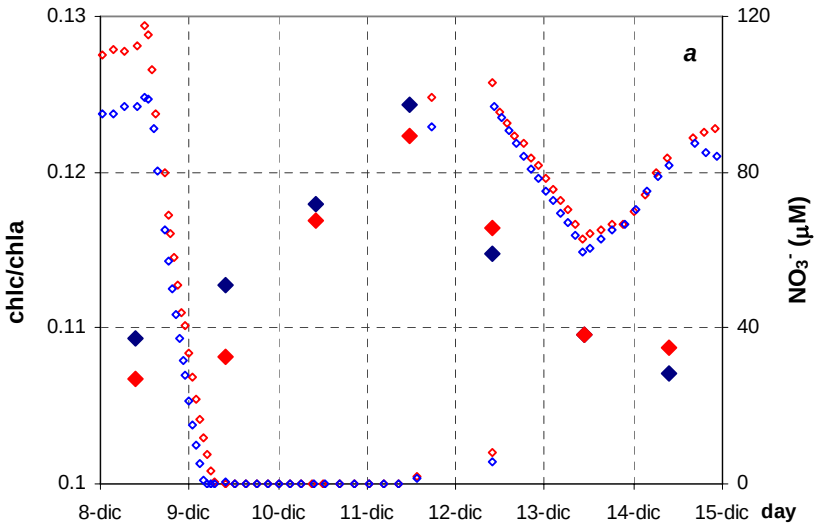

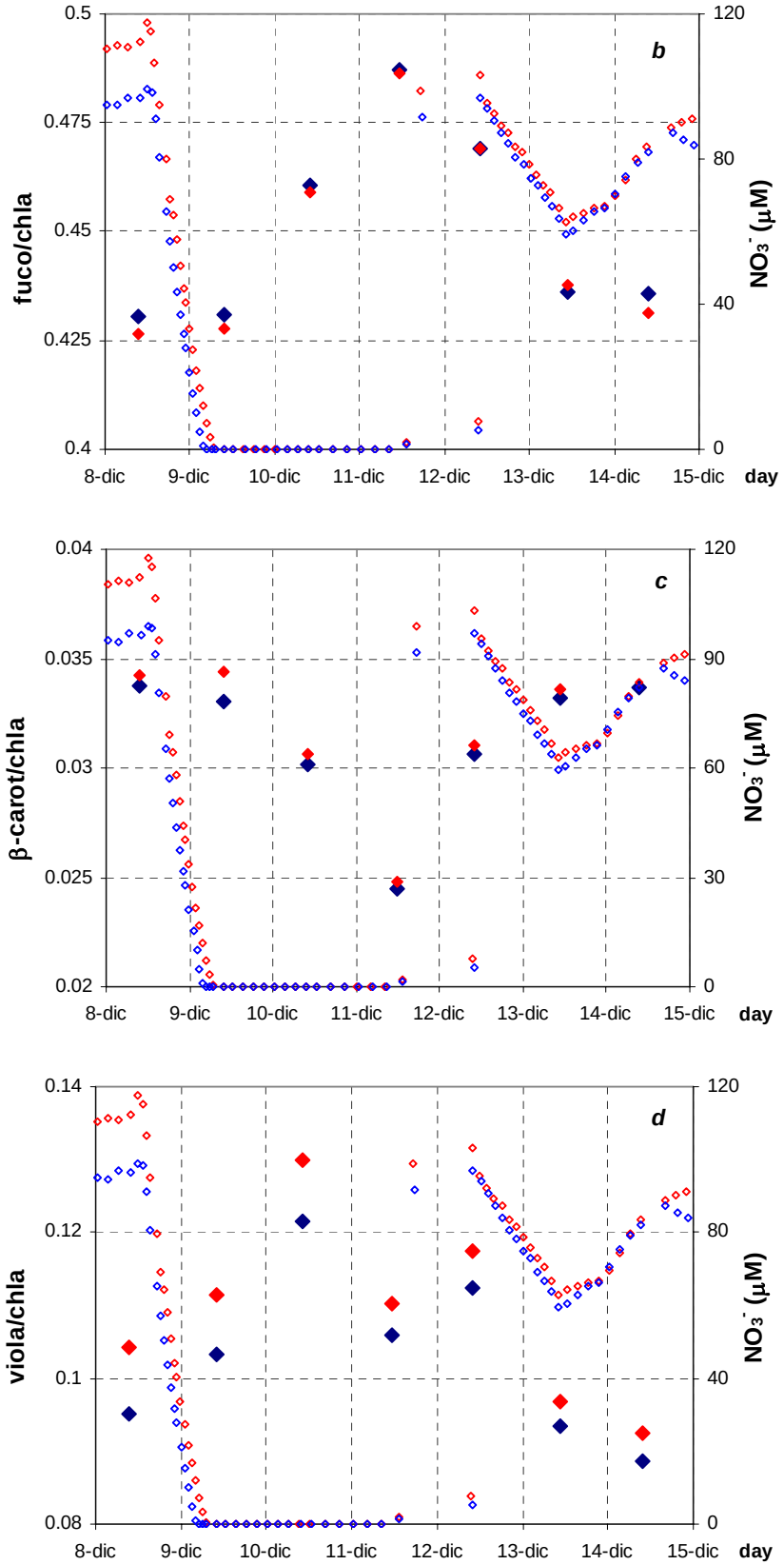

Fig.L.3.7: The ratios (a) chlorophyll-*c*/chlorophyll-*a* (chlc/chla), (b) fucoxanthin/chlorophyll-*a* (fuco/chla), (c) β-carotene/chlorophyll-*a* (β-carot/chla), and (d) violaxanthin/chlorophyll-*a* (viola/chla, closed symbols), and nitrate concentration (NO_3^-, µM, open symbols), with time, in chemostats C1 (red) and C2 (blue).

Antheraxanthin and zeaxanthin concentrations remain constant for the first two days after N-starvation, then they increase to more than twice their values a few hours before the re-supply, finally they quickly recover back within 1 day from the re-supply (figs.3.8a and b). Then the ratios antheraxanthin/chla and zeaxanthin/chla slowly increase from the N-starvation to a maximum just before the re-supply and they soon recover within one day from it.

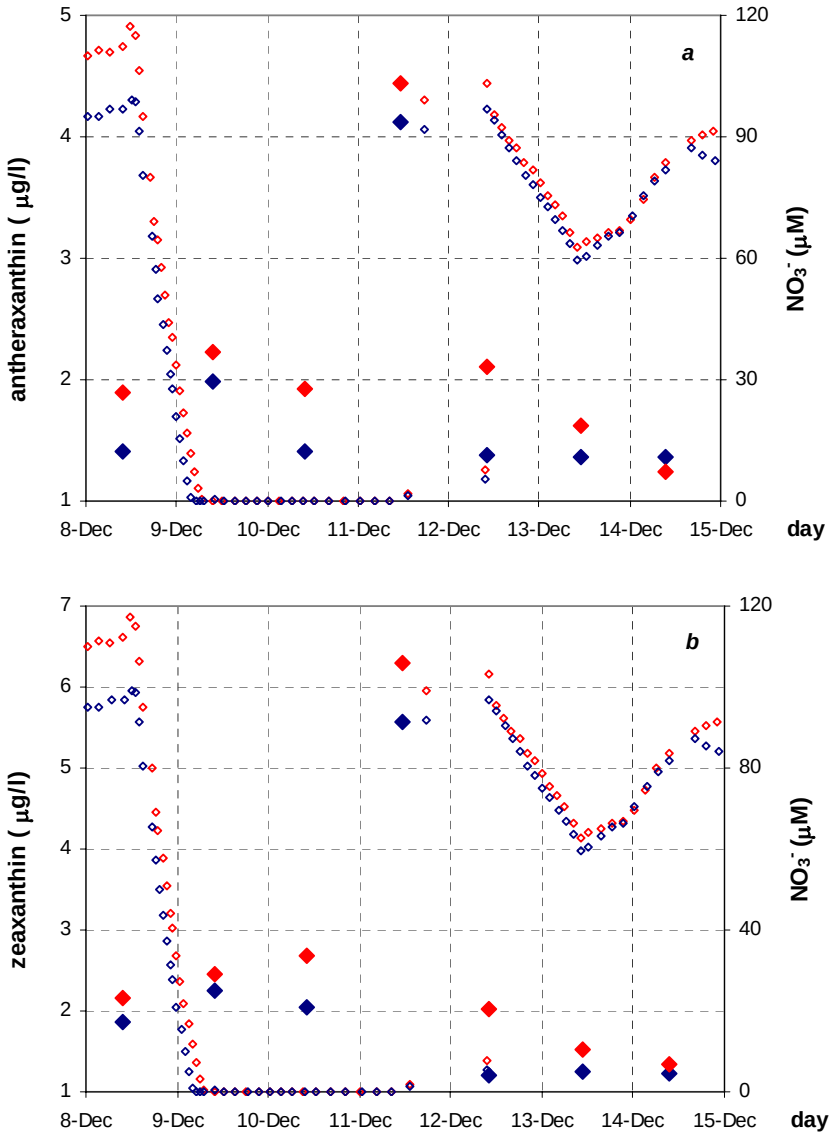

Fig.L.3.8: (a) antheraxanthin, and (b) zeaxanthin (µg/l, closed symbols), and nitrate concentration (NO_3^-, µM, open symbols), with time, in chemostats C1 (red) and C2 (blue).

As C-content and chla concentration, the ratio C/chla increases after one day from N-starvation and decreases back within one day from the re-supply (fig.L.3.9a).

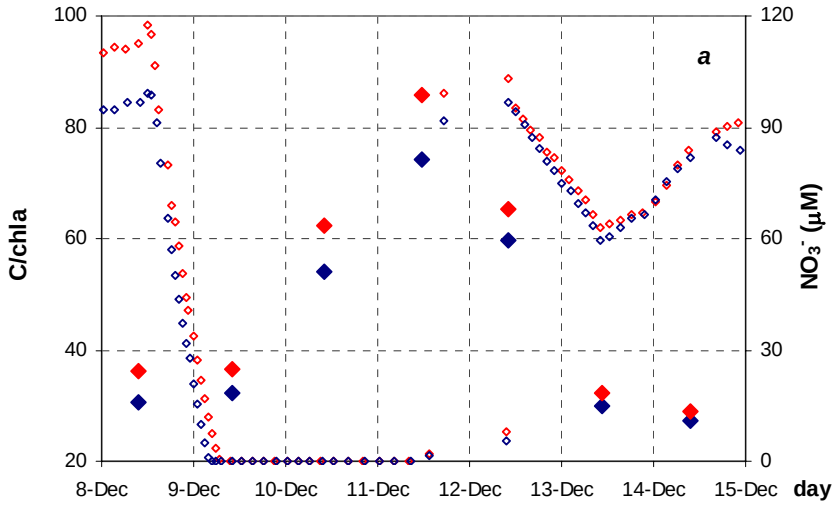

Fig.L.3.9: (a) The ratio C-content/chlorophyll-*a* (C/chla closed symbols), and nitrate concentration (NO_3^-, µM, open symbols), with time, in chemostats C1 (red) and C2 (blue).

Chlorophyll-*a* concentration per cell (chla/cell) increases a few hours before N-starvation, it decreases the following day, finally it recovers back within 2 days from the re-supply (fig.L.3.9b).

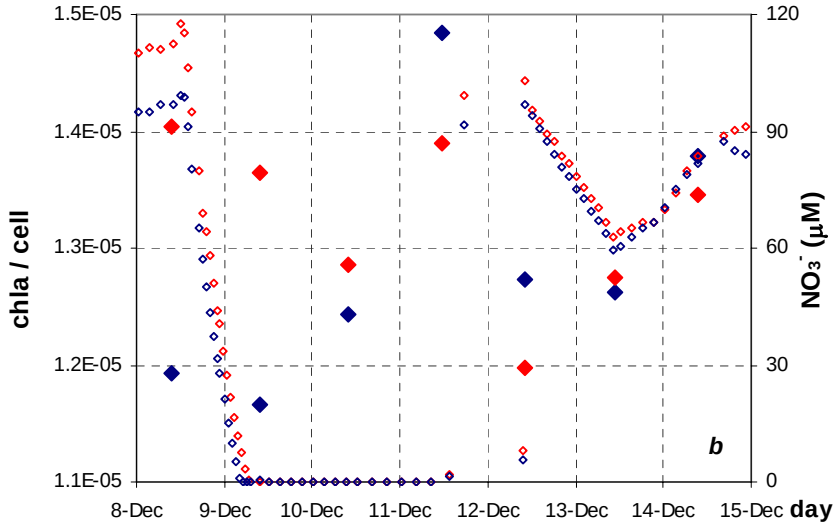

Fig.L.3.9: (b) The ratio chlorophyll-*a*/number of cells (chla/cell, µg $cell^{-1}$ closed symbols), and nitrate concentration (NO_3^-, µM, open symbols), with time, in chemostats C1 (red) and C2 (blue).

Chlorophyll-*a* concentration per unit of cell volume (chla/vol) decreases after the first day of N-starvation and needs two days more to recover when N is re-supplied (fig.L.3.9c).

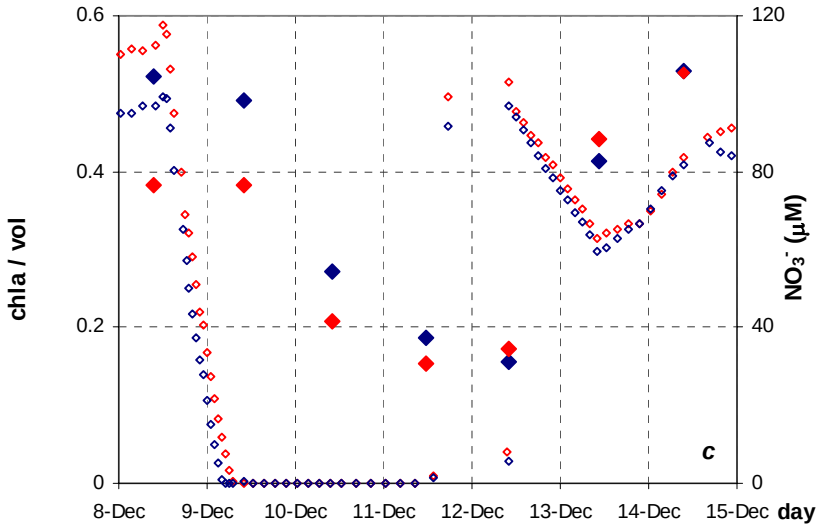

Fig.L.3.9: (c) The ratio chlorophyll-*a* / cell volume (chla/cell, µg chla µm^{-3}, closed symbols), and nitrate concentration (NO_3^-, µM, open symbols), with time, in chemostats C1 (red) and C2 (blue).

3.b.4 Experiment 4: sinusoidal light (3 days measurements)

Photosynthetic parameters by oxygen measurements: both α^b and $P^b max$ show diel changes. α^b has a maximum at midday or within 2 hours from it (16.00-18.00h) and a midnight minimum (1.8-fold lower, 4.00-5.00h, fig.L.4.1a). $P^b max$ shows maximums before midday (12.00-14.00h) and minimums before sunset (18.00-19.00h, 2.1 and 3.9-fold lower in C1 and C2 chemostats respectively, fig.L.4.1b). That means that it decreases sharply during the day and increases slowly during the night, and shows a slow down at around midnight. On the contrary, β^b doesn't show any diel periodicity (fig.L.4.1c).

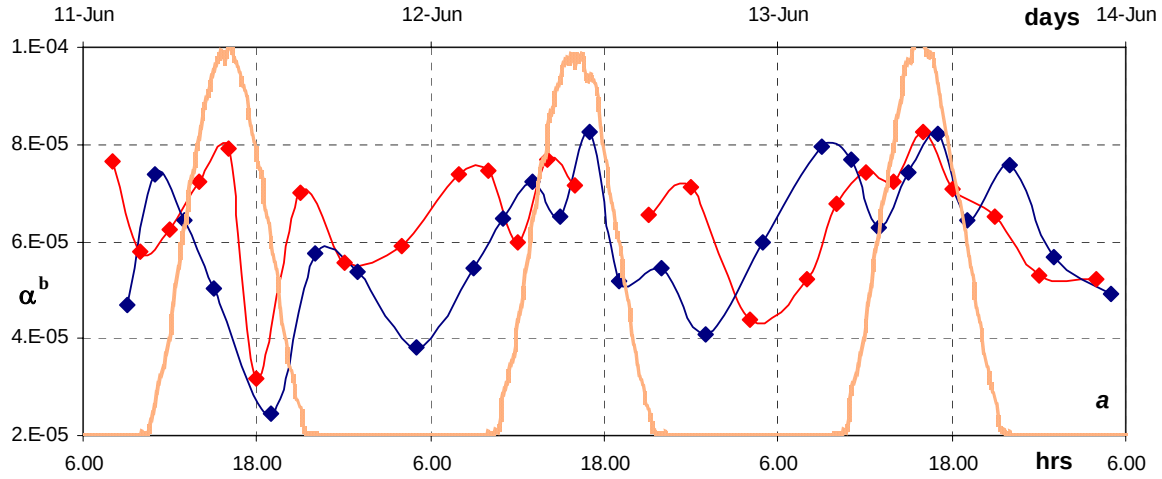

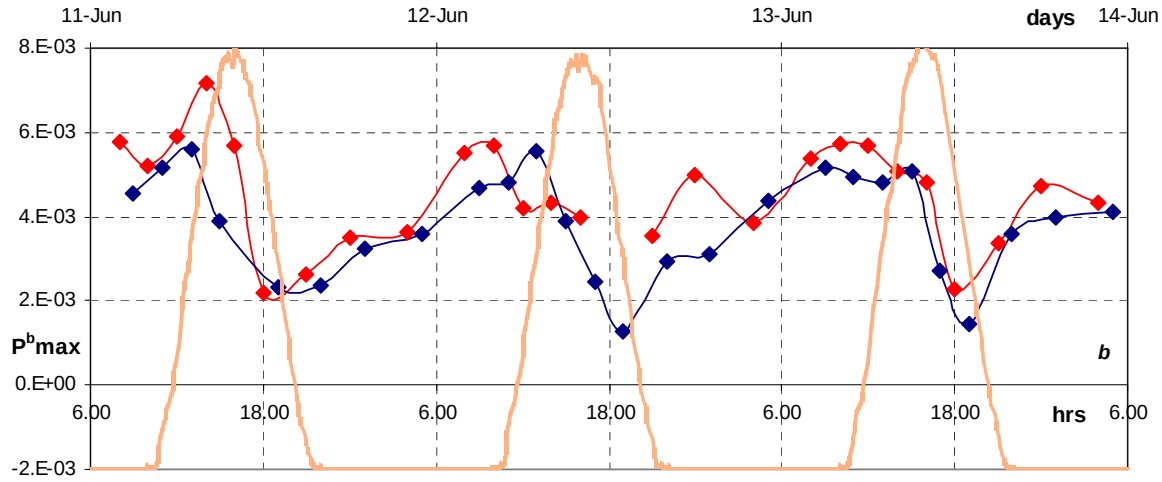

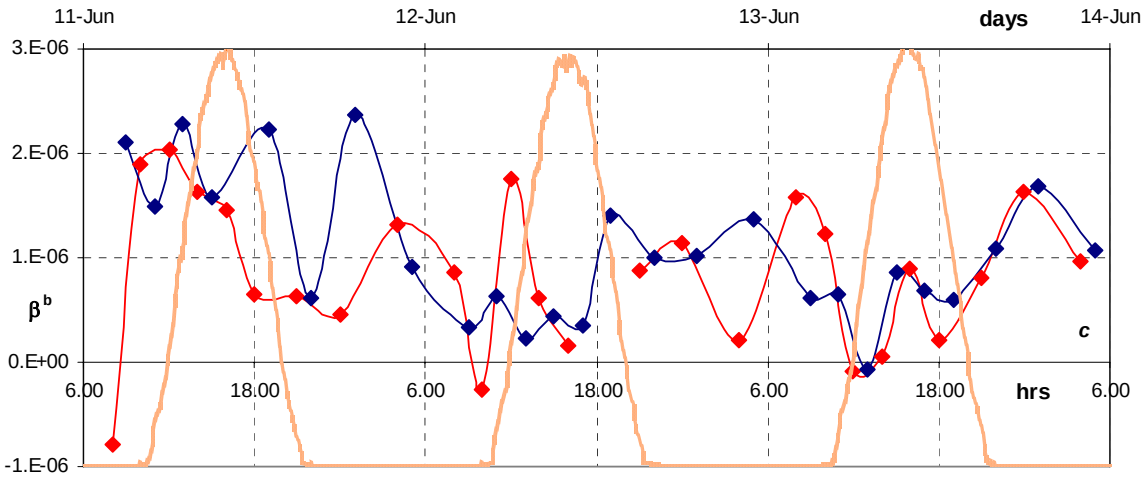

Fig.L.4.1: (a) the light-limited slope α normalized by chlorophyll-*a* (α^b, µmol O_2 (ml min)$^{-1}$ (µmol quanta m^{-2} s^{-1} µg chla l^{-1}) $^{-1}$), (b) the light-saturated rates of photosynthesis normalized by chlorophyll-*a* (P^bmax, µmolO_2 µg chla^{-1} s^{-1}), and (c) the photo-inhibited slope β normalized by chlorophyll-*a* (β^b, µmol O_2 (ml min)$^{-1}$ (µmol quanta m^{-2} s^{-1} µg chla l^{-1}) $^{-1}$), by net oxygen evolved measurements, in chemostats C1 (red) and C2 (blue), with time, in sinusoidal light (orange, from 0 to 300 µE m^{-2} s^{-1}).

Figs.4.2 clearly show photosynthetic parameters diel variations, from 6.30h on the 12th to 4.30h on the 14th of June: α^b, P^bmax, β^b and Ek values are the average between the two chemostats (C1 at time t and C2 at time t+2h), after the calculation by linear interpolation of every-2-hours values on each chemostat. α^b is maximum at 16.30h (midday) and shows a clear oscillation around its maximum, with two higher minimums at 12.30h and 18.30h and two lower maximums at 10.30h and 20.30h, while it's minimum at 4:30h (midnight, fig.L.4.2a). P^bmax has maximums at 10.30h (dawn) and minimums at 18.30h (before sunset, fig.L.4.2b). That means that Ek is maximum at 8.30h (before dawn) and minimum at 18.30h (before sunset, 3.5-fold lower, fig.L.4.2c).

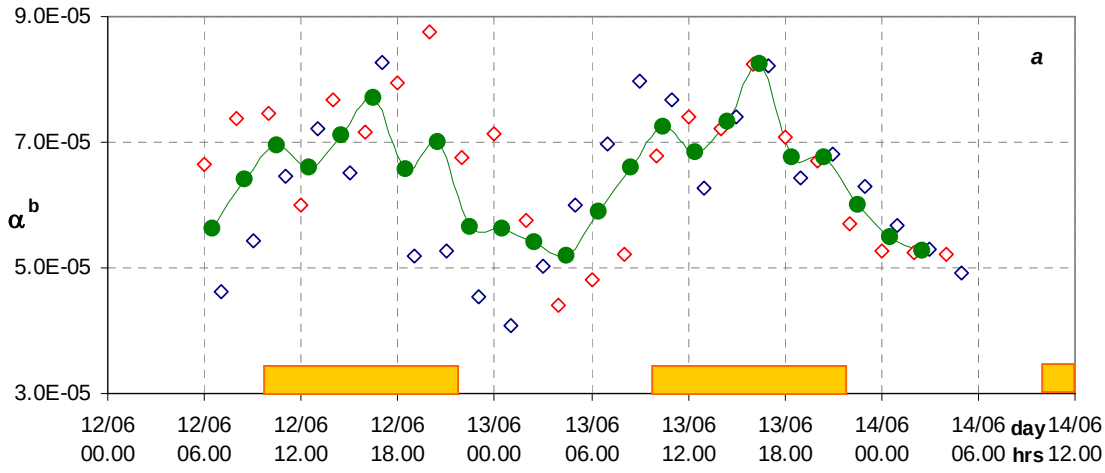

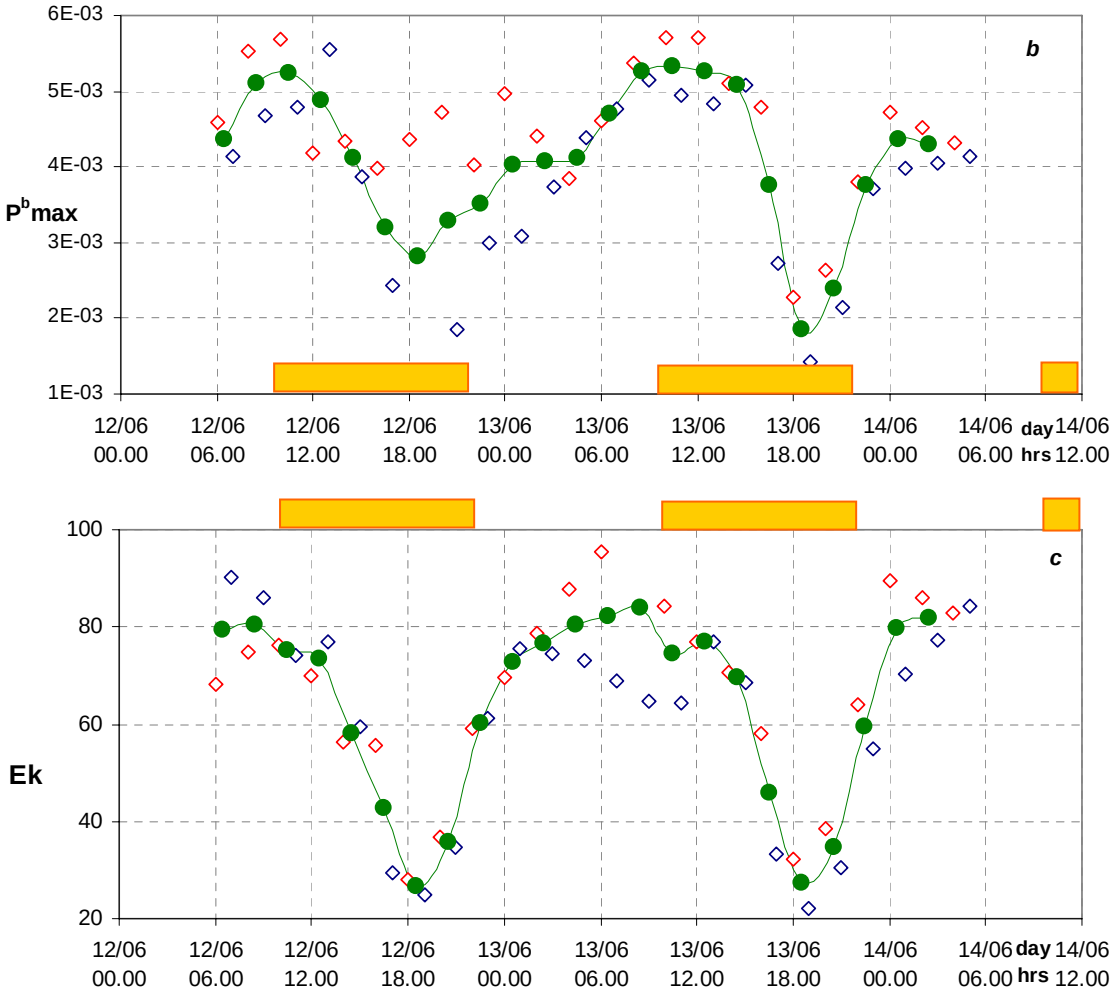

Fig.L.4.2: (a) the light-limited slope α normalized by chlorophyll-*a* (α^b, µmol O_2 (ml min)$^{-1}$ (µmol quanta m^{-2} s^{-1} µg chla l^{-1}) $^{-1}$), (b) the light-saturated rates of photosynthesis normalized by chlorophyll-*a* (P^bmax, µmolO_2 µg chla^{-1} s^{-1}), and (c) the the light-saturation index Ek=P^bmax/α^b (in µE $m^{-2}s^{-1}$), by net oxygen evolved measurements, in chemostats C1 (red) and C2 (blue), with time, in sinusoidal light (orange, from 0 to 300 µE m^{-2} s^{-1}). In green, the average between the two chemostats. The yellow bars indicate the light periods.

Then α^b and P^bmax covary from 2:30h to 12.30h (R^2=0.92, n=12, fig.L.4.3a), while the two parameters do not covary from mid-morning to midnight: from 18.30h to 20.30h P^bmax varies while α^b is almost constant (fig.L.4.3b), after midday (14.30-16.30h) and after sunset (22.30h-0.30h) α^b varies more than P^bmax (fig.L.4.3c). In fact Ek is constant only from midnight to mid-morning (Ek-independent variability): it decreases first, due to α^b variations, and increases then, first mainly due to P^bmax rather than to α^b (see fig.L.4.2c). Then, like in experiment 1, PE parameters have a three-phases pattern of variability: one phase of Ek-independence during the night until after-dawn, followed by two phases of Ek-dependence (= photoacclimation).

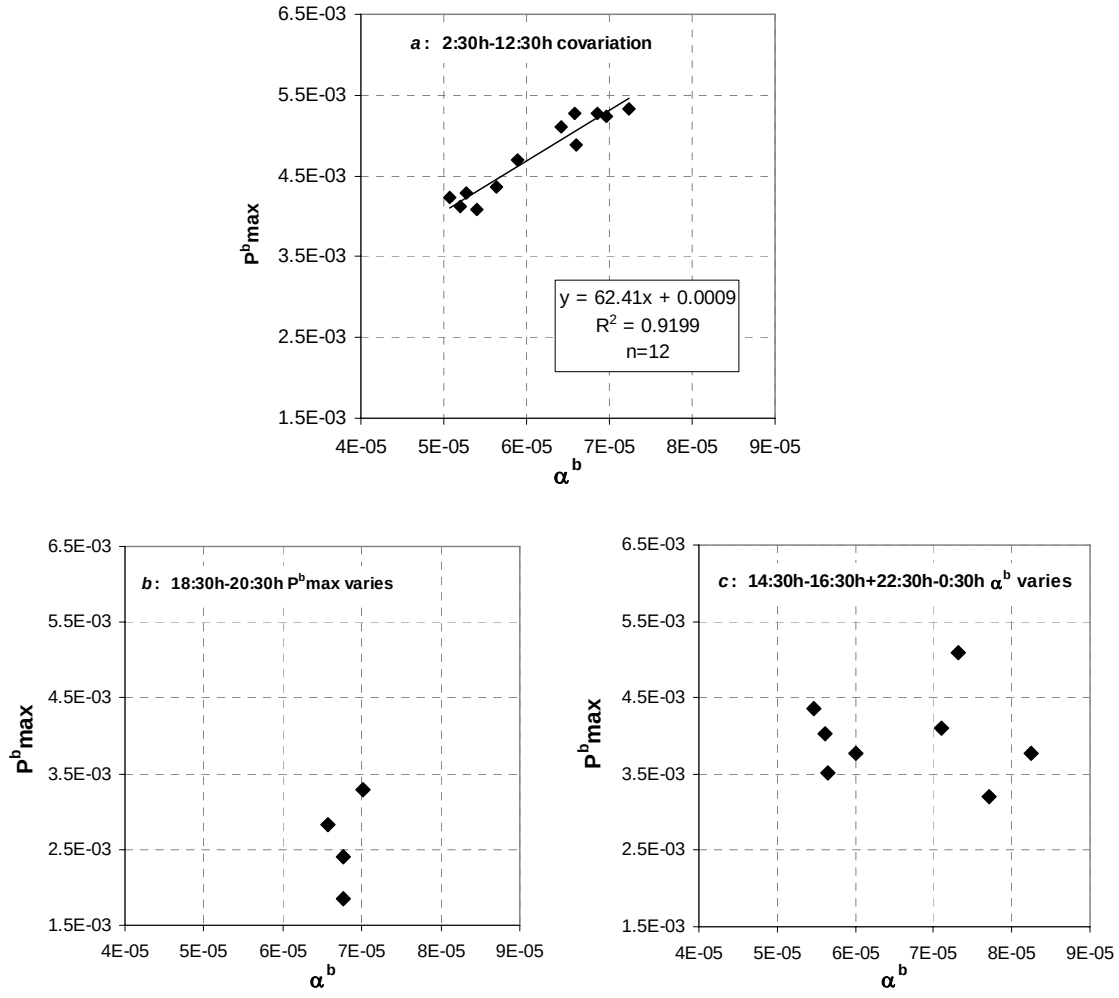

Fig.L.4.3: three-phases variation of α^b and P^bmax in both chemostats in sinusoidal light: (a) covariation from 2.30h to 12.30h, (b) after midday (18.30h-20.30h) P^bmax varies more than α^b, (c) before midday and after sunset α^b varies more than P^bmax, by net oxygen evolved measurements, in chemostats C1 (red) and C2 (blue).

Cell cycle: the number of cells is maximum at mid-morning (12.00-13.00h) and decreases during the day as far as the minimum before midnight (1.8-fold lower, between 1.00 and 2.30h, fig.L.4.4a). On the contrary, cell volume is minimum around dawn (11.00h) and increases to the maximum at sunset (2.1-fold higher, 20.30-21h, fig.L.4.4b). These results confirm experiment 1 results: at dawn all cell divisions are done, while cell volume increases during the day and cells are ready to divide again at sunset. Before midnight (around 0.00-4.00h) the slope of the cell volume pattern becomes slighter and cells number is minimum and constant.

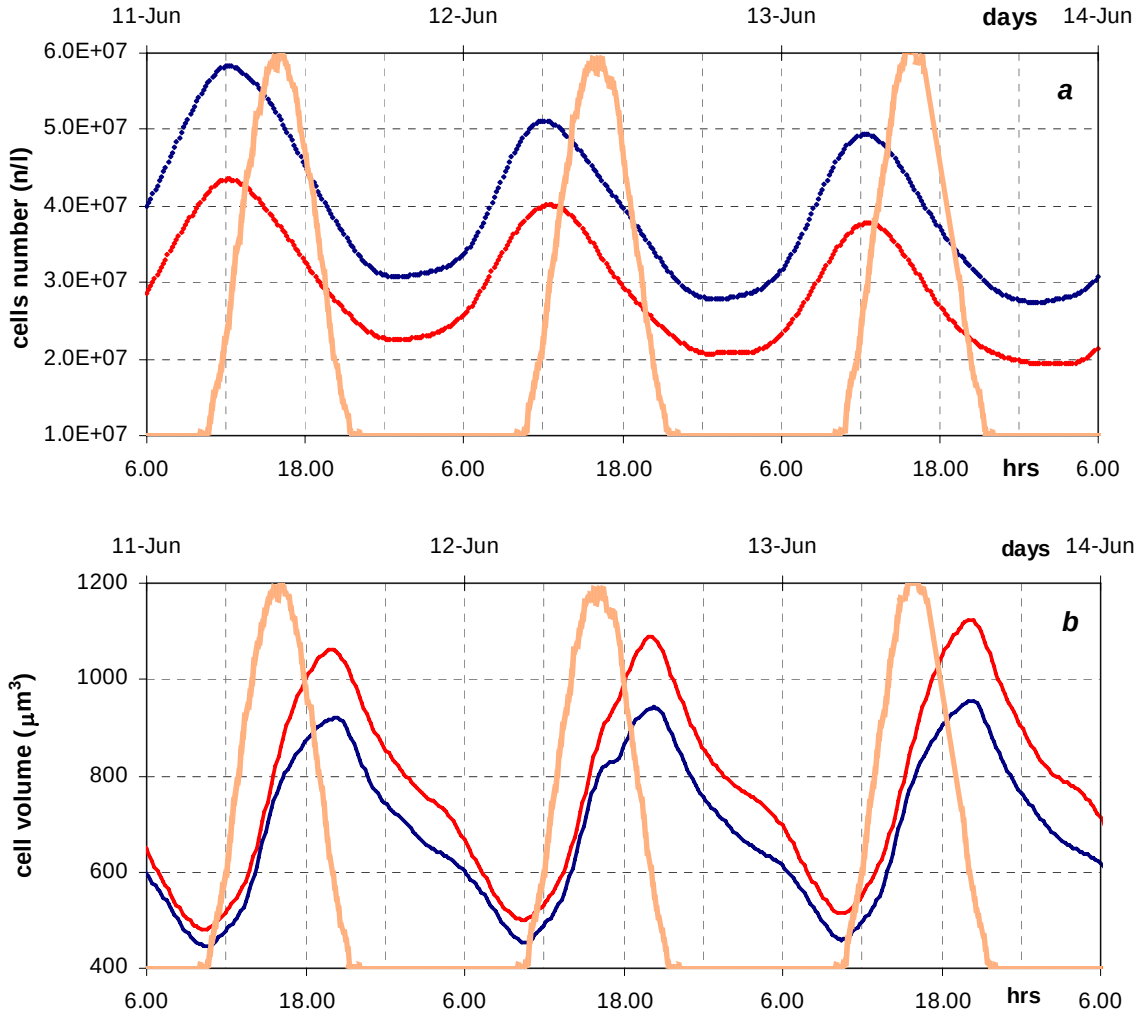

Fig.L.4.4: (a) cells number (n/l) and (b) cell volume (μm^3), in chemostats C1 (red) and C2 (blue), with time, in sinusoidal light (orange, from 0 to 300 $\mu E\ m^{-2}\ s^{-1}$).

Organic carbon and nitrogen: the ratio C/N has its minimum at mid-morning (12.00h) and it increases during the day to its after sunset maximum (1.4-fold higher, 21.00-0.00h, fig.L.4.5a). C follows the same pattern as C/N ratio (minimum 2 hours after dawn, maximum 1 hour after sunset, 1.6-fold higher, fig.L.4.5b), while N has its minimum at dawn (8.30-10.00h) and its maximum after midday (1.2-fold higher, 16.00-18.00h, fig.L.4.5c).

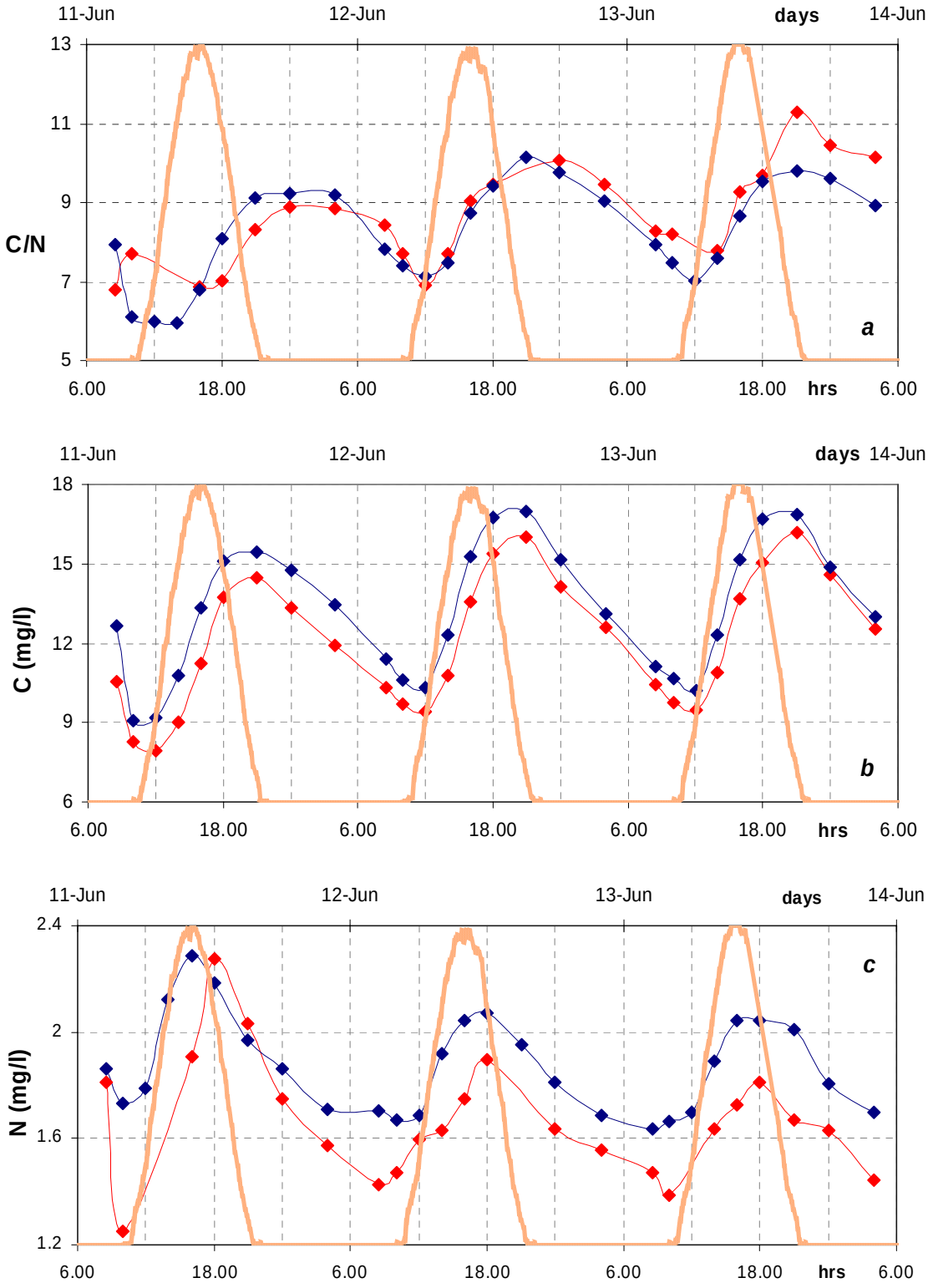

Fig.L.4.5: (a) C/N ratio, (b) C content (mg/l) and (c) N content (mg/l) in chemostats C1 (red) and C2 (blue), with time, in sinusoidal light (orange, from 0 to 300 µE m^{-2} s^{-1}).

Inorganic carbon and nitrogen: DIC is maximum at dawn (10.00h), minimum after midday (1.3-fold lower, 18.00h), due to C-assimilation by photosynthesis, then it increases back during the dark period (fig.L.4.6a). Inorganic nitrogen content (NO_3^- + NO_2^-) is minimum after midday (17.00-19.00h) and maximum at dawn (10.00-11.00h, 1.7-fold higher, fig.L.4.6b).

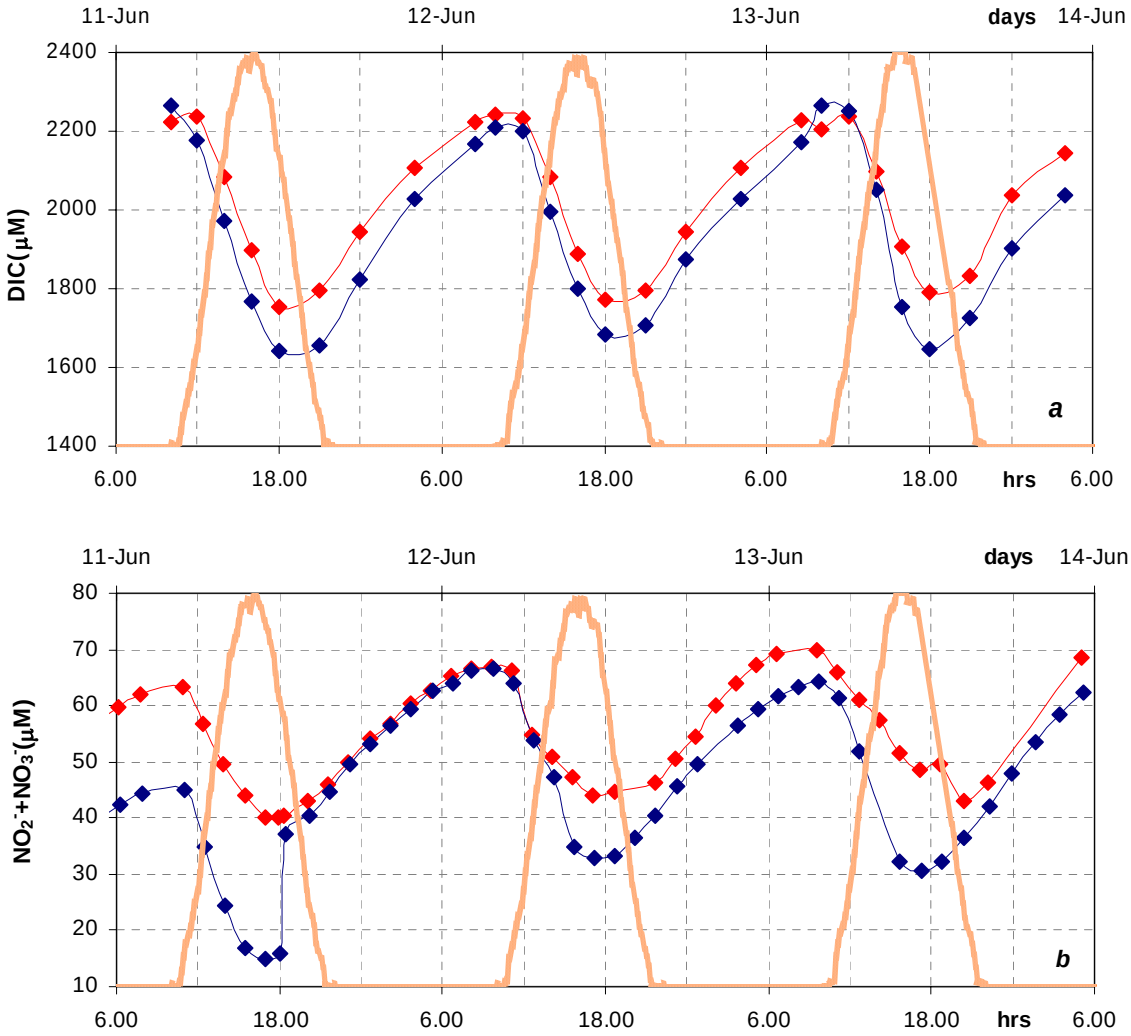

Fig.L.4.6: (a) Inorganic carbon (DIC, µM), and (b) nitrogen (NO_2^-+NO_3^-, µM), in chemostats C1 (red) and C2 (blue), with time, in sinusoidal light (orange, from 0 to 300 µE m^{-2} s^{-1}).

Pigments: chlorophyll-*a* (chla) and fucoxanthin variations confirm experiment 1 results: they vary from a minimum at dawn (10.00h) to a maximum at sunset (22.00, 1.2 and 1.3-fold higher respectively, fig.L.4.7a,c). Chlorophyll-*c* (c1+c2) period is 2 hours later shifted: chlc varies from a minimum at mid-morning (12.00h) to a maximum before midnight (0.00h, 1.3-fold higher, fig.L.4.7b).

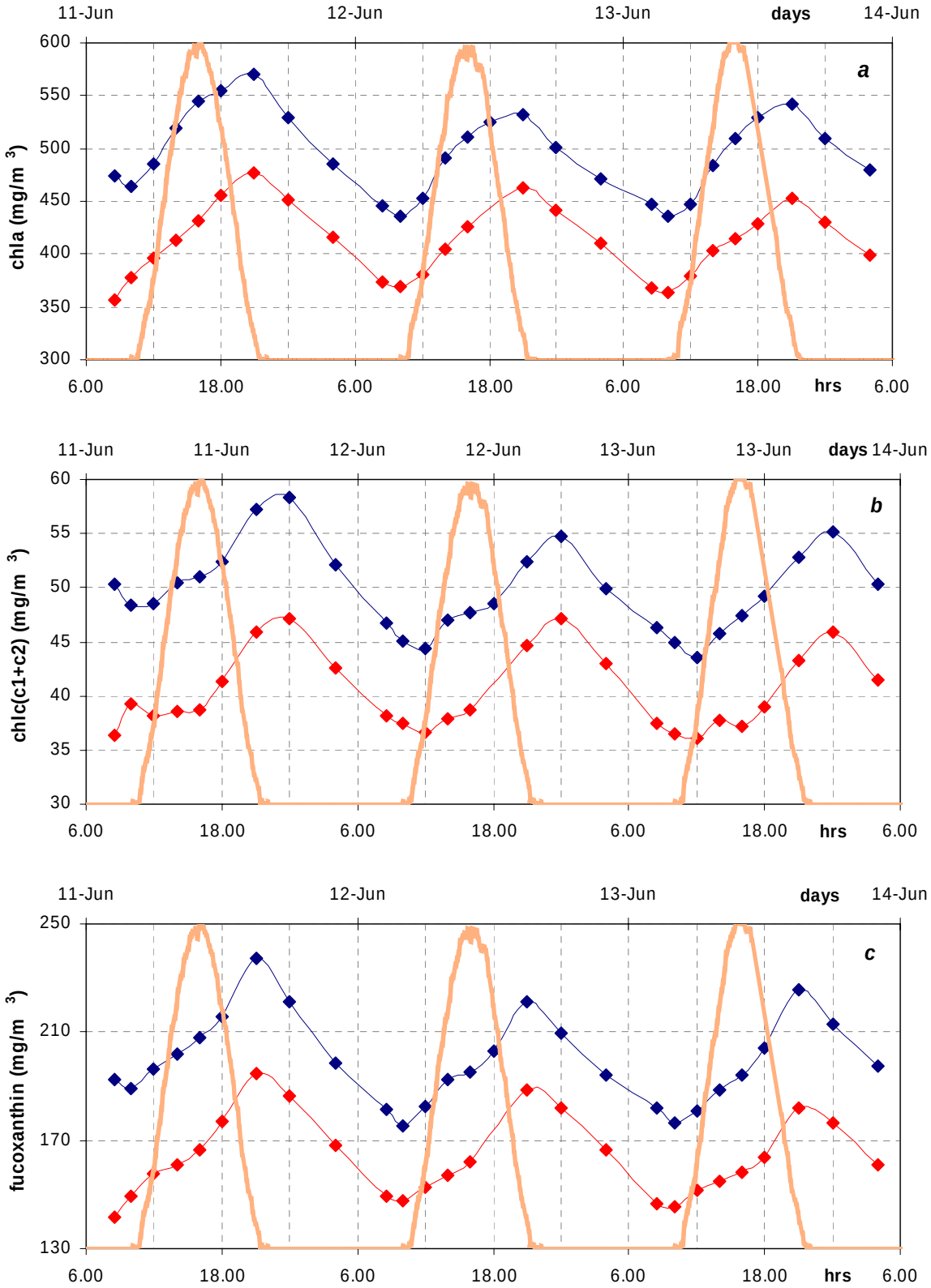

Fig.L.4.7: (a) Chlorophyll-*a* (chla, mg/m^3), (b) chlorophyll-*c1* + chlorophyll-*c2* (chlc(c1+c2), mg/m^3), and (c) fucoxanthin (mg/m^3) concentration, in chemostats C1 (red) and C2 (blue), with time, in sinusoidal light (orange, from 0 to 300 µE m^{-2} s^{-1}).

Both the ratios chlorophyll-c/chla and fucoxanthin/chla have a minimum at midday (16.00h) and a maximum after sunset (0.00h, 1.1 and 1.2-fold higher, fig.L.4.8a and b). Moreover, the patterns show a lower slope from 4.00h to 8.30h.

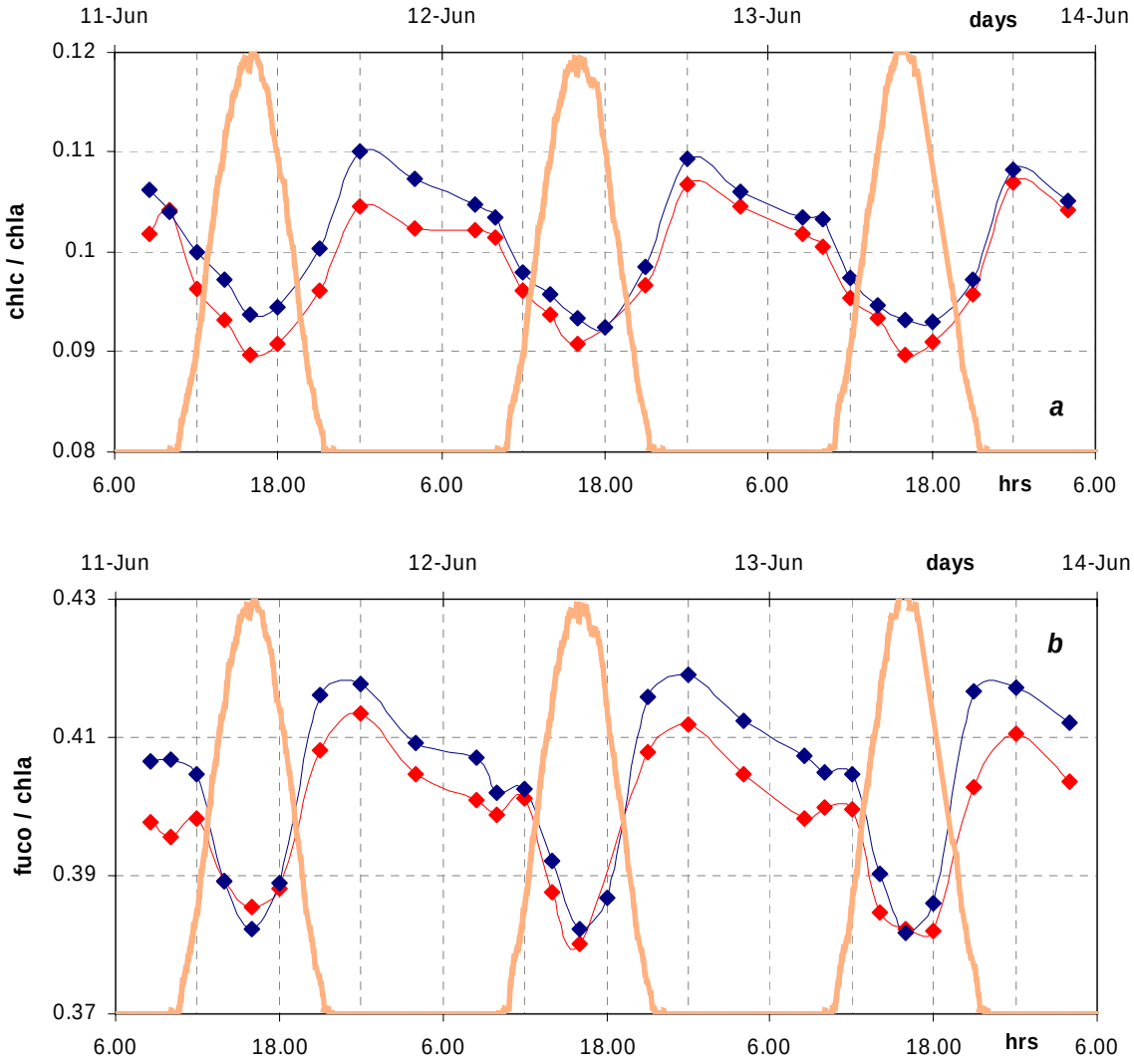

Fig.L.4.8: (a) The ratios chlorophyll-*c*/chlorophyll-*a* (chlc/chla), and (b) fucoxanthin/chlorophyll-*a* (fuco/chla), in chemostats C1 (red) and C2 (blue), with time, in sinusoidal light (orange, from 0 to 300 µE m^{-2} s^{-1}).

β-carotene has a maximum after midday (18.00h) and a minimum at dawn (1.2-fold lower, 10.00h, fig.L.4.9a). The ratio β-carotene/chla has its maximum at midday (16.00h) and it remains at its minimum from after sunset to midnight (1.1-fold lower, fig.L.4.9b).

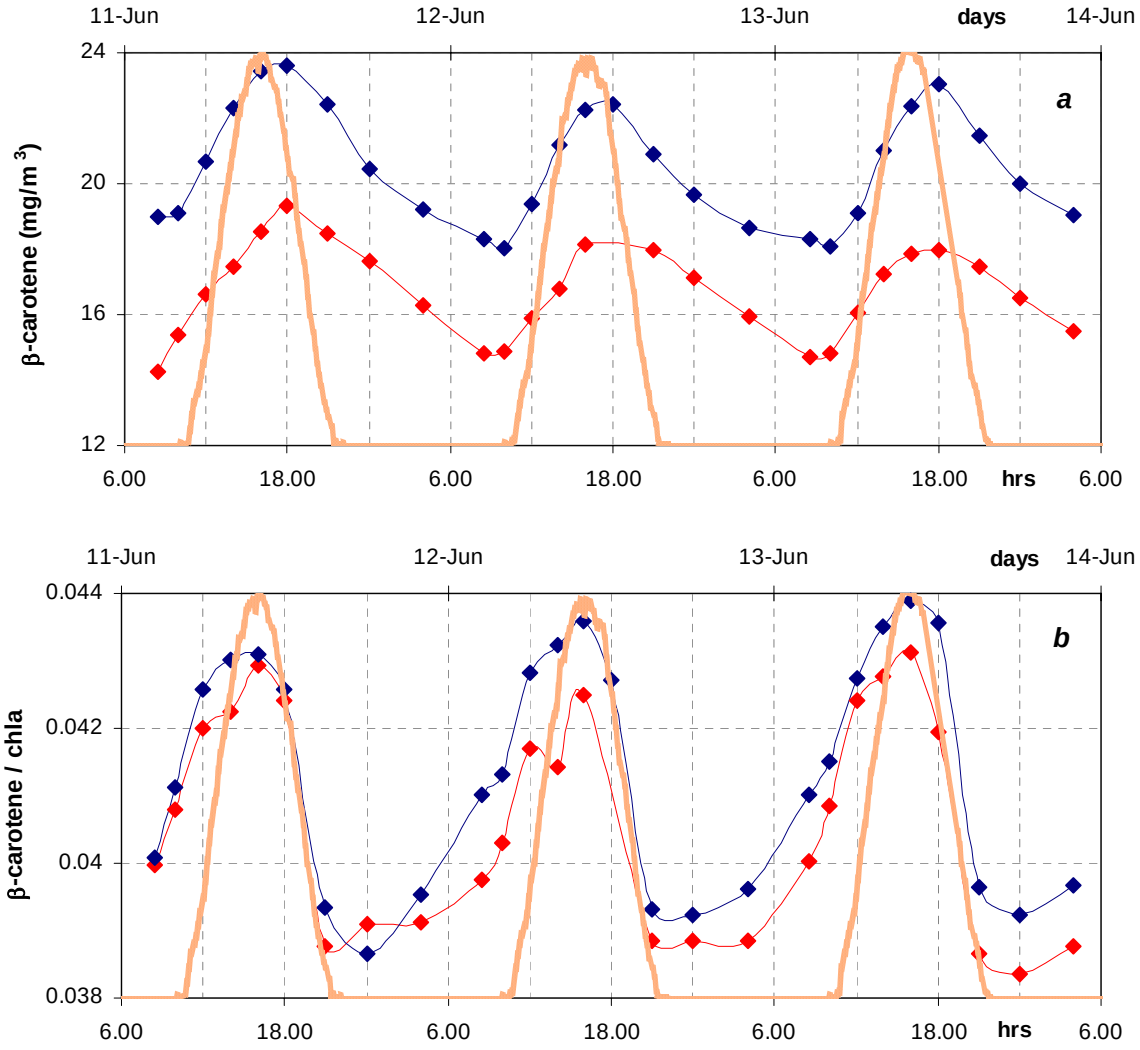

Fig.L.4.9: (a) β-carotene concentration (mg/m^3), and (b) the ratio β-carotene /chlorophyll-*a* (β-carot/chla), in chemostats C1 (red) and C2 (blue), with time, in sinusoidal light (orange, from 0 to 300 µE m^{-2} s^{-1}).

As in experiment 1, violaxanthin concentration is the lowest before midday (12.00h) and maximum after midday (1.9-fold higher, 18.00h), i.e. 2 hours after irradiance maximum (fig.L.4.10a). Then it decreases sharply as far as sunset, finally slowly during the night back to the minimum at dawn. Antheraxanthin and zeaxanthin show their maximum values at the maximum of irradiance (16.00h, fig.L.4.10b): they increase from 12.00h to 21.00h and are constant and minimum during the dark period (10.6 and 4.5-fold lower, respectively). The ratios violaxanthin/chla, antheraxanthin/chla and zeaxanthin/chla follow the same pattern as violaxanthin, antheraxanthin and zeaxanthin.

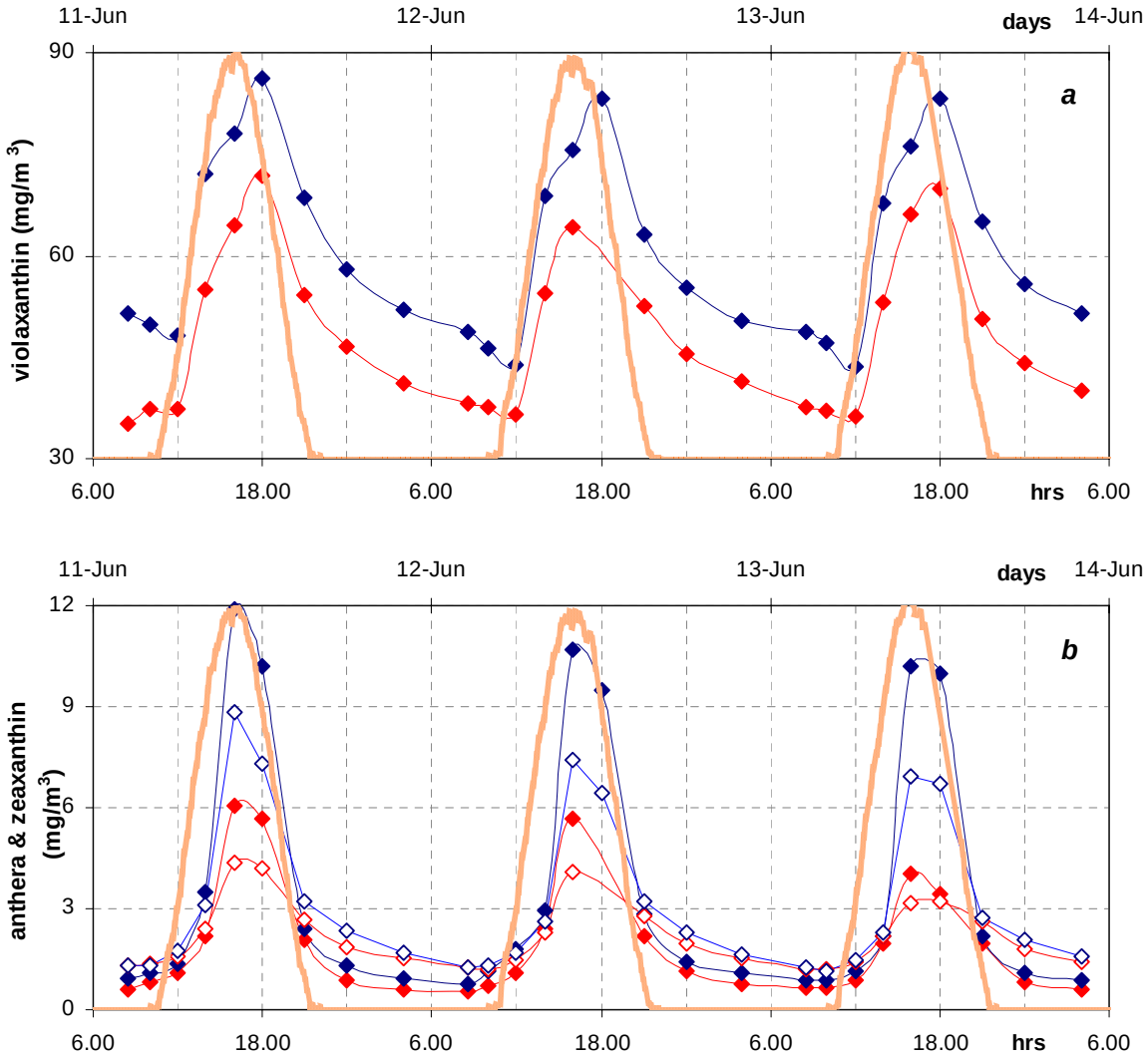

Fig.L.4.10: (a) Violaxanthin, and (b) antheraxanthin (closed symbols) & zeaxanthin (open symbols) concentrations (mg/m^3), in chemostats C1 (red) and C2 (blue), with time, in sinusoidal light (orange, from 0 to 300 µE m^{-2} s^{-1}).

The ratio C/chla has its minimum at mid-morning (12.00h) and reaches its maximum at sunset (1.4-fold higher, fig.L.4.11a). Then the light-increase is quicker than the dark-decrease.

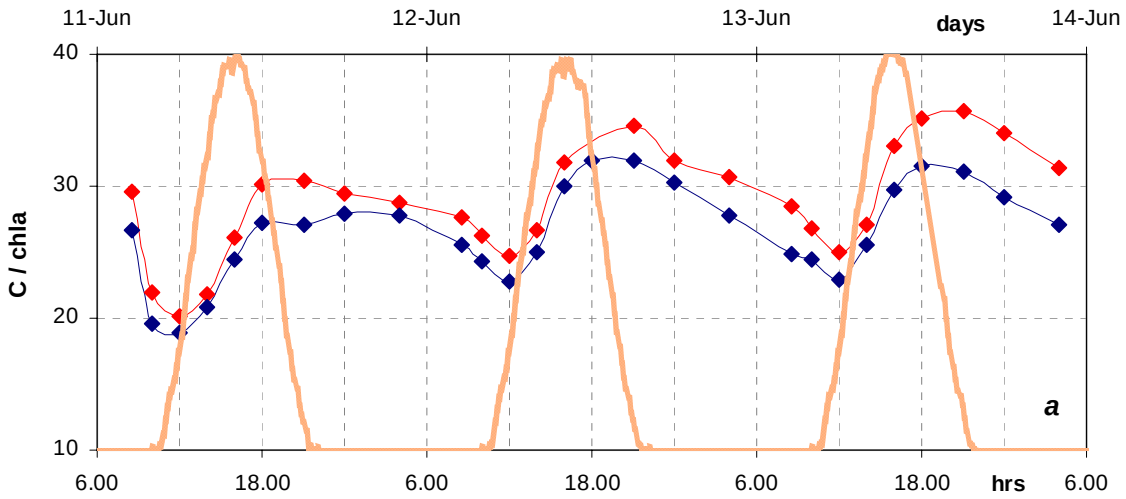

Fig.L.4.11a: The ratio C-content/chlorophyll-*a* (C/chla), in chemostats C1 (red) and C2 (blue), with time, in sinusoidal light (orange, from 0 to 300 µE m^{-2} s^{-1}).

Chlorophyll-*a* concentration per cell (chla/cell) is minimum at mid-morning, then increasing as far as the first hours of the night (2.1-fold higher, fig.L.4.11b).

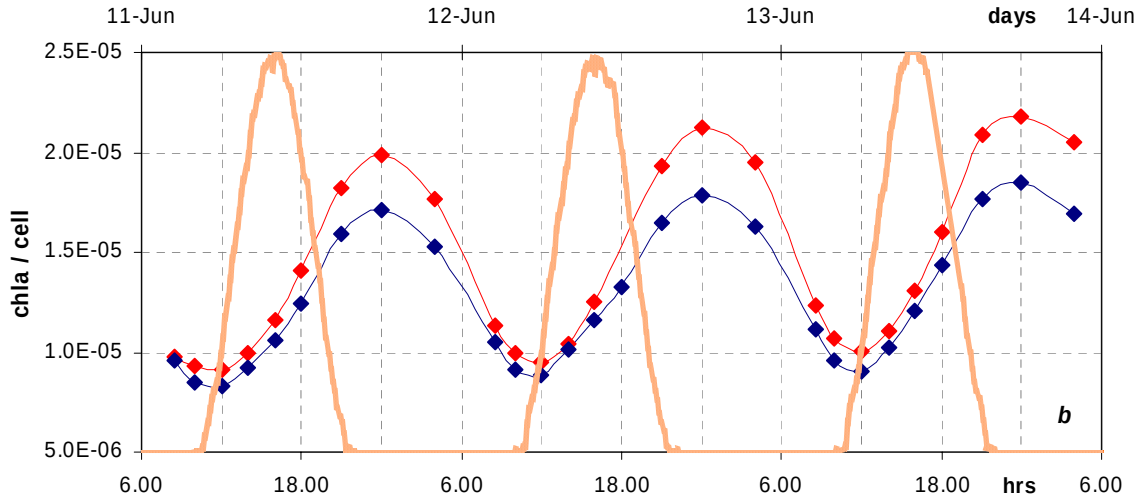

Fig.L.4.11b: The ratio chlorophyll-*a*/number of cells (chla/cell, µg $cell^{-1}$), in chemostats C1 (red) and C2 (blue), with time, in sinusoidal light (orange, from 0 to 300 µE m^{-2} s^{-1}).

Chlorophyll-*a* concentration per unit of cell volume (chla/vol) is maximum at dawn, minimum around sunset (1.6-fold lower, 18.00-21.00h, fig.L.4.11c).

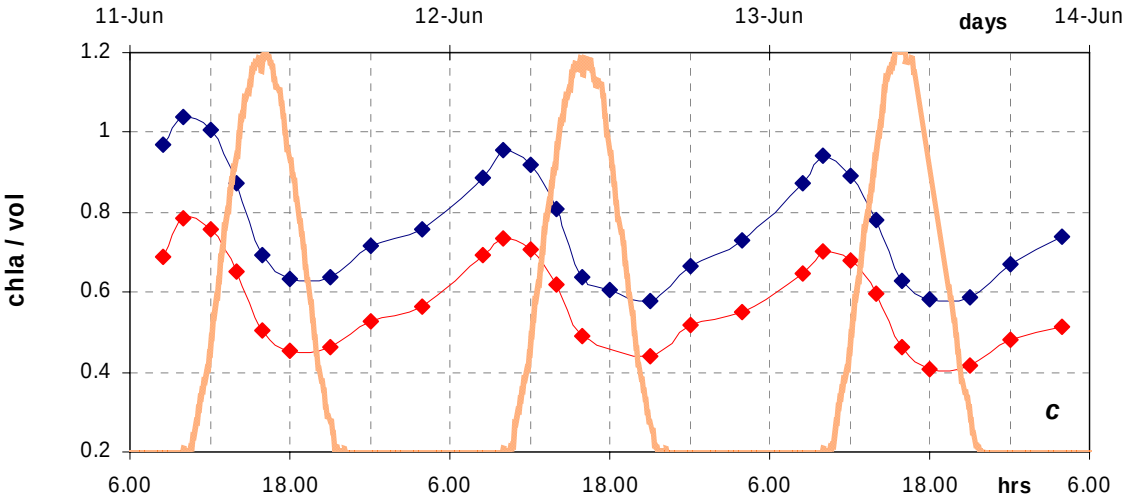

Fig.L.4.11c: The ratio chlorophyll-*a*/cell volume (chla/vol, µg l^{-1} μm^{-3}), in chemostats C1 (red) and C2 (blue), with time, in sinusoidal light (orange, from 0 to 300 µE m^{-2} s^{-1}).

3.b.5 Experiment 5: from sinusoidal to continuous light (~30 hours measurements)

Photosynthetic parameters by oxygen measurements: shifting the light from sinusoidal to continuous, α^b still shows a circadian rhythm but with a shorter period: it's maximum at 14.00-15.00h, minimum before midnight (1.00-4.00h), which means keeping its sinusoidal rhythm, then it increases around 8.30-9.00h, finally oscillates (fig.L.5.1a). P^bmax still shows it's maximum before midday, then decreases to a very low value at 4.00h, finally it oscillates on low values (fig.L.5.1b).

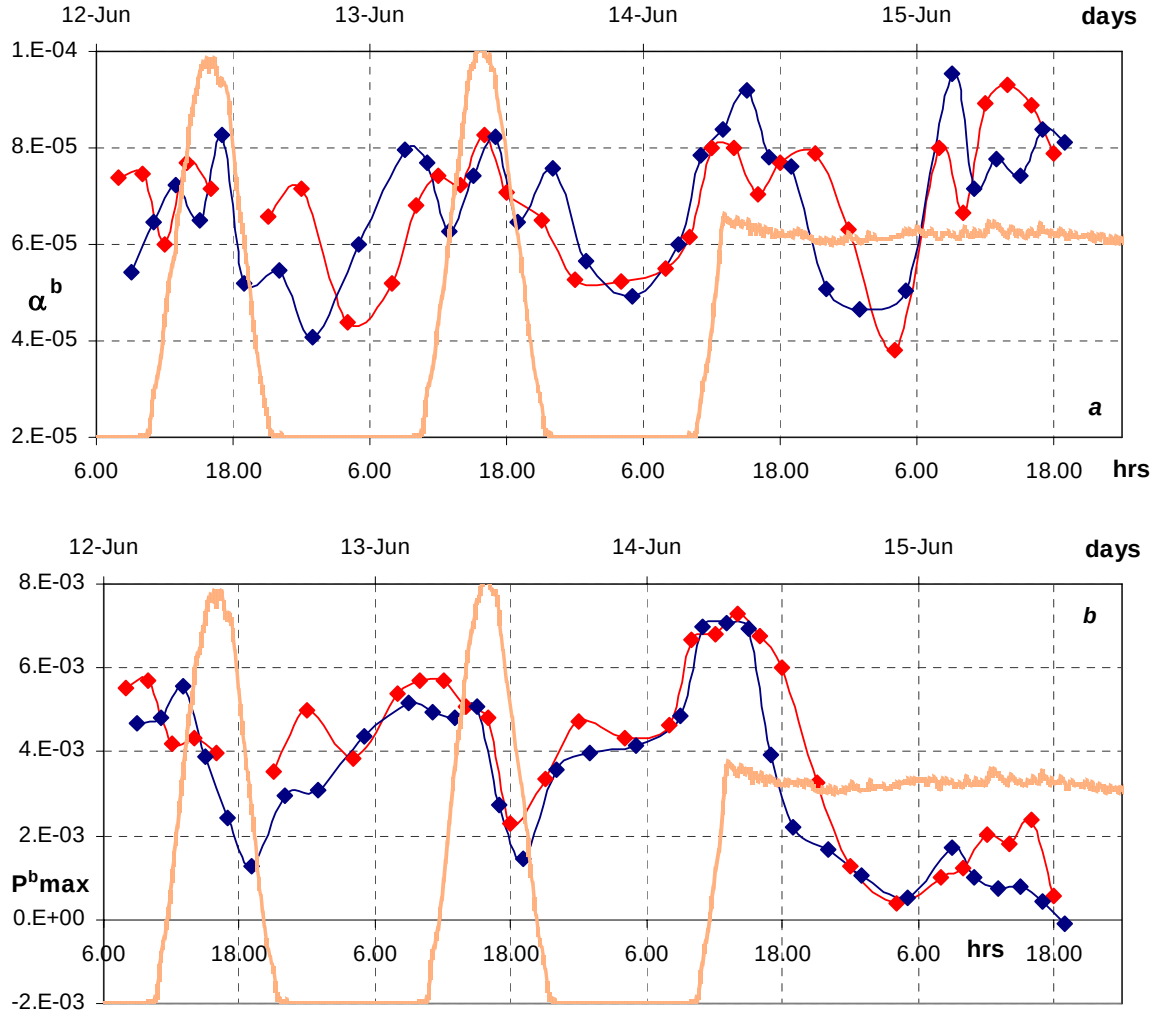

Fig.L.5.1: (a) the light-limited slope α normalized by chlorophyll-*a* (α^b, µmol O_2 (ml min)$^{-1}$ (µmol quanta m^{-2} s^{-1} µg chla l^{-1}) $^{-1}$), and (b) the light-saturated rates of photosynthesis normalized by chlorophyll-*a* (P^bmax, µmolO_2 µg chla^{-1} s^{-1}), by net oxygen evolved measurements, in chemostats C1 (red) and C2 (blue), with time, in sinusoidal light and shifting light from sinusoidal to continuous (orange, from 0 to 150 µE m^{-2} s^{-1}).

So both α^b and P^bmax decrease markedly from midday to the sinusoidal midnight, then they both oscillates around almost constant values. Figs. 5.2a and b show the strong covariation between the two parameters: during the first 12 hours following the

light shift, P^bmax varies much more than α^b (R^2=0.98, n=8, fig.L.5.2a), then P^bmax becomes almost constant since 6.30h (R^2=0.90, n=6, fig.L.5.2b).

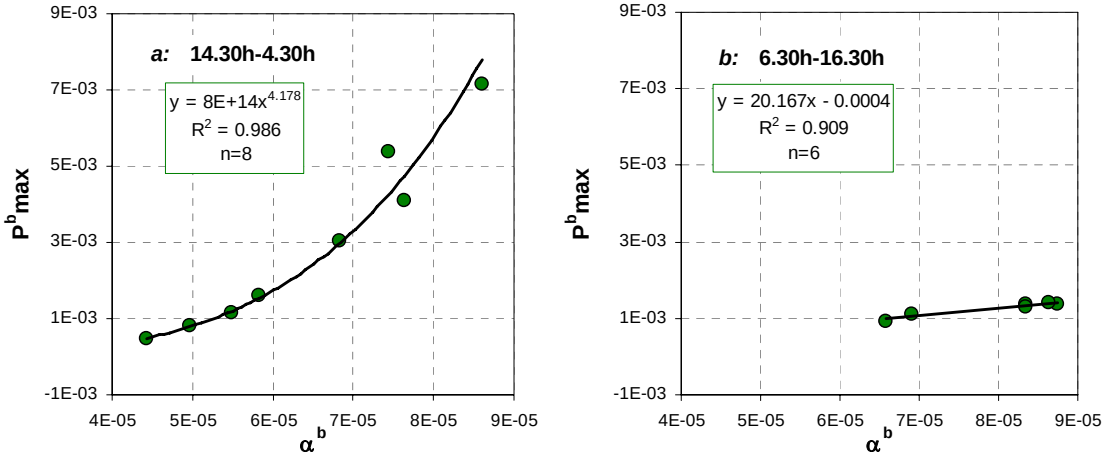

Fig.L.5.2: two-phases covariation of α^b and P^bmax after shifting light from sinusoidal to continuous (from 0 to 150 µE m^{-2} s^{-1}): (a) covariation from 14.30h to 4.30h, and (b) from 6.30h to 16.30h, by net oxygen evolved measurements, with time. Datas are the mean values between the 2 chemostats.

Please note that the best curve which fits to the 14.30h-4.30h datas is a potential one, in fact Ek is not constant in that phase (Ek-dependent variability = photoacclimation, fig.L. 5.3). That means that the two parameters have a 2-phases pattern of variability, but only the 2nd one is Ek-independent.

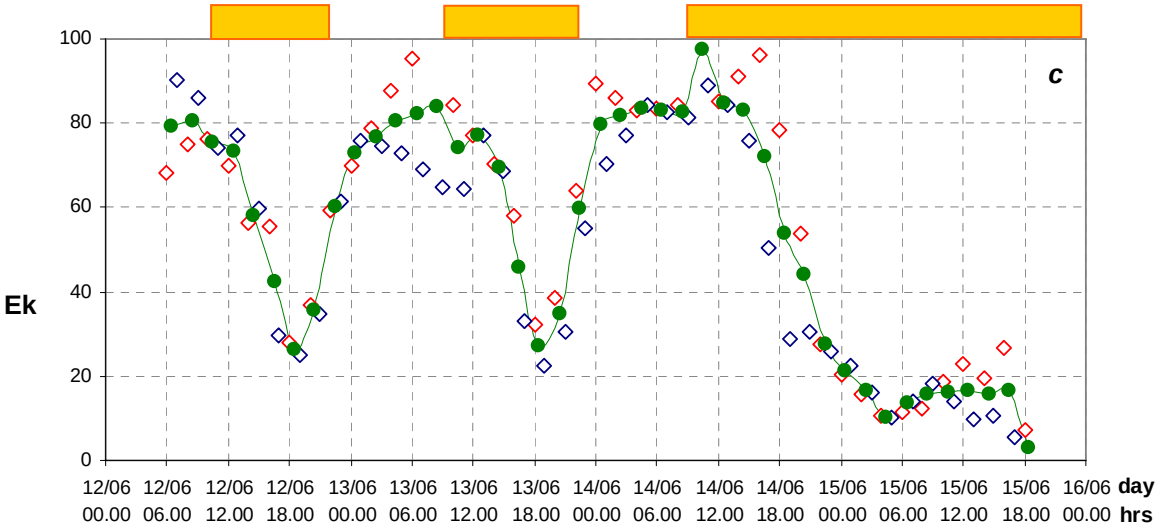

Fig.L.5.3: the light-saturation index Ek=P^bmax/α^b (in µE $m^{-2}s^{-1}$), by net oxygen evolved measurements, in chemostats C1 (red) and C2 (blue), with time, from sinusoidal to continuous light (from 0 to 150 µE m^{-2} s^{-1}). Green datas are the average between the two chemostats. The yellow bars indicate the light periods.

Cell cycle: shifting light from sinusoidal to continuous, after its maximum at 13.00h the minimum number of cells is postponed to after-midnight (5.00-6.30h), then it increases as far as the sinusoidal midday, but to a value which is 75-80% less than the sinusoidal

maximum. Finally, it decreases again slowly (fig.L. 5.4a). Cell volume keeps on increasing as far as the sinusoidal midnight (4.00-4.30h), so the maximum is postponed to 7 hours later, it remains almost constant for the following 2-3 hours, then it decreases as far as 12.00h (the sinusoidal before-midday), finally it increases again (fig.L.5.4b). Volume maximum value is about 75% higher than the sinusoidal one. So both cells number and volume keep their sinusoidal periodicity for about 9 hours after the light shift.

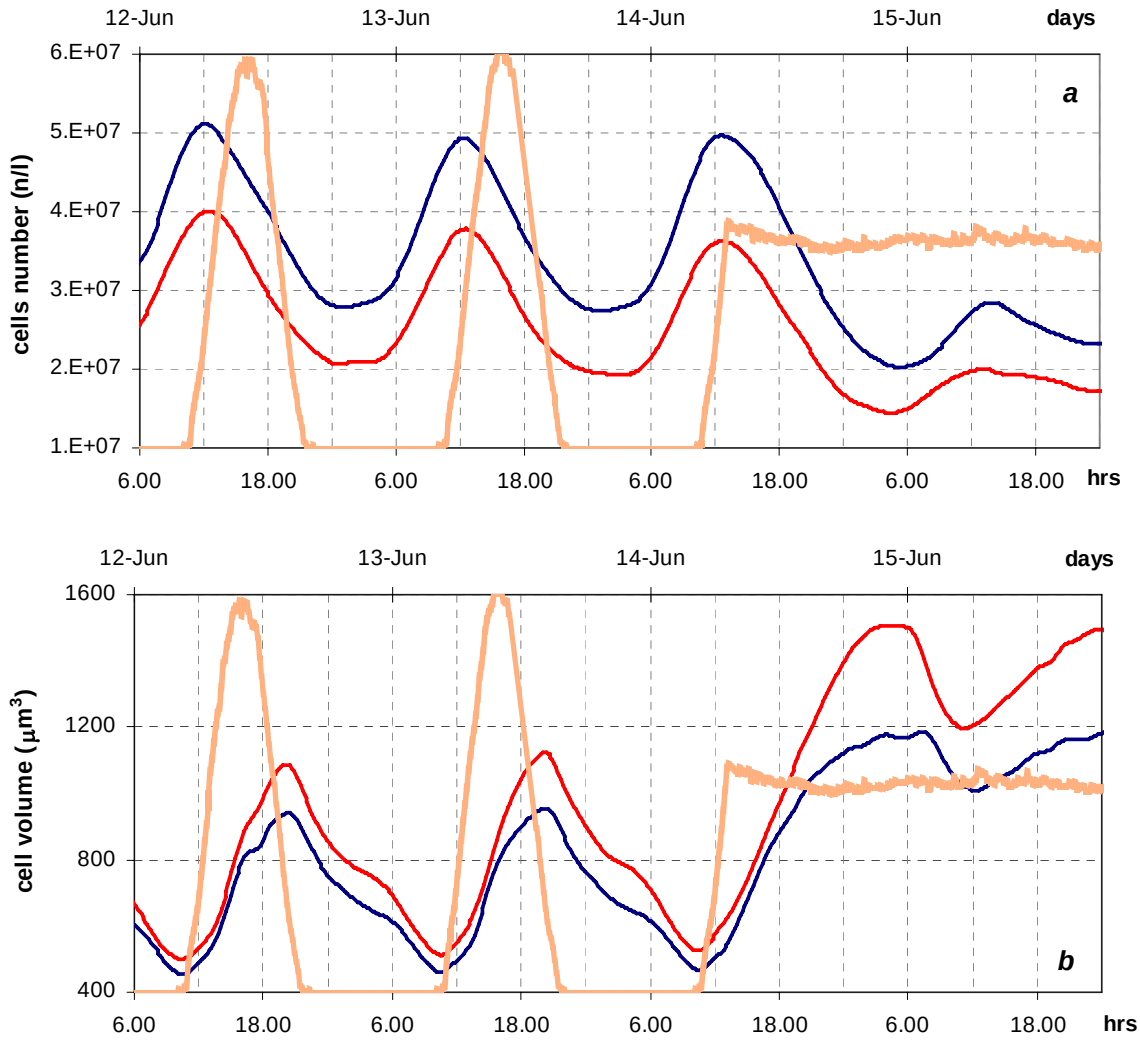

Fig.L.5.4: (a) cells number (n/l) and (b) cell volume (μm^3), in chemostats C1 (red) and C2 (blue), with time, in sinusoidal light and shifting light from sinusoidal to continuous (orange, from 0 to 150 $\mu E\ m^{-2}\ s^{-1}$).

Organic carbon and nitrogen: both the C/N ratio and C-concentration keep on increasing as far as 0.00h-4.00h, then remain quite stable (fig.L.5.5a and b). N-concentration keeps its sinusoidal cycle as far as 0.00h, then N-concentration is stable at the corresponding sinusoidal value at that PAR (fig.L.5.5c). Then, organic C and N-

content keep their sinusoidal cycle for 9 hours after the light shift, finally they become constant.

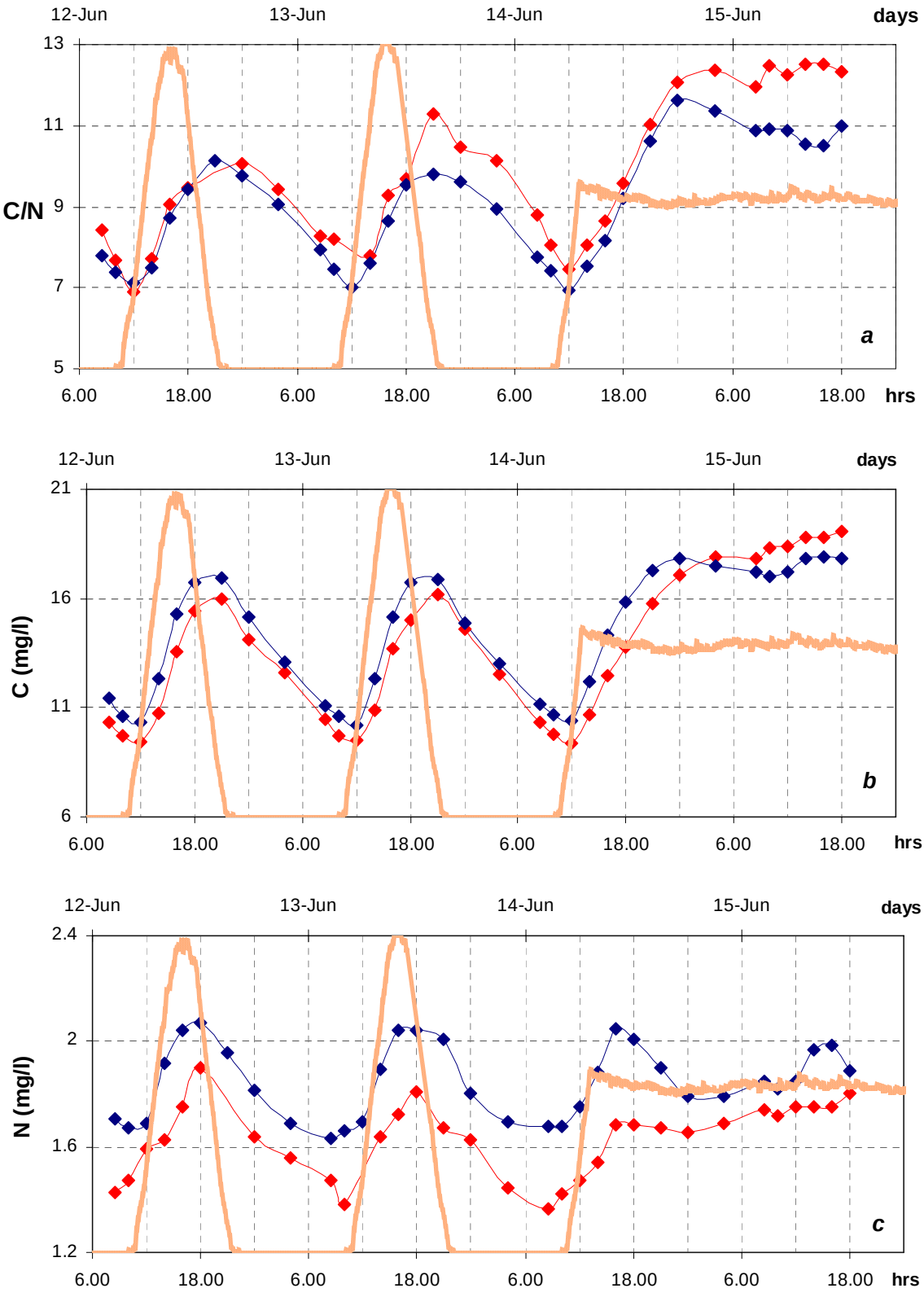

Fig.L.5.5: (a) C/N ratio, (b) C content (mg/l) and (c) N content (mg/l) in chemostats C1 (red) and C2 (blue), with time, in sinusoidal light and shifting light from sinusoidal to continuous (orange, from 0 to 150 μE m^{-2} s^{-1}).

Inorganic carbon and nitrogen: DIC remains stable at its minimum value since 0.00h (fig.L.5.6a). Inorganic nitrogen content (NO_3^- + NO_2^-) keeps its sinusoidal minimum (17.00-18.00h), then it increases as far as 0.30h (clear in chemostat C2), finally it decreases again (fig.L.5.6b). Then, both inorganic C and N-content keep their sinusoidal cycle for 9 hours after the light shift, finally they become constant.

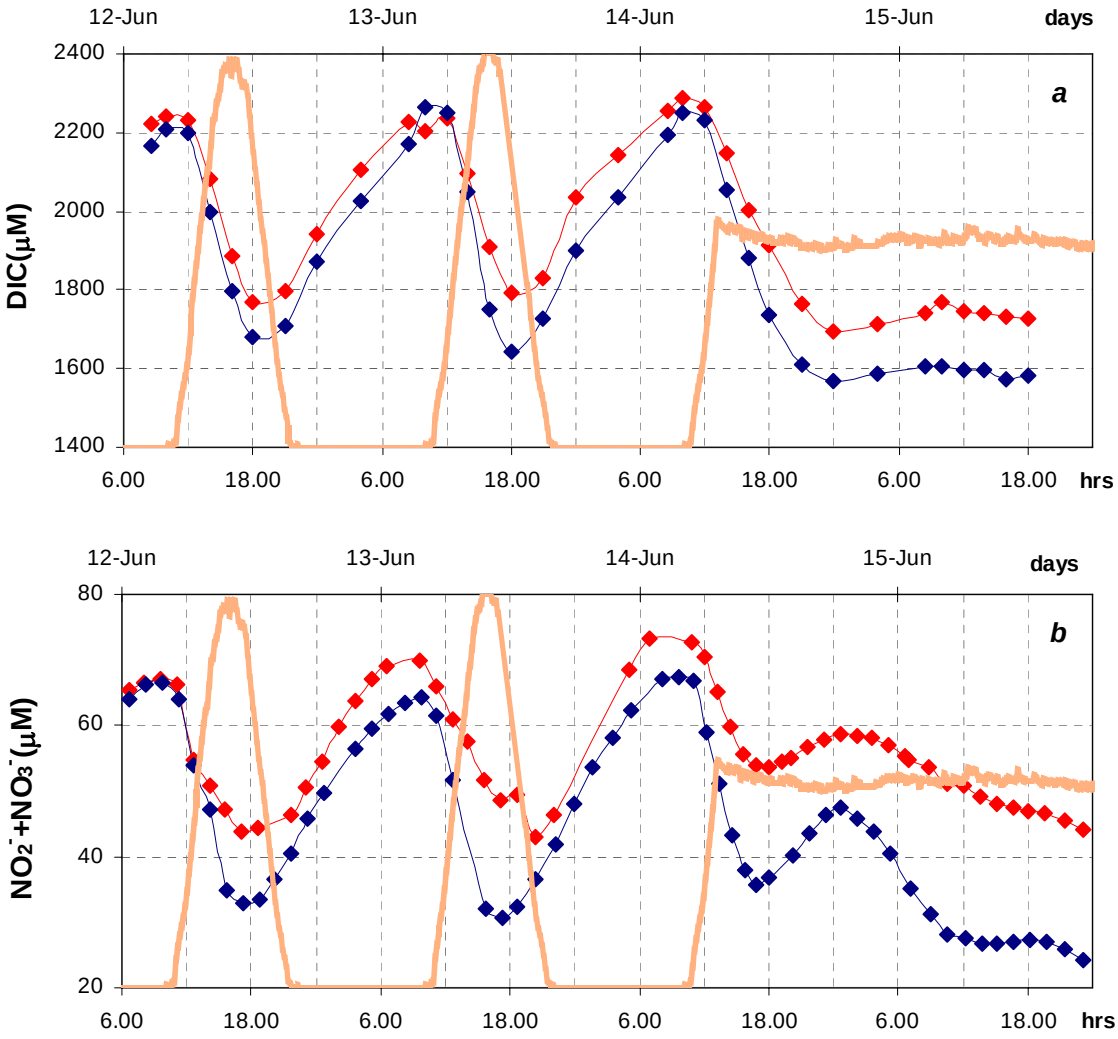

Fig.L.5.6: (a) Inorganic carbon (DIC, µM), and (b) nitrogen (NO_2^-+NO_3^-, µM), in chemostats C1 (red) and C2 (blue), with time, in sinusoidal light and shifting light from sinusoidal to continuous (orange, from 0 to 150 µE m^{-2} s^{-1}).

Pigments: chlorophyll-*a*, chlorophyll-c and fucoxanthin concentrations keep their sinusoidal cycle but they all start reducing their amplitude since 10.00-12.00h (fig.L.5.7a, b and c). So, their rhythm is maintained unaltered in period and amplitude for 9 hours after the light shift.

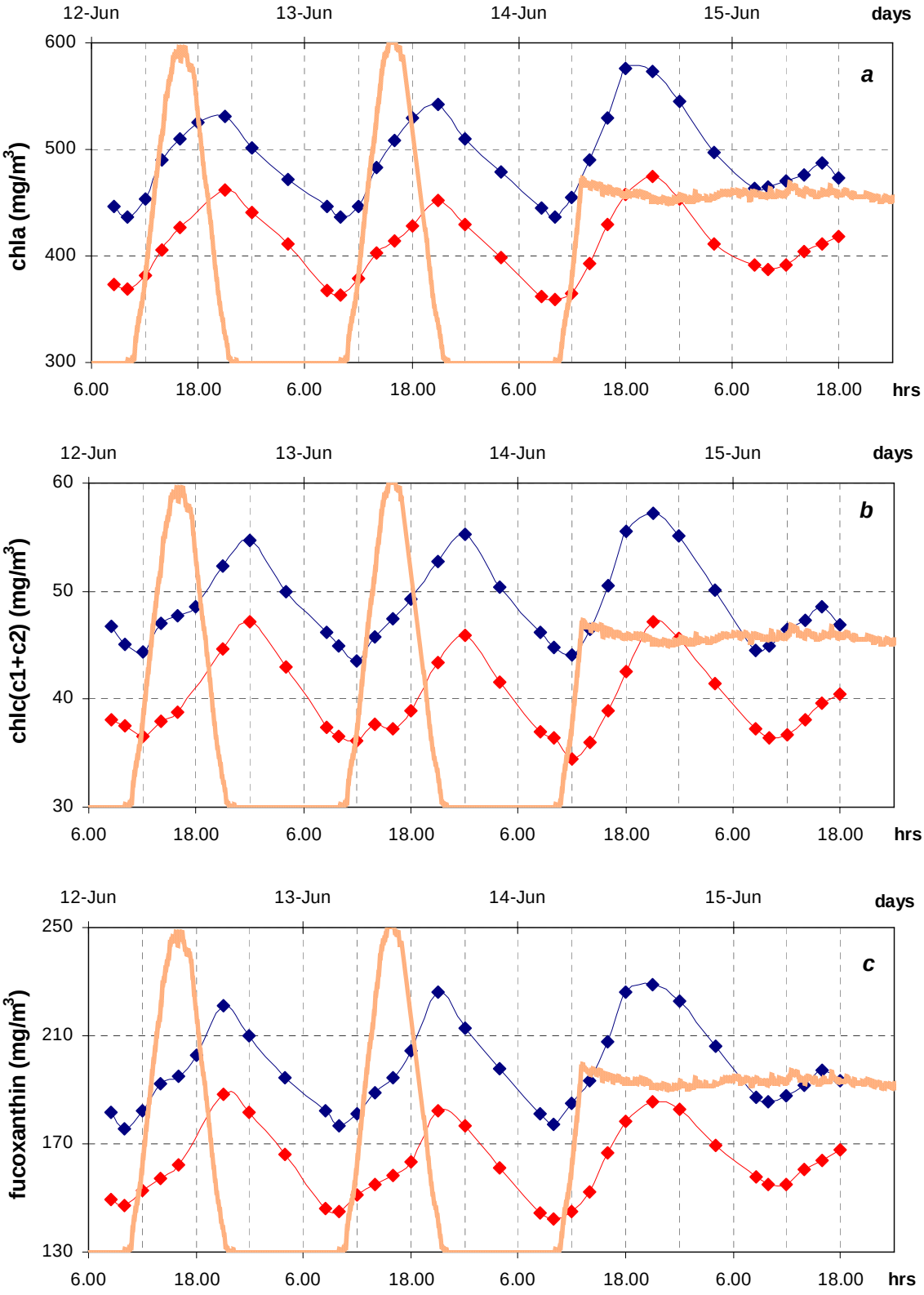

Fig.L.5.7: (a) Chlorophyll-*a* (chla, mg/m^3), (b) chlorophyll-*c1* + chlorophyll-*c2* (chlc(c1+c2), mg/m^3), and (c) fucoxanthin (mg/m^3) concentration, in chemostats C1 (red) and C2 (blue), with time, in sinusoidal light and shifting light from sinusoidal to continuous (orange, from 0 to 150 µE m^{-2} s^{-1}).

Both the ratios chlorophyll-c/chla and fucoxanthin/chla keep their minimums around midday, then they reduce their rhythms in period and amplitude (fig.L.5.8a and b).

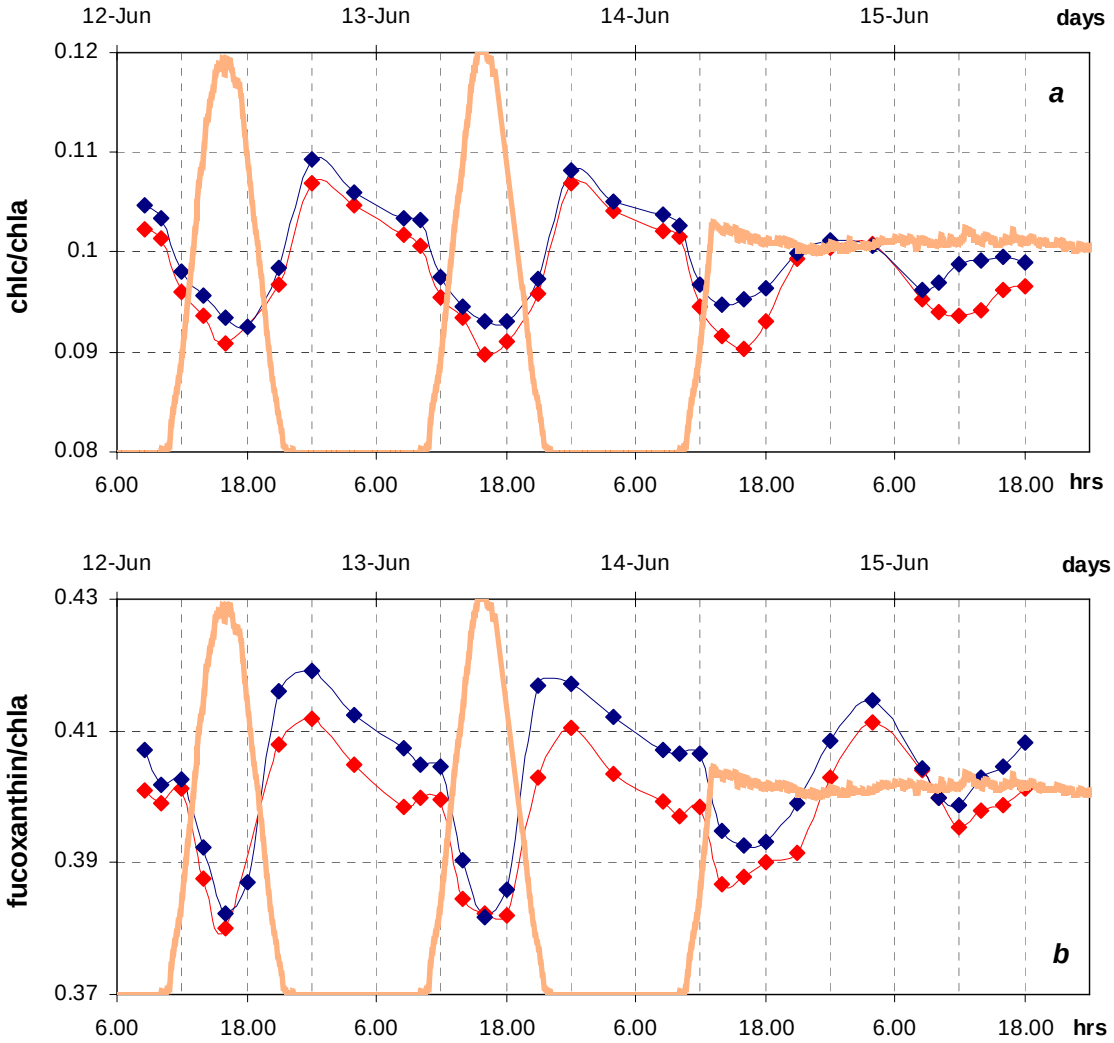

Fig.L.5.8: (a) The ratios chlorophyll-*c*/chlorophyll-*a* (chlc/chla), and (b) fucoxanthin/chlorophyll-*a* (fuco/chla), in chemostats C1 (red) and C2 (blue), with time, in sinusoidal light and shifting light from sinusoidal to continuous (orange, from 0 to 150 µE m^{-2} s^{-1}).

Shifting to continuous light, β-carotene still shows its maximum after midday (18.00h), then it decreases to a minimum value from 4.00h (fig.L.5.9a). The ratio β-carotene/chla keeps its rhythm for 24 hours from the light shift, then its cycle reduces in period and amplitude (maximum at 10.00h instead of 16.00h, fig.L.5.9b).

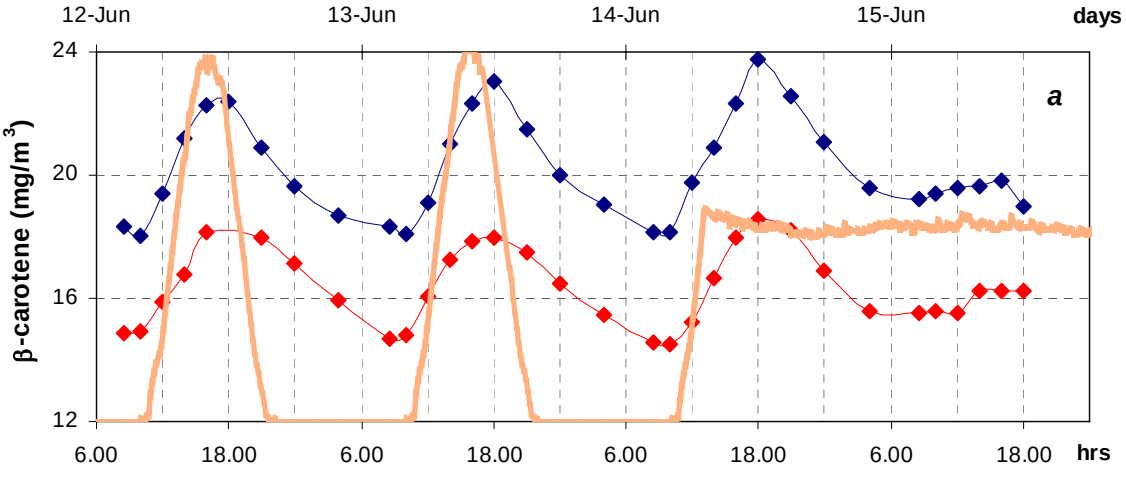

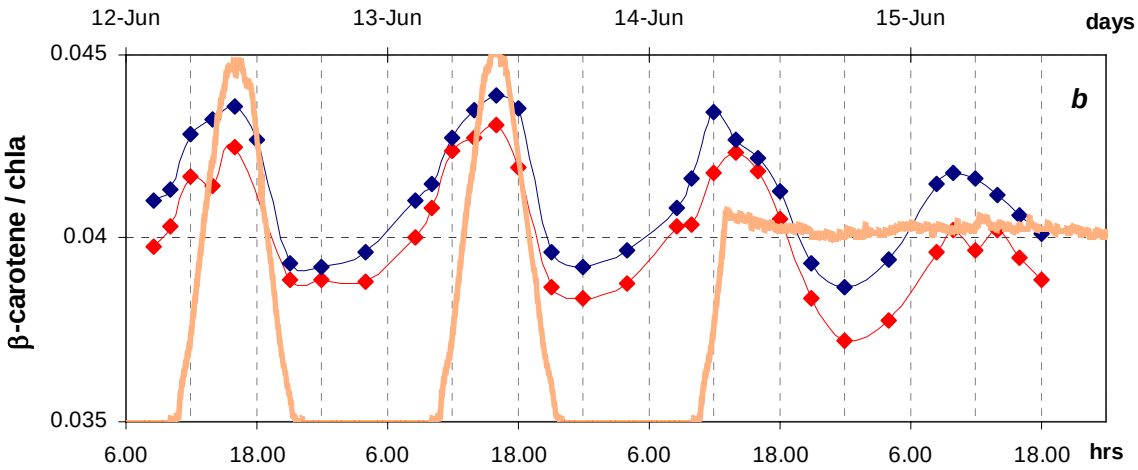

Fig.L.5.9: (a) β-carotene concentration (mg/m^3), and (b) the ratio β-carotene /chlorophyll-*a* (β-carot/chla), in chemostats C1 (red) and C2 (blue) with time, in sinusoidal light and shifting light from sinusoidal to continuous (orange, from 0 to 150 µE m^{-2} s^{-1}).

Violaxanthin concentration shows its maximum at 18.00h, even if lower than the sinusoidal one, then both period and amplitude reduce, finally it becomes constant 24 hours after the shift (fig.L.5.10a). Antheraxanthin and zeaxanthin still show their circadian rhythm as far as 8 hours after the light shift, then they start increasing, finally they become constant since 12.00h (24 hors after the light shift, fig.L.5.10b).

The ratios violaxanthin/chla, antheraxanthin/chla and zeaxanthin/chla follow the same pattern as violaxanthin, antheraxanthin and zeaxanthin.

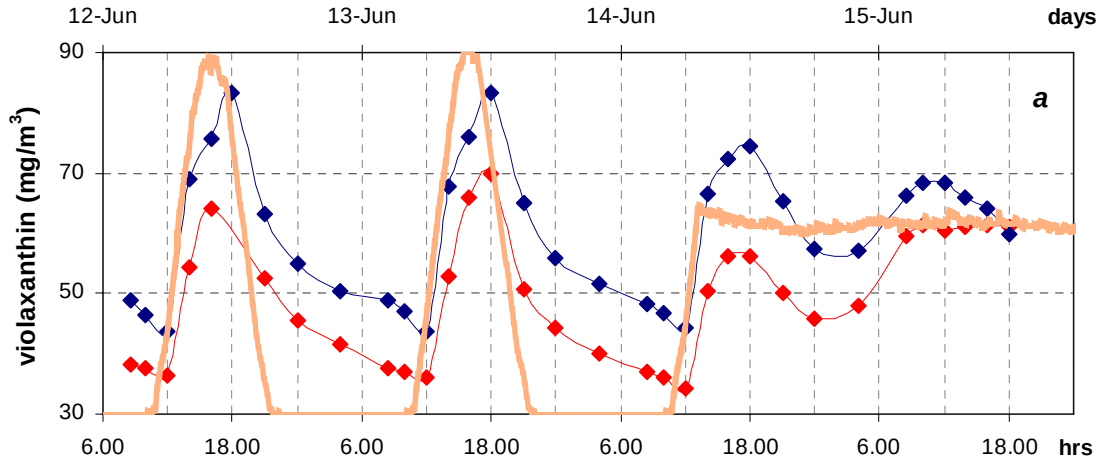

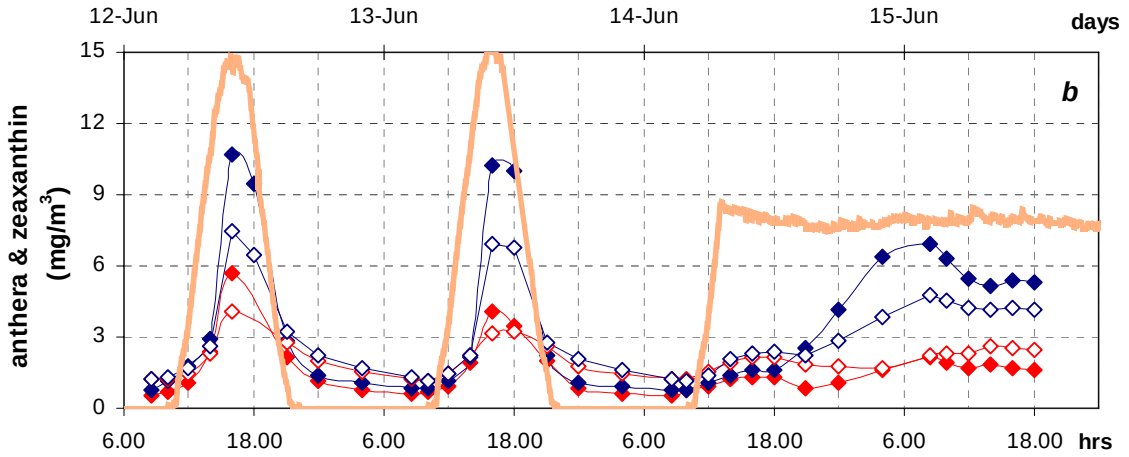

Fig.L.5.10: (a) Violaxanthin, and (b) antheraxanthin (closed symbols) & zeaxanthin (open symbols) concentrations (mg/m^3), in chemostats C1 (red) and C2 (blue), with time, in sinusoidal light and shifting light from sinusoidal to continuous (orange, from 0 to 150 µE m^{-2} s^{-1}).

The ratio C/chla increases as far as 10.00h on the second day of continuous-light measurements, then it becomes constant (fig.L.5.11a).

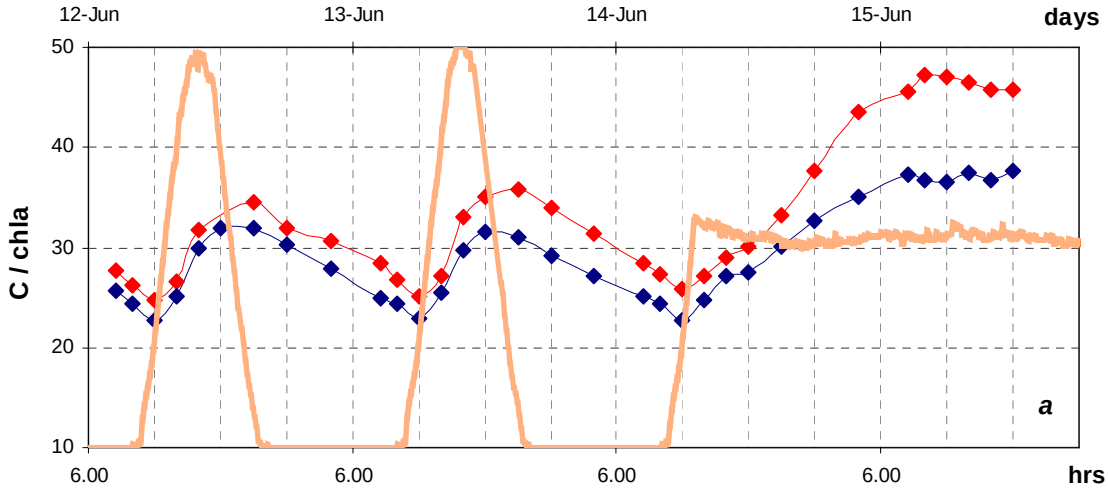

Fig.L.5.11a: The ratio C-content/chlorophyll-*a* (C/chla), in chemostats C1 (red) and C2 (blue), with time, in sinusoidal light and shifting light from sinusoidal to continuous (orange, from 0 to 150 µE m^{-2} s^{-1}).

Chlorophyll-*a* concentration per cell (chla/cell) keeps on increasing as far as 4.00h, then it decreases to the 12-00-14.00h minimum: then it keeps a 24 hours periodicity, but the minimum and the maximum are shifted to higher values when compared to the corresponding sinusoidal ones (fig.L. 5.11b).

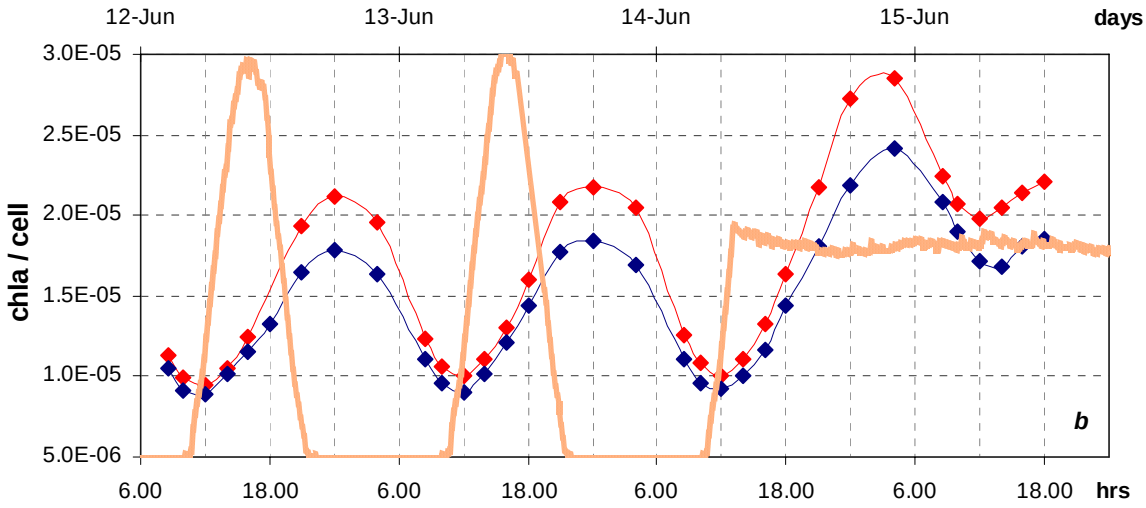

Fig.L.5.11b: The ratio chlorophyll-*a*/number of cells (chla/cell, µg cell^{-1}), in chemostats C1 (red) and C2 (blue), with time, in sinusoidal light and shifting light from sinusoidal to continuous (orange, from 0 to 150 µE m^{-2} s^{-1}).

Chlorophyll-*a* concentration per unit of cell volume (chla/vol) postpones its minimum at 4.00h, then it remains stable (fig.L. 5.11c).

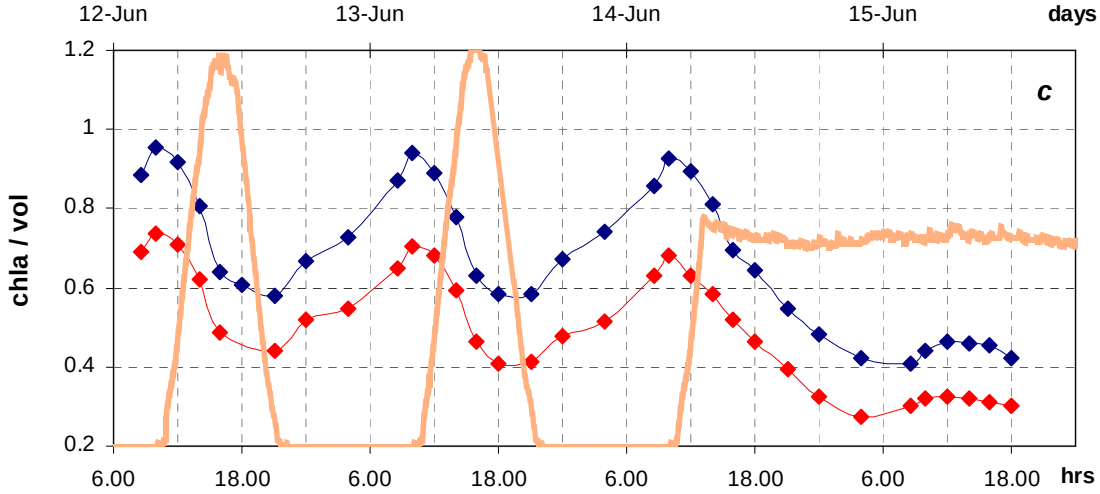

Fig.L.5.11c: The ratio chlorophyll-*a*/cell volume (chla/vol, µg l^{-1} µm^{-3}), in chemostats C1 (red) and C2 (blue), with time, in sinusoidal light and shifting light from sinusoidal to continuous (orange, from 0 to 150 µE m^{-2} s^{-1}).

3.b.6 Experiment 6: from continuous back to sinusoidal light (~14 hours measurements)

Photosynthetic parameter by oxygen measurements: shifting the light from continuous back to sinusoidal, α^b and P^bmax immediately turn back to their diel periodicity. P^bmax still show a circadian rhythm too, but with a longer and larger period: the maximum has a 2 hours delay, followed by a 10 hours delayed minimum, finally values remain stable and low (fig.L.6.1a and b).

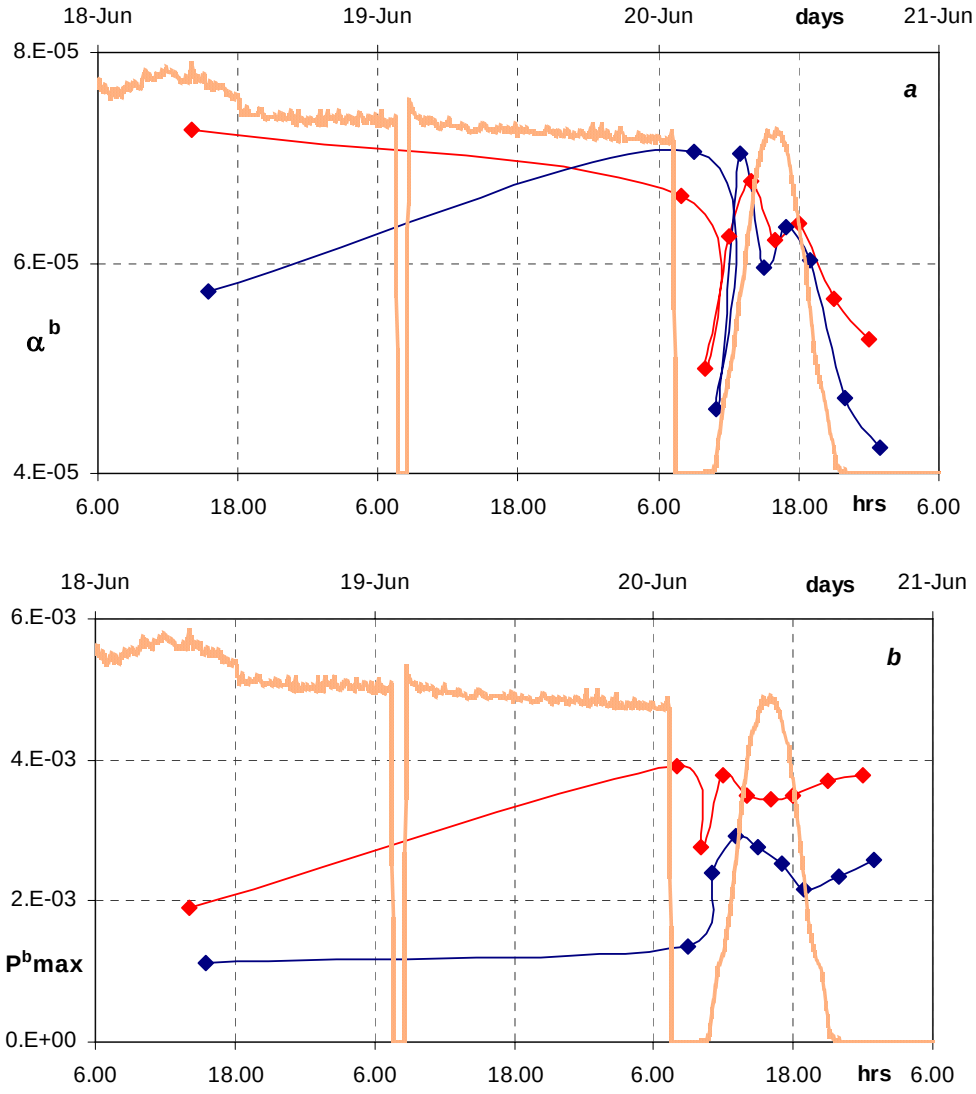

Fig.L.6.1: (a) the light-limited slope α normalized by chlorophyll-*a* (α^b, µmol O_2 (ml min)$^{-1}$ (µmol quanta m^{-2} s^{-1} µg chla l^{-1}) $^{-1}$), and (b) the light-saturated rates of photosynthesis normalized by chlorophyll-*a* (P^bmax, µmolO_2 µg chla^{-1} s^{-1}), by net oxygen evolved measurements, in chemostats C1 (red) and C2 (blue), with time, in continuous light and shifting light from continuous back to sinusoidal (orange, from 0 to 150 µE m^{-2} s^{-1}).

Moreover, the time-table of sampling doesn't allow to evidence the covariation between α^b and P^bmax (we stopped sampling at 1.00h), in fact Ek is not constant at the times of sampling (fig.L.6.1c).

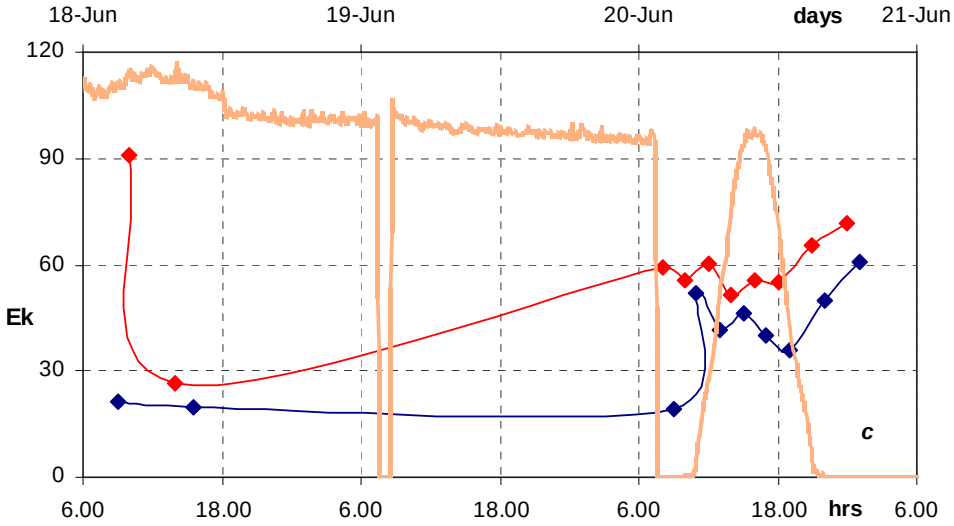

Fig.L.6.1: (c) the light-saturation index Ek=P^bmax/α^b (in µE $m^{-2}s^{-1}$), by net oxygen evolved measurements, in chemostats C1 (red) and C2 (blue), with time, in continuous light and shifting light from continuous back to sinusoidal (orange, from 0 to 150 µE m^{-2} s^{-1}).

Cell cycle: fig.L.6.2a shows that cells number is minimum after one day and a half from the shift (0.00-2.00h on the 16th of June), then it increases gradually, following the irradiance oscillations: when irradiance decreases, cells number increases, and vice versa. The shift back to a sinusoidal light regime causes an increase of cells number to a maximum at 16.00-17.00h, followed by a minimum at 21.30-23.30h (sunset). That means that cells number is going back to cyclic variations, but one day and a half is not enough time to make it turned back to its sinusoidal periodicity. After two days from the shift, any periodic variation of cell volume is lost (fig.L.6.2b): cell volume follows small oscillations, slightly decreasing with light decreasing. That is clear for example when lights is switched off accidentally for only 1 hour, at around 7.30h on the 19th of June. As light is turned back to sinusoidal, 24 hours are enough to bring back volume circadian periodicity: cell volume is minimum around 11.00-12.00h and maximum at around 19.00-20.00h.

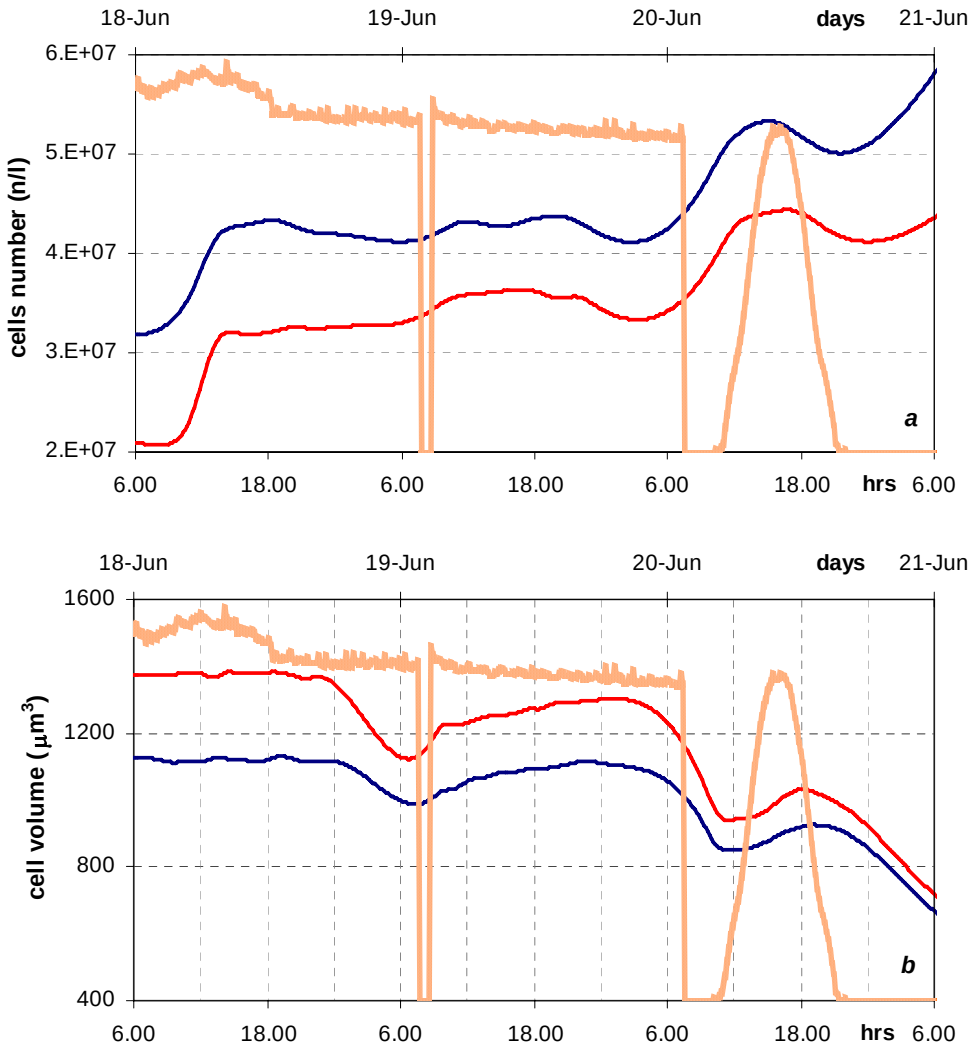

Fig.L.6.2: (a) cells number (n/l) and (b) cell volume (μm^3), in chemostats C1 (red) and C2 (blue), with time, in continuous light and shifting from continuous back to sinusoidal (orange, from 0 to 150 $\mu E\ m^{-2}s^{-1}$).

Organic carbon and nitrogen: the C/N ratio keeps on slowly decreasing under continuous light, then back to sinusoidal light it sharply decreases to a minimum at 14.00-16.00h (2 hours later then experiment 4), followed by a slighter decrease (fig.L.6.3a): one day and a half is not enough to recover C/N circadian rhythm. C-concentration slightly increases under continuous light, then under sinusoidal light it restores a mid-morning minimum, but the maximum is still 3 hours earlier than the experiment 4 one (fig.L.6.3b). After its increase under continuous light, N-concentration goes back to a circadian cycle under sinusoidal light in both chemostats it: C1 recovers experiment 4 minimum at 10.00h and maximum at 18.00h, while chemostat C2 has a 2 hours delay (fig.L.6.3c).

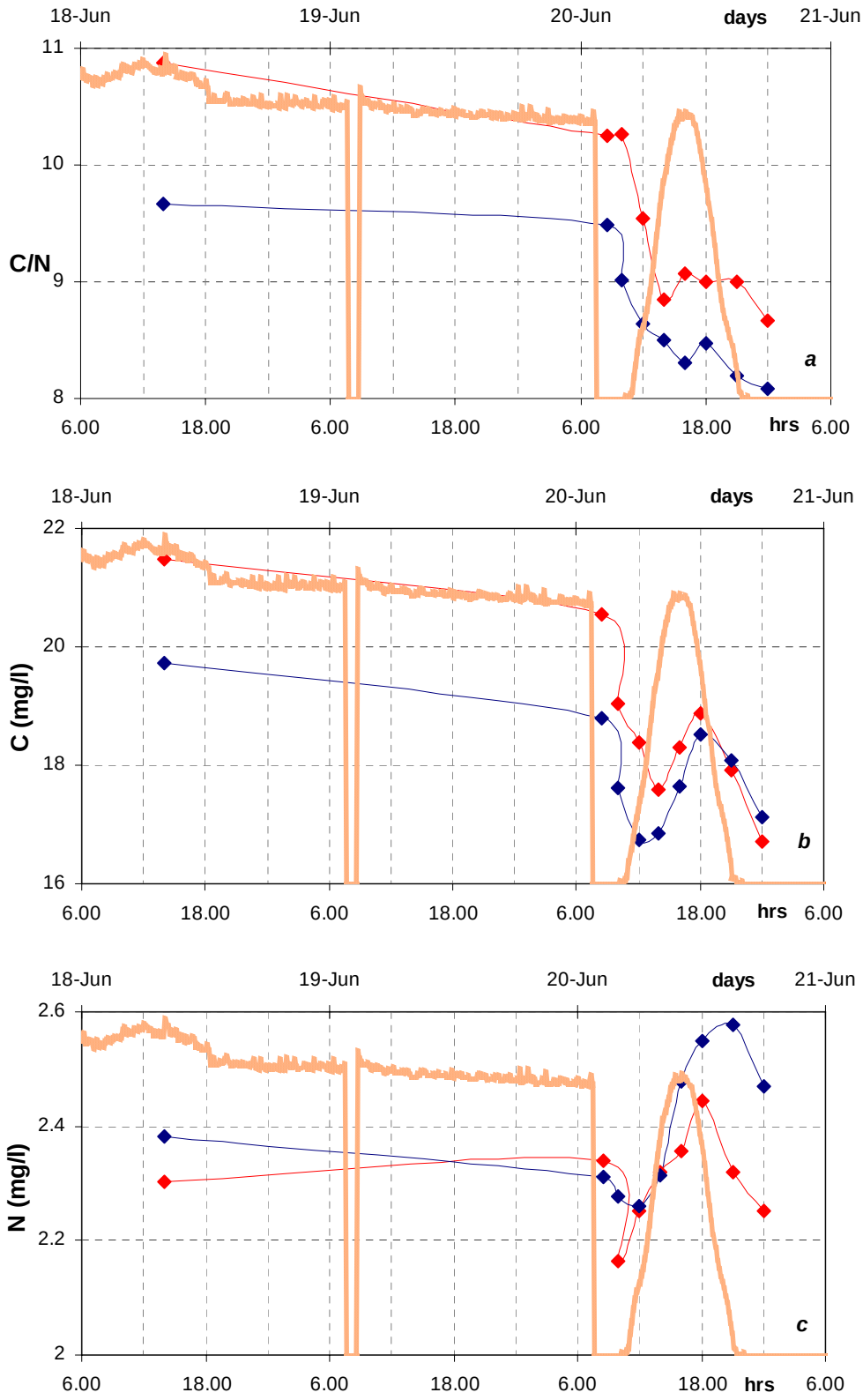

Fig.L.6.3: (a) C/N ratio, (b) C content (mg/l) and (c) N content (mg/l) in chemostats C1 (red) and C2 (blue), with time, in continuous light and shifting from continuous back to sinusoidal (orange, from 0 to 150 µE m^{-2} s^{-1}).

Inorganic carbon and nitrogen: in continuous light DIC is constant and after the shift back to sinusoidal light, DIC recovers immediately its sinusoidal cycle: its maximum at 12.00h and its minimum at 18.00h (fig.L.6.4a). Inorganic nitrogen concentration (NO_3^-

+NO_2^-) decreases for the first three days of continuous light, then it increases back to the minimum value soon after the shift, finally it recovers immediately its periodicity when back to sinusoidal light (fig.L.6.4b).

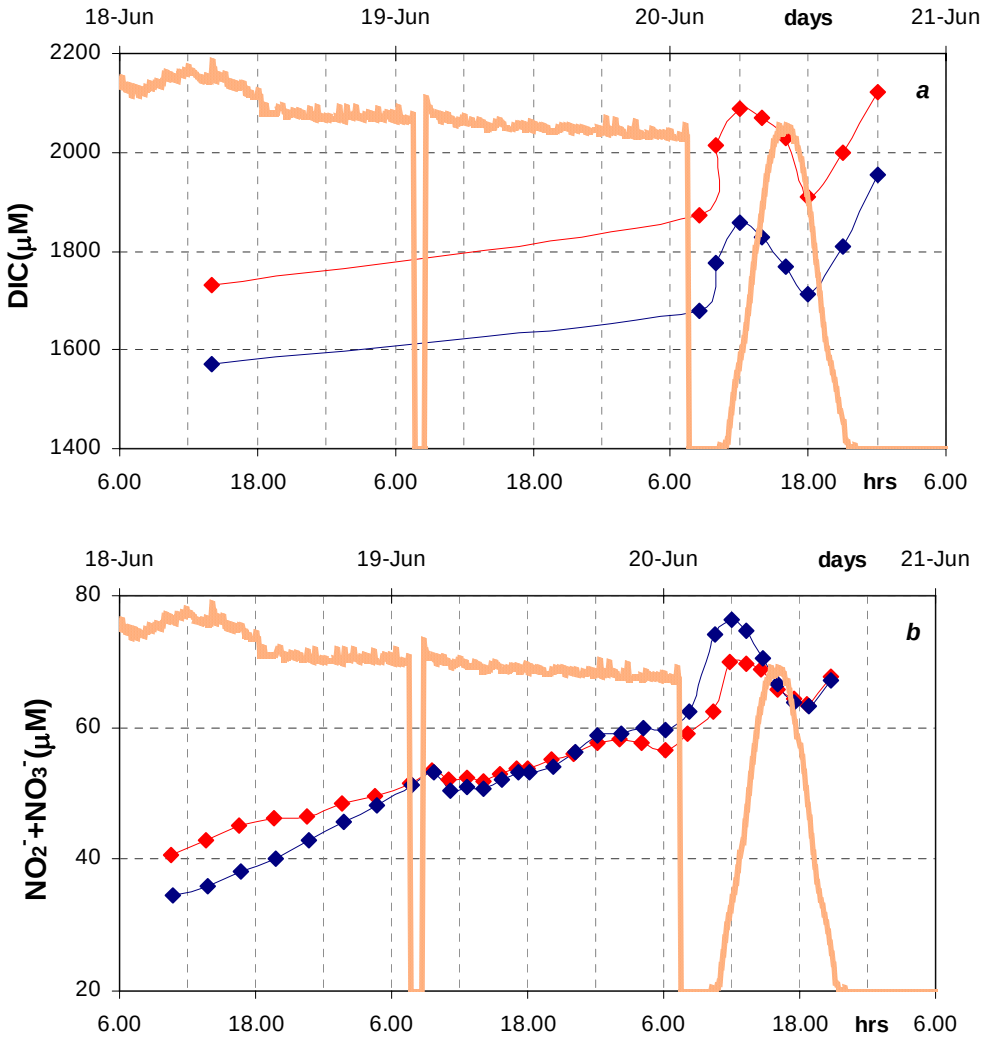

Fig.L.6.4: (a) Inorganic carbon (DIC, µM), and (b) nitrogen (NO_2^-+NO_3^-, µM), in chemostats C1 (red) and C2 (blue), with time, in continuous light and shifting from continuous back to sinusoidal (orange, from 0 to 150 µE m^{-2} s^{-1}).

Pigments: both chlorophyll-a and chlorophyll-c and fucoxanthin recover their sinusoidal cycle as soon as the light is shifted back to a sinusoidal cycle (figs. 6.5a, b and c).

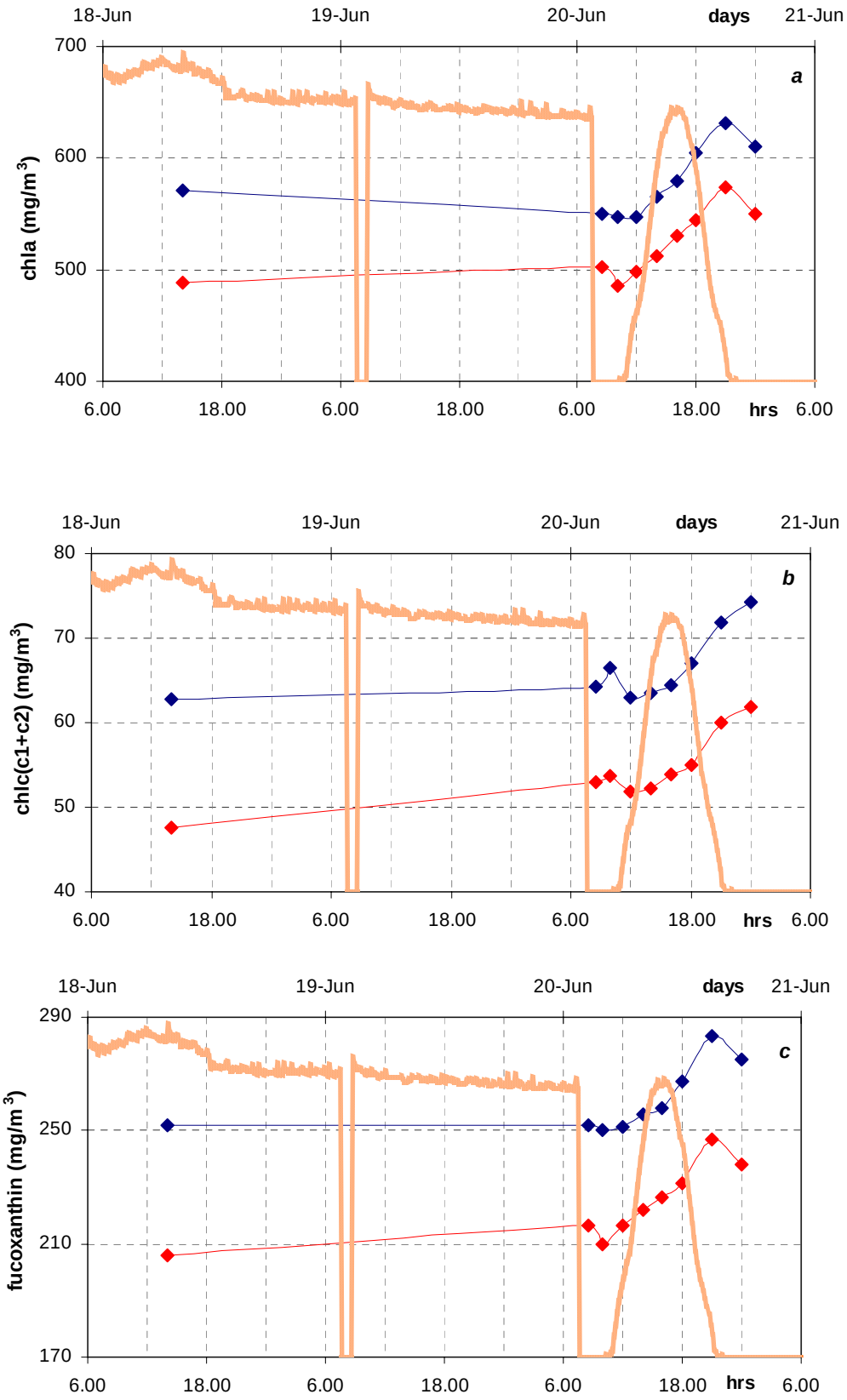

Fig.L.6.5: (a) Chlorophyll-*a* (chla, mg/m^3), (b) chlorophyll-*c1* + chlorophyll-*c2* (chlc(c1+c2), mg/m^3), and (c) fucoxanthin (mg/m^3) concentration, in chemostats C1 (red) and C2 (blue), with time, in continuous light and shifting from continuous back to sinusoidal (orange, from 0 to 150 µE m^{-2} s^{-1}).

The ratio chlorophyll-c/chla recovers a periodicity but it has a 2-hours delay in its maximum (at 18.00h instead of 16.00h, fig.L.6.6a), while the ratio fucoxanthin/chla recovers its periodicity and its minimum at 18.00h (fig.L.6.6b).

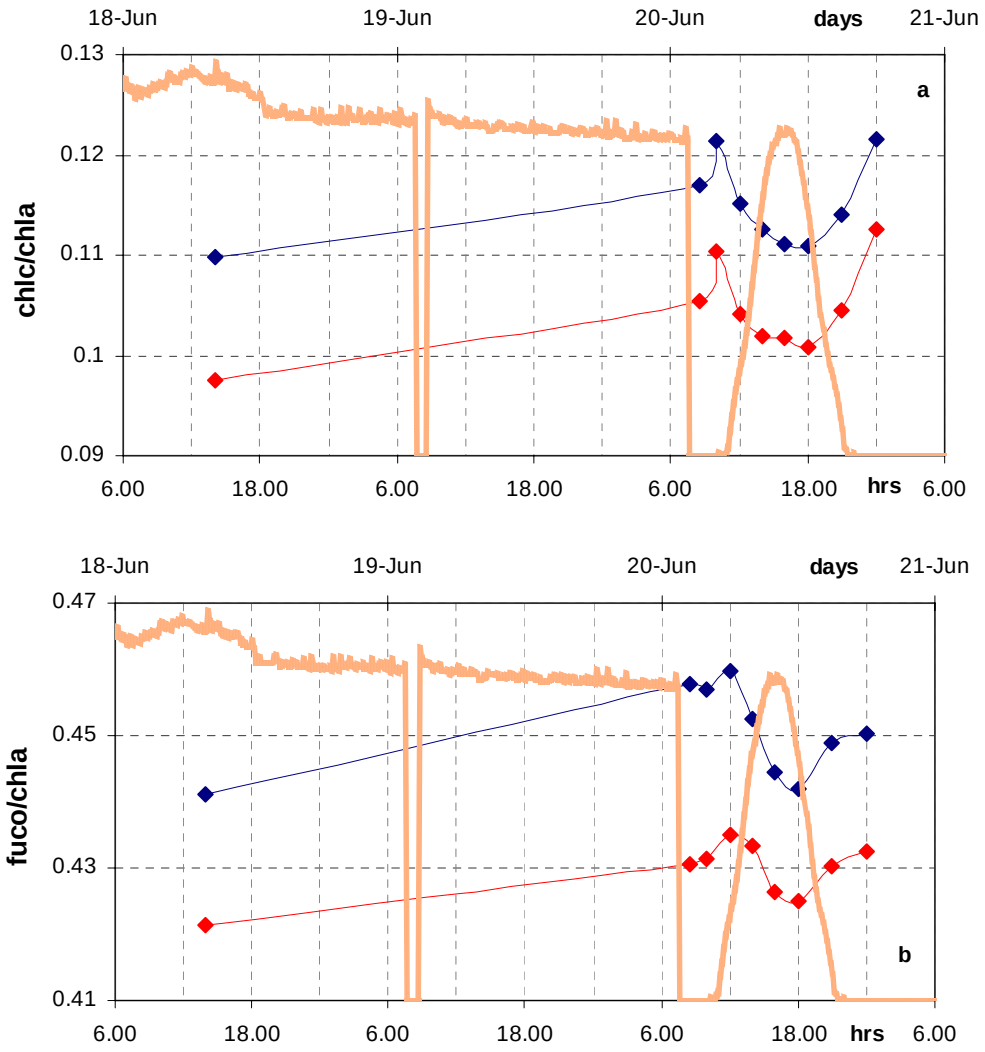

Fig.L.6.6: (a) The ratios chlorophyll-*c*/chlorophyll-*a* (chlc/chla), and (b) fucoxanthin/chlorophyll-*a* (fuco/chla), in chemostats C1 (red) and C2 (blue), with time, in continuous light and shifting from continuous back to sinusoidal (orange, from 0 to 150 µE m^{-2} s^{-1}).

β-carotene recovers a periodicity but it has a 2-hours delay: its minimum is at 12.00h (not yet at 10.00h) and its maximum at 21.00h (not yet 18.00h, fig.L.6.7a). The β-carotene/chla ratio recovers its sinusoidal periodicity right after the light shift (fig.L.6.7b).

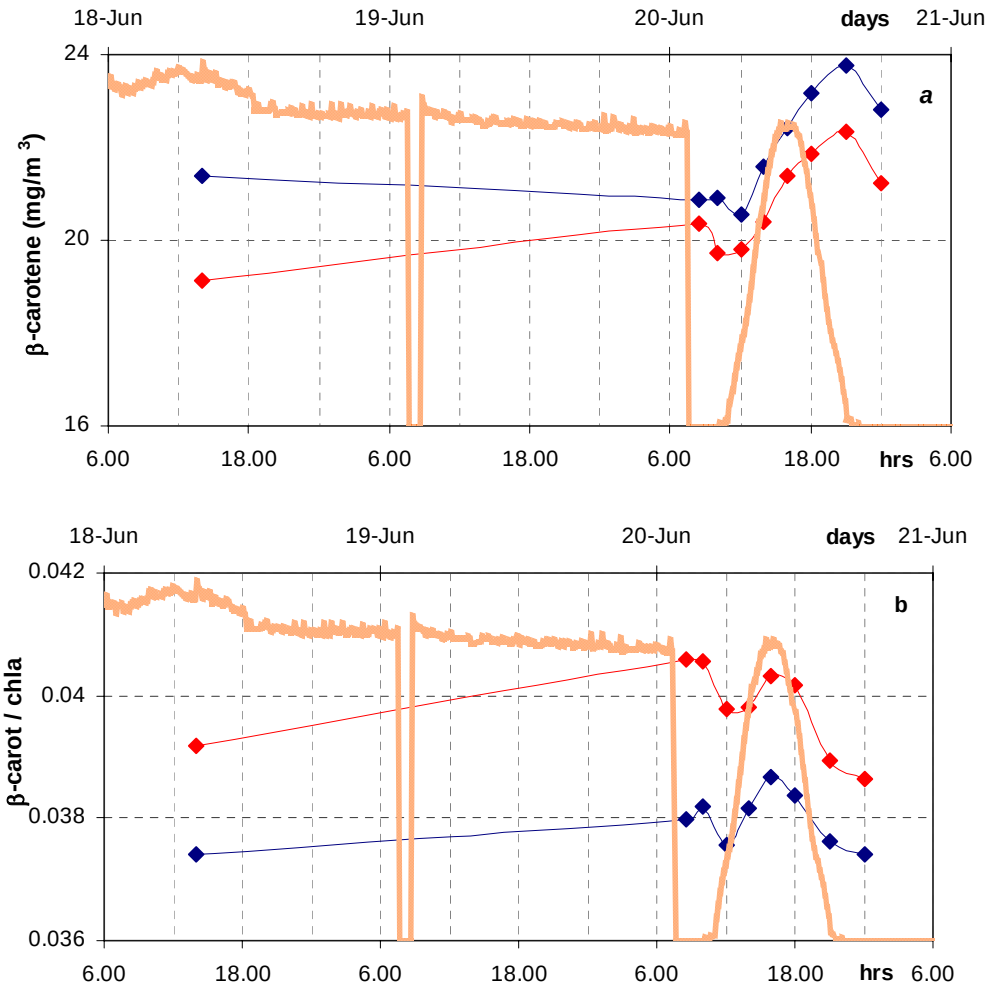

Fig.L.6.7: (a) β-carotene concentration (mg/m^3), and (b) the ratio β-carotene /chlorophyll-*a* (β-carot/chla), in chemostats C1 (red) and C2 (blue) with time, in continuous light and shifting from continuous back to sinusoidal (orange, from 0 to 150 µE m^{-2} s^{-1}).

Both violaxanthin and antheraxanthin and zeaxanthin (figs. 6.8a and b) and their corresponding ratios (violaxanthin/chla, antheraxanthin/chla and zeaxanthin/chla) recover their sinusoidal cycle as soon as the light is shifted back to a sinusoidal regime.

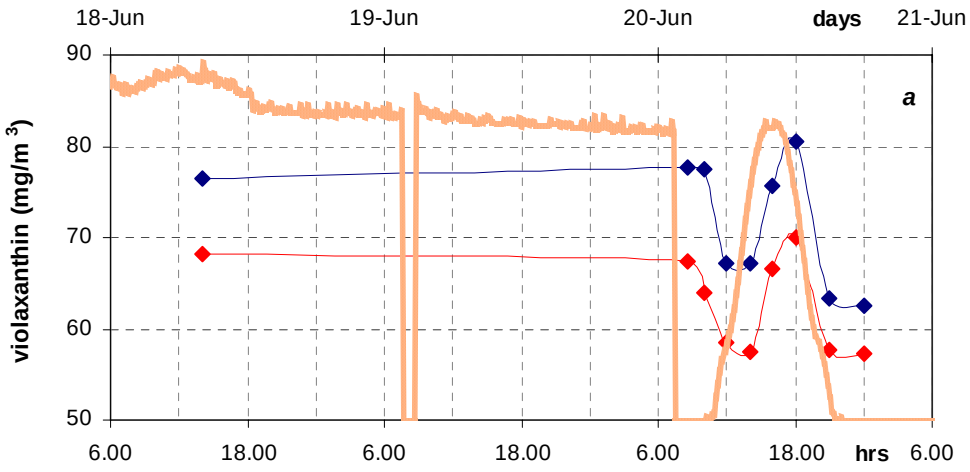

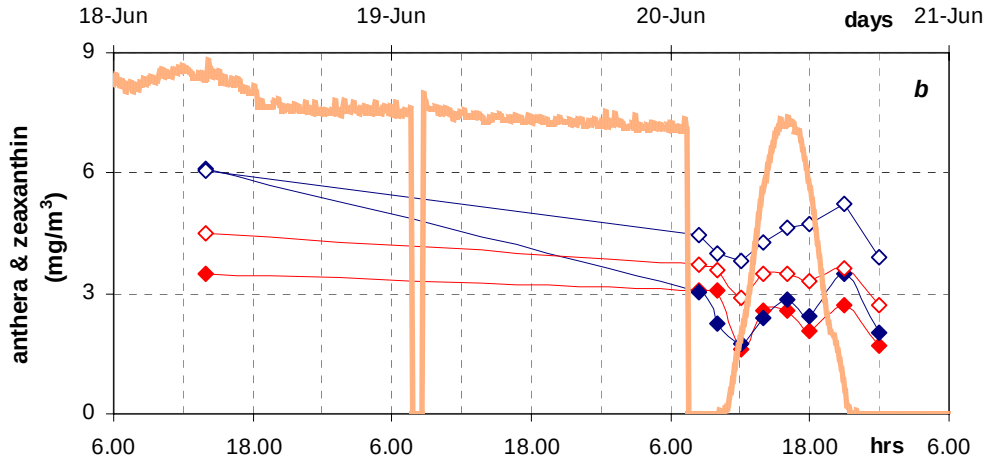

Fig.L. 6.8: (a) Violaxanthin, and (b) antheraxanthin (closed symbols) & zeaxanthin (open symbols) concentrations (mg/m^3), in chemostats C1 (red) and C2 (blue), with time, in continuous light and shifting from continuous back to sinusoidal (orange, from 0 to 150 µE m^{-2} s^{-1}).

Back to sinusoidal light, the ratio C/chla recovers a circadian rhythm but it has a 2-3 hours delay: at least in the first day of measurements, the minimum is at 14.00h instead of the sinusoidal 12.00h, and the maximum is at 18.00h instead of 21.00h (fig.L.6.9a).

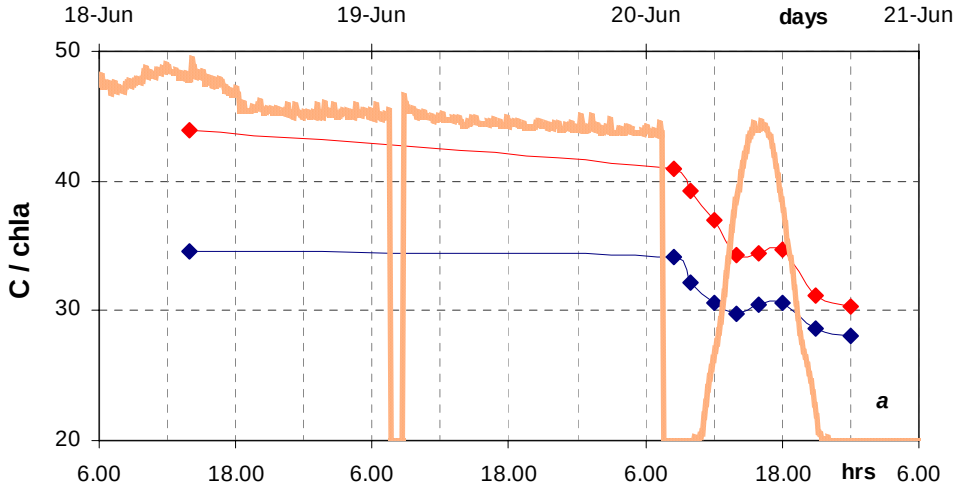

Fig.L.6.9a: The ratio C-content/chlorophyll-*a* (C/chla), in chemostats C1 (red) and C2 (blue), with time, in continuous light and shifting from continuous back to sinusoidal (orange, from 0 to 150 µE m^{-2} s^{-1}).

Chlorophyll-*a* concentration per cell (chla/cell) goes back to a sinusoidal cycle too, with its minimum at 12.00h, but the maximum is anticipated to 21.00h instead of 0.00h (fig.L.6.9b).

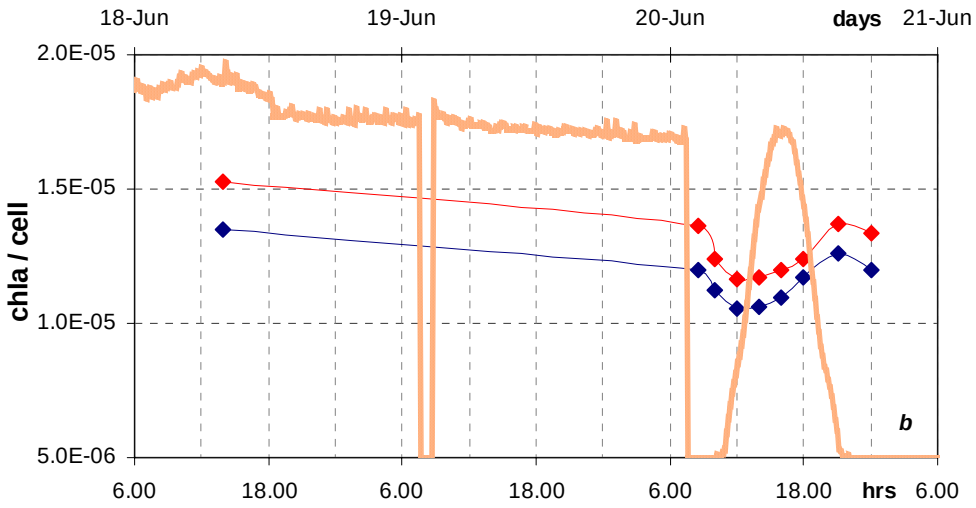

Fig.L.6.9b: The ratio chlorophyll-*a*/number of cells (chla/cell, µg cell^{-1}), in chemostats C1 (red) and C2 (blue), with time, in continuous light and shifting from continuous back to sinusoidal (orange, from 0 to 150 µE m^{-2} s^{-1}).

Chlorophyll-*a* concentration per unit of cell volume (chla/vol) postpones its maximum at 14.00h (instead of 10.00h), finally it goes back to its sinusoidal minimum at 18.00h (fig.L.6.9c).

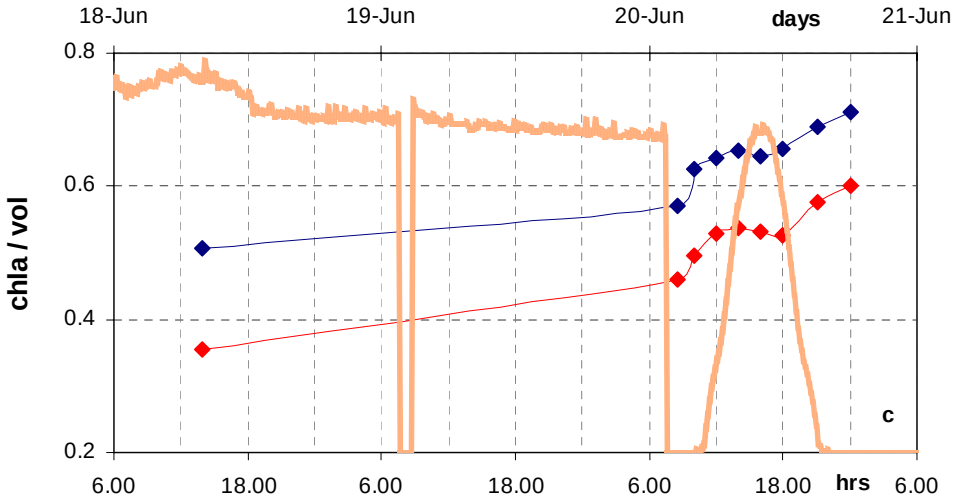

Fig.L.6.9c: The ratio chlorophyll-*a*/cell volume (chla/vol, µg l^{-1} µm^{-3}), in chemostats C1 (red) and C2 (blue), with time, in continuous light and shifting from continuous back to sinusoidal (orange, from 0 to 150 µE m^{-2} s^{-1}).

4. Discussion

4.a Field measurements

4.a.1 Hydrology and nutrients

In the Western Mediterranean Sea, the surface typical water is the Modified Atlantic Water (MAW), which constitutes a generally 200-m deep layer characterized by a salinity (s) <36.5 at its entrance at Gibraltar and a temperature T=14-15°C below the upper mixed layer. The MAW is the only water mass in the Atlantic and Gibraltar stations (stM25-M26, figs.f1a, 3a and 4a).

The MAW (s<36.9, σ_τ<27 kg/m^3, T>20°C) lays on a salty, denser and colder water, the Deep Mediterranean Water (DMW), which is made of an intermediate layer (WIW, Winter Intermediate Water, and LIW, Levantine Intermediate Water) and a deeper one (WDMW, Western Deep Mediterranean Sea, see the review by Millot 1999). Lacombe and Richez (1982) named Atlantic Mediterranean Interface (AMI) the mixing interface between the MAW and the DMW. The AMI is the sub-surface layer with s=37.0-37.5, σ_τ=27-27.5 kg/m^3 and T=15-20°C. Thus they referred as DMW to the water with s>37.5, σ_τ>27.7 kg/m^3, T<15°C. The three water layers are clearly detectable in figs.f 1, 3 and 4.

Figs.f1, 3 and 4 show that dense cold DMW upwells to very low depths in correspondence of stM16-A2-M17 and stM21 (<125m, s=38.3, σ_τ>27.7 kg/m^3, T<15°C). On the contrary, warmer MAW downwells deep in correspondence of stM13-M19-M22 (>110m, s=36.5-36.9, σ_τ<27 kg/m^3, T=15-20°C). That indicates the presence of two main mesoscale structures, a Western one in correspondence of stM21, and an eastern one in correspondence of stM16-A2-A4-M17 (figs.f1a and c). In particular, the eastern structure is a cyclonic gyre: it is 100 km wide and 400-500 m deep (aa.vv. 2006). Its dome is located below the strong sub-surface thermocline (around 25-m deep, figs.f4a and c), and it determines downwelling of MAW and coastal upwelling of Mediterranean water (at stA6 and stA1) along its edges. That cyclonic eddy likely derives from the unstable Algerian Current (see also fig.i.2) and it is located approximately in the same area as the one detected by Moran *et al.* (2001) in the same season (October 1996).

Finally, the G-transect, which is located between Almeria and Oran, shows a large picnocline, due to the gradual mixing of MAW and DMW (fig.f1b, 3b and 4b).

4.a.2 Phytoplankton community characterisation

The autotrophic biomass by chlorophyll-*a* fluorescence profiles (fig.f5) is mainly located from surface to 75 m, likely due to light availability. In particular, the highest concentrations can be detected right at the top of the 2 mesoscale structures (25-30 m deep) and deeper along their edges (40-50 m deep, figs.f5a and c), i.e. at the mixing interface between Atlantic and Mediterranean waters. Moreover, fluorescence values are high also deeper (40-45 m) in the coastal stations stG1-G4-J8, and at stA1 where fluorescence reaches its maximum (figs.f5b and c). On the contrary, MAW is generally poor in biomass, except for the Gibraltar stations.

Biomass distribution is generally strongly coupled with nutrients availability: the nutrient-rich Mediterranean water upwells and mixes with the surface nutrients-depleted Atlantic water, thus determining a fertilization event (Millot 1994), and as a consequence higher biomass concentrations right along the picnocline. In fact, in the Western Mediterranean, enhanced productivity is typically detected at upwelling (Gomez *et al.* 2000, Moran *et al.* 2001, Arin *et al.* 2002) and frontal zones (Fiala *et al.* 2004, Videau *et al*. 1994, Rodriguez *et al.* 1998, Leblanc *et al*. 2004). Our data confirm the link between biomass distribution and nutrients inputs: figs.f6, 7 and 8 reveal high concentrations of all the nutrients in the DMW just below the picnocline in correspondence of the two main mesoscale structures and along their edges, finally in the coastal stations stG1-J8. Both phosphate and silicate can reach higher values also in the AMI and in surface water in the eastern eddy, though phosphate distribution is rather patchy, also in DMW (figs.f7 and 8).

From surface to 65-m deep, data of biomass distribution by fluorescence emission are confirmed by both total cells abundances from microscopic countings (fig.f9) and total chlorophyll-*a* concentration by HPLC analysis (fig.f16). Phytoplanktonic cells are mainly localized in the surface and picnocline waters in the core area of the 2 mesoscale structures, in particular at the eastern one (stM17, 25 m: 200000 cell/l, chla=4.7 mg/m^3), but also at the picnocline and below it along the edges (chla=1.3-1.8 mg/m^3; stA1, 25 m: 393000 cell/l). These data agree with Moran *et al.* (2001) findings of increased chlorophyll-a concentrations in the central part of the cyclonic eddy and along its edges (chla>1.4 mg/m^3) and confirm the productive character of the central part of cyclonic eddies when compared to anticyclonic ones (see also Viala *et al.* 1994, Rodriguez *et al.* 1998).

Finally, along the G-transect phytoplankton is distributed mainly beneath the picnocline (40-45 m deep) in the coastal stations (chla=0.9-1.2 mg/m^3).

Microplanktonic algae generally dominate phytoplankton assemblages in nutrient-rich areas, like coastal zones and upwellings (Harris 1986). In particular, cyclonic eddies are known for microplanktonic large contribute to the total assemblage, especially when compared to anticyclonic eddies, which are generally dominated by nano- and picoplankton (Fiala *et al.* 1994, Videau *et al.* 1994, Rodriguez *et al.* 1998, Polonelli 2006).

Between microplankton, *Bacillariophyceae* main contribute is well documented in the mesoscale mixed areas of the Western Mediterranean, likely due to diatoms preference for turbulent, nutrient-rich (silicate-rich) and low-light waters (Gould and Wiesenburg 1990, Fiala *et al.* 1994, Videau *et al.* 1994, Arin *et al.* 2002, Leblanc *et al.* 2004, Mercado *et al.* 2005): small fast growing diatoms would take advantage of nutrients and turbulence would maintain them in the euphotic zone (Kiørboe 1993). Gould and Wiesenburg (1990) reported a mono-specific bloom of *Thalassiosira partheneia* Schrader, a small centric colony-forming diatom which resulted extremely abundant (>9.8 x 10^6 cell/l, chla=23.1 mg/m^3) in a 54-m deep sample collected along the Almeria-Oran front. That data was confirmed by Fiala *et al.* (1994), who recorded mono-specific diatom blooms in the frontal-jet: *Proboscia alata* (Brightwell) Sundström or *Thalassiosira* cf. *partheneia* Schrader, determining the DCM, with chla=1-2.6 mg/m^3. Our data partly confirm these reports, in fact our samples were dominated by a small centric colony-forming diatom too, likely *Thalassiosira partheneia* Schrader. The blooms were detected in turbulent 40-m deep areas of DMW upwelling, nevertheless only in the station stM18 along the edge of the eastern eddy, and at the coastal stations stG1 and stJ8 (fucoxanthin concentrations: stG1 40 m=0.25 mg/m^3, stJ8 40 m=0.13 mg/m^3, fig.f17b), and, at the highest abundance at stA1 (282000 cell/l, fig.f10c).

The phytoplankton surface and sub-surface assemblages of the eastern eddy are dominated by *Fibrocapsa japonica* Toriumi & Takano (Raphidophyceae, fig.f12), and Dinophyceans. *F. japonica* is a potentially harmful alga which is known for forming blooms in coastal and inland waters: it was reported for the first time in Japan (Okaichi 1972), where it was associated to mass fish mortality events (Toriumi and Takano 1973, Ono 1989). Since then, it was detected worldwide in temperate waters: in south California (Loeblich and Fine, 1977), along the American Atlantic coasts (Smayda and Villareal 1989, Lewitus and Holland 2003), in the Mexican coastal waters (Band-

Schmidt *et al.* 2004), in the southern-Atlantic (Odebrecht and Abreu 1995), in southern Australia and New Zealand (Rhodes *et al.* 1993). *F. japonica* has been reported in European waters as well (Billard 1992, Vrieling *et al.* 1995, Thomas 1998, Congestri *et al.* 2000, Cucchiari *et al.* 2006) and an analysis of genetic variation among nuclear ribosomial DNA ITS regions between different strains revealed a high degree of polymorphisms, likely due to hybridisaton mechanisms (Kooistra *et al.* 2001).

Though the exact mechanism of toxicity in the Raphidophyceans has not been established yet, *F. japonica* ichtyotoxicity has been linked to the production of abundant mucous which would cause clogging of fish gills (Fu 2003), ROS causing fish asphyxia (Oda *et al.* 1997), haemolytic compounds (Fu *et al.* 2004) and neurotoxins (brevetoxins, Khan *et al.* 1996). Experiments conducted on *F. japonica* suggest that it has a low efficiency in nutrient uptake (de Boer *et al.* 2004, Cucchiari *et al.* 2007), thus its growth is favoured by high-nutrient conditions (Riegman *et al.* 1996). It is considered an eurithermal species (growth optimum temperature T=21-24.5°C) and the European isolate from the German Wadden sea can survive to very low temperatures by cyst formation (de Boer *et al.* 2005). Finally, *F. japonica* appear well equipped against grazers, in fact its trichocycsts work as deterrent against pallium-feeding eterotrophic dinoflagellates (Tillmann and Reckermann 2002), moreover its haemolytic compounds may inhibit bacteria growth (van Rijssel *et al.* 2008), though it has been suggested that both dinoflagellate grazing (Tillmann and Reckermann 2002) and algicidal bacteria, rather than nutrient limitation, can contribute to its bloom decline, especially in eutrophic coastal regions (Liu *et al.* 2008).

To our knowledge, ours is the first report of *F. japonica* in the Alboran Sea, though Mercado *et al.* (2005) identified some Raphidophyceae in samples collected along the Malaga coasts. Moreover, it's the first report of this species in a not strictly coastal area, but it is rather localized in a cyclonic eddy (stM17, 25 m: 59500 *F. japonica* cells/l, fucoxanthin=1.2 mg/m^3; A-transect: fucoxanthin>0.3 mg/m^3, fig.f17b). Since Yoshimatsu (1987) reported cysts germination linked to low temperature, with high rates of germination when cysts were kept at 12°C, we suggest that low temperatures of DMW might have favoured cyst formation, while warmer nutrient-rich waters at the AMI in correspondence of the cyclonic eddy might have determined their germination. Moreover, since *F. japonica* is generally a coastal species, the possibility of a coastal origin of the bloom cannot be excluded. We can also assume that *F. japonica* ability to aggregate in mucous nets might have supported its bloom in such a turbulent area, as suggested for dinoflagellates by Smayda (2002). The risk involved in the abundant presence of a potentially toxic species in the phytoplanktonic assemblage of a mesoscale

structure lay in the potential of a quick and wide expansion of its distribution range. Though the preliminary investigation by PCR amplification of nuclear ITS regions confirmed its microscopic identification, further work needs to be done to reveal the possible dispersal route followed by the Alboran strain from a presumably known one. However, field salinity values at the eddy (s>37) might suggest a Mediterranean origin, since the Adriatic strain has a higher optimum salinity range (s=30-38) when compared to the Wadden Sea and North Sea (s=25-35, Khan *et al.* 1996, de Boer *et al.* 2004, Cucchiari *et al.* 2007).

Figs. 13 and 19 indicate that dinoflagellates co-dominate together with *Fibrocapsa japonica*, in particular at the eastern mesoscale structure, and they were abundant along the water column, both in the upper mixed layer and in the turbulent AMI waters. The most abundant species are small fast-dividing techates, like *Heterocapsa* spp., which might have taken advantage of turbulent nutrient-rich water to grow (Kiørboe 1993). Moreover, large abundance of the athecate *Gyrodinium* sp. cf. *fusiforme* Kofoid et Swezy might be linked to *F. japonica*: since in *Gyrodinium* spp. mixotrophy is well documented, thus we can suggest he might have grazed on *F. japonica* (Nakamura *et al.* 1992).

It's finally worth of notice the presence of a few harmful species of dinoflagellates (*Gymnodinium catenatum* Graham, *Karenia* sp., *Lingulodinium polyedricum* (Stein) Dodge, *Prorocentrum* spp., *Gonyaulax hyalina* Ostenfeld and Schmidt, and *Gonyaulax polygramma* Stein), which confirms the role of the Alboran sea as a corridor for Atlantic (toxic) species espansion eastward (Gomez 2003).

Together with diatoms, or with *F. japonica* and dinoflagellates, high abundances of *Prymnesiophyceae Coccolithophorales,* in particular *Emiliania huxleyi* (Lohmann) Hay et Mohler, and *Gephyrocapsa oceanica* Kamptner, were often detected: this class is abundant generally in deep turbulent nutrient-rich water, both in the eastern gyre, along its edge and at the coastal stations at depths around 40-60 m (fig.f 14 and 20). The high contribute of *Emiliania huxleyi* and *Gephyrocapsa oceanica* is well documented in frontal turbulent areas in Western Mediterranean (Estrada *et al.* 1999, Mercado *et al.* 2005), especially together with diatoms in correspondence of the mixing interface along the MAW jet (Fiala *et al.* 1994).

The map of 19'- Hesanoyloxyfucoxanthin distribution reveals the importance of large though rare species to the total biomass in the MAW, mainly *Discosphaera tubifer*

(Murray & Blackman) Ostenfeld, and *Helicosphaera carteri* (Wallich) Kamptner (figs.f14a and 20a).

Finally, nanoplanktonic flagellates were detected as well, both in correspondence of the two main mesoscale structures and along their edges, i.e. in turbulent waters, and in the upper mixed layer, i.e. nutrient-depleted MAW (fig.f15). Zeaxanthin and divinil chlorophyll-*a* concentrations by HPLC analysis suggest that *Cyanophyta* and *Prochlorophyta* as well are distributed mainly in surface waters, both on the Atlantic side and at the eastern eddy (figs.f24 and 25).

These results confirm previous findings of higher picoplanktonic abundances in surface, nutrient-depleted waters (Claustre *et al.* 1994, Rodriguez *et al.* 1998, Moran *et al.* 2001): the microplanktonic growth is limited by nutrients availability, thus it is strongly linked to fertilization events which take place at upwelling and frontal zones. The nano- and picoplanktonic fraction can take advantage of nutrient-rich waters as well (in fact it is abundant at the gyres too), but it determines the main contribute to total biomass in the oligotrophic surface waters (Fiala *et al.* 1994, Videau *et al.* 1994, Arin *et al.* 2002, Jacquet *et al.* 2002, Leblanc *et al.* 2004).

4.a.3 Photoprotective carotenoids

In the MAW assemblages along all the transects, we detected high ratios PPC/Tchla, meaning that high photoprotection is in progress, and decreasing ratios with depth along the water column, i.e. cells are less photoprotected when comparing MAW to AMI and to DMW (fig.f26). On the contrary, surface samples from the two main upwelling systems showed minimum ratios, i.e. photoprotection is very low, though in high light conditions. That would be confirmed also by the higher slope of the linear regression between chlorophyll-*a* and fluorescence in fig.f17b: a higher fraction of light energy would be dissipated as fluorescence as a photoprotective non-photochemical quenching mechanism (Schreiber *et al*. 1995). The increase in photoprotective pigment pool relative to chlorophyll-*a* is a long-term photoacclimation process occurring on time-scales from hours to days, involving the variation of photoprotective xanthophyll concentrations (Bidigare *et al.* 1987). The low PPC/Tchla ratio in the surface cyclonic waters thus indicates that the assemblage has experienced high irradiance for a time not long-enough (hours) to trigger that photoprotective mechanisms, while MAW samples exhibit high values from 0 to 30-35 m of depth, due to downward transport from surface (Claustre *et al.* 1994). That results are further confirmed for *F. japonica* through the analysis of the covariation between the ratios zeaxanthin / fucoxanthin and violaxanthin

/ zeaxanthin (fig.f27): zea/fuco < 1 and viola/zea < 0.45 indicate that *F. japonica* from surface samples is more photoprotected than the 25/30-m deep.

Thus, both these two indexes constitute a biological confirm of the upward direction of the mesoscale water flux: it is indeed a cyclonic structure and deep nutrient-rich water upwells, determining new, not-photoprotected biomass production.

4.a.4 Statistical analysis

The similarity analysis within stations by Kendall's τ coefficient reveals that the picnocline generally is a real barrier between above- and below-populations, in fact all the stations have higher values of τ when comparing samples which are both on the same side of the picnocline (fig.f28). Nevertheless, the similarity depends on the picnocline width: when the mixing interface is wide, the picnocline may be no more a barrier, like in stJ8, while when the picnocline is very strong, the mixing interface assemblage can separate and appear different from both the below- and the above- ones (as for stA4).

Moreover, the similarity analysis between stations (fig.f29) indicates that samples adjacent coming from the same depth are similar when water mass have similar origin: in fact, the highest τ can be detected when comparing two stations belonging to the same upwelling water (for example, the deep samples from stM16 and stM17) or from the same MAW (like surface samples along the G-transect). Finally, low τ from the A-transect picnocline area indicate a large horizontal diversity.

The aim of the Principal Component Analysis (PCA) was to detect the main factors determining biomass distribution in the investigated area, in an attempt to gain a general description of such an heterogeneous ecosystem. As expected in such an unstable area, both hydrological (temperature, salinity, density, nutrients) and biological (chlorophyll-*a* and total cells) factors are driven by the hydrodynamics of the water column, so that samples result separated on the factor-plan between MAW, AMI and DMW samples (fig.f32). Then, phytoplanktonic nutrient uptake allow to differentiate between fast-growing and fast nutrient-uptaking cells in the AMI, while nutrient-recycling cells in the oligotrophic MAW. When focusing on *F. japonica* (fig.f 34), nutrient release separates surface nutrient-depleted samples, which are rich in (likely)slowly growing cells, from nutrient-rich deep samples, which contains low cell abundances. In this case, the PCA might suggest us that *F. japonica* cells are in a post-bloom phase, and that the assemblage switched its metabolism on a nutrient recycling one. That would be

supported by post-bloom cell abundances values (maximum $6x10^4$ cell/l) and by the detection of cells often aggregated in mucous nets, as a result of stress-conditions. Alternatively, bacterial re-mineralization of nutrients might support *F. japonica* assemblage, or on the contrary bacteria might promote the bloom decline (Liu *et al.* 2008). Nevertheless, the PC1 suggest high cell abundances at turbulent depths, in contrast to the numerous documented reports on *F. japonica* and *Raphidophyceae* in general.

4.b Laboratory measurements:

Experiment 1: sinusoidal light.

Circadian rhythms are well known both in prokaryotic (like *Synechococcus sp.*) and in eukaryotic microalgae: diatoms, dinoflagellates, Chlorophytes, Chrysophytes, Prochlorococcus sp., Haptophyceae (for a detailed bibliography, see the following reviews: Suzuki and Johnson 2001, Behrenfeld *et al.* 2004, Bruyant *et al.* 2005, Mas *et al.* 2008), and Raphidophyceans too. In particular diel vertical migrations by *Goniostomum semen* (Salonen and Rosenberg 2000), *Chattonella spp*., *Fibrocapsa japonica* and *Heterosigma akashiwo* (Watanabe *et al.* 1988, Takahashi and Hara 1989, Handy *et al.* 2005, Takuji *et al.* 2006) were documented both in laboratory and in field experiments, both with or without stratification.

These rhythms are thought to allow the best timing between cellular processes and external resources availability, and this is particularly true for light and photosynthetic organisms (Suzuki and Johnson 2001). In fact, it's generally accepted that metabolic pathways oscillates when cells are grown in non-steady conditions, because cell requires light (i.e., it produces energy) or carbon (i.e., it consumes energy) according to the different phases of its cycle, and this generates a rhythm (Post *et al.* 1985).

Many cellular processes and features can show diel periodicity: the timing of cell division, the optical properties, photosynthetic activity, but also bioluminescence emission and UV-sensitivity, reflecting circadian mRNA transcription and/or translation periodicity (Suzuki and Johnson 2001).

Experiments 1 and 4 confirm the presence of diel rhythms in *Heterosigma akashiwo* grown under a sinusoidal light regime: photosynthetic parameters by oxygen evolved measurements, the timing of cell division, carbon, nitrogen and pigments content, and absorption properties all show a 24-hours periodicity.

Both the photosynthetic parameters α^b and $P^b max$ show diel variations, in particular they are both maximum after dawn (8.30h-9.30h), while $P^b max$ is minimum before sunset (18.30h) and α^b before midnight (0.30h, figs.L.1.1a and b), with 3-fold α^b and 4-fold $P^b max$ variations. Both the timing with respect to the light:dark cycle and the amplitude of variations are largely confirmed by literature: in fact, photosynthetic parameters can vary from 2-fold to more than 20-fold in the numerous phytoplanktonic species examined (diatoms, dinoflagellates, chlorophytes, chrysophytes, *Prochlorococcus* sp., *Synechococcus sp*.) and their usual timing during the 24 hours

indicates an increase during the last hours of the night with a peak in the morning or before noon, and a minimum in the evening (Behrenfeld *et al.* 2004). To our knowledge, this is the first report of photosynthetic parameters diel variations in a Raphidophycean, and it confirms also for α^b and P^bmax of *Heterosigma akashiwo* the typical pattern of daily variations.

Experiment 1 clearly shows that α^b varies slightly only from after-dawn to after-midday (10.30h-16.30h, fig.L.1.1a), in fact the Ek decrease is mainly due to P^bmax decreasing (fig.L.1.3d). During these 6 hours, the specific absorption cross-section a*676 increases (fig.L.1.13b), while the blue/red ratio is constant or slightly increasing (fig.L.1.13c), meaning constant or slightly decreased package effect (Morel and Bricaud 1981). This is due to the combination of two factors: (i) both chlorophyll-*a* and chlorophyll-*c* and fucoxanthin concentrations increase during the morning as light intensity increases (figs.L.1.8a, b and c), but the ratio chlc/chla is constant while fuco/chla markedly lowers (figs.L.1.9a and b); and (ii) both chla and cell volume (fig.L.1.5b) increase but the ratio chla/vol decreases (fig.L.1.14c). The consequence of that is the photosystems size and number reduction (see for a review, MacIntyre *et al*. 2002). Furthermore, photoprotective pigments (both β-carotene, violaxanthin, antheraxanthin and zeaxanthin, see below) markedly increase (figs.L.1.10a, 1.11a and b), meaning more efficient photoprotection in progress (Falkowski and Raven 1997). Nevertheless, both α^b and a*676 remain quite stable under strong irradiance, with the consequence of maintaining a high and stable light-harvesting efficiency.

In experiment 1, α^b lowers from after midday to before midnight, causing an Ek increase (fig.L.1.3d). From 18.30h to 20.30h, photosynthetic pigments concentrations lowers (fig.L.1.8), but chlorophyll-*a* marked decrease, which is reflected in a*676 lowering (fig.L.1.13b), results in the increase of photosynthetic pigments to chlorophyll-*a* ratios as far as the first hours of the night, thus in the increasing of photosystems size (fig.L.1.9). In fact, fig.L.1.13c shows that the blue/red ratio decreases, hence the package effect sharply increases. That is likely due to the cell volume decrease (fig.L.1.5b), confirmed by the chla/cell increase from 17:30 (fig.L.1.14c), meaning an increase in photosystems number as well. Moreover, as light intensity decreases, also photoprotective pigments decrease (figs.L.1.10a and 1.11), in particular β-carotene/chla, viola/chla, anthera/chla and zea/chla all remain stable around their minimum values (figs.L.1.10b and 1.12), meaning that the fraction of captured energy which would be dissipated is now reduced. Then, α^b decreases as light intensity lowers, as a consequence of a lower light-harvesting efficiency.

Finally, during the night (from before midnight to dawn) α^b increases back again (fig.L.1.1a), at the same time both the photosynthetic and the photoprotective pigments and all their ratios to chlorophyll-*a* (figs.L.1.8, 1.9, 1.10, 1.11 and 1.12) and chla/cell (fig.L.1.14b) lower, thus determining a reduction in photosystems size. Around midnight (0.30h-4.30h), cell number and volume are constant (fig.L.1.5), while both chla/vol (fig.L.1.14c) and a*676 (fig.L.1.13b) decrease. As a consequence the blue/red ratio starts increasing, meaning a lowering of the package effect (fig.L.1.13c), resulting in a first increase of light-harvesting efficiency, due to photosystems reduced number. Moreover, during the following 6 hours cells divide (fig.L.1.15), thus chla/vol increases (fig.L.1.14c), while chlc/chla is constant and fuco/chla turns back to its dawn value slowly (fig.L.1.9), nevertheless the package effect lowers (fig.L.1.13c) and a*676 (fig.L.1.13b) sharply increase, meaning that light-harvesting capacity keeps on increasing as far as α^b maximum value in the morning.

P^bmax decreases markedly from after-dawn to before-sunset (in fact the Ek decrease is mainly due to P^bmax, fig.L.1.3d), then it increases back to its maximum first slowly (19.30h-23.30h), then sharply (0.30h-9.30h, fig.L.1.1b). Fig.L.1.4 shows that P^bmax and β^b are positively correlated: this means that when photosynthetic rates are low, a low photoinibition is in progress, that is the case of the light period. The light period is the lag of maximum photoprotection, as resulting from photoprotective pigments patterns (figs.L.1.11 and 1.12). At high irradiance, generally Raphidophyceans dissipate light through the xanthophylls cycle, with violaxanthin de-epossidating in a two-steps process to antheraxanthin first, then to zeaxanthin (Demming-Adams *et al*. 1996, Mostaert *et al*. 1998). During experiment 1, antheraxanthin and zeaxanthin peaked at midday (16.00h, fig.L.1.11b), indicating the highest photoprotection in progress right at the highest irradiance level. Violaxanthin increased markedly soon after dawn (9.30h), peaking 2 hours after irradiance maximum (16.00h) and finally decreasing sharply within 1 hour after sunset back to its minimum value (21.00h, fig.L.11a): that indicates that part of violaxanthin is constitutive (as observed in higher plants by Eskling *et al*. 1997), moreover that there is a massive neosynthesis of violaxanthin before midday followed by an accumulation of violaxanthin, by re-epoxidation of antheraxanthin and zeaxanthin, within a few hours from the maximal irradiance. That is confirmed also by the viola/chla pattern (fig.L.1.12a), which shows a net decrease at midday, meaning that all the photoprotective violaxanthin fraction has been de-epossidated. On the contrary, P^bmax decreases during the dark period because high photoinibition is in progress when

photoprotective xanthophylls cycle is not active (figs.L.1.11 and 1.12). Therefore, P^bmax and β^b covariation appears strongly linked to the xanthophylls cycle.

It's worth of notice that β-carotene concentration starts increasing 2 hours earlier than violaxanthin (and so does the β-carot/chla ratio, fig.L.1.10), peaking 1 hour after midday then decreasing back to its minimum after sunset, thus imitating the day irradiance variation. The β-carot/chla ratio is maximum 2 hours before midday: since β-carotene acts as a photoprotective pigment as part of a constitutive safety valve (Niyogi 2000), the increase of β-carotene is likely the first photoprotective mechanism, which is triggered before dawn, thus anticipating the light increase: that would be confirmed also by β-carot/chla earlier increase right after midnight (fig.L.1.10b). Nevertheless, the xanthophylls cycle should be preferred to assure a powerful photoprotection when irradiance reaches its maximum.

From 10.30h to 18.30h, cell volume increases (fig.L.1.5b) due to active organic compounds photosynthesis and storage: in fact DIC concentration markedly lowers due to carbon assimilation and fixation, until after midday (15.30h, fig.L.1.7a), while on the contrary organic C content (fig.L.1.6b) and C/chla ratio (fig.L.1.14a) increase. Light-harvesting capacity is high and stable, then P^bmax decrease at high irradiance may be likely due to a/some "downstream" of PSII processe(es). *Heterosigma akashiwo* is known for direct CO_2 assimilation (Nimer *et al.* 1997), then the absence of CO_2 concentration mechanisms in Raphidophyceans could be a very-limiting step for photosynthesis (Fu *et al*. 2008). However, since organic C concentration is still linearly increasing 2 hours later than DIC decrease (figs.L.1.6b and 1.7a), we can exclude the possibility that the rate of carbon procurement was a limiting factor for P^bmax: a not-limiting CO_2 concentration in the vessels has been presumably assured by the culture bubbling (see Materials and Methods). Then, the rate-limiting step(s) for light-saturated photosynthesis must involve component(s) of the photosynthetic electron transport chain, the RUBISCO and/or the RUBISCO activase enzymes, and/or component(s) of the Calvin cycle.

On the contrary, P^bmax increases back from sunset, first slowly (19.30h-23.30h), then sharply (0.30h-9.30h) to its after-dawn maximum (fig.L.1.1b): in the dark, no downstream PSII component likely limits it, but rather high photoinibition in progress. At the same time, DIC increases (fig.L.1.7a) and organic C lowers (fig.L.1.6b) due to consumption by respiration in the dark period, which determines the lowering of C/chla ratio (fig.L.1.14a).

α^b and P^bmax do not covary during the light period, i.e. photosynthetic parameters show an Ek-dependent pattern of variability, and this means photoacclimation in progress. On the contrary, they are positively correlated during the night to after-dawn (fig.L.1.3a), showing a phase of Ek-independence.

In experiment 1, cell division starts after midnight (3.00h), as indicated by cells number marked increase and cell volume reduction, and it completes around 11.00h (fig.L.1.5). At the same time, inorganic carbon and nitrogen are released (DIC and NO_2+NO_3 increasing as far as 7.30h by respiration, fig.L.1.7), while both organic carbon and the C/N ratio decrease slowly, indicating a new Calvin cycle and light-harvesting components synthesis. Thus, the driving process during the night is cell division, which asks for a large reductants amount (Behrenfeld *et al*. 2004), which is reflected in α^b and P^bmax covariation (fig.L.1.2).

On the contrary, during the light period energy is used for carbon fixation and compounds storage, for amino acids and pigments synthesis (as confirmed by figs.L.1.6, 1.7 and 1.8), thus the dominant pathway asks for ATP, but since α^b and P^bmax do not covary (fig.L.1.2), *Heterosigma akashiwo* appears not in need of an extra ATP amount through the suggested metabolic pathways. Behrenfeld *et al*. (2004) suggested that back-reactions to the photosystems are the main mechanism to additional ATP generation in the light. Moreover, raphidophytes are known for producing very large amounts of reactive oxygen species (ROS, Oda *et al*. 1997), in particular *Heterosigma akashiwo* can produces very high level of superoxide (Marshall *et al*. 2005). Kim *et al*. (2004) demonstrated in *Chattonella antiqua* an increase of ROS concentration during the light period and a decrease in the dark one, that they linked to photosynthesis. ROS are produced through the oxidation of NADPH to $NADP^+$, partly associated with photosynthesis (Twiner and Trick 2000, Marshall *et al*. 2002) and partly not, but rather related to a plasma membrane NADPH-dependent enzymatic pathway, at least in *Chattonella marina* (Kim *et al*. 2000, Liu *et al*. 2007). Thus we can make the hypothesis of a large consumption of reductants due to ROS production during the light period in *Heterosigma akashiwo*, thus explaining the absence of diurnal α^b and P^bmax covariation, but also determining an increased nocturnal reductants demand, thus explaining the night α^b and P^bmax covariation.

It's finally worth of notice that Raphidophyceans, like other microalgae, can produce high levels of mycosporine-like amino acids (MAAs, Jeffrey *et al*. 1999), which are known for their photoprotective function against UV-radiation, but also against high PAR, and are supposed to serve as antioxidant as well (Dunlap and Yamamoto 1995),

by neutralizing ROS toxic effect in case of high production under high light conditions (Marshall and Newman 2002).

Experiment 2: from sinusoidal to continuous light.

α^b and P^bmax loose their diel periodicity when shifting from sinusoidal to continuous light: α^b doesn't lower from 16:30h, but it remains nearly constant for the following 4 hours, then it shows ample oscillations (fig.L.2.1a), while P^bmax doesn't start recovering from 18.30h, but keeps on decreasing (fig.L.2.1b). Thus the night covariation between α^b and P^bmax disappears: the two parameters show now an only 2-phases pattern variability, meaning an Ek-dependent variability, i.e. photoacclimation in progress.

α^b and P^bmax maintain their typical diel patterns just for the first 5 hours following the light shift. In fact, like in experiment 1, α^b is rather stable from after-dawn to after-midday (10.30h-16.30h, fig.L.2.1a), as a consequence Ek decreasing is due to P^bmax decrease (fig.L.2.2c). Both chlorophyll-*a* and chlorophyll-*c* and fucoxanthin concentrations increase (fig.L.2.7), but following a linear slow pattern, because the irradiance is now only half of the sinusoidal maximum, so the ratios chlc/chla and fuco/chla are stable and low (fig.L.2.8). Moreover, both chla and cell volume (fig.L.2.4b) increase, but the volume increase is linear and slow too, so that the chla/vol ratio is constant (fig.L.2.13c). Thus the light-harvesting complexes likely are constant in number. However, since cell number is constant between 12.00h and 16.00h (fig.L.2.4a), chla/cell increases from 12.00 (fig.L.2.13b), consequently photosystems are increasing in size. The consequence is an increase of the package effect, which is confirmed by the decreasing blue/red ratio right after the light shift (fig.L.2.12c) and by the coincident decrease in a*676 (fig.L.2.12b). Nevertheless, α^b is constant in continuous light 5 hours after the shift. Like in sinusoidal light, P^bmax sharply decreases from dawn to before-sunset (fig.L.2.2a). Fig.L.2.3 shows the good correlation between P^bmax and β^b, meaning that light-saturated photosynthesis lowers when photoinibition lowers, that means that photoprotection is in progress. Violaxanthin starts increasing after dawn, then it reaches its maximum 2 hours after the light shift and remains stable for the following 2 hours, then it sharply decreases to its minimum value at 17.30h (fig.L.2.10a). Simultaneously, antheraxanthin and zeaxanthin reach their maximums (17.30h, fig.L.2.10b): since zeaxanthin concentration is very high when compared to violaxanthin and antheraxanthin, it's likely that the whole photoprotective fraction of

violaxanthin has been de-epoxidated to antheraxanthin and mainly to zeaxanthin. Thus, the xanthophyll cycle assures photoprotection when shifting light to continuous, assuring a high stable and efficient energy use, though photosystems size increase.

From 16.30h to 19.30h, α^b is still rather constant (fig.L.2.1a). At the same time, chlorophyll-*a*, chlorophyll-*c* and fucoxanthin, and the chlc/chla and fuco/chla ratios all keep on increasing (as far as 19.30h, figs.L.2.7 and 2.9a). Cells are reducing in number but are larger (fig.L.2.4): since chla/vol is decreasing (fig.L.2.13c) due to cell volume linear increase (fig.L.2.4b), photosystems may be reducing in number but their size may be increasing. That is likely confirmed by chla/cell increase (fig.L.2.13b), then photosystems are few but large, and as a consequence the package effect should be high: that is confirmed by the low blue/red ratio and by the a*676 reduction (fig.L.2.12b and c), indicating a reduction of light-harvesting efficiency. Nevertheless, α^b is still constant 9 hours after the light shift to continuous light. From 17.30h (=7 hours after the light shift), violaxanthin starts increasing linearly, while antheraxanthin remains stable on its 17.30h-value, finally zeaxanthin sharply decreases back to its minimum value (fig.L.2.10). Since the viola/chla, anthera/chla and zea/chla ratios follow the corresponding pigment pattern (fig.L.2.11), the fraction of violaxanthin per photosystem increases, but it doesn't work as a photoprotective pigment, since antheraxanthin and zeaxanthin do not increase. Presumably, though light is continuous, from 17.30h the effectively harvested fraction is never high enough to trigger the xanthophylls cycle.

β-carotene follows the same pattern as the other photosynthetic pigments (fig.L.2.9a), but β-carot/chla ratio maintains its sinusoidal cycle, with its concentration peaking 1 hour after dawn, then decreasing back to its minimum after sunset (fig.L.2.9b). At a lower (half), though continuous light intensity, β-carotene mediated de-excitation could be likely preferred so as to assure photoprotection when irradiance is not sufficient to trigger the xanthophylls cycle, in particular in this second lag of time.

As already mentioned, Raphidophytes are known for producing very large amounts of ROS, only partly associated with photosynthetic processes. Though Liu *et al*. (2007) report for *Chattonella marina* the absence of any effect on ROS production of the length of the photoperiod under a sinusoidal light regime, Kim *et al*. (2004) demonstrated a clear increase of ROS concentration during the light period in *Chattonella antiqua*. A continuous light regime could induce a larger synthesis of ROS, that would thus work as a photoprotective mechanism through dissipation of excessive energy.

From 10.30h to 18.30h, P^bmax decreases following the same pattern as in sinusoidal light: cell volume increases (fig.L.2.4b) due to photosynthesis and storage of organic compounds, in fact DIC concentration markedly lowers due to carbon assimilation and fixation (fig.L.2.6a) and on the contrary organic C content (fig.L.2.5b) and C/chla ratio (fig.L.2.13a) increase. Since light-harvesting efficiency and utilization is high and stable, P^bmax decrease, under continuous irradiance as well, may be due to the saturation of a/some "downstream" of PSII processe(s).

Finally, since 19.30h α^b clearly oscillates (fig.L.2.1a): photosynthetic pigments markedly decrease as far as 6.00h, when they reach a constant value which is the mean value between the sinusoidal maximum and minimum (fig.L.2.7). Cell number decreases and becomes constant and minimum from 5.30h (fig.L.2.4a), so chla/cell is high and constant since 23.30h (fig.L.2.13b), thus indicating large photosystems size. Cell volume keeps on increasing but very slowly (fig.L.2.4b), so chla/vol become lowers to the minimum at 6.00h too (fig.L.2.13c), indicating a reduction of photosystems number. The consequence is a reduced package effect (= increasing blue/red ratio, fig.L.2.12c), which assures a high a*676 again (fig.L.2.12b).

After 18.30h, P^bmax continues to decrease, though slowly (fig.L.2.1b): both the organic and the inorganic carbon concentrations are constant, indicating a constant maximum rate of carbon fixation and storage (confirmed by cell volume increase, fig.L. 2.4b, and by C/chla increase, fig.L.2.13a) and a constant minimum consumption by respiration, from 7 hours after the light shift (figs.L.2.5b and 2.6b). Inorganic nitrogen is constant from 18.30h to 22.30h, then it decreases markedly and linearly during the following 12 hours (fig.L.2.6b), on the contrary its organic concentration slightly increases from 18.30h to 22.30h (fig.L.2.5c), thus determining the slow decrease of the C/N ratio (fig.L.2.5a): these is likely due to the synthesis of pigments and proteins belonging to the larger light-harvesting complexes and photosystems.

Thus α^b light shifting to continuous (from 220 $\mu E\ m^{-2}\ s^{-1}$ to 110 $\mu E\ m^{-2}\ s^{-1}$), oscillates on high values, indicating that the acclimation to continuous light maintains efficient both light-harvesting and energy conversion likely through a gradual increase of the package effect, obtained by increasing photosystems size and, on the contrary, reducing their number.

Our results show that *Heterosigma akashiwo* completely lost its diel periodicity 7-8 hours after the light shift to continuous, indicating that even if capable of phototaxis, its sinusoidal variations were not driven by an endogenous clock, but it's rather an

acclimation to the cyclic availability of light (Owens *et al*. 1980). Thus, our data confirm Handy *et al*. (2005) findings on *Heterosigma akashiwo* from the Delaware Inland Bays.

Moreover, we found that *Heterosigma akashiwo* is able to maintain a high and stable light-harvesting efficiency through different mechanisms of excessive energy dissipation: within 5 hours from the light shift the xanthophylls cycle + β-carotene de-excitation, then mainly changing the package effect by enlargement of photosystems size.

Raphidophyceans are known for growing well in high light conditions: Zhang *et al.* (2006) measured optimum growth rate (μ=0.8 d^{-1}) for H. akashiwo over the light range of 100-600 μEm^{-2} s^{-1}, while both Watanabe *et al.* (1988) and Handy *et al.* (2005) report its vertical migration to the surface right in correspondence of midday. In particular, Ono *et al.* (2000) reported the highest toxicity at the highest growth irradiance (in that case, 200 μEm^{-2} s^{-1}). Warner and Madden (2007) explained the absence of variations in α, ETRmax and NPQ in *Chattonella subsalsa* grown in continuous light when shifted from low to high irradiance (from 30 μEm^{-2} s^{-1} to 200 or 600 μEm^{-2} s^{-1} for short times, i.e. 8 minutes) as resulting from a variation of the active PSII reaction centers number. Moreover, for longer exposure (24 and 48 hours), both α and ETRmax significantly decrease, and the analysis of Fv/Fm recovery indicate a low turnover rate of proteins associated with photosystem PSII reaction center and then a low efficiency in repairing PSII. That would suggest that they are good in avoiding excessive-energy capture (for example, increasing their package effect), and that they prefer it to absorbed energy dissipation. Moreover, they suggested the possibility for carotenoids to act as antioxidants against ROS, not necessarily linked to the xanthophylls cycle, and they supported the hypothesis that state transitions and cyclic electron flow around the photosystem PSI may play an important role in energy dissipation in Raphidophyceans. Gao *et al.* (2007) reported in *Heterosigma akashiwo* a significant inhibition in progress around midday (measured as decreasing Fv/Fm), due to intense light exposure, under both a natural summer (PAR: 0-2800 μEm^{-2} s^{-1}) and an autumn daily cycle (PAR: 0-1850 μEm^{-2} $s^{-}1$), which recovers progressively with time, especially when shifted to very low PAR (9 μEm^{-2} $s^{-}1$), indicating photoacclimation in progress. Moreover, the recovery is quicker when cell density is high, meaning that self-shading can work well as a defense mechanism from high PAR. Finally, MAAs concentration increases as a photoprotective strategy against high PAR (Marshall and Newman 2002, Gao *et al*. 2007), though there is no report of MAAs variations measured on a short time-scale (<

days): a peak in the UV-region is actually present in *H. akashiwo* spectra (data not shown).

Experiment 3: N-starvation in continuous light.

Within 1 day from the beginning of the experiments, cultures are not yet N-starved, but only N-limited (as defined by Young and Beardall 2003), nevertheless the N decrease to ¼ of its initial value has lowered both P^bmax and β^b by oxygen evolved measurements (figs.L.3.1b and c), and α_f, ETRmax and Fv/Fm by variable fluorescence measurements, while both α^b (fig.L.3.1a) and β_f (fig.L.3.2d) are constant.

Chlorophyll-*a*, chlorophyll-*c*, fucoxanthin and β-carotene concentrations (fig.L.3.6), cell volume (fig.L.3.3b) and then chla/vol (fig.L.3.9b) are constant, meaning that photosystems number is stable. However, since cell number is slightly increases, chla/cell has lowered (fig.L.3.9c), thus determining a reduction of photosystems size. Under continuous light, the consequence is a reduced light-harvesting capacity, which causes both α_f and Fv/Fm decreases. Within the first 24 hours, both inorganic and organic C concentration are constant (figs.L.3.5 and 3.4b): since organic N has already started decreasing (fig.L.3.4c), the C/N ratio is increasing (fig.L.3.4a). That means that still nothing changed in C fixation and in the respiratory rates, as confirmed by α^b. Moreover, violaxanthin, antheraxanthin and zeaxanthin concentrations slightly increased (figs.L.3.6e and 3.9), indicating a potential higher photoprotection, and a lower photoinibition, as confirmed by β^b decrease. So ETRmax and P^bmax decreases are the result of reduced both "upward of PSII" and "downward of PSII" processes.

Under N-starvation conditions, both P^bmax and β^b by oxygen evolved, and Fv/Fm and ETRmax by variable fluorescence markedly decrease (figs.L.3.1b,c and 3.2a,c). Fig.L.3.6 shows that N-starvation determines a progressive decrease of all pigments, and likely, proteins concentration (RUBISCO too, Geider 1993). Since chlorophyll-*a* decreases faster, the ratios chlc/chla, fuco/chla and viola/chla increase (figs.L.3.7a,b and d), thus lowering both photosystems size and the efficiency in energy utilization, after the transfer to the reaction centers. Since cell volume linearly increases (fig.L.3.3b), the ratio chla/vol decreases (fig.L.3.9b), thus indicating that photosystems are reduced in number too, as a consequence light-harvesting efficiency is reduced, thus explaining Fv/Fm, ETRmax and P^bmax decrease (fig.L.3.1a). Moreover, antheraxanthin and zeaxanthin concentrations on the 2nd day from N-starvation are very high, indicating

high photoprotection (fig.L.3.9): pigments and proteins decrease generally causes an increase of photoinibition because the cell can't support the photodamaged PSII turn-over (MacIntyre *et al.* 2002), thus cell may dissipate a high fraction of absorbed light through the xanthophylls cycle to avoid PSII photodamage, which could not likely be repaired. Since the ratio β-carot/chla decreases (fig.L.3.7c), the xanthophylls would be preferred to β-carotene for excessive energy dissipation. That would determine an increase in β_f , i.e a reduction of the electron transport rate at high PAR by high energy dissipation, and on the contrary β^b decrease (low photoinibition).

Of course, N-starvation lowers organic nitrogen content (fig.L.3.4c), while organic carbon increases (fig.L.3.4b), thus determining C/N increase (fig.L.3.4a). Moreover, DIC start increasing during N-starvation, due to a lower inorganic C uptake for photosynthetic fixation (fig.L.3.5). Nevertheless, cell volume likely increases due to storage of organic compounds, in particular sticky mucous substances (pers. observ.).

Finally, photosynthetic parameters by oxygen evolved recover within 1 day from N-resupply, then both P^bmax and β^b furtherly increase (fig.L.3.1), while PE parameters by fluorescence measurements recover within 2 (fig.L.3.2). That is likely due to the slow recovery of photosystems efficiency, which depends on pigments, turning back to their initial values within 3 days from N-resupply (figs.L.3.6 and 3.9). Cell volume and number (fig.L.3.3) turn back to their values within 2 days, so also chla/vol and chla/cell manage to recover in the same lag of time (figs.L.3.9b and c). Moreover, like pigments, organic C and N content recovery took place 3 days after the N-resupply as well, confirming the link between photosystems reorganization, light-harvesting efficiency and then photosynthetic rates increase.

On the contrary, fig.L.3.5. shows that DIC concentration increases right a few hours after N-addiction to the medium, finally decreasing to recover its initial value within 2 days. That could be due to a massive degradation and consumption of organic storage compounds to be used in new synthesis of proteins and pigments.

However, it's worthy of notice that complete recovery is quicker than the decrease/increase induced by N-limitation and starvation. That may constitute an opportunistic strategy for a fast uptake in case of a sudden increase of nitrogen availability (Young and Beardall 2003).

Thus, both $\alpha^b$and P^bmax, and α_f and ETRmax co-lower only partially, meaning the absence of a general increase of ATP demand, which could be supported by oxidation of reductants in respiratory back-reactions, without involving new organic compounds production, a s suggested by Behrenfeld *et al.* (2004).

The analysis of nutrients effects on Raphidophyceans is of particular importance because it's largely accepted that nutrients availability is the main factor determining their blooms, which are detected typically in eutrophic inlands and coastal waters (cita). In particular, phosphorus availability resulted the limiting factor for many Raphidophyceans (de Boer *et al.* 2004, Zhang *et al.* 2006, Cucchiari *et al.* 2007), so that the benefit of diel vertical migrations by *G. semen* in Lake Valkea-Kotinen (Salonen and Rosenberg 2000), and by *C. subsalsa* and *H. akashiwo* in the Delaware Inland Bays (Handy *et al.* 2005) is thought to be the uptake of phosphate.

Some Raphidophyceae can grow well under low nutrient conditions as well, and this may constitute an advantage in inter-specific competition (Yamaguchi *et al*. 2008). Experiments made on an isolate of *H. akashiwo* from the Delaware Inland Bays showed that it was well adapted to grow at low nutrients concentrations, likely due also to its small size (Zhang *et al*. 2006), in particular *H. akashiwo* has an optimum growth over the range 0.6-20 μM of phosphate, 5-100 μM of nitrate and 2-25 μM of ammonium. Cell density indicates however that it grows better when nitrogen source is nitrate (200 μM) than in ammonium (25 μM), and that it can grow well using organic nitrogen substrates, both urea and glutamic-acid N (50 μM). These data are confirmed by Herndon and Cochlan (2007) who showed that H. akashiwo can grow well using both NH_4^+, NO_3^- and urea as N sources, though at high light levels it prefers NO_3^- and urea, while at low light NO_3^- determines the slowest growth, but are in contrast with numerous other reports, showing different preferences from other strains of the same species. However, there are numerous reports comparing growth and nutrients uptake rates with nutrients concentration in Raphidophyceae, but none of them measures N-starvation effects on photosynthesis.

Experiment 4: sinusoidal light.

Experiment 4 largely confirms experiment 1 findings, in fact photosynthetic parameters α^b and P^bmax show again diel changes (fig.L.4.1). Please, remember that the light: dark cycle is shifted to 2 hours later than for experiment 1.

α^b has a maximum at midday or within 2 hours from it (16.00-18.00h), though it oscillates on high values from dawn to before-sunset (10.30h-20.30h), then it decreases to its midnight minimum (4.00-5.00h), finally it increase back to the dawn value (fig.L.4.1a). The light-limited slope α^b is linked to the light-harvesting mechanisms and to the photosynthetic energy conversion efficiency: chlorophyll-*a*, chlorophyll-*c* and

fucoxanthin increase from dawn to sunset (fig.L.4.7), but all their ratios to chlorophyll-*a* decrease to the midday minimum and increased back to the sunset maximum (fig.L.4.8), thus indicating that the photosystems size is reduced to minimum at midday when irradiance is maximum. At the same time, cell volume markedly increases (fig.L.4.4), so that chla/vol decreases (fig.L.4.11c), reducing photosystems number too: a lower photosystem size and number help preventing photodamage caused by excessive energy capture. It's worthy to notice that the ratio β-carot/chla starts increasing to its midday maximum at midnight (fig.L.4.9b), so since dawn photosystems are well protected from photodamage.

α^b decreases from sunset to midnight (fig.L.4.1a). Photosynthetic pigments concentrations and their corresponding ratios to chlorophyll-*a* keep on increasing from 21.00h to 0.00h, then they lower within midnight (4.00h, fig.L.4.7 and 8). Moreover, chla/cell increases as far as its maximum at 0.00h, then it lowers during the night time (fig.L.4.11b), resulting in an increase of photosystems size as far as the first half of the night, and in its decrease in the second half of it. Since from 18.00h, chla/volume is always increasing during the night (fig.L.4.11c), thus the number of photosystems is always increasing. α^b decrease can thus be due to a reduced light-harvesting efficiency, which is determined by an increased package-effect: within 0.00h, it is induced only by the higher photosystems size, after it by both higher size and number.

Finally, α^b recovers back from midnight (fig.L.4.1a), at the same time both the photosynthetic pigments and their ratios to chlorophyll-*a* (figs.L.4.7 and 4.8) and chla/cell (fig.L.4.11b) lower, thus determining a reduction in photosystems size and in the possibility to excessive photons capture, which would determine photodamage. As a consequence, the light-harvesting efficiency increases as well.

P^bmax shows maximums before midday (12.00-14.00h)., then decreases to the before-sunset minimums (18.00-19.00h, fig.L.4.1b). During the day period, cell volume increases (fig.L.4.4b) by active organic compounds photosynthesis and storage, in fact DIC concentration markedly lowers due to carbon assimilation and fixation, until after midday (18.00h, fig.L.4.6a), while on the contrary organic C content (fig.L.4.5b) and C/chla ratio (fig.L.4.11a) increase. Since light-harvesting capacity is high and stable, we suggest that P^bmax decrease at high irradiance may be due to a/some "downstream" of PSII processe(s), like component(s) of the electron transport chain, the RUBISCO and/or the RUBISCO activase enzymes, and/or component(s) of the Calvin cycle.

Though β^b doesn't show any diel periodicity (fig.L.4.1c), and thus photoinibition doesn't covary with P^bmax, efficient photoprotection is in progress during the day

period. Fig.L.4.10 shows the xanthophyll cycle patterns, which is exactly the same as in experiment 1, with antheraxanthin and zeaxanthin maximum concentrations right at midday and violaxanthin high values before and after midday, due to neo-synthesis and re-epoxidation, respectively.

On the contrary, P^bmax increases back from 2 hours after midday in a linear way (fig.L.4.1b): as light intensity decreases, P^bmax may only be light-limited, no downstream PSII components likely limits photosynthesis. At the same time, DIC increases (fig.L.4.6a) while organic C lowers (fig.L.4.5b), due to respiratory consumption in the dark, thus determining C/chla lowering (fig.L.4.11a).

Like in experiment 1, α^b and P^bmax do not covary during the light period, i.e. they show an Ek-dependent pattern of variability, meaning photoacclimation in progress. On the contrary, they are positively correlated from midnight to mid-morning (Ek-independent variability, fig.L.4.2). Fig.L.4.1 confirms also in experiment 4 a nocturnal cell division, which results completed at dawn. Cell division asks for a high reductants demand, so our data would agree again with Behrenfeld *et al.*'s (2004) suggestion of a high reductants demand reflected in α^b and P^bmax covariation.

Experiment 5: from sinusoidal to continuous light.

Shifting the light from sinusoidal to continuous, α^b still shows its maximum at midday, then it decreases around 1.00h-4.00h, finally it oscillates (fig.L.5.1a), thus as far as 19 hours after the shift (8.30h) it shows its sinusoidal periodicity. P^bmax still shows it's maximum before midday, then decreases to a very low value (4.00h), finally it oscillates on low values (fig.L.5.1b), thus it maintains its rhythm only as far as 18.30h (5 hours after the shift). Thus, like in experiment 2, both α^b and P^bmax loose their diel periodicity within 1 day, but α^b maintains its rhythm for a longer time.

Moreover, Ek values averaged on the 2 chemostats (fig.L.5.3) indicates that α^b and P^bmax vary according to a 2-phases pattern: Ek decreases markedly from the light shift to 4.30h due to P^bmax decrease (Ek-dependent variability=photoacclimation), then Ek is constant because the amplitude of α^b and P^bmax oscillations lowers, so their mean values resulted smoothed and constant, thus their variability is an Ek-independent one.

Photosynthetic pigments keep their sinusoidal cycle, though reduced in amplitude from 21-23 hours after the shift (10.00h-12.00h, fig.L.5.7), while both chlc/chla and fuco/chla loose their periodicity around 0.00h (11 hours after the shift, fig.L.5.8). The

timing of cells division is the same as in sinusoidal light, though the division is slower (fig.L.5.4a), and cell volume increases faster under continuous light, so that much higher values are reached (fig.L.5.4b). The consequences are much higher chla/cell (fig.L.5.11b) and much lower chla/vol values (fig.L.5.11c). Thus, α^b variation can be explained as in sinusoidal light, at least as far as pigments and cell volume and number maintain their sinusoidal pattern. So, within 0.00h α^b is high due to an efficient light-harvesting and reduced photosystems size and number, to avoid excessive photons capture and prevent photodamage.

α^b reaches a minimum value around 1.00h-4.00h (fig.L.5.1): pigments are still decreasing (fig.L.5.7), but the ratio chlc/chla is constant, while fuco/chla is at its maximum value (fig.L.5.8). Chla/vol has reached the minimum too (fig.L.5.11c), while chla/cell is the highest (fig.L.5.11b), because both cell volume and number are stable (fig.L.5.4). Then photosystems are minimum in number, but increasing in size. We can thus assume that both light-harvesting efficiency and light utilization have lowered due to a low number of photosystems and increasing package effect. At the same time (0.00h-4.00h), the photoprotective mechanisms are well working, in fact both violaxanthin, antheraxanthin and zeaxanthin concentrations, and β-carot/chla are increasing (figs.L.5.10 and 5.9b).

Finally, α^b increase again reaching high and stable values (fig.L.5.1): both photosynthetic pigments concentration and their ratios to chlorophyll-*a* and chla/cell decrease as far as 8.00h-10.00h, then they increase again (figs.L.5.7, 5.8 and 5.11b), so photosystems size decreases and then increases back, while their number is constant (chla/vol constant, fig.L. 5.11c). Then α^b variations from 15 hours after the light shift depend mainly on photosystems size variations. In the meantime, both violaxanthin, antheraxanthin and zeaxanthin concentrations, and β-carot/chla reached a constant value (figs.L.5.10 and 5.9b).

Thus α^b variations after shifting light to continuous result from (i) the gradual reduction in amplitude and period of pigments ratios to chlorophyll-*a*, which determines a re-organization of photosystems light-harvesting complexes, and from (ii) the different timing of cell division, which determines chla/cell and chla/vol patterns, resulting in photosystems variations in size and number.

P^bmax keeps its sinusoidal cycle as far as 18.30h (fig.L.5.1b), organic C content increases, determining cell volume increase due to organic compounds storage (fig.L.5.4b), and DIC concentration lowers (figs.L.5.5b and 5.6a). P^bmax decreasing is linked to some “down-stream to PSII” limiting factor. Photoprotection is in progress, in

fact both β-carot/chla (fig.L.5.9b) and xanthophylls (fig.L.5.10) maintain their typical pattern, though xanthophylls concentrations are markedly lower than in sinusoidal light (please, remember that the continuous intensity irradiance is half of the sinusoidal maximum).

P^bmax keeps on lowering as far as 4.00h (fig.L.5.1b). From 0.00h, both organic C content increases to a constant value (fig.L.5.5b), while DIC lowers to its minimum (fig.L.5.6a). As a consequence, cell volume increases due to photosynthetic compounds storage (fig.L.5.4b). P^bmax decrease is likely due to a(some) step-limiting components, both "upward" and "downward to PSII".

Finally P^bmax slightly increases again (fig.L.5.1b): since both C and DIC concentrations are constant (figs.L.5.5b and 5.6a), its increase is likely linked to α^b increase, i.e. "upward of PSII" processes don't limit it anymore.

Our results thus confirm that *Heterosigma akashiwo* lost its diel periodicity 7-8 hours after the light shift to continuous, indicating that it has not an endogenous clock, but it can acclimate to the cyclic availability of light. It's worthy to notice however, that it is possible to detect well the progressive lowering in both amplitude and length of the periodicity, at least in pigments variations, which was so for experiment 2. That could be due partly to the longer sampling in experiment 4: 30 hours instead of 26, i.e. 4 measurements more. Moreover, in contrast to experiment 2, cell division is not suppressed: cells start dividing at around 5.30h, determining cell volume decrease from 6.00h, and division is completed in only 8 hours (13.30h, fig.L.5.4).

Experiment 6: from continuous back to sinusoidal light.

When light is turned back to its sinusoidal cycle, α^b and P^bmax turn back to their diel periodicity. In particular α^b turns back to its high midday values, followed by the before-sunset decrease, while P^bmax still shows a longer and larger period than in experiment 4 in chemostat C1 (fig.L.6.1). It's not possible to detect any covariation between the 2 parameters, but only an Ek-dependence, simply due to the short sampling time-table (fig.L.6.1c).

Photosynthetic pigments increase during the day light (fig.L.6.5), though the ratios chlc/chla and fuco/chla are constant or decreasing (fig.L.6.6). Since the ratio chla/vol is constant (fig.L.6.9c), due to cell volume increase (fig.L.6.2b), while chla/cell increases (fig.L.6.9b), photosystems are constant in size and increasing in number. β-carotene and xanthophylls assure photoprotection in high light: β-carot/chla, antheraxanthin and

zeaxanthin are maximum right at midday (figs.L.6.7b and 6.8b), while violaxanthin shows its typical maximum shifted to 2 hours after the midday (fig.L.6.8a).

At the same time, organic C content increases due to its photosynthetic fixation and storage, while DIC lowers (figs.L.6.3b and 6.4a). P^bmax results limited to some "downstream to PSII" processes in chemostat C1, not yet in C2 (fig.L.6.1b).

Thus, all the measured parameters soon recover their daily periodicity when shifted back to a sinusoidal light:dark cycle, nevertheless not the timing of cell division: 24 hours are enough to bring back volume circadian periodicity (volume is minimum at midmorning and maximum before sunset), but not cells number (fig.L.6.2).

Our results confirm once more that *Heterosigma akashiwo* has not an endogenous clock, but rather optimize the use of light according to the exogenous availability, thanks to a very efficient light-harvesting obtained by a very fast re-organization of photosystems.

5. Conclusions

Our field measurements confirmed the high hydrodynamism of the Alboran sea, due to the Atlantic waters proceeding eastward and progressively mixing with the resident Mediterranean waters. In particular we detected two main cyclonic structures: the western one is a narrow cyclonic structure which had likely origin from the MAW anticyclonic circulation near Gibraltar, while the eastern cyclonic gyre had its origin from the Algerian Current, due to its instability which generally determines the formation of filaments, meanders and/or eddies. Thus, both mesoscale structures are characterized by the upwelling of cold and dense nutrient-rich Mediterranean water and the downwelling of nutrient-depleted warmer Atlantic water. In particular, the station stM21 has a sub-surface AMI, while the stM16-A2-M17 show a strong halo- and thermo-cline.

The mesoscale structures determine an increase of nutrient concentrations in the euphotic zone, both in the AMI and below the picnocline. Nutrient availability is clearly the main limiting factor in the euphotic zone in the Alboran sea, since our data indicates a strong coupling between nutrients and autotrophic biomass distribution: phytoplankton is mainly located from surface to 75 m deep and the highest concentrations can be detected right at the top of the 2 mesoscale structures and deeper along their edges, finally also in coastal stations, due to local deep upwellings. On the contrary, the MAW is generally poor in biomass. Then our data confirm the importance of these fertilization events in determining a localized increased productivity.

The phytoplankton assemblage is dominated by microplankton in turbulent, nutrient-rich waters, i.e. in correspondence of the cyclonic upwellings and at the coastal upwellings around 40-60 m deep. On the contrary the main contribute to total biomass in oligotrophic surface waters is nano- and picoplanktonic. These small cells can grow in nutrient-rich waters as well, in fact they are abundant at the gyres too, but due to their size they can take advantage of oligotrophic waters too, where they determine the main contribute to total biomass.

Diatoms and *Prymnesiophyceae Coccolithophorales* dominate in correspondence of the coastal upwellings around 40-60 m deep: *Bacillariophyceae* and coccolitophores are known for their preference for turbulent, nutrient-rich and low-light waters, in fact their presence in coastal and cyclonic upwellings in the Alboran sea is largely documented.

Nevertheless, the main microplanktonic component in surface and sub-surface samples of the eastern eddy is the Raphidophycean *Fibrocapsa japonica*, a potentially harmful alga which is known for forming worldwide blooms in coastal and inland waters. This is the first report of *F. japonica* in the Alboran Sea, moreover we detected it as the dominant species in a cyclonic eddy, i.e. in very hydrodynamic structure rather than in stratified shallow coastal or inland waters. Since *F. japonica* has a low efficiency in nutrient uptake, its growth has been likely favoured by the high-nutrient conditions of the eddy and probably its ability to aggregate in mucous nets might have maintained the assemblage in the euphotic zone, thus supporting its bloom in such a turbulent area. Since our preliminary genetic investigation didn't reveal the possible dispersal route from a presumably known European strain, we can assume that the low temperatures of DMW might have favoured its cysts formation, while warmer nutrient-rich waters at the AMI in correspondence of the cyclonic eddy might have determined their germination. Nevertheless, the possibility of a costal origin for such a typically coastal species can't be entirely excluded. However, the low cell abundances and the high abundances of mixotrophic and heterotrophic dinoflagellates seems to suggest that *F. japonica* cells were in a post-bloom slow-growth phase. This assumption has been supported by the principal component analysis, which revealed a mainly nutrient-recycling metabolism. Under that point of view, the PCA could reveal itself as an useful statistical instrument which can help in establishing such a physiological evaluation. This may be of particular importance when analysing such a fragile organism as a Raphidophycean.

As already mentioned, Raphidophyceans are known for growing well in high light conditions. Low long-term scale photoprotection mechanisms (low PPC/Tchla ratio) were measured in the DMW when comparing it to AMI and especially to MAW, though its high light conditions. This indicates that the assemblage had not experienced high irradiance for such a long time to trigger a significant increase of all the photoprotective carotenoids. Nevertheless, the ratios zea/fuco and viola/zea, which evaluate the shorter-term scale photoprotection through the xanthophylls cycle, indicated that *F. japonica* from surface samples was more photoprotected than the 25-30 m deep ones, which is consistent with the upwelling movement of the cyclonic structure.

Moreover, our laboratory experiments confirmed that the Raphidophycean *Heterosigma akashiwo* is capable of efficient light-harvesting and energy utilization under different light regimes.

When grown in sinusoidal light, *Heterosigma akashiwo* cells divide during the night. The study of PE curve parameters and pigments variations (experiment 1 and 4) indicates that in the light period *H. akashiwo* maintains an high light-harvesting capacity (α^b and a*676) reducing photosystems size and number. Moreover, the photoprotective mechanisms (β-carotene energy dissipation and the xanthophylls cycle) are actively working: β-carotene concentration increases 2 hours earlier than violaxanthin and it varies following the irradiance pattern, while a large neo-synthesis of violaxanthin from after dawn assures the maximum of antheraxanthin and zeaxanthin right at midday, i.e. the highest photoprotection in action right at the highest irradiance level. During the day, organic compounds are photosynthesized and stored, in fact cell volume increases, and the light-saturated photosynthesis P^bmax is limited by a/some "downstream" of PSII processe(s): the photosynthetic electron transport components, and/or to the Calvin cycle components, and/or activity of the enzyme RUBISCO. Photoacclimation processes are in progress, in fact α^b and P^bmax do not covary (Ek-dependent variability). On the contrary, during the night cells divide and α^b and P^bmax co-increase: the nocturnal metabolism consumes both organic compounds by respiration and reductants, by alternative electron-sink pathways (likely back-reactions too). This temporal separation between the two driving metabolic pathway allows an optimal exploitation of the main limiting factor under these growth conditions, i.e. light availability.

This metabolic plasticity is confirmed by the lost of the rhythm when shifted to continuous light conditions (experiment 2 and 5): α^b and P^bmax loose their diel periodicity, thus they don't covary anymore, meaning that photoacclimation is in progress. For the first few hours from the shift, *H. akashiwo* maintains high α^b values thanks to well working photoprotection mechanisms, in particular, all the photoprotective violaxanthin fraction results de-epoxidated: photosystems variations are too slow to avoid excessive light capture. On the contrary, later on light-harvesting has been reduced so that the xanthophylls cycle is not triggered anymore, and de-excitation by β-carotene is likely preferred. Finally, many data reports suggest a key role of ROS production in helping excessive energy dissipation, but also low efficiency in damaged photosystem PSII repair in Raphidophyceans. Thus, these results would suggest that *H. akashiwo* may be good in avoiding absorption of excessive light and, in case of need, also in dissipating the excessive fraction.

This assumption is likely confirmed also by experiment 3: when these algae are N-starved, light-harvesting capacity is reduced, nevertheless antheraxanthin and zeaxanthin concentrations increase, likely to avoid photodamaged PSII repair.

Moreover, the recovery back to the initial values in all the parameters is faster than the decrease/increase induced by N-limitation and starvation, suggesting an opportunistic strategy for a fast uptake, in case of a sudden increase of nitrogen availability.

Similarly, when shifted back to a sinusoidal cycle (experiment 6), *H. akashiwo* soon recovers its daily periodicity, confirming once more that it has not an endogenous clock, but it can exploit light according to the exogenous availability, thanks to its efficient light-harvesting acclimation through photosystems re-organization.

Thus, both our laboratory results on *Heterosigma akashiwo*, and our field measurements and previous reports on *Fibrocapsa japonica* suggest that *Fibrocapsa japonica* might have taken advantage of high irradiance availability in the upper mixed layer of the eastern eddy to fast growing thanks to its efficient photoprotective mechanisms: its photophysiology might have made it more competitive than diatoms (generally considered low-light acclimated) in exploiting the resources of such a turbulent area.

In conclusion Raphidophyceans, due to their photo-physiological characteristics, among the microplanktonic algae, can reveals themselves as very good competitors against diatoms in a cyclonic eddy, in taking advantage of both the high-nutrient and the high-light availability of the upper layers in a cyclonic eddy. For this reason, further investigations should be done for evaluating the potential risk of an harmful species blooming in a mesoscale dynamic structure. Such an event, in fact, could play a key role in determining a quick and wide expansion of the algal distribution range of these interesting and crucial microalgae.

6. Bibliography

aa.vv., 2006 – MEDBIO06-MEDGOOS13 - Rapporto Campagna – 28 settembre - 8 novembre 2006, Borghini M, Ribotti, A. (Eds).

Arin, L., Morán, X. A. G., Estrada, M., 2002 – Phytoplankton size distribution and growth rates in the Alboran Sea (SW Mediterranean): short term variability related to mesoscale hydrodynamics. J. Plank. Res., 24(10): 1019-1033.

Asada, K., 1999 – The water-water cycle in chloroplast: scavenging of active oxygens and dissipation of excess photons. Annu. Rev. Plant Physiol. Plant Mol. Biol., 50: 601-639.

Badger, M. R., and Price, G. D., 1992 – The CO2 concentrating mechanism in cyanobacteria and microalgae. Physiol. Plant., 84: 606-615.

Band-Schmidt, C. J., Morquecho, L., Hernández-Becerril, D. U., Reyes-Salinas, A., Bravo-Sierra, E., 2004 – Raphidophyceans on the coasts of Mexico. Hydrobiologia, 515: 79-89.

Barlow, R. G., Cummings, D. G., and Gibb, S. W., 1997 – Improved resolution of mono- and divinyl chlorophylls *a* and *b* and zeaxanthin and lutein in phytoplankton extracts using reverse-phase C-8 HPLC. Mar. Eco. Pro. Ser., 161: 303-307.

Barlow, R., H., Sathyendranath, S., Platt, T., Kywealyanga, M., Clementson, L., Fukaawa, M., Watanabe, S., Devred, E., 2007 – Seasonal patterns of surface phytoplankton in the subtropical southern hemisphere. Deep-Sea Res. I, 54:1687-1703.

Behrenfeld, M. J., Prasil, O., Kolber, Z. S., Babin, M., Falkowsli, P. G., 1998 – Compensatory changes in photosystem II electron turnover rates protect photosynthesis from photoinibition. Photosynth. Res., 58: 259-268.

Behrenfeld, M. J., Prasil, O., Babin, M., and Bruyant, F., 2004 – In search of a physiological basis for covariations in light-limited and light-saturated photosynthesis. J. Phycol. 40: 4-25.

Bérard-Therriault, L., Poulin, M., Bossé, L., 1999 - Guide d'identification du phytoplancton marin de l'estuaire et du Golfe du Saint-Laurent incluant également certain protozoaires. Publ. Spec. Can. Sci. Halieut. Aquat., 128, 387 pp.

Bidigare, R. R., Smith, R. C., Baker, K. S., Marra, J., 1987 – Oceanic primary production estimates from measurements of spectral irradiance and pigment concentrations. Global Biogeochem. Cycles, 1 : 171-186.

Billard, C., 1992 - *Fibrocapsa japonica* (Raphidophyceae), planktonic marine alga reported for the first time in France. Cryptogamie Algol., 13: 225-231.

Bruyant, F., Babin, M., Genty, B., Prasil, O., Behrenfeld, M. J., Claustre, H., Bricaud, A., Garczarek, L., Holtzendorff, J., Koblizek, M., Dousova, H., Partensky, F.,

2005 – Diel variations in the photosynthetic parameters of *Prochlorococcus* strain PCC 9511 : Combined effects of light and cell cycle. Limnol. Oceanogr., 50(3): 850-863.

Catalano, G., Ribera d'Alcalà, M, e Saggiomo, V., 1990 – Silicati, in: Innamorati M., Ferrari I., Marino D., Ribera d'Alcalà M., 1990 – Metodi nell'ecologia del plancton marino. Nova Thalassia vol. 11.

Claustre, H., Kerhervé, P., Marty, J.-C., Prieur, L., 1994 – Phytoplankton photoadaptation related to some frontal physical processes. J. Mar. Syst., 5: 251-265.

Congestri, R., Albertano, P., Ravizza, P., Le Foche, M., Caldarini, J., Zaottini, E., 2000 – On blooms of *Fibrocapsa* along the middle Tyrrhenian Sea (Mediterranean Sea), Italy, in spring-summer 1999. In: Proceedings of the ASLO Meeting. Copenaghen, June 2000, Abstract Book.

Connell, L., 2002 – Rapid identification of marine algae (Raphidophyceae) using three-primer PCR amplification of nuclear internal transcriber spacer (ITS) regions from fresh and archived material. Phycologia, 41(1):15-21.

Cucchiari, E., Boni, L., Guerrini, F., Matteucci, G., Penna, A., Totti, C., Pistocchi, R., 2006 – Crescita e tossicità di *Fibrocapsa japonica* (Raphidophyceae) dell'Adriatico Settentrionale. In: Proceedings V Congress CoNISma, Viareggio, 2006, 14-18 November.

Cucchiari, E., Guerrini, F., Penna, A., Totti, C., Pistocchi, R., 2007 – Effect of salinity, temperature, organic and inorganic nutrients on growth of cultured *Fibrocapsa japonica* (Raphidophyceae) from the northern Adriatic Sea. Harmful Algae, 7(4): 405-414.

Davies, P., Folkard, A., Chabert d'Hières, G., 1993 – Remote sensing observations of filament formation along the Almeria-Oran front. Ann. Geophysicae, 11: 419-430.

de Boer, M. K., Tyl, M. R., Vrieling, E. G., van Rijssel, M., 2004 – Effects of salinity and nutrient conditions on growth and haemolytic activity of *Fibrocapsa japonica* (Raphidophyceae). Aquat. Microb. Ecol., 37: 171-181.

de Boer, M. K., Tyl, M. R., Vrieling, E. G., van Rijssel, M., 2005 – Temperature responses of three *Fibrocapsa japonica* strains (Raphidophyceae) from different climate regions. J. Plankton Res., 27: 47-60.

Decho, R. H., 1990 – Microbial exopolymer secretions in ocean environments: their roles in food webs and marine processes. Oceanogr. Mar. Bio. Ann. Rev., 28:73-153.

Demming-Adams, B., Gilmore, A. M., Adams, III W. W., 1996 – *In vivo* functions of carotenoids in higher plants. FASEB J., 10: 403-412.

Dunlap, W. C., and Yamamoto, Y., 1995 – Small molecule antioxidants in marine organisms: antioxidant activity of mycosporine–glycine. Comp. Biochem. Physiol., 12B: 105-114.

Eskling, M., Arvidsson, P.-O., Åkerlund, H.-E., 1997 – The xanthopyll cycle, its regulation and components. Physiologia Plantarum, 100:806-816.

Estrada, M., Varela, R., Salat, J., Cruzado, A., Arias, E., 1999 – Spatio-temporal variability of the winter phytoplankton distribution across the Catalan and North Balearic fronts (NW Mediterranean). J. Plank. Res., 21: 1-20.

Evens, T. J., Kirkpatrick, G. J., Millie, D. F., Chapman, D. J., Schofield, O. M. E., 2001 – Photophysiological responses of the toxic red-tide dinoflagellates *Gymnodinium breve* (Dinophyceae) under natural sunlight. J. Plank. Res., 23: 1177-1193.

Falkowski, P. G., and Raven J., 1997 – Aquatic photosynthesis. Blackwell Science. New York, 375 pp.

Fiala, M., Sournia, A., Clausure, H., Marty, J.-C., Prieur, L., Vétion, G., 1994 – Gradients of phytoplankton abundance, composition and photosynthetic pigments across the Almeria-Oran front (SW Mediterranean Sea). J. Mar. Syst., 5:223-233.

Fu, M., 2003 – Isolation and characterisation of toxins from *Fibrocapsa japonica* (Raphidophyceae). PhD Thesis, University Oldenburg, Germany.

Fu, M., Koulman, A., van Rijssel, M., Lützen, A., de Boer, M. K., Tyl, M. R., Liebezeit, G., 2004 – Chemical characterisation of three haemolytic compounds from the microalgal species *Fibrocapsa japonica* (Raphidophyceae). Toxicon, 43: 355-363.

Fu, F.- X., Zhang, Y., Warner, M., Feng, Y., Sun, J., Hutchins, D., 2008 – A comparison of future increased CO_2 and temperature effects on sympatric *Heterosigma akashiwo* and *Prorocentrum minimum*. Harmful Algae, 7(1): 76-90.

Gao, K., Guan, W., Helbling, E. W., 2007 – Effects of solar ultraviolet radiation on photosynthesis of the marine red tide alga *Heterosigma akashiwo* (Raphidophyceae). J. Photochem. Photobiol. B: Biol., 86: 140-148.

Geider, R. J., 1993 – Quantitative phytoplankton physiology: implications for primary production and phytoplankton growth. ICES Marine Science Symposium, 197: 52-62.

Genty, B., Briantais, J-M. and Baker, N. R., 1989 – The relationship between the quantum yield of photosynthetic electron transport and quenching of chlorophyll fluorescence. Bioch. et Biophy. Acta, 990: 87-92.

Gómez, F., Echevarría, F., García, C. M., Prieto, L., Ruiz, J., Reul, A., Jiménez-Gómez, F., Varala, M., 2000 – Microplankton distribution in the strait of Gibraltar: coupling between organisms and hydrodynamic structures. J. Plank: Res., 22(4): 603-617.

Gomez, F., 2003 – The toxic dinoflagellate *Gymnodinium catenatum*: an invader in the Mediterranean Sea. Acta Bot. Croat., 62(2): 65-72.

Gould, R. W., and Wiesenburg, D. A., 1990 – Single-species dominance in a subsurface phytoplankton concentration at a Mediterranean Sea front. Limnol. Oceanogr., 35(1): 211-220.

Green, E. J. and Carritt, D. E., 1967 – Oxygen solubility in sea water: thermodynamic influence of sea salt. Science, 157: 191-193.

Guillard, R. R. L. and Ryther, J. H., 1962 – Studies of marine planktonic diatoms. I. *Cyclotella nana* Hustedt and *Detonula confervacea* (Cleve). Gran. Can. J. Microbiol., 8: 229-239.

Handy, S. M., Coyne, K. J., Portune, K. J., Demir, E., Doblin, M. A., Hare, C. E., Cary, S. C., Hutchins, D. A., 2005 – Evaluating vertical migration behaviour of harmful raphidophytes in the Delaware Inland Bays utilizing quantitative real-time PCR. Aquat. Microb. Ecol., 40: 121-132.

Hansatech Instruments Ltd., 2000 - Oxygen measurements in the liquid – phase. System Manual.

Harris, G. P., 1986 – Phytoplankton ecology. Structure, function and fluctuations. Chapman and Hall. London, New York, 384 pp.

Hasle, G.R., Syversten, E.E., 1997. Marine Diatoms. In: Tomas C.R. (ed.). 1997. Identifying Marine Phytoplankton. Academic Press, San Diego, 5-385.

Heimdal, B.R., 1997 - Modern Coccolithophorids. In: Tomas C.R. (ed.). 1997. Identifying Marine Phytoplankton. Academic Press, San Diego, 731-833.

Henley, W. J., 1993 – Measurements and interpretation of photosynthetic light-response curves in algae in the context of photoinibition and diel changes. J. Phycol., 29: 729-739.

Herndon, J., and Cochlan, W., 2007 – Nitrogen utilization by the raphidophytes *Heterosigma akashiwo*: Growth and uptake kinetics in laboratory cultures. Harmful Algae, 6: 260-270.

Horner, R. A., 2002 - A taxonomic guide to some common marine phytoplankton. Biopress Ltd. Bristol, 195 pp.

Hotelling, H., 1933 – Analysis of a complex of statistical variables into principal components. J. Educ. Psychol. 24:417-441, 498-520.

Jacquet, S., Prieur, L., Avois-Jacquet, C., Lennon, J.-F., Vaulot, D., 2002 – Short-timescale variability of picophytoplankton abundance and cellular parameters in surface waters of the Alboran Sea (western Mediterranean). J. Plank. Res., 24(7): 635-651.

Jeffrey, S. W., MacTavish, H. S., Dunlap, W. C., Vesk, M., Groenewoud, K., 1999 – Occurrence of UVA- and UVB- absorbing compounds in 152 species (206 strains) of marine microalgae. Mar. Ecol. Prog. Ser., 189: 35-51.

Journel, A.G., and Huijbregts, C., 1978 – Mining Geostatistics, Academic Press, 600 pp.

Kana, T. M., Geider, R. J., Critchley, C., 1997 – Regulation of photosynthetic pigment in microalgae by multiple environmental sensor: a dynamic balance hypothesis. New. Phytol., 137: 628-638.

Kendall, M. G., 1948 – Rank correlation methods. Charles Griffin & Co., London. ix + 197 pp.

Khan, S., Arakawa, O., Onoue, Y., 1996 – Growth characteristics of a neurotoxin-producing Chloromonad *Fibrocapsa japonica* (Raphidophyceae). J. World Aquacult. Soc., 27: 247-253.

Kim, D., Nakamura, A., Okamoto, T., Komatsu, N., Oda, T., Iida, T., Ishimatsu, A., Muramatsu, M., 2000 – Mechanisms of Superoxide anion generation in the toxic red tide phytoplankton *Chattonella marina*: possible involvement of NADPH oxidase. Biochim. Biophys. Acta, 1524: 220-227.

Kim, D., Watanabe, M., Nakayasu, Y., Kohata, K., 2004 – Production of superoxide anion and hydrogen peroxide associated with cell growth of *Chattonella antiqua*. Aquat. Microb. Ecol., 35: 57-64.

Kiørboe, T., 1993 – Turbulence, phytoplankton cell size, and the structure of pelagic food webs. Adv. Mar. Biol., 29: 1-73.

Kirk, J.T.O., 1994 - Light and photosynthesis in aquatic ecosystems. Cambridge University Press.

Kirkwood, D. S., 1992 – Stability of solutions of nutrient salts during storage. Marine Chemistry, 38: 151-164.

Kooistra, W. H. C. F., de Boer, M. K., Vrieling, E. G., Connell, L. B., Gieskes, W. W. C., 2001 – Variation along ITS markers across strains of *Fibrocapsa japonica* (Raphidophyceae) suggests hybridisation events and recent range expansion. J. Sea Res., 46: 213-222.

Krause, G.H. and Weis, E., 1991 – Chlorophyll fluorescence and photosyntesis: the basics. Ann. Rev. Plant Physiol. Plant Mol. Biol., 42:313-49.

Lacombe, H., and Richez, C., 1982 – The regime of the strait of Gibraltar. In: Nihoul, J. C. J. (Ed.), Hydrodynamics of Semi-enclosed Seas. Elsevier, Amsterdam.

Lavaud, J., Rousseau, B., van Gorkom, H. J., Etienne, A. L., 2002 - Influence of the diadinoxanthin pool size on photoprotection in the marine planktonic diatom *Phaeodactylum tricornutum*. Plant Physiol., 129: 1398-1406.

Leblanc, K., Quéguiner, B., Prieur, L., Claustre, H., Oubelkheir, K., Bruyant, F., 2004 – Siliceous phytoplankton production and export related to trans-frontal dynamics of the Almeria-Oran frontal system (western Mediterranean Sea) during winter. J. Geophys. Res., 109: C07010, doi:10.1029/2003JC001878.

Lévy, M., Mémery, L. and André, J.-M., 1998 – Simulation of primary production and export fluxes in the Northwestern Mediterranean Sea. J. Mar. Res., 56: 197-238.

Lewitus, A. J., and Holland, A. F., 2003 – Initial results from a multi-institutional collaboration to monitor harmful algal blooms in South Carolina. Environ. Monitor. Assess., 81: 361-371.

Liu W., Au, D. W. T., Anderson, D. M., Lam, P. K. S., Wu, R. S. S., 2007 – Effects of nutrients, salinity, pH and light: dark cycle on the production of reactive oxygen species in the alga *Chattonella marina*. J. Exp. Mar. Biol. Ecol., 346: 76-86.

Liu, J., Lewitus, A. J., Kempton, J. W., Wilde, S., 2008 – The association of algicidal bacteria and raphidophytes blooms in South Carolina brackish detention ponds. Harmful Algae, 7: 184-193.

Loeblich, A. R. I., and Fine, K., 1977 – Marine chloromonads: more widely distributed in neritic environments than previously thought. Proc. Biol. Soc. Wash., 90: 388-399.

Lomas, M. W., and Gilbert, P. M., 1999 – Temperature regulation of nitrate uptake: a novel hypothesis about nitrate uptake and reduction in cool-water diatoms. Limnol. Oceanogr., 44: 556-572.

MacIntyre, H. L., and Geider, R. J., 1996 – Regulation of Rubisco activity and its potential effect on photosynthesis during mixing in a turbid estuary. Mar. Ecol. Prog. Ser., 144: 247-264.

MacIntyre, H. L., Kana, T. M., Geider, R. J., 2000 – The effects of water motion on short-term rates of photosynthesis by marine phytoplankton. Trends in Plant Science, 5(1): 12-17.

MacIntyre, H. L., Kana, T. M., Anning, T., Geider, R., 2002 – Photoacclimation of photosynthesis irradiance response curves and photosynthetic pigments in microalgae and cyanobacteria. J. Phycol., 38: 17-38.

Malara, G. and Sciandra, A., 1991 – A multiparameter phytoplanktonic culture system driven by microcomputer. J. Appl. Phyc. 3: 235-241.

Marshall, J.-A., Hovenden, M., Oda, T., Hallegraef, G. M., 2002 – Photosynthesis does influence Superoxide production in the ichtyotoxic alga *Chattonella marina* (Raphidophyceae). J. Plankton Res., 24(11): 1231-1236.

Marshall, J. A., and Newman, S., 2002 – Differences in photoprotective pigment production between Japanese and Australian strains of *Chattonella marina* (Raphidophyceae). J. Exp. Mar. Biol. Ecol., 272: 13-27.

Marshall, J.-A., de Salas, M., Oda, T., Hallegraeff, G., 2005 – Superoxide production by marine microalgae. I. Survey of 37 species from 6 classes. Marine Biology, 147: 533-540.

Mas, S., Roy, S., Blouin, F., Mostajir, B., Therriault, J.-C., Nozais, C., and Demers, S., 2008 – Diel variations in optical properties of *Imantonia rotunda* (Haptophyceae) and *Thalassiosira pseudonana* (Bacillariophyceae) exposed to different irradiance levels. J. Phycol., 44: 551-563.

Mercado, J. M., Ramírez, T., Cortés, D., Sebastián, M., Vargas -Yáñez, M., 2005 – Seasonal and inter-annual variability of the phytoplankton communities in an

upwelling area of the Alboran Sea (SW Mediterranean Sea). Sci. Mar., 69: 451-465.

Millot, C., 1994 – Models and data: a synergetic approach in the western Mediterranean Sea. In: Malanotte-Rizzoli, P., Robinson, A. R. (Eds), Erice School Proceedings, Ocean Processes in Climate Dynamics: Global and Mediterranean Examples. Kluwer Academic Publishers, Dordrecht, pp. 407-425.

Millot, C., 1999 – Circulation in the Western Mediterranean Sea. J. Mar. Sys., 20: 423-442.

Minas, H. J., Coste, B., Le Corre, P., Minas, M., Raimbault, P., 1991 – Biological and geochemical signatures associated with the water circulation through the Strait of Gibraltar and the western Alboran Sea. J. Geophysical Res., 96: 8755-8771.

Mitchell, B. G., and Holm-Hansen, O., 1991: Observations and modelling of the Antarctic phytoplankton crop in relation to mixing depth. Deep-Sea Res., 96: 8755-8771.

Morán, X. A. G., and Estrada, M., 2001 – Short-term variability of photosynthetic parameters and particulate and dissolved primary production in the Alboran Sea (SW Mediterranean). Mar. Ecol. Prog. Ser., 212: 53-67.

Morán, X. A. G., Taupier-Letage, I., Vásquez-Domínguez, E., Ruiz, S., Arin, L., Raimbault, P., Estrada, M., 2001 – Physical-biological coupling in the Algerian Basin (SW Mediterranean): Influence of mesoscale instabilities on the biomass and production of phytoplankton and bacterioplankton. Deep-Sea Res. I, 48: 405-437.

Morel, A., and Bricaud, A., 1981 – Theoretical results concerning light absorption in a discrete medium, and application to specific absorption of phytoplankton. Deep-Sea Res., 28A: 1375- 1393.

Mostaert, A. S., Karsten, U., Hara, Y., Watanabe, M. M., 1998 – Pigments and fatty acids of marine raphidophytes: A chemotaxonomic re-evaluation. Phycological Research, 46: 213-220.

Nakamura, Y., Yamazaki, Y., Hiromi, J., 1992 – Growth and grazing of a heterotrophic dinoflagellate, *Gyrodinium dominans*, feeding on a red tide flagellate, *Chattonella antiqua*. Mar. Ecol. Prog. Ser., 82: 275-279.

Nimer, N. A., Iglesias-Rodriguez, M. D., Merrett, M. J., 1997 – Bicarbonate utilization by marine phytoplanktonic species. J. Phycol., 33: 625-631.

Niyogi, K. K., Biörkman, O., Grossman, A. R., 1997 – *Chlamydomonas* xanthophylls cycle mutants identified by video imaging of chlorophyll fluorescence quenching. Plant Cell, 9: 1369-1380.

Niyogi, K. K., 2000– Safety valves for photosynthesis. Current Opinion in Plant Biology, 3: 455-460.

Oda, T., Nakamura, A., Shikayama, M., Kawano, I., Ishimatsu, A., Muramatsu, T., 1997 – Generation of reactive oxygen species by raphidophycean phytoplankton. Biosci. Biotechnol. Biochem., 61: 1658-1662.

Odebrecht, C., and Abreu, P. C., 1995 – Raphidophyceans in southern Brazil. Harmful Algae News, 12/13, 4.

Okaichi, T., 1972 – Occurrence of red-tides related to neritic water pollution. In: Anonymous (Ed.). The cause of Red-Tide in neritic waters. Japan. Ass. Protec. Fish. Resour., Tokyo, pp. 58-76.

Ono, C., 1989 – Red-tides problems in the Seto Inland sea. Japan. In: Okaichi, T., Anderson, D. M., Nemoto, T. (Eds.). Red Tides: Biology, Environmental Science and Toxicology. Elsevier, New York, pp. 137-142.

Ono, K., Khan, S., Onoue, Y., 2000 – Effects of temperature and light intensity on the growth and toxicity of *Heterosigma akashiwo* (Raphidophyceae). Aquaculture Research, 31: 427-433.

Owens, T. G., Falkowski, P. G., Withledge, T. E., 1980 – Diel periodicity in cellular chlorophyll content in marine diatoms. Mar. Biol., 59: 71-77.

Peragallo, H., Peragallo, M., 1965 - Diatomèes marines de France et des districts maritimes voisins. Vol. 2: Texte, Atlas. Tempère M. J. (ed.), 1897-1908, rèimpression Asher & Co., Amsterdam.

Pierattini, I., 2005 – Analisi dei pigmenti del fitoplancton mediante HPLC ed applicazioni in oceanografia biologica. Laurea Thesis, Università degli Studi di Firenze, Firenze, 49 pp.

Platt, T., Gallegos, C. L. and Harrison, W. G., 1980 – Photoinibition of photosynthesis in natural assemblages of marine phytoplancton. J. Marine Res., 38(4): 687-701.

Polonelli, F., 2006 – Cenosi fitoplanctoniche delle strutture dinamiche nei mari italiani. PhD Thesis, University of Florence, Italy.

Post, A. F., Eijgenraam, F., and Murr, L. R., 1985 – Influence of light period length on photosynthesis and synchronous growth of the green alga *Scenedesmus protuberans*. Br. Phycol. J., 20: 391-397.

Prasil, O. Z., Kolber, J. Berry, J. A., Falkowski, P- G., 1996 – Cyclic electron flow around photosystem II in vivo. Photosyn. Res., 48: 395-410.

Prieur, L., and Sournia, A., 1994 – "Almofroont-1" (April-May 1991): an interdisciplinary study of the Almeria-Oran geostrophic front, SW Mediterranean Sea. J. Mar. Syst., 5: 187-203.

Rampi, L., Bernhard, M., 1980 - Chiave per la determinazione delle Peridinee pelagiche mediterranee. *RT/BIO* (81) 8, CNEN, Roma.

Rampi, L., Bernhard, M., 1981 - Chiave per la determinazione delle Coccolitoforidee mediterranee. *RT/BIO* (81) 13, CNEN, Roma.

Ribera d'Alcalà, M, Catalano, G., e Saggiomo, V., 1990a – Nitriti, in: Innamorati M., Ferrari I., Marino D., Ribera d'Alcalà M., 1990 – Metodi nell'ecologia del plancton marino. Nova Thalassia vol. 11.

Ribera d'Alcalà, M, Catalano, G., e Saggiomo, V., 1990b – Nitrati, in: Innamorati M., Ferrari I., Marino D., Ribera d'Alcalà M., 1990 – Metodi nell'ecologia del plancton marino. Nova Thalassia vol. 11.

Riegman, R., de Boer, M., de Senerpont Domis, L., 1996 – Growth of harmful algae in multispecies cultures. J. Plankton Res., 18(10): 1851-1866.

Rodhes, L., Haywood, A. J., Ballantine, W. J., MacKenzie, A. L., 1993 – Algal blooms and climate anomalies in north-east New Zealand, August-December 1992. New Zealand Journal of Marine and Freshwater Research, 27: 419-430.

Rodriguez, J., Blanco, J. M., Jiménez-Gómez, F., Echevarria, F., Gil, J., Rodriguez, V., Ruiz, J., Bautista, B., Guerriero, F., 1998 – Patterns in the size structure of the phytoplankton community in the deep fluorescence maximum of the Alboran Sea (southwestern Mediterranean). Deep-Sea Res. I, 45: 1577-1593.

Saggiomo, V., Catalano, G., e Ribera d'Alcalà, M., 1990 – Ortofosfati, in: Innamorati M., Ferrari I., Marino D., Ribera d'Alcalà M., 1990 – Metodi nell'ecologia del plancton marino. Nova Thalassia vol. 11.

Salonen, K., and Rosenberg, M., 2000 – Advantages from diel vertical migration can explain the dominance of *Gonyostomum semen* (Raphidophyceae) in a small, steeply-stratified humic lake. J. Plank. Res., 22(10): 1841-1853.

Sambrook, J., Fritsch, E. F., Maniatis, T., 1989 – Molecular Cloning – A Laboratory Manual. Cold Spring Harbour Laboratory Press.

Savitzky, A. and Golay, M. J. E., 1964 - Smoothing and Differentiation of Data by Simplified Least Squares Procedures. Analytical Chemistry, 36: 1627–1639.

Schiller, J., 1933-1937 - Dinoflagellatae (Peridineae). Monographischer Behandlung. In: Rabenhorst's Kriptogamen-Flora von Deutschland, Osterreich und der Schweiz. X band (3): Teil 1 (1931-1937); Teil 2 (1935-1937). Akademische Verlag., Leipzig.

Schmetterer, G., 1994 – Cyanobacterial Respiration. In: Bryant, D. A. (Ed.), The Molecular Biology of Cyanobacteria. Kluwer Academic Publishers, Dordrecht, pp. 409-435.

Schreiber, U., Bilger, W. and Neubauer C., 1995 – Chlorophyll fluorescence as a nonintrusive indicator for rapid assessment of in vivo photosynthesis. In: Schulze and M. M. Caldwell (Editors) Ecophysiology of Photosynthesis. Ecological Studies, vol. 100. Springer – Verlag, Berlin, pp. 49-70.

Schubert, H., Forster, R. M., Sagert, S., 1995 – In situ measurements of state transition in cyanobacterial blooms: kinetics and extent of the state change in relation to underwater light and vertical mixing. Mar. Ecol. Prog. Ser., 128: 99-108.

Send, U, Font, J., Krahmann, G., Millot., C., Rhein, M., Tintoré, J., 1999 – Recent advances in observing the physical oceanography of the western Mediterranean Sea. Progress in Oceanography, 44: 37-64.

Smayda, T. J., and Villareal, T., 1989 – The 1985 "brown tide" and the open phytoplankton niche in Narragansett Bay during summer. In: Cosper, E. M.,

Bricelj, V. M., Carpenter, E. J. (Eds), Novel Phytoplankton Blooms: Causes and Impacts of Recurrent Brown Tides and Other Unusual Blooms. Springer-Verlag, Berlin, pp. 165-187.

Smayda, T. J., 2002 – Turbolence, watermass stratification and harmful algal blooms: an alternative view and frontal zones as "pelagic seed banks". Harmful Algae, 1: 95-112.

Sournia, A., 1986 – Atlas du phytoplancton marin volume I : Introduction, Cyanophycées, Dicyochophycées, Dinophycées et Raphidophycées. In: Atlas du phytoplancton marin. Sournia A. (ed.), Paris: 219 pp.

Steeman Nielsen, E., and Jørgensen, E. G., 1968 – The adaptation of plankton algae. I. General part. Physiol. Plant., 21: 401-413.

Steidinger, K.A., Tangen, K., 1997. Dinoflagellates. In: Tomas C.R. (ed.). 1997. Identifying Marine Phytoplankton. Academic Press, San Diego, 387-584.

Suzuki, L., and Johnson, C. H., 2001 – Algae know the time of day: circadian and photoperiodic programs. J. Phycol. 37: 933-942.

Takahashi, M., Hara, Y., 1989 – Control of diel vertical migration and cell division rhythm of *Heterosigma akashiwo* by day and night cycles. In: Okaichi, T., Anderson, D. M., Nemoto, T. (eds.). Red tides: biology, environmental science, and toxicology. Elsevier Science Publishing, New York, p. 265-268.

Takuji, N., Koji, Y., Toshiyuki K., Masataka N., Tsuneo H., 2006 - Relationships of Diurnal Vertical Migrations of *Ceratium furca* (Dinophyceae) and *Chattonella spp.* (Raphidophyceae) with Pycnocline Layer Level in Ariake Sea. Journal of Japan Society on Water Environment, 29(8): 489-494.

Throndsen, J., 1983 - The planktonic marine flagellates. In: Tomas C.R. (ed.). Marine phytoplankton. A guide to Naked Flagellates and Coccolithophorides. Accademic Press, San Diego: chapter 2: 7-145.

Tillmann, U., and Reckermann, M., 2002 – Dinoflagellate grazing on the raphidophytes *Fibrocapsa japonica*. Aquat. Microb. Ecol., 26: 247-257.

Tintoré, J., Gomis, D., Alonso, S., Parrilla, G., 1991 – Mesoscale dynamics and vertical motion in the Alboran Sea. Journal of Physical Oceanography, 21: 811-823.

Tomas, C. R., 1998 – Blooms of potentially harmful Raphidophycean flagellates in Florida coastal waters. In: Reguera, B., Blanco, J., Fernández, M. L., Wyatt, T. (Eds), Harmful Algae. Xunta de Galicia and Intergovernamental Oceanographic Commission of UNESCO, Santiago de Compostela, Spain, pp. 101-103.

Toriumi, S., and Takano, H., 1973 – *Fibrocapsa*, a new genus in Chloromonadophyceae from Atsumi Bay, Japan. Bull. Tokai Regional Fish. Res. Lab., 76: 25-35.

Twiner, M. J., and Trick, C. G., 2000 – Possible mechanisms for production of hydrogen peroxide by the ichtyotoxic flagellate *Heterosigma akashiwo*. J. Plankton Res., 22(19): 1961-1975.

van Rijssel, M., de Boer, M. K., Tyl, M. R., Gieskes, W. W. C., 2008 – Evidence for inhibition of bacterial luminescence by allelochemicals from *Fibrocapsa japonica* (Raphidophyceae), and the role of light and microalgal growth rate. Hydrobiologia, 596: 289-299.

Venrick, E. L., 1992 – Phytoplankton species structure in the central North-Pacific: Is the edge like the center? J. Plankton Res. 14: 665-680.

Videau, C., Sournia, A., Prieur, L., Fiala, M., 1994 – Phytoplankton and primary productivity characteristics at selected sites in the geostrophic Almeria-Oran front system. J. Mar. Sist., 5: 235-250.

Vidussi, F., Claustre, H., Bustilloz-Guzmàn, J., Cailliau, C., and Marty, J.-C., 1996 – Rapid HPLC method for determination of phytoplankton chemotaxinomic pigments: Separation of chlorophyll a from divinyl-chlorophyll a and zeaxanthin from lutein. J. Plankton Res. 18: 2377-2382.

Vrieling, E. G., Koeman, R. P. T., Nagasaki, K., Ishida, Y., Peperzak, L., Gieskes, W. W. C., Veenhuis, M., 1995 – *Chattonella* and *Fibrocapsa* (Raphidophyceae): first observation of, potentially harmful, red tide organisms in Dutch coastal waters. Neth. J. Sea. Res., 33(2): 183-191.

Walz, H.G., 1987 – Chlorophyll fluorescence measuring system. 2.105/3.87 Edition July 1987.

Warner, M. E., and Madden, M., 2007 – The impacts to elevated irradiance on the growth and photochemical activity of the harmful algae *Chattonella subsalsa* and *Prorocentrum minimum* from Delaware. Harmful Algae, 6: 332-342.

Watanabe, M., Kohata, K., Kunugi, M., 1988 - Phosphate accumulation and metabolism by *Heterosigma akashiwo* (Raphidophyceae) during diel vertical migration in a stratified microcosm. J. Phycol., 24(1): 22-28.

Yamaguchi, H., Sakamoto, S., Yamaguchi, M., 2008 – Nutrition and growth kinetics in nitrogen- and phosphorus-limited cultures of the novel red tide flagellate *Chattonella ovata* (Raphidophyceae). Harmful Algae, 7: 26-32.

Yoshimatsu, S., 1987 - The cysts of *Fibrocapsa japonica* (Raphidophyceae) found in a bottom sediment in Harima-Nada, Eastern Inland Sea of Japan. Bulletin of the Plankton Society of Japan, 34: 25-31.

Young, E. B., and Beardall, J., 2003 – Photosynthetic function in *Dunaliella tertiolecta* (Chlorophyta) during a nitrogen starvation and recovery cycle. J. Phycol., 39: 897-905.

Zhang, Y., Fu, F. X., Whereat, E., Coyne, K. J., Hutchins, D. A., 2006 – Bottom-up controls on a mixed-species HAB assemblage: a comparison on sympatric *Chattonella subsalsa* and *Heterosigma akashiwo* (Raphidophyceae) isolates from the Delaware Inland Bays, USA. Harmful Algae, 5: 310-320.

Zingone, A., Honsell, G., Marino, D., Montresor, M., e Socal, G., 1990 – Fitoplancton, in: Innamorati M., Ferrari I., Marino D., Ribera d'Alcalà M., 1990 – Metodi nell'ecologia del plancton marino. Nova Thalassia vol. 11.

7. Appendix: List of phytoplankton taxa	
Bacillariophyceae	
Amphora sp. 70 µm	
Asterionellopsis glacialis	(Castracane) Round
Asteromphalus sp. cf. *flabellatus*	(Brébisson) Greville
Asteromphalus spp.	
Bacteriastrum furcatum	Shadbolt
Chaetoceros sp. cf. *affinis*	Lauder
Chaetoceros spp. ≤ 20 µm	
Cylindrotheca closterium	(Ehrenb.) Lewin and Reimann
Dactyliosolen blavyanus	(H. Peragallo) Hasle
Detonula pumila	(Castracane) Gran
Diploneis spp. ≥ 20 µm	
Ditylum brightwellii	(West) Grunow
Guinardia cilyndrus	(Cleve) Hasle
Guinardia sp. cf. *delicatula*	(Cleve) Hasle
Guinardia striata	(Stolterfoth) Hasle
Haslea wawrikae	(Hustedt) Simonsen
Helicotheca tamesis	(Shrubsole) Ricard
Hemiaulus hauckii	Grunow in Van Heurck
Hemiaulus sp. cf. *membranaceus*	Cleve
Leptocylindrus mediterraneus	(H. Peragallo) Hasle
Leptocylindrus minimus	Gran
Lioloma pacificum	(Cupp) Hasle
Lioloma sp.	
Meuniera membranacea	(P.T. Cleve) Silva
Naviculaceae spp. ≤ 20 µm	
Naviculaceae spp. ≥ 20 µm	
Naviculaceae spp. ≥ 50 µm	
Nitzschia sp. 71 µm	
Planktoniella sol	(Wallich) Schűtt
Pleurosigma sp. cf. *normannii*	Ralf in Pritchard
Pleurosigma spp. ≥ 50 µm	
Proboscia alata	(Brightwell) Sundstrőm
Pseudonitzschia sp. cf. *delicatissima*	(Cleve) Heiden
Pseudonitzschia sp. cf. *pseudodelicatissima*	(Hasle) Hasle
Pseudonitzschia sp. cf. *pungens*	(Grunow ex Cleve) Hasle
Pseudonitzschia sp. cf. *subcurvata*	(Hasle) Fryxell
Pseudonitzschia spp. ≥ 20 µm	
Pseudonitzschia spp. ≥ 50 µm	
Rhizosolenia sp. cf. *clevei*	Ostenfeld
Rhizosolenia sp. cf. *hyalina*	Ostenfeld
Rhizosolenia sp. cf. *imbricata*	Brightwell
Rhizosolenia sp. cf. *setigera*	Brightwell
Rhizosolenia sp. cf. *styliformis*	Brightwell
Rhizosoleniaceae spp.	
Skeletonema sp. cf. *costatum*	(Greville) Cleve
Skeletonema spp.	
Synedra sp. cf. *affinis*	(Kutzing) Grunow

Synedra spp. ≥ 20 µm	
Synedra spp. ≥ 50 µm	
Thalassionema frauenfeldii	(Grunow) Hallegraeff
Thalassionema sp. 12 µm	
Thalassionema sp. cf. *nitzschioides*	(Grunow) Grunow ex Hustedt
Thalassionema sp. cf. *pseudonitzschioides*	(Schuette & Schrader) Hasle
Thalassionema spp. ≥ 50 µm	
Thalassiosira rotula	Meunier
Thalassiosira sp. cf. *anguste-lineata*	(Schmidt) Fryxell et Hasle
Thalassiosira sp. cf. *mediterranea*	(Schrőder) Hasle
Thalassiosira sp. cf. *partheneia*	Schrader
Thalassiosira spp. ≤ 20 µm	
Thalassiosira spp. ≥ 20 µm	
Thalassiothrix sp. cf. *longissima*	Cleve & Grunow
Thalassiothrix spp. ≥ 50 µm	
Undetermined centric diatoms ≤ 20 µm	
Undetermined centric diatoms ≥ 20 µm	
Undetermined centric diatoms ≥ 50 µm	
Undetermined pennate diatoms ≤ 20 µm	
Undetermined pennate diatoms ≥ 20 µm	
Undetermined pennate diatoms ≥ 50 µm	
Dinophyceae	
Amphidinium sp. cf. *sphenoides*	Wulff
Amphidoma caudata	Halldall
Amphisolenia bidentata	Schrőder
Amphisolenia globifera	Stein
Brachydinium capitatum	Taylor
Centrodinium maximum	Pavillard
Ceratium belone	Cleve
Ceratium carriense	Gourret
Ceratium cf *tripos*	(O.F. Műller) Nitzsch
Ceratium contortum var. *karstenii*	(Pavillard) Sournia
Ceratium declinatum f. *majus*	Jőrgensen
Ceratium extensum	(Gourret) Cleve
Ceratium furca	(Ehrenb.) Claparéde & Lachmann
Ceratium furca var. *furca*	(Ehrenb.) Claparéde & Lachmann
Ceratium fusus	(Ehrenb.) Dujardin
Ceratium fusus var. *seta*	(Ehrenb.) Dujardin
Ceratium horridum	(Cleve) Gran
Ceratium pentagonum	Gourret
Ceratium pentagonum f. *turgidum*	(Jőrg.) Jőrgensen
Ceratium pentagonum var. *robustum*	(Cleve) Jőrgensen
Ceratium sp. cf. *falcatum*	(Kofoid) Jőrgensen
Ceratium sp. cf. *kofoidii*	Jőrgensen
Ceratium sp. cf. *macroceros*	(Ehrenb.) Vanhöffen
Ceratium spp.	
Ceratium trichoceros	(Ehrenb.) Kofoid
Ceratium trichoceros var. *contrarium*	(Gourret) Schiller
Ceratium tripos var. *atlanticum*	Ostenfeld
Ceratocorys horrida	Stein
Cochlodinium sp. cf. *brandtii*	Wulff

Cochlodinium sp. cf. *citron*	Kofoid & Swezy
Cochlodinium sp. cf. *pulchellum*	Lebour
Cochlodinium sp. 18 µm	
Cochlodinium spp. ≥ 20 µm	
Cochlodinium spp. ≥ 50 µm	
Dicroerisma psilonereiella	Taylor & Cattell
Dinophysis caudata	Saville-Kent
Dinophysis fortii	Pavillard
Dinophysis sp. cf. *expulsa*	Kofoid & Michener
Dinophysis sp. cf. *mitra*	(Schütt) Abé vel Balech
Dinophysis sp. cf. *parva*	Schiller
Dinophysis sp. cf. *rotundata*	Claparéde & Lachmann
Diplopsalis sp. 39 µm	
Goniodoma polyedricum	(Pouchet) Jőrgensen
Gonyaulax polygramma	Stein
Gonyaulax sp. cf. *hyalina*	Ostenfeld & Schmidt
Gonyaulax spinifera	(Clap. & Lachmann) Diesing
Gymnodiniaceae spp. ≤ 20 µm	
Gymnodiniaceae spp. ≥ 20 µm	
Gymnodiniaceae spp. ≥ 50 µm	
Gymnodinium catenatum	Graham
Gymnodinium sp. cf. *biconicum*	Schiller
Gymnodinium sp. cf. *elongatum*	Hope
Gyrodinium sp. cf. *fusiforme*	Kofoid & Swezy
Gyrodinium spp. ≤ 20 µm	
Gyrodinium spp. ≥ 20 µm	
Heterocapsa minima	Pomroy
Heterocapsa niei	(Loeblich) Morrill & Loeblich III
Heterocapsa rotundata	(Lohmann) Hansen
Histioneis depressa	Schiller
Histioneis sp. cf. *longicollis*	Kofoid
Kofoidinium velleloides	Pavillard
Lingulodinium polyedrum	(Stein) Dodge
Mesoporos adriaticus	(Schiller) Lillick
Micracanthodinium setiferum	(Lohmann) Deflandre
Minuscula bipes	(Paulsen) Lebour
Noctiluca scintillans	(Macartney) Kofoid & Swezy
Ornithocercus magnificus	Stein
Oxytoxum adriaticum	Schiller
Oxytoxum coronatum	Schiller
Oxytoxum curvatum	Kofoid
Oxytoxum diploconus	Stein
Oxytoxum laticeps	Schiller
Oxytoxum longiceps	Schiller
Oxytoxum longum	Schiller
Oxytoxum parvum	Schiller
Oxytoxum scolopax	Stein
Oxytoxum sp. cf. *caudatum*	Schiller
Oxytoxum sp. cf. *crassum*	Schiller
Oxytoxum sp. cf. *mediterraneum*	Schiller
Oxytoxum sp. cf. *sceptrum*	(Stein) Schrőder
Oxytoxum spp.	

Oxytoxum variabile	Schiller
Oxytoxum viride	Schiller
Phalacroma sp. cf. *argus*	Stein
Podolampas palmipes	Stein
Podolampas spinifer	Okamura
Pronoctiluca pelagica	Fabre-Domerque
Prorocentrum balticum	(Lohm.) Loeblich (Krakhmalny & Terenko)
Prorocentrum compressum	(Bailey) Abé ex Dodge
Prorocentrum dentatum	Stein
Prorocentrum lima	(Ehrenb.) Stein
Prorocentrum micans	Ehrenberg
Prorocentrum minimum	(Pavillard) Schiller
Prorocentrum sp. cf. *dactylus*	(Stein) Dodge
Prorocentrum sp. cf. *obtusidens*	Schiller
Prorocentrum sp. cf. *scutellum*	Schiller
Prorocentrum sp. cf. *vaginulum*	Schiller
Prorocentum gracile	Schűtt
Protoperidinium breve	(Paulsen) Balech
Protoperidinium diabolus	(Cleve) Balech
Protoperidinium divergens	(Ehrenberg) Balech
Protoperidinium quarnerense	(Schröder) Balech
Protoperidinium sp. cf. *conicum*	(Bailey) Balech
Protoperidinium sp. cf. *depressum*	(Bailey) Balech
Protoperidinium sp. cf. *ovum*	(Schiller) Balech
Protoperidinium sp. cf. *subinerme*	(Paulsen) Loeblich III
Protoperidinium steinii	(Jőrgensen) Balech
Protoperidinium spp. ≥20 μm	
Ptychodiscus sp. *(Karenia* sp.*)*	
Scrippsiella spp. ≤ 20 μm	
Scrippsiella spp. ≥ 20 μm	
Scrippsiella trochoidea	(Stein) Loeblich III
Torodinium robustum	Kofoid & Swezy
Undetermined athecate *Dinophyceae*	
Undetermined thecate *Dinophyceae* ≤ 15 μm	
Undetermined thecate *Dinophyceae* ≤ 20 μm	
Undetermined thecate *Dinophyceae* ≥ 20 μm	
Undetermined thecate *Dinophyceae* ≥ 50 μm	
Prymnesiophyceae Coccolithophorales	
Acanthoica aculeata	Kamptner
Acanthoica quattrospina	Lohmann
Algirosphaera quadricornu	(Schiller) Norris
Algirosphaera robusta	(Lohmann) Norris
Alisphaera ordinata	(Kamptner) Heimdal
Anoplosolenia brasiliensis	(Lohmann) Deflandre
Anthosphaera fragaria	Kamptner
Calcidiscus leptoporus	(Murray & Blackman) Loeblich & Tappan
Calciosolenia murrayi	Gran
Calyptrolithophora gracillima	(Kamptner) Heimdal
Calyptrosphaera spp.	
Corisphaera sp.cf. *arethusae*	Kamptner
Coronosphaera sp. cf. *binodata*	(Kamptner) Gaarder

Coronosphaera sp. cf. *mediterranea*	(Lohmann) Gaarder
Dactylethra pirus	(Kamptner) Norris
Discosphaera tubifer	(Murray & Blackman) Ostenfeld
Emiliania huxleyi	(Lohmann) Hay & Mohler
Florisphaera profunda	Okada & Honjo
Gephyrocapsa oceanica	Kamptner
Halopappus adriaticus	Schiller
Helicosphaera carteri	(Wallich) Kamptner
Helladosphaera sp. cf. *cornifera*	(Schiller) Kamptner
Michaelsaria elegans	Gran
Ophiaster hydroideus	(Gran) Manton & Oates
Periphyllophora sp. cf. *mirabilis*	(Schiller) Kamptner
Rhabdosphaera claviger	Murray & Blackman
Syracosphaera sp. cf. *histrica*	Kamptner
Syracosphaera pulchra	Lohmann
Syracosphaera sp. cf. *nodosa*	(Kamptner) Okada & McIntyre
Syracosphaera spp.	
Thorosphaera flabellata	Halldall & Markali
Umbilicosphaera sibogae	(Weber van Bosse) Gaarder
Zigosphaera sp. cf. *hellenica*	Kamptner
Prynmnesiophyceae Prymnesiales	
Chrysochromulina sp. cf. *hirta*	Manton
Chrysochromulina sp. cf. *parkeae*	Green & Leadbeater
Chrysochromulina sp.	
Phaeocystis sp.	
Chrysophyceae	
Actinomonas sp.	
Dinobryon faculiferum	(Willén) Willén
Dinobryon sp. 6 μm	
Meringosphaera tenerrima	Schiller
Ollicola vangoorii	(Conrad) Vőrs
Cryptophyceae	
Cryptomonadaceae spp.	
Dictyochophyceae	
Dictyocha fibula	Ehrenberg
Dictyocha speculum	Ehrenberg
Mesocena sp.	
Prasinophyceae	
Pseudoscourfieldia marina	(Throndsen) Manton
Pyramimonas spp.	
Tetraselmis sp. 1	
Prasinophyceae spp. $\leq$ 10 μm	
Raphidophyceae	
Fibrocapsa japonica	Toriumi & Takano
Heterosigma akashiwo	(Hada) Hada ex Hara & Chihara

Incertae sedis	
Leucocryptos marina	(Braarud) Butcher
Paulinella ovalis	Johnson, Hargraves & Sieburth
Undetermined nanoplanktonic flagellates	

Index:

1. Introduction

1.1 Photoacclimation in phytoplankton, p.1

1.2 Photoprotective and photoinhibiting mechanisms, p.2

1.3 How to measure photoacclimation: photosynthesis-irradiance (PE) curves, p.3

1.4 Photosynthetic parameters covariation, p.5

1.5 Aim of the research, p.6

2. Materials and Methods

2.a Field measurements

2.a.1 Sampling strategy and measurements, p.10

2.a.2 Pigments analysis, p.11

2.a.3 Nutrients analysis, p.12

2.a.4 Microscopic analysis, p.12

2.a.5 Statistical analysis, p.13

2.a.6 Genomic DNA extraction and PCR amplification, p.14

2.b Laboratory experiments

2.b.1 Experimental design and sampling strategy, p.16

2.b.2 Nutrient measurements and particle counting and sizing, p.18

2.b.3 Particulate organic and inorganic carbon and nitrogen (POC, PON and DIC), p.18

2.b.4 Pigments analysis, p.19

2.b.5 Light absorption coefficients a(λ), p.19

2.b.6 Photosynthesis-irradiance (PE) curves by oxygen measurements, p.19

2.b.7 Photosynthesis-irradiance (PE) curves by variable fluorescence, p.20

3. Results

3.a Field measurements

3.a.1 Hydrology, p.22

3.a.2 *In vivo* fluorescence, p.28

3.a.3 Phytoplankton biomass density and composition, p.29

3.a.4 Pigment composition, p.38

3.a.5 Photoprotective carotenoids, p.47

3.a.6 Statistical analysis, p.50

3.b Laboratory experiments

3.b.1 Experiment 1: sinusoidal light (26-hours measurements)

- Photosynthetic parameters by oxygen measurements, p.60
- Cell cycle, p.64
- Organic carbon and nitrogen, p.64
- Inorganic carbon and nitrogen, p.66
- Pigments, p.66
- *In vivo* absorption, p.71

3.b.2 Experiment 2: from sinusoidal to continuous light (26-hours measurements)

- Photosynthetic parameters by oxygen measurements, p.75
- Cell cycle, p.78
- Organic carbon and nitrogen, p.78
- Inorganic carbon and nitrogen, p.80
- Pigments, p.80
- *In vivo* absorption, p.85

3.b.3 Experiment 3: N-starvation in continuous light (8-days measurements)

- Photosynthetic parameters by oxygen measurements, p.89
- Photosynthetic parameters by variable fluorescence measurements, p.90
- Cell cycle, p.91
- Organic carbon and nitrogen, p.92
- Inorganic carbon, p.94
- Pigments, p.94

3.b.4 Experiment 4: sinusoidal light (3 days measurements)

- Photosynthetic parameters by oxygen measurements, p.101
- Cell cycle, p.104
- Organic carbon and nitrogen, p.105
- Inorganic carbon and nitrogen, p.106
- Pigments, p.107

3.b.5 Experiment 5: from sinusoidal to continuous light (~30 hours measurements)

- Photosynthetic parameters by oxygen measurements, p.114
- Cell cycle, p.115
- Organic carbon and nitrogen, p.116
- Inorganic carbon and nitrogen, p.118
- Pigments, p.118

3.b.6 Experiment 6: from continuous back to sinusoidal light (~14 hours measurements)

- Photosynthetic parameter by oxygen measurements, p.124
- Cell cycle, p.125
- Organic carbon and nitrogen, p.126
- Inorganic carbon and nitrogen, p. 127
- Pigments, p.128

4. Discussion

4.a Field measurements

4.a.1 Hydrology and nutrients, p. 134

4.a.2 Phytoplankton community characterisation, p.135

4.a.3 Photoprotective carotenoids, p.139

4.a.4 Statistical analysis, p.140

4.b Laboratory experiments

4.b.1 Experiment 1: sinusoidal light, p.142

4.b.2 Experiment 2: from sinusoidal to continuous light, p.147

4.b.3 Experiment 3: N-starvation in continuous light, p.151

4.b.4 Experiment 4: sinusoidal light, p.153

4.b.5 Experiment 5: from sinusoidal to continuous light, p.155

4.b.6 Experiment 6: from continuous back to sinusoidal light, p.157

5. Conclusions p.159

6. Bibliography p.163

7. Appendix p.174

Index